Modeling and Analysis of High Frequency Interconnects Using Doped Multilayer Graphene Nanoribbon

A Thesis

submitted in fulfillment of the requirement for the award of the degree of

Doctor of Philosophy

in

Department of Electronics and Communication Engineering

Submitted by

Akanksha Upadhyay

Reg. No. 901806001

Under the Supervision of

Dr. Mayank Kumar Rai
Professor
DECE

Dr. Rajesh Khanna
Professor
DECE

Department of Electronics & Communication Engineering
Thapar Institute of Engineering and Technology
Patiala-147001

February, 2025

Declaration

I, **Akanksha Upadhyay,** hereby declare that the work contained in the thesis entitled "Modeling and Analysis of High Frequency Interconnects Using Doped Multilayer Graphene Nanoribbon" being submitted by me to Department of Electronics and Communication Engineering, Thapar Institute of Engineering and Technology, Patiala in fulfillment for the award of degree of "Doctor of Philosophy" is a record of authentic research work carried out by me under the supervision of Dr. Mayank Kumar Rai and Dr. Rajesh Khanna. The matter presented in this thesis does not incorporate any material previously published or written by any other person except where due reference is made in the text. The results obtained in this thesis have not been submitted in part or full to any other institute or University for the award of degree or diploma.

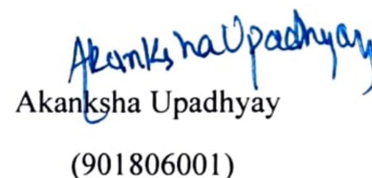

Date: 6/02/2025

Akanksha Upadhyay

(901806001)

This is to certify that the above statement made by the candidate is correct and true to the best of my knowledge and belief. She has worked under my supervision and fulfilled the requirements for the submission of this thesis which has reached the requisite standard.

Dr. Mayank Kumar Rai

Professor (DECE)

TIET, Patiala

Date: 6/02/2025

Dr. Rajesh Khanna

Professor (DECE)

TIET, Patiala

Date: 6/02/2025

…..to my loved ones

Abstract

The increasing need for faster communication and computing systems has created a demand for interconnects capable of handling sharper signal transitions and operating at higher frequencies. At the same time, driven by the need for enhanced performance, the semiconductor industry has aggressively scaled down the size of devices and interconnects. However, the continuous evolution and rapid scaling of device integration technology, have led to significant performance challenges for conventional copper (Cu) based high-speed on-chip interconnects. Hence, researchers are on a quest to find a suitable alternative that addresses these limitations while ensuring efficient and reliable performance in future high-speed, nanoscale systems.

Recently, intercalation-doped multilayer graphene nanoribbons (MLGNRs) have emerged as a promising alternative for Cu interconnects, offering remarkable electronic, transport, mechanical, and thermal properties. However, despite the promising enhancements offered by intercalation doping, the practical application of MLGNR as on-chip interconnects is limited by extrinsic scatterers and skin effect at high frequencies, thereby aggravating signal integrity issues and compromising the overall performance, functionality, and reliability of high-speed systems. Further research is crucial to mitigate these challenges and fully realize the potential of MLGNR for high-speed on-chip interconnects.

In this thesis, an impedance model is developed by incorporating the scattering-limited realistic effective mean free path (MFP), $\lambda_R(T)$, for various configurations of MLGNR interconnects to extract frequency-independent circuit parameters. The MLGNR configurations include undoped MLGNR (viz., horizontal top-contact (HTC), horizontal side-contact (HSC), and vertical top-contact (VTC)), and intercalation-doped HTC-MLGNR (with AsF_5, $FeCl_3$, and Li dopants). The optimistic intrinsic-phonon-limited effective MFP, $\lambda_P(T)$, for perfect MLGNR is also considered for impedance analysis. The circuit parameters for MLGNR variants are analyzed and compared to mixed carbon nanotube (MCNT) bundles, and smooth and rough Cu variants across a temperature range of 300 K to 500 K. Further, the impact of corrugation amplitudes (10 pm to 170 pm) on the circuit parameters of MLGNR and Cu interconnects are analyzed at 300 K. The findings indicate that the extrinsic scattering sources, particularly structural edge roughness (SER) of GNR and corrugations of dielectric surface, significantly

increase the resistance of both undoped and doped MLGNR interconnects compared to Cu variants.

Subsequently, a methodology incorporating the scattering-limited realistic effective MFP and a finite-thickness-dependent skin effect model is proposed for extracting the frequency-dependent impedance of MLGNR interconnects. By employing the proposed methodology, the frequency-dependent characteristics of circuit parameters for MLGNR interconnects are obtained and compared with MCNT bundle and Cu interconnects over a frequency range of 1 GHz - 10^4 GHz at a temperature of 300 K. The results show that due to skin effect at high frequencies, more pronounced impact of scatterers is observed, thereby exacerbating effective resistance of MLGNR interconnects.

After establishing the scattering-limited, frequency-independent impedance model, this work performs a temperature-dependent comparative analysis of MLGNR, MCNT bundles, and Cu interconnects in capacitively coupled configurations. Using SPICE simulations, crosstalk-induced delay is evaluated, revealing that MLGNR variants outperform MCNT bundles and Cu interconnects for $\lambda_P(T)$, but show inferior performance compared to Cu for $\lambda_R(T)$. Among MLGNR and MCNT bundle interconnects, lithium intercalation-doped HTC-MLGNR (Li-D HTC-MLGNR) achieves the lowest crosstalk-induced delay for both $\lambda_P(T)$ and $\lambda_R(T)$. An ABCD parameter-based analytical model further examines transient response, 3-dB bandwidth, and relative stability, showing MLGNR's superior stability despite Cu's advantage in step response and bandwidth. Moreover, Li-D HTC-MLGNR interconnects, without SER and placed on substrates like Silicon carbide (SiC) and Boron Nitride (BN), exhibit faster rise times than Cu counterparts. These findings underscore the need to eliminate scattering sources like SER and corrugations on dielectric surface for MLGNR's practical on-chip applications.

Furthermore, the frequency-dependent circuit parameters are employed for evaluating frequency varying crosstalk-induced delay, overshoot amplitude, and overshoot width for MLGNR interconnects using SPICE simulations for frequency range of 1 GHz to 10^4 GHz. Comparisons with MCNT bundles and Cu interconnects reveal that MLGNR and MCNT bundles, for $\lambda_R(T)$ and placed on Silicon dioxide (SiO_2), exhibit inferior performance compared to Cu variants due to skin effect and scatterers. However, optimized Li-D HTC-MLGNR (O-Li-D HTC-MLGNR) placed on SiC, in the absence of substrate polar phonons (SPPs) and SER, demonstrates the minimal impact from frequency variations and skin effect, and superior performance. Therefore, to benefit from the advantages of MLGNR-based interconnects at high

frequencies, intercalation doping with Li, utilizing SiC as dielectric, and eliminating scatterings with rough edges and substrate SPPs are desired.

Subsequently, the frequency-dependent traits of crosstalk-induced delay and noise area, and the mean time to failure due to electromigration (EM-MTF) are analyzed for O-Li-D HTC-MLGNR interconnects under the influence of scatterers, skin effect, and process and temperature variations. As a result of variations in process parameters and temperature, the O-Li-D HTC-MLGNR exhibits an increase in variations of crosstalk-induced delay and noise area, accompanied by a reduction in variations of EM-MTF as the frequency increases. The impact of process and temperature variations gets enhanced at higher frequencies for O-Li-D HTC-MLGNR and, hence, must be eradicated for reliable interconnect design and operation.

Finally, a MLGNR-based single-tier on-chip nanoscale via-interconnect scheme (VIS) is proposed, which combines the Li-D VTC-MLGNR via and Li-D HTC-MLGNR interconnect, as a prospect for monolithic 3D (M-3D) ICs. To go beyond the simplifying assumptions of perfect MLGNR and conventional skin effect, this study incorporates the impact of extrinsic scatterers in a realistic MLGNR and considers the one-dimensional skin depth formula for MLGNR-based interconnect and via. A combined equivalent circuit model is developed to analyze the challenges induced by crosstalk effects in perfect and realistic MLGNR VIS. The results show that for width in the range of 5 nm - 30 nm, perfect VIS outperforms realistic VIS in terms of crosstalk-induced delay. Moreover, at high frequencies ranging from 1 GHz-10^4 GHz with a width of 16 nm, realistic VIS demonstrates a performance decline of 243.18% (5.3934×10^3%) for l=4.8 μm (1 mm), respectively, in comparison to perfect VIS. Hence, in order to leverage the potential of MLGNR-based VIS for M-3D ICs at high frequencies, it is imperative to integrate Li-intercalation doping and mitigate the impact of extrinsic scatterers in MLGNR.

Acknowledgement

First and foremost, I would like to extend my deepest gratitude to the Divine Universe for bestowing me with patience and strength to complete this thesis. At this juncture, I have many people to thank with open arms for their help, and words will probably fall short.

I would like to express my heartfelt gratitude to my thesis supervisors, Dr. Mayank Kumar Rai, Professor, DECE, TIET and Dr. Rajesh Khanna, Professor, DECE, TIET. Their exceptional guidance, encouragement, and timely support have been instrumental in this thesis. Their invaluable advice has profoundly shaped both my professional and personal growth.

I extend my sincere thanks to the administration and management of TIET for their unwavering support during my studies. Special appreciation goes to the Director, TIET, Patiala, for his consistent encouragement. I am deeply thankful to my doctoral committee members, Dr. Shalini Batra, Professor and Head, DCSE, TIET, Dr. Sanjay Sharma, Professor, DECE, TIET, and Dr. Shireesh Kumar Rai, Assistant professor, DECE, TIET, for their valuable insights and contributions to my work. My gratitude also goes to Dr. Kulbir Singh, Professor and Head, DECE, TIET, for his kind support throughout my studies.

Special thanks to my friends, Himani Thakur, Ritika Sharma, Rashbha Sharma, Garima Thakur, Aditi Bajaj, Sukhmani Kaur, Shailza Sharma, Nitika Sharma, and Kiran Sharma, their unwavering support and friendship have been a source of strength.

My deepest gratitude goes to my parents, Mrs. Indu Bala and Mr. Lalit Kumar Sharma, and my in-laws, Mrs. Nirmla Thakur and Mr. Hari Chand Thakur, for their continuous support and patience. I extend my heartfelt thanks to my husband, Hanit Thakur, his support, encouragement, and patience have been my cornerstone, and without his understanding and sacrifices, this achievement would not have been possible. A Special thanks to my younger brother, Akshat Sharma, for his encouragement and support.

I am immensely grateful to everyone who has supported me, directly or indirectly, throughout this journey.

Akanksha Upadhyay

Table of Contents

Title	Page No.
Declaration	**ii**
Dedication	**iii**
Abstract	**iv**
Acknowledgement	**vii**
Table of Contents	**viii**
List of Figures	**xi**
List of Tables	**xvi**
List of Abbreviations	**xviii**
List of Symbols	**xx**
Chapter 1 Introduction	1
1.1 Introduction	1
1.2 Problem Statement	4
1.3 Thesis Organization	5
Chapter 2 MLGNR-Based High-Frequency Interconnects: A Review	7
2.1 Introduction	7
2.2 Interconnects	7
2.2.1 MLGNR-Based Interconnects	10
2.2.2 MLGNR Interconnect Configurations and Intercalation Doping	10
2.2.3 Hybrid Interconnects	12
2.2.4 Growth of MLGNR Interconnects	13
2.2.5 Performance Limiting Factors in MLGNR	14
2.3 Performance Evaluation of MLGNR Interconnects	18
2.3.1 Crosstalk Effects in MLGNR Interconnects	18
2.3.2 High-Frequency Skin Effect Aware Analysis	25
2.3.3 Electromigration Effects in MLGNR Interconnects	27
2.3.4 Impact of Process and Temperature Variations	29
2.4 MLGNR: Prospect for Monolithic 3D ICs	30
2.5 Chapter Summary	33

Chapter 3 High-Frequency Impedance Modeling and Analysis of MLGNR Interconnects 35

3.1 Introduction 35

3.2 Frequency-Independent Circuit Modeling and Analysis 36

3.2.1 Circuit Modeling for MLGNR Interconnects 36

3.2.2 Temperature-Dependent Analysis of Circuit Parameters: MLGNR Versus MCNT Bundle, and Cu interconnects 41

3.2.3 Corrugation-Amplitude-Dependent Analysis of Circuit Parameters for MLGNR and Cu interconnects 45

3.3 Frequency-Dependent Circuit Modeling and Analysis 48

3.3.1 Frequency-Dependent Circuit Modeling for MLGNR Interconnects 48

3.3.2 Frequency-Dependent Analysis of Circuit Parameters: MLGNR Versus MCNT bundle and Cu interconnects 52

3.4 Chapter Summary 59

Chapter 4 Signal Integrity Analysis in MLGNR Interconnects 61

4.1 Introduction 61

4.2 Frequency-Independent Crosstalk Analysis 62

4.2.1 Temperature-Dependent Crosstalk-Induced Delay Analysis 63

4.2.2 Optimizing Width for Minimum Crosstalk-Induced Delay 66

4.2.3 Transient Response and 3-dB Bandwidth Analysis 68

4.2.4 Relative Stability Analysis 73

4.3 Frequency-Dependent Crosstalk Analysis 75

4.4 Chapter Summary 80

Chapter 5 High-Frequency Challenges under Process and Temperature Variations 82

5.1 Introduction 82

5.2 Impact of Process and Temperature Variations on Circuit Parameters 83

5.3 Impact of Process and Temperature Variations on Frequency-Dependent MLGNR Performance 85

5.4 Impact of Process and Temperature Variations on MLGNR Performance at Fixed Frequency 88

5.5 Chapter Summary 91

Chapter 6 MLGNR-Based Via-Interconnect Scheme (VIS) for Monolithic 3D ICs 93

6.1 Introduction 93

6.2 Equivalent Circuit Modeling of MLGNR-Based VIS 94

6.2.1 Frequency-Independent Circuit Model 95

6.2.2 Frequency-Dependent Circuit Model 96
6.3 Analysis of Circuit Parameters for MLGNR-Based VIS 97
6.3.1 Width-Dependent Analysis 98
6.3.2 Frequency-Dependent Analysis 103
6.4 Crosstalk Analysis in MLGNR-Based VIS 105
6.4.1 Width-Dependent Analysis 106
6.4.2 Frequency-Dependent Analysis 109
6.5 Chapter Summary 110
Chapter 7 Conclusions and Future Scope 112
7.1 Introduction 112
7.2 Summary of Key Findings 112
7.2.1 High-Frequency Impedance Modeling and Analysis of MLGNR Interconnects 113
7.2.2 Signal Integrity Analysis in MLGNR Interconnects 114
7.2.3 High-Frequency Challenges under Process and Temperature Variations 116
7.2.4 MLGNR-Based Via-Interconnect Scheme (VIS) for Monolithic 3D ICs 117
7.3 Main Research Contributions 118
7.4 Future Scope of the Work 119
References 121
List of publications 139

List of Figures

Figure No.	Title	Page No.
Figure 1.1	Structure of (a) armchair GNR, and (b) zigzag GNR [25].	2
Figure 2.1	Vertical levels of interconnects on an IC [1].	8
Figure 2.2	Configurations of MLGNR (a) HTC-MLGNR, (b) HSC-MLGNR, and (c) VTC-MLGNR [72, 73].	11
Figure 2.3	Schematic of (a) Cu-carbon nanotube (Cu-CNT) composite, (b) Cu-Graphene hybrid, and (c) Cu-Carbon hybrid [77, 80, 81].	13
Figure 2.4	Fabrication steps for $FeCl_3$-doped HTC-MLGNR [15].	14
Figure 2.5	Fabrication steps for Vertical MLG [72, 74].	14
Figure 2.6	(a) Two and (b) three coupled interconnect line configurations.	18
Figure 2.7	Void formation in Cu interconnects due to electromigration [131]	27
Figure 3.1	Schematics of MLGNR configurations (a) U-HTC-MLGNR, (b) stage-2 AsF_5-D HTC-MLGNR, (c) stage-1 $FeCl_3$-D HTC-MLGNR, (d) stage-1 Li-D HTC-MLGNR, (e) U-VTC-MLGNR and, (f) U-HSC-MLGNR [72, 73].	37
Figure 3.2	The equivalent circuit model for a single GNR layer [122].	38
Figure 3.3	Resistive network of (a) HTC-MLGNR, (b) HSC-MLGNR and (c) VTC-MLGNR [19, 72].	40
Figure 3.4	Mean free path versus temperature curves for GNR.	42
Figure 3.5	Mean free path versus corrugation amplitude for GNR.	45
Figure 3.6	Effective mean free path versus corrugation amplitude for GNRs with (having different w and p) and without SER.	46
Figure 3.7	Resistance p.u.l versus corrugation amplitude for (a) undoped and intercalation-doped MLGNR (with SER, p=1) and Cu interconnects, and (b) Li-D HTC-MLGNR (without SER and with SER (p=1 and p=0.6)) and Cu interconnects.	47

Figure 3.8 The scattering-source-dependent, temperature-dependent, and frequency-dependent equivalent transmission line model for MLGNR interconnect [150]. 48

Figure 3.9 Schematic of (a) electric field (E_x) in the x-direction inside an MLGNR interconnect, and (b) exponentially decaying electric field strength inside an MLGNR interconnect along the y-direction [41, 151]. 50

Figure 3.10 Mean free path as a function of (a) temperature (T), and (b) corrugation amplitude (δA) (T=300 K) for GNRs. 53

Figure 3.11 Skin depth variation with frequency for (a) MLGNR (case 2), Cu variants, and MCNT bundle, (b) Li-D HTC-MLGNR (placed on various dielectric substrates for case 1 and case 2) and Cu variants. 55

Figure 3.12 Resistance p.u.l. ($R(\omega,T)$) versus frequency for (a) MLGNR (case 2), Cu variants, and MCNT bundle, (b) Li-D HTC-MLGNR (placed on various dielectric substrates for case 1 and case 2) and Cu variants. 56

Figure 3.13 High-frequency p.u.l. resistance ($R(\omega,T)$) to dc resistance ($R(T)$) ratio for (a) MLGNR (case2), Cu variants, and MCNT bundle, (b) Li-D HTC-MLGNR (placed on various dielectric substrates for case 1 and case 2), and Cu variants, as a function of frequency. 57

Figure 3.14 Inductance p.u.l. $L(\omega,T)$ for (a) MLGNR (case 2), Cu variants, and MCNT bundle, (b) Li-D HTC-MLGNR (placed on various dielectric substrates for case 1 and case 2), and Cu variants, as a function of frequency. 58

Figure 3.15 Comparison of (a) the skin depth model outlined in this work with models from [40-42], and [44,45], and (b) the resistance and inductance model from this work with the model outlined in [40, 42], for Li-D HTC-MLGNR on SiC (case 1), as a function of frequency. 59

Figure 4.1 Schematic of three capacitively coupled interconnects. 62

Figure 4.2	Equivalent capacitively coupled three-line DIL architecture.	63
Figure 4.3	Crosstalk-induced delay vs temperature curves for undoped MLGNR (viz., VTC, HSC, and HTC), intercalation-doped HTC-MLGNR (with AsF_5, $FeCl_3$, and Li dopants), smooth and rough Cu, and MCNT bundle interconnects.	65
Figure 4.4	(a) Number of conducting channels ($N_{TM}(T)$), and (b) number of layers (N_H/N_V) as a function of interconnect width for undoped MLGNR (viz., VTC, HSC, and HTC), and intercalation-doped HTC-MLGNR (with AsF_5, $FeCl_3$, and Li dopants) (T=300 K).	67
Figure 4.5	Crosstalk-induced delay variation with interconnect width for U-MLGNR (viz., VTC, HSC, and HTC), D-HTC-MLGNR (with AsF_5, $FeCl_3$, and Li dopants), and Smooth and Rough Cu for (a) $\lambda_P(T)$, and (b) $\lambda_R(T)$ (T=300 K).	68
Figure 4.6	Equivalent circuit model of decoupled victim net.	69
Figure 4.7	Step response of undoped and intercalation-doped MLGNR (with SER, p=1, and δA =170 pm) and Cu interconnects.	70
Figure 4.8	Frequency response of undoped and intercalation-doped MLGNR (with SER, p=1, and δA=170 pm) and Cu interconnects.	71
Figure 4.9	Step response of Li-D HTC-MLGNR (without SER and with SER (p=1)) and Cu interconnects.	72
Figure 4.10	Step response of Li-D HTC-MLGNR using analytical transfer function and TSPICE simulation.	73
Figure 4.11	Nyquist plot of MLGNR (δA=170 pm, p=1) and Cu interconnects.	74
Figure 4.12	Nyquist plot of Li-D HTC-MLGNR interconnect with (having different δA and p=1), and without edge roughness (for various δA).	74
Figure 4.13	Aggressor-victim configuration for capacitively coupled MLGNR interconnects with CMOS as the driver.	76
Figure 4.14	Overshoot amplitude variation with frequency for (a) MLGNR (case 2), Cu, and MCNT bundle interconnects, (b) Li-D HTC-	77

MLGNR (placed on various dielectric substrates for case 1 and case 2), and Cu variants.

Figure 4.15 Overshoot width versus frequency for (a) MLGNR (case 2), Cu, and MCNT bundle interconnects (b) Li-D HTC-MLGNR (placed on various dielectric substrates for case 1 and case 2), and Cu variants. 78

Figure 4.16 Crosstalk-induced delay for (a) MLGNR (case 2), Cu, and MCNT bundle interconnects, (b) Li-D HTC-MLGNR (placed on various dielectric substrates for case 1 and case 2), and Cu variants, as a function of frequency. 79

Figure 5.1 Resistance and inductance as a function of frequency, considering variations in (a) δA, (b) T, (c) w, (d) E_f, and (e) δ_s for O-Li-D HTC-MLGNR. 84

Figure 5.2 Maximum variations (Δ_{max}) in (a) crosstalk-induced delay and (b) crosstalk-induced noise area with frequency for O-Li-D HTC-MLGNR, considering process and temperature variations. 87

Figure 5.3 Variations in crosstalk delay and crosstalk noise area with (a) corrugation amplitude (δA) and (b) temperature (T) for O-Li-D HTC-MLGNR at f=10^4 GHz. 89

Figure 5.4 Variations in (a) crosstalk-induced delay, (b) crosstalk-induced noise area, and (c) EM-MTF with width (w), fermi energy (E_f), and van der Waals gap (δ_s) for O-Li-D HTC-MLGNR at f=10^4 GHz. 90

Figure 6.1 Schematic showing (a) Li intercalation-doped HTC-MLGNR (Li-D HTC-MLGNR) interconnect, (b) undoped VTC-MLGNR via (U-VTC-MLGNR via), (c) Li-D VTC-MLGNR via, and (d) equivalent single-tier driver-via-interconnect-load (DVIL) circuit for a M-3D IC [15, 49, 58]. 95

Figure 6.2 (a) Effective mean free path (MFP) of realistic GNR ($\lambda_R(T)$) and perfect GNR ($\lambda_P(T)$) varying with width. (b) Number of transverse modes ($N_{TM}(T)$), and (c) Number of layers (N_L) varying with width for corresponding GNR-based interconnect and via materials. 98

Figure 6.3 Resistance versus width for realistic ($\lambda_R(T)$) and perfect ($\lambda_P(T)$) configurations of (a) Li-D HTC-MLGNR interconnect, and (b) undoped and Li-D VTC-MLGNR via. 100

Figure 6.4 Inductance and Capacitance versus width for (a) Li-D HTC-MLGNR interconnects, and (b) undoped and Li-D VTC-MLGNR via. 102

Figure 6.5 Skin depth varying with frequency for realistic ($\lambda_R(T)$) and perfect ($\lambda_P(T)$) configurations of (a) Li-D HTC-MLGNR interconnects, and (b) Li-D VTC-MLGNR via. 103

Figure 6.6 (a) Resistance, and (b) Inductance versus frequency for realistic ($\lambda_R(T)$) and perfect ($\lambda_P(T)$) configurations of (a) Li-D HTC-MLGNR interconnects, and (b) Li-D VTC-MLGNR via. 104

Figure 6.7 Mutually-coupled three-line single-tier DVIL architecture. 106

Figure 6.8 Normalized crosstalk-induced delay versus width for MLGNR-based VIS with undoped via and Li-D VTC-MLGNR via. 106

Figure 6.9 Normalized crosstalk-induced delay of MLGNR-based VIS with Li-D VTC-MLGNR via for (a) l=4.8 µm and 1 mm, and (b) realistic ($\lambda_R(T)$) VIS and perfect ($\lambda_P(T)$) VIS, at varying widths. 107

Figure 6.10 Crosstalk-induced delay versus frequency for MLGNR-based VIS with Li-D VTC-MLGNR via. 109

Figure 6.11 Crosstalk-induced delay versus via resistance (R_{via}) for (a) MLGNR-based realistic ($\lambda_R(T)$) VIS, and (b) MLGNR-based perfect ($\lambda_P(T)$) VIS, with Li-D VTC-MLGNR via at f=10^4 GHz. 110

List of Tables

Table No.	Title	Page No.
Table 3.1	Different properties of undoped MLGNR (viz., HTC, VTC, and HSC) and intercalation-doped HTC-MLGNR (with AsF_5, $FeCl_3$, and Li dopants) interconnects [18, 91].	42
Table 3.2	Interconnect circuit parameters for undoped MLGNR (viz., VTC, HTC, and HSC), intercalation-doped HTC-MLGNR (with AsF_5, $FeCl_3$, and Li dopants) and MCNT bundle, considering effective MFPs $\lambda_P(T)$ and $\lambda_R(T)$ (T=300 K - 500 K).	43
Table 3.3	Interconnect circuit parameters for rough and smooth Cu (T=300 K - 500 K).	43
Table 3.4	Properties of different interconnect variants.	54
Table 4.1	Optimal number of repeaters to reduce crosstalk-induced delay of intercalation-doped and undoped MLGNR, and Cu interconnects (l =1 mm).	64
Table 4.2	t_d, t_r, and 3-dB bandwidth for different configurations of undoped and intercalation-doped MLGNR (with SER, p=1, and δA =170 pm), and Cu interconnects.	71
Table 5.1	Interconnect parameters (viz., process and temperature) with their nominal values and variation range.	83
Table 5.2	Maximum variations (Δ_{max}) in EM-MTF with frequency for O-Li-D HTC-MLGNR considering process and temperature variations.	88
Table 5.3	Variations in EM-MTF with corrugation amplitude (δA) and temperature (T) for O-Li-D HTC-MLGNR at f=10^4 GHz.	89
Table 6.1	Comparison of MFP ($\lambda_R(T)$) values from present work with reported data.	99
Table 6.2	Properties of Li-D HTC-MLGNR interconnect and Li-D VTC-MLGNR via.	102

Table 6.3	Comparison of skin depth (Δ_{SD}) model from present work with existing models.	103
Table 6.4	Relative percentage increase in crosstalk delay τ (%) of MLGNR-based VIS with Li-D VTC-MLGNR via for realistic VIS ($\lambda_R(T)$) with respect to perfect VIS ($\lambda_P(T)$) at l=4.8 µm and 1 mm.	108
Table 6.5	Comparison of crosstalk delay for coupled single-tier VIS from present work with reported data [113].	109

List of Abbreviations

IC	Integrated circuit
Cu	Copper
VLSI	Very large scale integration
GNR	Graphene nanoribbon
CNT	Carbon nanotube
SLGNR	Single-layer graphene nanoribbon
MLGNR	Multilayer graphene nanoribbon
MFP	Mean free path
SER	Structural edge roughness
MCNT	Mixed carbon nanotube
IRDS	International roadmap for devices and systems
M-3D	Monolithic three-dimensional
2D	Two-dimensional
TSV	Through silicon vias
VIS	Via-interconnect scheme
CMOS	Complementary metal-oxide semiconductor
DSM	Deep sub-micron
Cu-CNT	Copper-Carbon nanotube
1D	One-dimensional
HSC-MLGNR	Horizontal side contact multilayer graphene nanoribbon
HTC-MLGNR	Horizontal top contact multilayer graphene nanoribbon
VTC-MLGNR	Vertical top contact multilayer graphene nanoribbon
CVD	Chemical vapor deposition

EBL	Electron-beam lithography
MOS	Metal-oxide semiconductor
MWCNT	Multi-walled carbon nanotube
SWCNT	Single-walled carbon nanotube
ESC	Equivalent single conductor
EMRA	Exponential matrix-rational approximation
FDTD	Finite-difference time-domain
SPICE	Simulation Program with Integrated Circuit Emphasis
EM-MTF	Mean time to failure due to electromigration
BEOL	Back-end-of-line
ILD	Interlayer dielectric
p.u.l.	Per unit length
SPP	Surface polar phonons
CI	Charged impurities
ITRS	International technology roadmap for semiconductors
DIL	Driver interconnect load
DVIL	Driver-via-interconnect-load
AR	Aspect Ratio

List of Symbols

$R(T)$	Equivalent p.u.l. temperature-dependent resistance
$L(T)$	Equivalent p.u.l. temperature-dependent inductance
$C(T)$	Equivalent p.u.l. temperature-dependent capacitance
w	Interconnect width
t	Interconnect thickness
y_{ILD}	Interlayer dielectric thickness
s	Spacing between two interconnects
δ_s	Van der Waals gap separating GNR layers
R_{mc}	Resistance of imperfectly coupled contact pad and GNR layer
$R_Q(T)$	Quantum contact resistance
$R_S(T)$	Scattering resistance
$R_T(T)$	Total p.u.l. resistance of single GNR layer
L_e	Magnetic inductance
$L_k(T)$	Kinetic inductance
C_e	Electrostatic capacitance
$C_q(T)$	Quantum capacitance
dx	Length of distributed section of the interconnect
l	Length of the interconnect
$\lambda_{eff}(T)$	Effective MFP of GNR
$N_{TM}(T)$	Number of transverse modes
$\lambda_P(T)$	Effective MFP of intrinsic-phonon-limited perfect GNR
$\lambda_R(T)$	Effective MFP of scattering-limited realistic GNR
$\lambda_{ac}(T)$	Temperature-dependent MFP in GNR due to acoustic phonon

$\lambda_{op}(T)$	Temperature-dependent MFP in GNR due to non-polar optical phonons
λ_{RS}	MFP due to resonant scatterers
λ_{CI}	MFP in GNR due to scatterings from charge impurities
$\lambda_{SPP}(T)$	Temperature-dependent MFP due to substrate SPPs
λ_{CD}	MFP due to atomic roughness of corrugated dielectric surface
λ_{SER}	MFP due to rough GNR edges
p	Probability of diffusively scattered electrons at the edge of GNR
E_i	E_i is the lowest/highest energy of ith conduction/valence sub-band for metallic armchair GNR
E_f	Fermi energy
δA	Corrugation amplitude of dielectric surface
N_H	Number of layers in HSC-MLGNR and HTC-MLGNR
N_L	Number of layers in VTC-MLGNR
R_Y	c-axis resistance between GNR layers
$\sigma_{c\text{-}axis}$	Conductivity in c-axis
v_f	Fermi velocity
h	Planck's constant
k_B	Boltzmann's constant
T	Temperature
f	Frequency
ω	Angular frequency
$Z_e(\omega,T)$	Effective p.u.l. frequency-dependent series impedance
$Y_e(\omega,T)$	Effective p.u.l. frequency-dependent shunt admittance
$R(\omega,T)$	Effective p.u.l. frequency-dependent resistance
$L(\omega,T)$	Effective p.u.l. frequency-dependent inductance
$C(\omega,T)$	Effective p.u.l. frequency-dependent capacitance

μ	Permeability of GNR
$\sigma(\omega,T)$	Frequency-dependent conductivity
$\sigma_{dc}(T)$	Effective dc conductivity
$\tau(T)$	Momentum relaxation time
α	Attenuation constant
β	Phase constant
Δ_{SD}	One-dimensional skin depth
Δ'	Conventional skin depth
R_d	Driver resistance
C_d	Driver capacitance
C_L	Load capacitance
R_L	Lumped resistance
C_c	Coupling capacitance
t_d	Delay time
t_r	Rise time
M	Mutual inductance

Chapter 1 Introduction

1.1 Introduction

Interconnects serve as the backbone for transmitting electrical signals among various electronic components, circuits, and systems within an integrated circuit (IC) [1]. Over the past few decades, the minimum feature size used to fabricate ICs in the semiconductor industry has decreased exponentially. This relentless reduction in feature size gives rise to several challenges for conventional copper (Cu) interconnects, such as electromigration, joule heating, surface roughness, grain-boundary scattering, and surface scattering [2–6]. Consequently, Cu experiences increased resistivity and diminished current carrying capacity, leading to performance limitations [2, 7, 8]. As a result of the issues faced by conventional Cu interconnects, researchers are on a quest to find a suitable candidate for very large scale integration (VLSI) on-chip interconnects. In recent years, the impressive electromigration reliability, high conductivity, and exceptional transport properties of carbon-based nanomaterials, such as graphene nanoribbons (GNRs) and carbon nanotubes (CNTs), have garnered significant attention for realizing on-chip interconnects [9–12]. Among these, GNRs are particularly preferred over CNTs as on-chip interconnects due to their planar structure, which aligns well with the semiconductor industry's fabrication technology. Furthermore, GNRs exhibit good chirality control during fabrication, making them more consistent and reliable for such applications [10, 13, 14].

Graphene sheets are patterned to form narrow strips of GNR with width in nanometer range [15, 16]. As illustrated in Fig. 1.1, GNRs can be categorized based on their chirality—i.e., the alignment of carbon atoms along the GNR edges—into armchair GNRs, which exhibit either metallic or semiconducting properties, and zigzag GNRs, which display metallic properties [16, 17]. Additionally, GNRs are classified based on the number of stacked GNR layers into single-layer GNRs (SLGNRs) and multilayer GNRs (MLGNRs). SLGNRs, with their single layer of graphene, possess very high intrinsic resistance. To achieve lower resistance and improved performance, MLGNRs are proposed for nano interconnects, where multiple GNR layers are stacked on top of one another [18, 19].

Significant interest has emerged in utilizing intercalation-doped MLGNRs as on-chip interconnects [10, 15, 18, 20–22]. Experimental findings indicate that the enhancement of

intrinsic mobility, conductivity, current-carrying capacity (approximately 10^8A/cm^2), fermi energy, mean free path (MFP), and overall performance of MLGNR is achieved by intercalation doping [10, 15, 18, 20, 23, 24]. This improvement renders MLGNRs more suitable for practical applications.

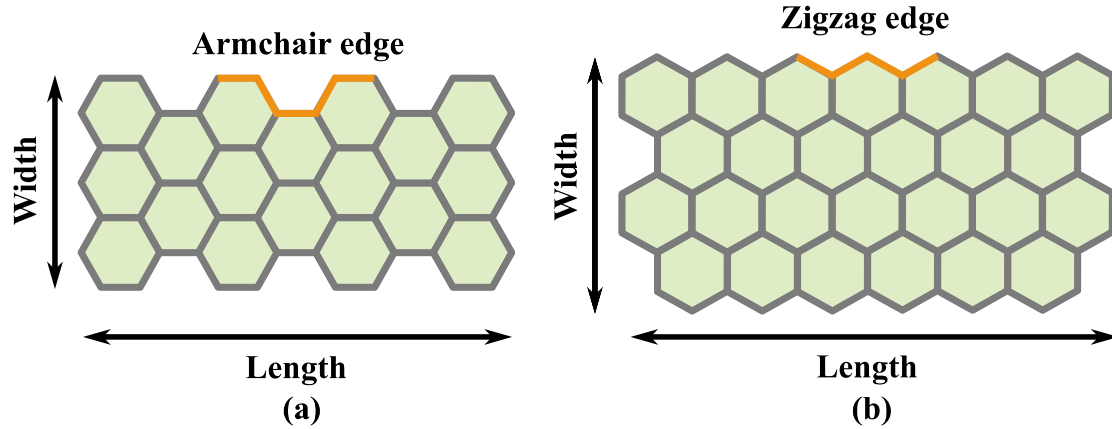

Figure 1.1 Structure of (a) armchair GNR and (b) zigzag GNR [25].

Despite the substantial interest and extensive experimental endeavors, the practical application of MLGNR as on-chip interconnects has been impeded by the existence of extrinsic scattering sources, limiting the electron MFP to less than one micrometer [10, 15, 16, 26–28]. As per the reports [15, 16, 26], the MFP is limited to a few nanometers and the conductivity of GNR is constrained by extrinsic scatterers. The extrinsic scatterers include structural edge roughness (SER) of GNR and dielectric-substrate-induced scatterers, such as charge impurities, temperature-dependent polar phonons, and atomic roughness of corrugated dielectric surface [26–29]. Several MFP and circuit models have been proposed considering all the scattering sources except SER [10, 17, 19, 22, 26, 28, 30]. Also, in a low-bias regime, the electrical transport in MLGNR depends on the temperature [31].

Thus, in this work, a new model for the scattering-source-dependent realistic effective MFP has been proposed, which incorporates SER and the corrugations of the dielectric surface for various configurations of MLGNR interconnects. Based on the realistic effective MFP, a temperature-dependent and scattering-source-dependent distributed transmission line equivalent model is considered for analysing the crosstalk effect, transient step response, frequency response, and relative stability of MLGNR interconnects. Furthermore, the results obtained for intercalation-doped MLGNR variants are compared with undoped MLGNR variants, mixed carbon nanotube (MCNT) bundles, and conventional Cu interconnects.

In the literature, MLGNR interconnects have been examined using essential performance indicators, including crosstalk-induced effects such as propagation delay and noise waveform [17, 22, 30, 32–36]. However, the proposed models relied on circuit models with frequency-invariant parameters. At high operational frequencies, circuit parasitics of MLGNR interconnects become dependent on frequency due to skin effect which exacerbates effective resistance, thereby worsening crosstalk-induced effects [37–39]. The high-frequency impedance models outlined in [40–43] fail to incorporate the impact of extrinsic scatterers present in GNR and the dependency of skin depth on the finite thickness of the MLGNR interconnects. Also, the impact of momentum relaxation time is not included in the one-dimensional effective skin depth model for miniaturized interconnects with finite thickness, as presented in [44, 45]. Moreover, these studies lack the performance analysis of MLGNR interconnects, particularly with respect to crosstalk effects. Therefore, in this work, a new method has been introduced for extracting the impedance of MLGNR interconnects across various frequencies, incorporating both the realistic effective MFP model limited by extrinsic scattering sources and a one-dimensional effective skin depth model. The frequency-dependent crosstalk effects are analyzed for intercalation-doped MLGNR interconnects and compared to those of undoped MLGNR variants, MCNT bundles, and conventional Cu interconnects.

Furthermore, electromigration poses a limitation on the reliability of MLGNR interconnects by reducing their lifetime and mean time to failure [36, 46–49]. Moreover, while recent studies have examined the effects of process and temperature variations on crosstalk-induced delay, noise waveform, and noise waveform area [50–55], the challenges posed by these variations in the presence of extrinsic scatterers, skin effect, crosstalk, and electromigration effects at high frequencies are not addressed. This work analyzes uncertainties in the performance of intercalation-doped MLGNR interconnect due to process and temperature variations for high-frequency applications.

The 2022 report by the International Roadmap for Devices and Systems (IRDS) recommended monolithic three-dimensional (M-3D) ICs as a promising alternative to overcome the challenges faced by two-dimensional (2D) ICs and through silicon vias (TSV) based 3D ICs [2, 56]. Various studies have explored potential materials for via-interconnect scheme (VIS) in M-3D ICs [15, 20, 49, 57, 58]. However, the impact of extrinsic scatterers, skin effect, and crosstalk effects on the performance of MLGNR-based VIS at high frequencies has not been documented. This work further investigates MLGNR-based VIS as a potential solution for M-

3D ICs and assesses the challenges arising from extrinsic scatterers, skin effect, and crosstalk effect at high frequencies.

1.2 Problem Statement

The limitations of conventional Cu interconnects have driven recent research towards alternative materials, with intercalation-doped MLGNR emerging as a promising candidate for high-speed on-chip interconnect applications. While intercalation doping offers notable advantages, the practical deployment of MLGNRs is impeded by extrinsic scattering mechanisms, including SER and dielectric-related scatterers. Additionally, the skin effect becomes increasingly significant at high frequencies, altering the circuit parasitics of MLGNR interconnects and exacerbating signal integrity issues.

Signal integrity challenges, such as crosstalk, signal delay, dielectric losses, process variations, and high-frequency losses, severely affect the performance, reliability, and functionality of modern ICs. These issues become more pronounced with the scaling of technology and increasing interconnect density, leading to signal distortion, reliability degradation, and intensified crosstalk effects that ultimately constrain the performance of high-speed circuits, particularly at GHz frequencies and beyond.

To address these challenges, it is imperative to develop a high-frequency impedance model that incorporates the effects of extrinsic scattering mechanisms and the skin effect for accurate and realistic performance analysis under worst-case scenarios. Furthermore, analyzing crosstalk behavior in coupled MLGNR interconnects using this model is crucial for mitigating its impact. The performance of MLGNR interconnects is also highly sensitive to process and temperature variations, which further complicates their reliability in high-frequency applications. Therefore, assessing and optimizing the performance of MLGNR interconnects under these variations is essential for ensuring their viability in nanoscale VLSI systems. From the above discussed research problem statement, **the objectives** of this thesis have been identified as follows:

1. To develop and analyze high-frequency impedance model for doped MLGNR interconnect.
2. To analyze the crosstalk induced noise in mutually coupled doped MLGNR interconnects.

3. Performance evaluation of the effects of process and temperature variations on crosstalk induced noise in mutually coupled interconnects of doped MLGNR.
4. To compare the results obtained through doped interconnects of MLGNR with undoped MLGNR and MCNT bundle interconnects.

1.3 Thesis Organization

This work presents a detailed modeling and characterization of impedance and circuit parameters for MLGNR interconnects, accounting for extrinsic scattering sources and skin effect. The performance of MLGNR interconnects is evaluated at high operational frequencies, comparing intercalation-doped MLGNRs with undoped MLGNRs, MCNT bundles, and Cu interconnects. The study also examines the impact of process and temperature variations on MLGNR performance at high frequencies. Additionally, the MLGNR-based via-interconnect scheme (VIS) is analyzed as a potential solution for monolithic 3D ICs (M-3D ICs), considering the effects of extrinsic scatterers, skin effect, and crosstalk. The thesis is organized into seven chapters, with a summary of each chapter provided below:

Chapter 1 introduces the thesis and highlights intercalation-doped MLGNRs as a promising alternative to conventional on-chip interconnects. It outlines the challenges of implementing MLGNR interconnects in practical high-frequency applications and defines the objectives based on the problem statement.

Chapter 2 provides a comprehensive review of the literature related to impedance and performance characteristics of MLGNR interconnects. The effects of intercalation doping, extrinsic scattering sources, high-frequency skin effect, crosstalk, electromigration, and process and temperature variations on MLGNR performance are reviewed extensively. Moreover, applications of MLGNR-based interconnects and via in M-3D ICs have been discussed.

Chapter 3 presents two equivalent impedance models for MLGNR interconnects: one with frequency-independent circuit parameters and the other with frequency-dependent circuit parameters. Both models incorporate the impact of extrinsic scattering sources as well as temperature effects. The temperature-dependent and corrugation-amplitude-dependent analysis of circuit parameters is done for intercalation-doped MLGNR interconnects and compared with undoped MLGNR, MCNT bundle, and Cu interconnects. Furthermore, in the

presence of high-frequency skin effect, frequency-dependent analysis of circuit parameters is presented for intercalation-doped MLGNR interconnects and compared to undoped MLGNR, MCNT bundles, and Cu interconnects.

Chapter 4 presents signal integrity analysis in three coupled MLGNR interconnects constrained by the impact of extrinsic scattering sources, temperature, skin effect, and crosstalk. Firstly, an impedance model with frequency-independent circuit parameters is utilized for temperature-dependent crosstalk-induced delay analysis of MLGNR interconnects using SPICE simulations. The results obtained are compared with those of the MCNT bundle and Cu interconnects. Additionally, interconnect width is optimized to obtain minimum crosstalk-induced delay. Subsequently, an analytical model and decoupling technique are utilized to analyse the transient response, 3-dB bandwidth, and relative stability of MLGNR interconnects. Secondly, the frequency-dependent impedance model is incorporated to evaluate frequency-varying crosstalk-induced delay, overshoot amplitude, and overshoot width for MLGNR interconnects using SPICE simulations. The results obtained are compared with those of the MCNT bundle and Cu interconnects.

Chapter 5 analyzes the impact of process and temperature variations on circuit parameters of MLGNR interconnects, considering the influence of extrinsic scattering sources and skin effect at high frequencies. The maximum variations in crosstalk-induced delay, and noise waveform area along with mean time to failure due to electromigration with frequency are analyzed and discussed considering process and temperature variations. Next, the effect of variations in corrugation amplitude, temperature, width, fermi energy, and van der Waals gap on crosstalk-induced delay, and noise area, as well as electromigration-induced mean time to failure are examined for MLGNR at f=10^4 GHz.

Chapter 6 presents the frequency-independent and frequency-dependent equivalent circuit model for MLGNR-based VIS as a prospect for M-3D ICs. The impact of extrinsic scatterers, and skin effect is incorporated in the equivalent circuit model. Subsequently, width-dependent and frequency-dependent analysis of circuit parameters is carried out for MLGNR-based VIS. The performance of MLGNR-based VIS is analyzed in terms of crosstalk-induced delay varying with width and frequency.

Chapter 7 summarizes the research findings, presents conclusions drawn from the analysis, and outlines future directions to address challenges in current interconnect technologies.

Chapter 2 MLGNR-Based High-Frequency Interconnects: A Review

2.1 Introduction

In the semiconductor industry, devices and interconnects have witnessed aggressive scaling to keep pace with the evolving demands of advanced technology [1]. However, the conventional copper (Cu) on-chip interconnects encounter substantial size effects, increased resistivity, and reduced current carrying capability when the wire width is reduced to sub-40 nm dimensions [2–6, 15]. Therefore, in order to address future integrated circuit (IC) requirements, researchers are exploring alternative high-performance interconnect solutions. Significant interest has emerged in utilizing graphene-derived multilayer graphene nanoribbon (MLGNR) as an on-chip interconnect due to its impressive electromigration reliability, high conductivity, and exceptional electronic and transport properties [9, 10, 12]. However, the electronic and transport properties of realistic nanoscale graphene nanoribbons (GNRs) are constrained by extrinsic scattering sources, including structural edge roughness (SER) and dielectric-induced scatterers. This leads to reduced conductivity and mean free path (MFP) in GNRs, consequently limiting the performance of MLGNR-based interconnects. Moreover, the global demand for faster communication and computing technology continues to rise, driving the need for systems that can handle sharper signal transitions and operate at higher frequencies. As a result, the growing demand for high-speed applications has significantly increased the performance requirements of interconnects, bringing attention to signal integrity issues that were once considered negligible. Signal integrity challenges such as signal delay, crosstalk, electromigration, dielectric losses, process variations, and high-frequency skin effect have become significant bottlenecks in achieving optimal performance, functionality, and reliability in high-speed systems. Therefore, this chapter offers a literature survey and thorough background on nanoscale on-chip interconnects based on Cu and MLGNR, followed by a comprehensive review on performance characteristics of MLGNR interconnects in the presence of extrinsic scatterers, skin effect, process and temperature variations, crosstalk, and electromigration effects.

2.2 Interconnects

Interconnect is the wiring system that links various functional blocks, transistors, and other circuit elements on the ICs. These interconnects are essential for providing clock, power,

ground, and other signals to the various nodes of the circuits and systems on the chip [1, 7]. Interconnects are typically organized into multiple vertical levels on a chip, as depicted in Fig. 2.1 and can be categorized into three types: local, intermediate, and global [1]. Local interconnects, situated close to the transistors, are thin and short, connecting closely packed components. Intermediate interconnects are slightly longer and broader than local interconnects and are responsible for distributing clock signals and other signals within a functional block. Global interconnects, located higher up in the ICs, are thicker, longer, and widely separated, facilitating connections between different functional blocks of the circuit. Via serves as connections between the vertical interconnect levels, allowing signals and power to transmit from one layer to the next, as shown in Fig. 2.1.

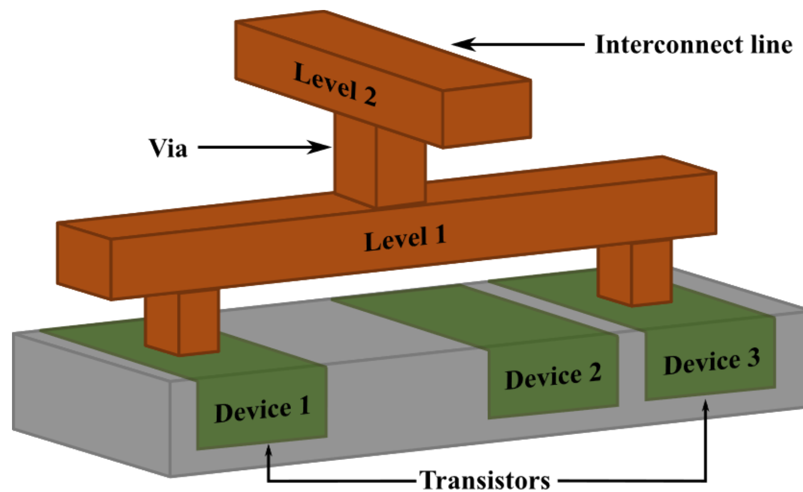

Figure 2.1 Vertical levels of interconnects on an IC [1].

Earlier, aluminium (Al) was widely used for interconnects due to its strong adhesion to silicon dioxide (SiO_2), good conductivity, and low cost. However, chip manufacturers adopted Cu as the preferred material for interconnects due to limitations of Al, such as high resistivity (2.7 μΩ·cm) and susceptibility to electromigration under high current densities [1, 25]. Cu offers a lower resistivity of 1.7 μΩ·cm, higher melting point, better conductivity, and resistance to electromigration. Moreover, the ability of Cu to handle higher current densities further enhanced its reliability [1, 25].

Initially, IC performance was limited by transistor speed, with interconnects treated as ideal conductors. However, as the complementary metal-oxide semiconductor (CMOS) technology continues to scale down, device dimensions shrink, resulting in reduced transistor delay [8, 59]. On the contrary, conventional Cu interconnects face significant challenges as their dimensions

are reduced below 40 nm [2, 5–8]. At this scale, size effects like grain-boundary and surface scattering become more prominent, causing a nonlinear increase in resistivity. This rise in resistivity leads to higher levels of joule heating, which negatively impacts the reliability of the interconnects by accelerating electromigration. As a result, the current carrying capability of these interconnects is significantly reduced, posing a serious limitation to their use in advanced ICs.

Earlier, the conventional Cu interconnects were considered to have homogeneous smooth surfaces. However, the Cu surface may become rough during the fabrication process, further degrading the performance of on-chip Cu interconnects [3, 4]. This effect gets further aggravated when the technology node scales aggressively in the deep sub-micron (DSM) regime, which can be a serious issue in nanoscale ICs. Kumar *et al.* [3] developed an analytical model for calculating Cu resistivity and MFP, incorporating the impact of surface roughness, grain-boundary scattering and surface scattering. Cu interconnects with smooth surface (smooth Cu) exhibit lower resistivity and higher MFP than rough surface Cu interconnects (rough Cu) for technology nodes in the 7 nm to 45 nm range. Moreover, a circuit model for rough Cu interconnects is proposed by Kumar *et al.* [4] using the Mandelbrot-Weierstrass fractal function. Rough Cu exhibits around 71%, 8%, and 37% higher resistance, capacitance, and inductance values, respectively, compared to smooth Cu interconnects at 7 nm technology node. Pathania *et al.* [60] compared the performance of smooth Cu and rough Cu in terms of crosstalk-induced delay considering three adjacent capacitively coupled global interconnect lines at 7 nm and 13 nm technology nodes. The crosstalk-induced delay is significantly higher at the 7 nm node than the 13 nm node for both smooth and rough Cu interconnects. This is attributed to the increasing impact of scatterings and surface roughness as the technology node decreases. Moreover, at the 7 nm technology node, rough copper exhibits a 17-fold increase in crosstalk-induced delay compared to smooth copper.

In recent years, one-dimensional (1D) carbon-based nanomaterials like carbon nanotubes (CNTs) and GNRs are of significant interest in various applications like electronic devices, very large-scale integration (VLSI) on-chip interconnects, through silicon via (TSVs) for three-dimensional (3D) ICs, sensors, optics, medicine, mechanics, spintronics and energy storage devices, owing to their exceptional electronic, optical, thermal and mechanical properties [11, 61–65]. Moreover, both GNRs and CNTs show higher current densities, electrical, and thermal conductivities than Cu [9, 10, 12]. Hence, researchers proposed GNRs and CNTs as emerging

alternatives to conventional Cu for VLSI on-chip interconnects [9, 10, 12, 66, 67]. The mixed CNT (MCNT) bundle has been recognized as the most practical and effective configuration for CNT-based interconnects [68, 69]. However, GNRs are preferred over CNTs because their planar structure contributes to a straightforward fabrication approach consistent with industry standards [10, 13, 14].

2.2.1 MLGNR-Based Interconnects

GNR is a 1D structure with limited width (<50 nm), derived by patterning two-dimensional (2D) graphene, which is a one-atom-thick layer of sp^2-bonded carbon atoms arranged in a honeycomb lattice structure [70]. GNRs can carry much higher current densities, exceeding 10^8 A/cm², compared to traditional Cu interconnects [9, 10, 59]. This capability is attributed to their strong sp^2 hybridized bonds and resistance to the severe electromigration reliability issues in Cu interconnects [10]. Additionally, GNRs have much higher thermal conductivities (3-5×10^3 W/mK) compared to Cu. Furthermore, GNRs exhibit substantially longer carrier MFPs spanning several micrometers, which result in significantly higher electrical conductance than Cu [10].

The primary concern for using GNRs as interconnects is their metallic properties [9]. Patterning GNRs introduces transverse confinement, and the resulting material can be either metallic or semiconducting depending on its geometry and chirality [16]. After patterning, GNR edges can take on either an armchair or zigzag configuration. Zigzag GNRs are always metallic, while armchair GNRs with perfect edges can exhibit semiconducting properties when the number of carbon atoms across the width (N_C) is $3a$ or $3a$+1 and metallic properties when N_C is $3a$+2, where a is an integer [16]. It is observed that metallic armchair GNRs possess a greater number of conducting channels and exhibit lower resistivity compared to zigzag GNRs [16]. A single layer of GNR (SLGNR) exhibits high intrinsic resistance, hence, the stacked structure of multiple SLGNR sheets, i.e., multilayer GNR (MLGNR) interconnect, has been proposed [18, 19]. Experimental results show a better resistivity of ~0.5×10^{-7} Ω.m for five-layered GNR in comparison to Cu and CNT interconnects [71].

2.2.2 MLGNR Interconnect Configurations and Intercalation Doping

Depending on the connection of contact pads with other interconnects and devices in the vicinity, MLGNR is categorized as horizontal top-contact MLGNR (HTC-MLGNR) and

horizontal side-contact MLGNR (HSC-MLGNR), as shown in Figs. 2.2(a) and (b), respectively [18, 19]. HSC-MLGNR has lower effective resistance, thereby showing superior performance compared to HTC-MLGNR because all the SLGNR sheets are physically connected to the contact pads in HSC-MLGNR. In contrast, only the topmost SLGNR sheet is coupled to the contact pads in HTC-MLGNR [18, 19]. More importantly, in view of fabrication complexity, it was demonstrated that the fabrication of contact pads in HTC-MLGNR is less challenging and practically feasible than HSC-MLGNR [18, 19].

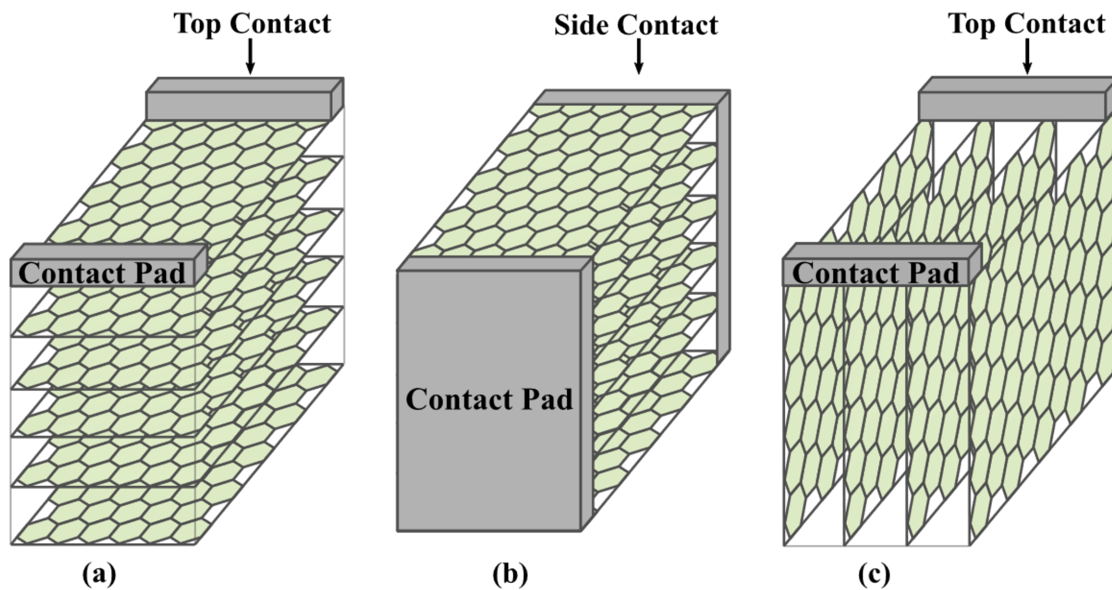

Figure 2.2 Configurations of MLGNR (a) HTC-MLGNR, (b) HSC-MLGNR, and (c) VTC-MLGNR [72, 73].

Recently, vertical top-contact MLGNR (VTC-MLGNR), illustrated in Fig. 2.2(c), has emerged as an alternative to HTC-MLGNR [72, 74]. The equivalent resistance of VTC-MLGNR is substantially lower because, unlike HTC-MLGNR, all layers of VTC-MLGNR are connected to contact pads, leading to electron transport on each layer. Hence, VTC-MLGNR may become a suitable candidate for MLGNR interconnects. However, fabricated VTC-MLGNRs are not yet available, and their related fabrication process is not fully developed to produce highly aligned VTC-MLGNRs [72].

To optimize the performance of HTC-MLGNR for potential use as on-chip interconnects, researchers have focused on improving conductivity by fabricating stage-2 Arsenic Pentafluoride (AsF_5), stage-1 Ferric Chloride ($FeCl_3$), and stage-1 Lithium (Li) intercalation-doped HTC-MLGNR [15, 23, 24]. Intercalation doping between MLGNR layers involves the insertion of atomic or molecular layers of intercalants such as AsF_5, $FeCl_3$, and Li [75]. These

intercalants can be classified as electron acceptors (AsF_5 and $FeCl_3$) [15, 24] and donors (Li) [23]. The stage index indicates the level of intercalation in MLGNRs i.e., stage-*n* signifies that between each adjacent pair of intercalant layers there are *n* number of GNR layers [10, 75].

The volume doping concentration of intercalated AsF_5 is $4.2\times10^{21}cm^{-3}$ [24], whereas the surface doping concentration of $FeCl_3$ and Li is as high as $\sim1.75\times10^{14}$ cm^{-2} [15] and 6×10^{14} cm^{-2} [23], respectively. An improvement in charge density is observed due to charge transfer from intercalation dopants to GNR layers [10]. The improved charge density leads to a shift in the fermi energy of intercalation-doped MLGNRs [15, 23, 24, 76]. Moreover, intercalation doping suppresses scattering between GNR layers by increasing interlayer spacing, which leads to an enhancement in MFP values [10]. Studies have shown that intercalation doping significantly enhances in-plane conductivity, fermi energy, MFP, and c-axis conductivity of HTC-MLGNR, resulting in an overall performance enhancement [10, 15, 18, 22–24].

2.2.3 Hybrid Interconnects

Recent studies have highlighted the electrical and thermal advantages of hybrid interconnects combining Cu with carbon-based nanomaterials, such as Cu-carbon nanotube (Cu-CNT) composite [77–79], Cu-Graphene hybrid [80], and Cu-Carbon hybrid [81, 82], as shown in Figs. 2.3(a-c), respectively. These materials are being explored as potential alternatives to traditional Cu interconnects. Cu-CNT composites formed by electrodepositing Cu into a CNT line provide better conductivity. However, achieving uniform CNT-Cu distribution and ensuring effective interfacial interaction between Cu-CNT are its main challenges [83]. Improved reliability is observed for the Cu-Graphene hybrid formed by a few layers of graphene encapsulating Cu nanowires. However, the compatibility of fabricated Cu-Graphene hybrid with CMOS technology is not certain [80]. Cu-Carbon hybrid interconnects formed by Cu-CNT composite being encapsulated by graphene layers, combine the advantages of improved conductivity and reliability. However, it is worth noting that the related fabrication of the Cu-Carbon hybrid is not yet reported [81]. As these emerging solutions are still in the early stages of development, GNR-based interconnect technology remains the most viable option for upcoming technology nodes.

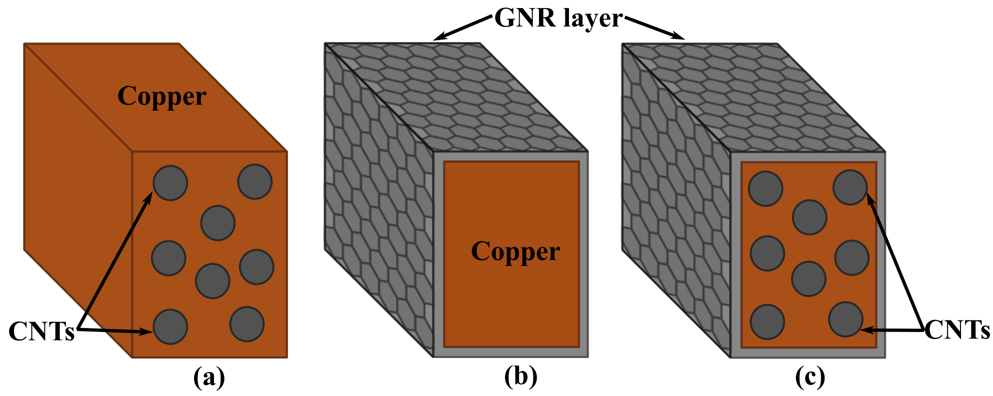

Figure 2.3 Schematic of (a) Cu-carbon nanotube (Cu-CNT) composite, (b) Cu-Graphene hybrid, and (c) Cu-Carbon hybrid [77, 80, 81].

2.2.4 Growth of MLGNR Interconnects

In this subsection, fabrication methods for various configurations of the MLGNR are discussed. Graphene, being the prospective material for future electronic devices in high-speed and radio-frequency applications, has gained a lot of interest from researchers in the past, for example, in the fabrication of graphene technology-based Gigahertz range ICs with the possibility of achieving complex functionality and performance [84, 85]. Ten-layered GNR [86] and stacked multilayer graphene (MLG) with five layers [71] were fabricated. Subsequently, titanium gold (Ti/Au) contact pads were formed for resistivity measurements, which were shown to be comparable to Cu interconnects. Many research works have already been carried out to increase the carrier density and MFP in MLG using intercalation doping; for example, stage-2 AsF_5 intercalation doping was done by direct interaction of vaporising AsF_5 with highly oriented pyrolytic graphite (HOPG) in the reactor [24]. The in-plane conductivity of AsF_5-doped HOPG was measured to be 6.3×10^5 $(\Omega.cm)^{-1}$, which is higher in comparison to 0.26×10^5 $(\Omega.cm)^{-1}$ for undoped HOPG. In [23], Li-D HTC-MLG is fabricated by placing a Li pellet and ultrathin graphite on a hall-bar contact electrode and covering them firstly with Lithium hexafluorophosphate ($LiPF_6$) followed by glass. Intercalation-doped Li samples exhibited lower resistivity compared to undoped Li samples. Fabrication steps for stage-1 $FeCl_3$-doped HTC-MLGNR are given in Fig. 2.4 [15]. A chemical vapor deposition (CVD) process was employed to grow MLG on a copper-nickel (Cu-Ni) alloy catalyst. Next, MLG is transferred to a Silicon dioxide (SiO_2) substrate, followed by MLGNR patterning using electron-beam lithography (EBL). $FeCl_3$ powder and MLGNR samples were heated up to 633 K in high-pressure titanium reactor to diffuse MLGNR with p-type $FeCl_3$ dopant vapors. Finally, nickel

gold (Ni/Au) contact pad formation was done using EBL. The $FeCl_3$-doped HTC-MLGNR showed better performance with respect to Cu. Vertical MLG fabrication steps are shown in Fig. 2.5 [72, 74]. First, horizontal MLG is grown on a cobalt (Co) catalyst. Thereafter, dense vertical MLG is grown using thermal-CVD under horizontal MLG, and finally, horizontal MLG is removed using argon (Ar) plasma etching. Vertical MLGNRs are obtained by patterning vertical MLG layers.

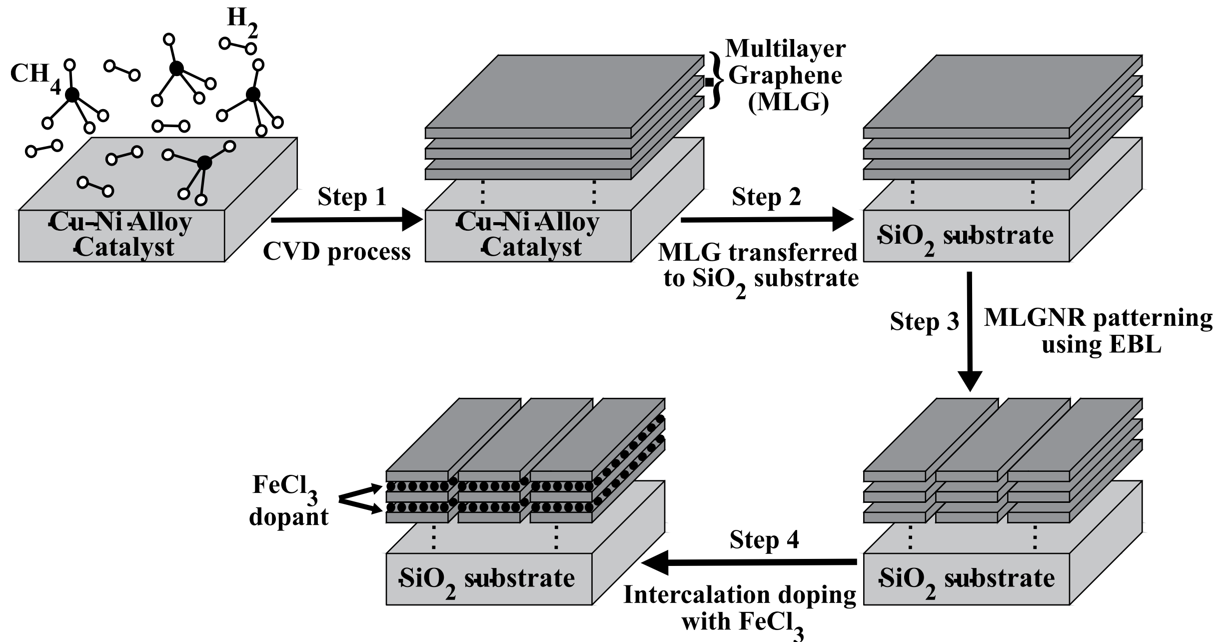

Figure 2.4 Fabrication steps for $FeCl_3$-doped HTC-MLGNR [15].

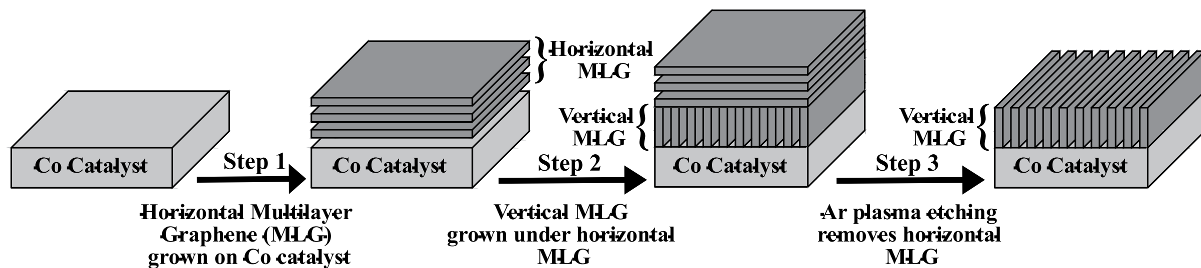

Figure 2.5 Fabrication steps for Vertical MLG [72, 74].

2.2.5 Performance Limiting Factors in MLGNR

Despite significant interest and extensive experiments, the practical use of MLGNR as on-chip interconnects faces challenges by extrinsic scatterings, high-frequency skin effect, process and temperature variations, crosstalk, and electromigration.

In the past, numerous experimental efforts have focused on fabricating high-quality suspended graphene sheets with longer MFPs ranging from 1-7 μm [87–89]. The MFP of electrons is in the micrometer range when scattered with intrinsic sources like acoustic and optical phonons present in suspended graphene, which is quite optimistic [16, 26, 28]. However, at the nanoscale, in addition to intrinsic scatterers, the extrinsic scattering sources also affect the electronic and transport properties of GNR. This results in reduced conductance of MLGNR interconnects, leading to degraded performance in terms of signal delay, crosstalk, and electromigration reliability. The reports indicate that fabricating defect-free and impurity-less MLGNRs while preserving their edge specularity presents a major challenge [15, 27, 72, 76]. Additionally, the dielectric-supported (Si/SiO_2) graphene, when patterned into GNRs, exhibits MFP limited to a few nanometers and a lower conductivity value [26, 88]. This reduction is primarily due to the interaction and scattering of charge carriers with acoustic and optical phonons, charged impurities, polar phonons, resonant scatterers, corrugated surface of dielectric, and rough GNR edges [26, 88]. Experimental data shows that the MFP for a 2 nm wide two-layer GNR is approximately 14 nm [90], while for a 20 nm wide 36-layer $FeCl_3$-doped GNR, the MFP is around 44.13 nm [15]. Hence, the conductance of MLGNR is limited by the presence of extrinsic scattering sources, which imposes a limit on its performance as well. This reveals that scattering sources need to be considered in a realistic scenario to analyze the potential use of MLGNR over Cu as an on-chip interconnect.

Several works have been done to model the effective MFP for GNR, which considers the scattering sources like acoustic and optical phonons, resonant scatterers, edge roughness and dielectric-substrate-induced scatterers like trapped charge impurities, polar phonons, and atomic roughness of corrugated dielectric surfaces [10, 18, 19, 26, 28, 30, 34, 35, 80, 91]. Although dielectric-substrate-induced scattering sources are considered dominant factors in reducing the MFP and conductivity of GNRs [28], it has been shown that structural edge roughness (SER) can critically deteriorate the electronic properties and performance of GNRs as an on-chip interconnect [27]. Moreover, the previously used edge roughness models were based either on diffusive scattering probability [10, 18, 26, 28, 34, 35, 80, 91] or perturbation theory [92]. For both modeling approaches, the predictions are accurate only when the nominal width of GNR is relatively large compared to edge roughness [27]. However, if the nominal width becomes comparable to the edge roughness amplitude of GNR, it invalidates one of the primary assumptions of the models. Moreover, both diffusive and perturbation-based edge roughness models failed to conform with the experimental data and overestimated the values

of effective MFP [27]. In contrast, a recent study by Contino et al. [27] suggests that the realistic SER model predicts the effective MFP drop in accordance with the experimental data, whereas the earlier models of edge roughness overestimate the value of effective MFP. Also, the mobilities calculated using the SER model comply with experimental data [27]. The mobility values plotted in experimental data are derived from graphene conductivity measurements using Drude's model [27]. The SER model depends on graphene width variations, diffusive scattering probability, and the edge roughness auto-correlation length and standard deviation. However, no reported studies have employed a realistic, effective MFP model based on experimental data, incorporating SER, to analyze the actual performance benefits of using MLGNRs as global-level on-chip interconnects. This reveals that developing SER-limited realistic effective MFP model is necessary for realistic performance analysis of MLGNR interconnects in the worst-case scenario.

Crosstalk occurs when signals on different interconnect lines within a system interfere with each other. This phenomenon is primarily caused by the electromagnetic coupling between the closely packed, high-density interconnects required for high-performance, compact systems. Crosstalk affects the signal propagating through interconnects at high frequencies, potentially causing unintended switching, timing issues, or system malfunctions [38, 39]. As a result, crosstalk poses a significant challenge for high-speed designs.

The substantial frequency components present in digital signals in VLSI interconnects extend to the gigahertz range [37, 41]. With technology scaling down, these frequencies are anticipated to rise further. At such high operational frequencies, circuit parasitics of MLGNR become dependent on frequency due to skin effect [37–42]. Skin effect exacerbates effective resistance, thereby worsening signal integrity issues [39–42]. Moreover, due to the skin effect at high frequencies, a more pronounced impact of scatterers is observed, significantly deteriorating the performance of MLGNR interconnects [40, 42]. Hence, impedance modeling that considers the frequency dependence of circuit parameters is required to take these effects into account. Skin depth and impedance extraction methods have been reported for CNT bundle interconnects at high frequencies [41, 43, 93]. Deblina et al. [40, 42] proposed AsF_5-intercalation-doped MLGNRs as a suitable material for high-frequency applications and modeled skin depth and impedance formula considering edge roughness. Moreover, research has revealed that MLGNRs possess large momentum relaxation time, attributed to their longer optimistic MFP values [40, 42]. As a result, MLGNRs possess larger skin depths that saturate

earlier at lower frequencies and demonstrate the low impact of the skin effect. However, several fundamental issues with the existing high-frequency models in [40, 42] need to be addressed. First, the MFP tending to the nanometer scale has been theoretically [10, 26] and experimentally [15, 27] observed for a realistic MLGNR plagued by extrinsic scatterers that adversely impact relaxation time and skin effect. The models in [40, 42] do not take into account the extrinsic scatterers in MLGNR; hence, they need to be considered in high-frequency skin depth and impedance modeling. Second, a study by Wentworth et al. [45] proposed a skin depth model without incorporating momentum relaxation time for practical interconnects having a finite thickness. Yungseon et al. [44] formulated a mathematical expression for one-dimensional skin depth in miniaturized conductors but exempted the impact of momentum relaxation time. However, the conventional skin depth models presented in existing literature consider MLGNR interconnects with semi-infinite dimensions [40, 42].

Reliability has emerged as a critical limiting factor and design challenge for VLSI nano-interconnects due to the high failure rates in the DSM regime. Future ICs are anticipated to exhibit signs of aging due to reliability concerns much more quickly than previous generations [94]. Among the various reliability concerns, electromigration in interconnects is particularly concerning. Electromigration poses a limitation on the reliability of MLGNR interconnects by reducing their lifetime and mean time to failure [36, 46–48].

Due to the intricate nature of the manufacturing processes involved, variations and uncertainties are introduced in the physical and geometrical parameters of the interconnect [50–54]. Process-related parametric variations, along with temperature variations dependent on operational conditions, lead to uncertainties and variations in interconnect performance metrics [50, 52, 53]. Recently, several studies have explored the impact of process and temperature variations on interconnect performance metrics such as single-line propagation delay and crosstalk-induced delay, noise, and noise area [50–55].

The subsequent subsections present a comprehensive overview of various studies related to the performance analysis of MLGNR interconnects, considering the crosstalk and electromigration effects. Moreover, the impact of process and temperature variations and high-frequency skin effect on the performance of MLGNR is also discussed.

2.3 Performance Evaluation of MLGNR Interconnects

The practical applications of MLGNR as an on-chip interconnect are hindered by the presence of factors such as extrinsic scatterers, skin effect, process and temperature variations, crosstalk, and electromigration effects, as discussed in subsection 2.2.5. Recently, several studies have explored the impact of these factors on the performance of MLGNR interconnects, as outlined in the following subsections.

2.3.1 Crosstalk Effects in MLGNR Interconnects

The electromagnetic coupling between densely packed interconnects leads to crosstalk effects, which impact the functionality, reliability, and timing of the propagating signal [38, 39, 95]. The coupling between adjacent interconnects is induced when active signal energy from an aggressor interconnect is transferred to a victim interconnect by mutual inductance and capacitance [96, 97]. Figures 2.6(a) and (b) show the inductively and capacitively coupled configurations of two and three interconnect lines placed above the ground plane at a distance of y_{ILD}, respectively.

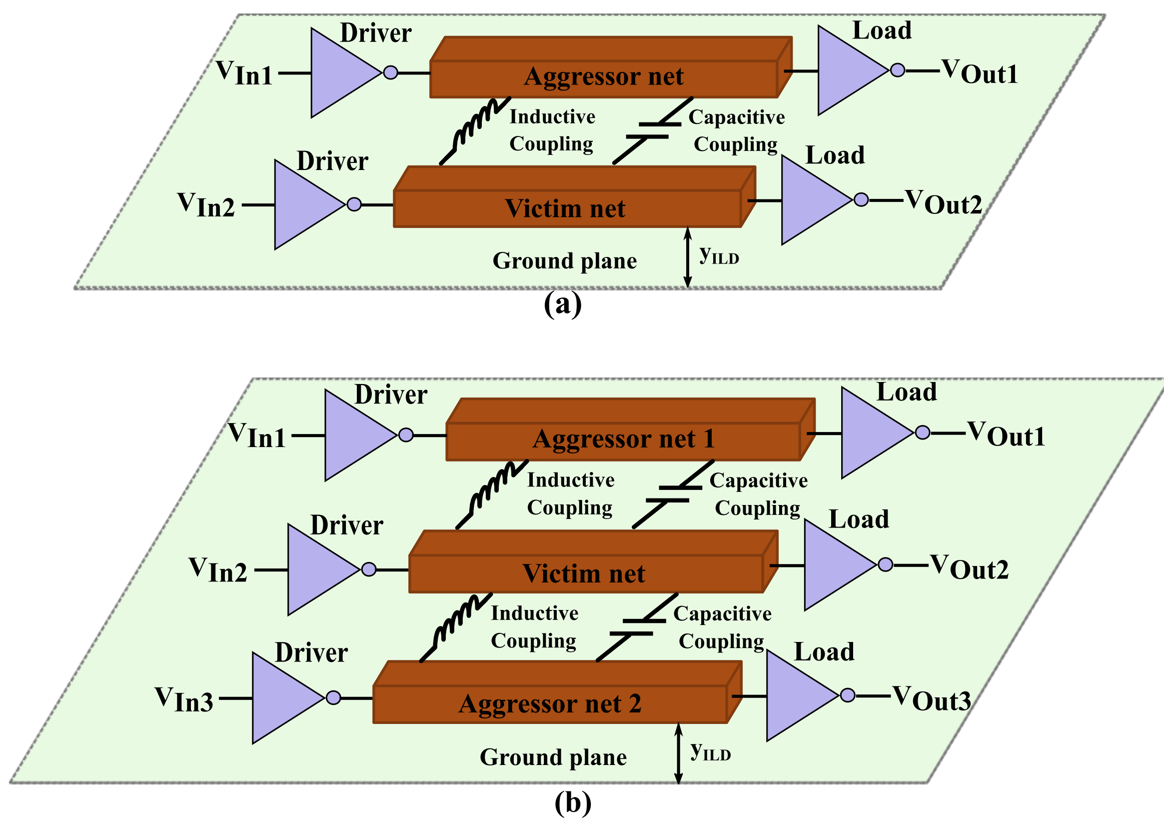

Figure 2.6 (a) Two and (b) three coupled interconnect line configurations.

Crosstalk between coupled interconnect lines increases delay-induced timing estimation complexity and raises reliability concerns due to noise-induced device stress in MLGNR interconnects [21, 30, 34, 98–100]. In the case of crosstalk-induced noise, the voltage level of the victim line goes below 0V (undershoot) or above the power supply (overshoot). Overshoot/undershoot subjects ultra-thin gate oxide of metal-oxide semiconductor (MOS) devices to significant electrical stress, ultimately resulting in permanent failure over time and causing reliability issues in ICs [21, 98, 101]. Moreover, delay induced by crosstalk effects can cause timing issues in ICs [98]. Furthermore, the electrical interconnect circuit models show transient behavior because line parasitics like resistance, inductance and capacitance are unavoidable in such systems [102]. Consequently, rise time degradation arises and directly impacts transient-state response, 3-dB bandwidth, and relative stability of the MLGNR interconnects [102, 103].

Kumar et al. [104] developed a resistance model that considers an MFP model based on defect and edge scatterings in undoped HTC-MLGNR interconnects. The model considers an optimistic MFP value of 1 μm and a realistic value of 300 nm due to defect scatterings in GNRs. The results indicate that the propagation delay and energy-delay product of undoped HTC-MLGNR are lower than those of Cu interconnects for lengths up to 100 gate pitches, assuming smooth GNR edges. However, the performance of MLGNR interconnects with rough edges deteriorates compared to copper interconnects. Moreover, an MFP model was developed by Rakheja et al. [26] that incorporates the scatterings due to dielectric-substrate-induced disorders, phonons, and defects along with rough GNR edges. A GNR placed on an ideal substrate with smooth edges exhibits the highest mobility values. However, the mobility of GNR decreases as edge roughness and substrate non-idealities increase. Nishad et al. [18] have done equivalent single conductor (ESC) modeling and thickness optimization of edge and dielectric-substrate-induced scattering-limited doped HTC-MLGNR interconnect. It is observed that Li-D HTC-MLGNRs show lower delay and energy-delay product than Cu interconnects, even in the presence of rough edges. Zhao et al. [72] proposed an ESC model for HTC-MLGNR and VTC-MLGNR interconnects and compared their performance on the basis of propagation delay at 7.5 nm technology node. HTC-MLGNR and VTC-MLGNR interconnects have similar performance when smooth MLGNR edges are considered. However, at a specularity parameter of 0.8, VTC-MLGNR interconnects exhibit superior performance than Cu counterparts, whereas HTC-MLGNR interconnects lose its advantage. Moreover, Li-D VTC-MLGNR interconnects demonstrate lower propagation delay compared

to AsF_5-doped VTC-MLGNR, undoped VTC-MLGNR, and Cu interconnects. Das et al. [91] considered temperature-dependent phonon and edge scattering-based MFP to derive the ESC model of MLGNR variants. It shows that the performance of scattering-limited HTC-MLGNR interconnects can be improved by intercalation doping and improving edge specularity during fabrication. In [18, 26, 72, 91, 104], the researchers have proposed scattering-based circuit modeling and performance analysis for MLGNR interconnects, with a focus on single-line propagation delay and energy-delay product. However, it should be noted from the aforementioned discussion that crosstalk effects between coupled interconnects have not been considered in the analysis.

Agarwal et al. [96] developed a generic analytical model for calculating crosstalk-induced delay and noise peaks using transmission line equations. The crosstalk model is applicable for two capacitively and inductively coupled symmetric as well as asymmetric interconnect lines. The results clearly indicate that simultaneous switching coupled lines exhibit two modes of propagation i.e., in-phase and out-phase. Switching of both lines in the same direction and opposite direction leads to in-phase and out-phase modes of propagation, respectively. Moreover, functional crosstalk noise occurs when a voltage spike is induced on a quiet line as a result of switching activity on a neighboring line. The analysis of noise waveforms indicates that capacitive coupling produces a positive-polarity noise pulse because the even-mode voltage step, which is positive, arrives at the far end earlier than the negative odd-mode step. In contrast, inductive coupling results in a negative-polarity noise pulse since the negative odd-mode step travels faster than the positive even-mode step. The proposed model has a very low error rate of 6.5% in estimating crosstalk-induced noise. However, the model assumes a low-loss approximation to account for resistance-related losses and, therefore, is unsuitable for interconnect lines with high resistance.

Cui et al. [105] presented an ESC model for undoped HSC-MLGNR interconnects considering an MFP value of 419 nm due to electron hopping between layers of bulk graphite. Crosstalk analysis of two capacitive and inductive edge-coupled MLGNR interconnects is done using the decoupling technique and analytical equations for delay calculations at 14 nm and 22 nm technology nodes. It is observed that crosstalk-induced delay reduces with an increase in fermi energy and technology node. Moreover, at both 14 nm and 22 nm technology nodes, the MLGNR interconnect exhibits a lower delay than the Cu counterpart when the fermi energy is

0.21 eV. However, at fermi energy of 0 eV, Cu outperforms MLGNR interconnect in terms of crosstalk delay.

Zhao et al. [97] developed an ESC model for undoped HSC-MLGNR and HTC-MLGNR interconnects based on an MFP model that accounts for inter-sheet electron hopping and diffusive edge scattering. The analysis indicates that the resistance values of HSC-MLGNR and HTC-MLGNR are comparable for global interconnects. Out-phase crosstalk-induced delay simulations have been performed for three capacitively and inductively coupled MLGNR interconnects at 13.4 nm and 21 nm technology nodes. The results indicate that MLGNR interconnect outperforms Cu counterpart in terms of crosstalk-induced delay and noise peak voltage for interconnect length in the range of 10 μm to 1000 μm. However, diffusive scattering at the edges degrades the performance of MLGNR interconnects.

Rai et al. [106] compared temperature-independent and temperature-dependent ESC models for undoped HSC-MLGNR interconnects, taking into account intrinsic scatterers such as acoustic and optical phonons at a 22 nm technology node. Single and three capacitively coupled MLGNR interconnect lines are employed for the analysis. The study demonstrates that the temperature-dependent model offers improved performance over the temperature-independent model in terms of single-line propagation delay, power dissipation, and time duration of noise due to crosstalk for interconnect lengths between 200 μm and 1000 μm. Moreover, MLGNR interconnects exhibit better performance than Cu in the temperature range of 300 K - 500 K for global interconnect lengths of 1000 μm. This advantage is primarily due to the weak temperature dependence of MLGNR resistance.

Sanaeepur et al. [107] proposed an ESC model for HSC-MLGNR interconnects that incorporates the atomic roughness of corrugated dielectric surface in addition to intrinsic phonons, defects, and diffusive edge scatterings. The crosstalk-induced delay, step response, and stability of HSC-MLGNR interconnects placed on different dielectric substrates like silicon dioxide (SiO_2), silicon carbide (SiC), and boron nitride (BN) have been analyzed and compared to Cu interconnects. The findings indicate that as substrate corrugation amplitude increases, crosstalk-induced delay also increases, and the step response becomes more sluggish. However, the stability of HSC-MLGNR interconnects improves with an increase in substrate corrugations. HSC-MLGNR interconnect placed on SiC and BN outperforms Cu, whereas Cu exhibits better performance compared to HSC-MLGNR interconnect placed on SiO_2.

Hamedani et al. [108] evaluated crosstalk-induced delay, noise area, and power consumption of five capacitively coupled MLGNR interconnects and compared the results with multi-walled CNT (MWCNT) interconnects at 7 nm and 10 nm technology nodes. The effective MFP model considers intrinsic phonons, defects, and diffusive edge scatterings. Crosstalk mitigation using active and passive shielding techniques has also been demonstrated. The active shielding improves crosstalk-induced delay and noise area compared to passive shielding and normal configuration of interconnects. However, shielding techniques tend to increase power consumption. The actively shielded MLGNR interconnects exhibit 54% and 41% lower crosstalk-induced delay compared to MWCNT counterparts for 7 nm and 10 nm technology nodes, respectively. However, 36% and 50% improvements in power consumption are observed for MLGNR interconnects at 7 nm and 10 nm technology nodes, respectively, compared to MWCNT interconnects.

Based on the scattering-limited MFP model incorporating intrinsic phonons, defects, and diffusive edge scatterings, Kaur et al. [109] calculated temperature-dependent circuit parasitics for AsF_5-doped HTC-MLGNR interconnects, and the results are compared to MCNT bundle and Cu counterparts over 300 K - 500 K temperature range at 14 nm technology node. The simulation setup for crosstalk analysis considers two capacitively coupled interconnects. Crosstalk-induced noise peaks along with in-phase and out-phase delay due to crosstalk effects are observed to be lower in AsF_5-doped HTC-MLGNR compared to MCNT bundle, and Cu interconnects at global interconnect length of 1000 μm. In the presence of crosstalk effects, the propagation delay of coupled lines is always higher compared to single line due to the impact of coupling between interconnect lines.

Nishad et al. [110] analyzed the performance of edge-doped armchair GNR interconnects with transition metals like ruthenium, rhodium, platinum, and palladium. Three capacitively and inductively coupled driver interconnect load structure are simulated to calculate crosstalk-induced delay and energy-delay product. Ruthenium edge-doped armchair GNRs exhibit the lowest delay and energy-delay product compared to hydrogen, rhodium, platinum, and palladium edge-doped GNRs.

Kumar et al. [111] employed exponential matrix-rational approximation (EMRA) to study crosstalk effects in two capacitively and inductively coupled MLGNR interconnects. The impact of scatterers like intrinsic phonons, defects, and edge roughness has been incorporated into the effective MFP model. For 10 μm long interconnect lines, peak noise voltage for a

smooth edge and rough edge MLGNR is 198.21 mV and 235.83 mV, respectively, at 14 nm technology node. Moreover, smooth-edged and rough-edged MLGNRs exhibit 7.5 ps (21.35 ps) and 17.2 ps (48.14 ps) values for in-phase (out-phase) crosstalk delay, respectively. The EMRA model deviates from SPICE simulation results by 1% only. The EMRA model developed in [111] has been utilized in [112] to study crosstalk effects in MLGNR, considering scatterings from phonons, defects, and edge roughness along with corrugations of dielectric surface. The performance of MLGNR interconnects degrades with an increase in edge roughness and corrugations of the dielectric substrate surface.

Kumari et al. [113] enhanced the performance and reliability of AsF_5-doped, $FeCl_3$-doped, and Li-D HSC-MLGNR interconnects by optimizing their aspect ratio using numerical techniques. The optimization considered performance metrics such as crosstalk-induced delay, power consumption, noise-delay product, power-delay product, and breakdown power, and the obtained results are compared to those of Cu and cobalt (Co) interconnects. For aspect ratios ranging from 0.4 to 3.4, Li-D HSC-MLGNR demonstrates the lowest figure of merit compared to Cu, Co, and other doped MLGNRs for 1000 μm long global interconnects. The optimal figure of merit value for balancing performance and reliability is achieved at an aspect ratio of 0.5 for Li-D HSC-MLGNR.

Sidhu et al. [114] presented a scattering-based circuit model and performance analysis for Li-D HTC-MLGNR, Cu-CNT composite, Cu-Graphene hybrid, and Cu-Carbon hybrid. Further, they compared the results with those of Cu and single-walled CNT (SWCNT) bundle interconnects in the subthreshold region. Cu-carbon hybrid demonstrates the lowest crosstalk-induced delay and noise duration but exhibits the highest noise peak voltage and 3-dB bandwidth for the temperature range of 300 K - 500 K. However, it is worth noting that the related fabrication of the Cu-Carbon hybrid is not yet reported.

In the past, various techniques have been developed for modeling and analysis of non-linear CMOS drivers and interconnect lines [33, 105, 107, 115–120]. CMOS driver has been modeled as an equivalent resistive driver to perform a transient analysis of capacitively and inductively coupled interconnect lines [105, 107, 115, 116]. Subsequently, a more precise equivalent CMOS driver model, i.e., alpha-power law model [117, 118], and its transient analysis using the finite-difference time-domain (FDTD) model [119, 120], have been proposed. Deepthi et al. [33] proposed an FDTD technique with unconditionally stable conditions to analyze crosstalk effects in capacitively and inductively *n*-coupled MLGNR interconnects. However,

in ESC models, the interconnect and load are modeled by distributed and lumped elements. Hence, by taking practical CMOS drivers into account will increase the complexity. Moreover, the FDTD method is both memory-intensive and time-consuming, making it unsuitable for quickly estimating the impact of crosstalk at the chip level. ABCD parameter model has been employed for transient analysis of three coupled interconnect lines considering an equivalent *RC* model for CMOS driver, with high accuracy as Simulation Program with Integrated Circuit Emphasis (SPICE) and requires comparatively lesser computational time [121]. Moreover, the ABCD parameter model is proven to be advantageous in terms of time and memory usage compared to the FDTD method [121].

Previously, Kumar et al. [122] have done an ABCD parameter-based frequency response and relative stability analysis for a single interconnect line considering the diffusive edge scattering model. The AsF_5-doped MLGNR interconnects exhibit 43.72% and 86.13% lower delay and power dissipation, respectively, compared to Cu counterparts. Akbari et al. [123] evaluated the performance of two coupled MLGNR interconnect lines in terms of step response and Nyquist stability with scatterings induced by substrate defects and diffusive edges. Cheng et al. [80] and Qian et al. [124] have analyzed the delay, frequency, and transient response of two mutually coupled interconnects, taking the diffusive edge scattering model into account.

Kaur et al. [125] developed an ABCD parameter-based analytical model that incorporates temperature-dependent circuit parasitics for performance analysis of two capacitively coupled MLGNR interconnects considering crosstalk effects. The impact of scatterers like intrinsic phonons, defects, and diffusive edge roughness has been incorporated into the effective MFP model. It is observed that MLGNR interconnects doped with $FeCl_3$ and AsF_5 dopants exhibit improved 3-dB bandwidth and delay compared to undoped MLGNR, MCNT bundle, and Cu interconnects. However, the Cu interconnect is most stable due to the higher rise time values than the MCNT bundle and undoped and doped MLGNR interconnects. However, as an improvement, the ABCD parameter-based transfer function proposed by Sahoo et al. [121] considered three capacitively coupled interconnects with intrinsic-phonon-based scatterings. By employing the decoupling technique, transfer functions for crosstalk-induced delay and noise calculations are presented, with high accuracy as SPICE and require comparatively lesser computational time [121].

After a thorough review of the literature on performance characterization of MLGNR interconnects, focusing on metrics like crosstalk-induced delay, noise waveform, and noise

area, transient response, 3-dB bandwidth gain, and relative stability, it is noted that the impact of SER-limited realistic effective MFP, and thickness-dependent skin effect, is not considered on MLGNR impedance parameters and performance characteristics. Given the superior performance of intercalation-doped MLGNRs compared to CNT and Cu counterparts, it is essential to examine the performance metrics while accounting for factors such as SER-limited realistic effective MFP, skin effect, and crosstalk effects.

2.3.2 High-Frequency Skin Effect Aware Analysis

As the frequency of operation increases, the changing magnetic field inside a conductor produces eddy currents that lead to uneven current distribution such that current tends to concentrate more near the surface of the conductor, and this phenomenon is termed as the skin effect [39, 41]. The influence of non-uniform current distribution on resistance and inductance of interconnect becomes a more significant issue at higher operating frequencies, primarily due to the skin effect [40, 41, 43, 93].

For modern ICs, the thickness of the conductor is approximately equivalent to a skin depth. Yungseon et al. [44] formulated a mathematical expression for one-dimensional skin depth in miniaturized conductors having finite thickness but exempted the impact of momentum relaxation time. A study by Wentworth et al. [45] proposed a one-dimensional skin depth model without incorporating momentum relaxation time for practical interconnects having a finite thickness.

Many researchers have previously formulated models to compute the impedance parameters of graphene-based on-chip interconnects at high frequencies, taking into account the skin effect [40–43, 126]. Li et al. [41] developed an impedance model to extract frequency-dependent circuit parasitics for MWCNT and SWCNT. An optimistic MFP model is considered for impedance modeling, leading to a large momentum relaxation time. This results in the skin depth reaching saturation earlier at lower frequencies, which in turn limits the increase in resistance with frequency. It is noted that the impact of skin effect on the impedance of SWCNT, and MWCNT is comparatively lower than the Cu counterparts at high frequencies. However, GNRs are preferred as on-chip interconnects over CNTs because they have a planar structure that allows for good chirality control during fabrication [10, 13, 14].

Deblina et al. [40] proposed AsF_5-doped MLGNRs as a suitable material for high-frequency applications and developed models for skin depth and impedance that account for edge roughness. The MLGNRs exhibit a large momentum relaxation time, attributed to their longer, optimistic MFP values. Due to this large MFP, MLGNRs are also susceptible to the anomalous skin effect (ASE), which occurs when the MFP and skin depth become comparable. The study developed and compared impedance models based on normal skin effect (NSE) and ASE. For 2 μm wide and thick AsF_5-doped MLGNRs, the per unit length resistance increases and inductance decreases as the frequency rises from 1 GHz to 10^3 GHz. AsF_5-doped MLGNR with specular edges exhibits lower resistance and inductance values compared to rough-edged MLGNRs.

Using the developed model in [40], Deblina et al. [42] analyzed the skin depth and impedance of both undoped and AsF_5-doped MLGNR in the presence of edge roughness, and the results are compared with Cu, SWCNT, and MWCNT. It has been shown that AsF_5-doped MLGNR with smooth edges exhibit lower resistance compared to undoped MLGNR, Cu, and SWCNT interconnects. However, rough and smooth-edged AsF_5-doped MLGNR exhibits lower resistance compared to MWCNT interconnects up to 50 GHz and 80 GHz, respectively.

Li et al. [127] studied the performance characteristics of MLGNR, intercalated with hexagonal boron nitride (hBN), in the high-frequency range of 300 GHz - 3000 GHz for resonator applications. hBN-doped MLGNR demonstrates lower surface resistance and skin depth compared to undoped MLGNRs. Moreover, skin depth and surface resistance remain constant as frequency increases, implying negligible impact of skin effect on hBN-doped MLGNR.

Based on the skin effect models formulated in [40, 42], Kaur et al. [128] compared skin depth of undoped MLGNR, AsF_5-doped MLGNR, MWCNT, and Cu in the frequency range of 1 GHz - 1000 GHz. AsF_5-doped MLGNR and MWCNT are least impacted by skin effect, whereas due to the lowest conductivity, undoped MLGNR is most impacted by skin effect. Furthermore, Kaur et al. [129] compared skin depth of undoped MLGNR, AsF_5-doped MLGNR, and Cu to Li-D MLGNR considering optimistic MFPs. AsF_5-doped MLGNR, being the most conductive material among them, demonstrated the lowest skin depth and minimal reductions in skin depth across the frequency range of 1 GHz to 1000 GHz. AsF_5-doped MLGNR exhibits the lowest surface resistance that increases with frequency.

A review of the literature on skin depth and impedance models for MLGNR interconnects at high frequencies reveals that the conventional skin depth models presented in existing literature consider MLGNR interconnects with semi-infinite dimensions. Moreover, the impact of extrinsic scatterers and one-dimensional skin depth on impedance parameters and performance characteristics of practical MLGNR interconnects having a finite thickness have not been addressed at high frequencies. Thus, developing a high-frequency impedance model that incorporates extrinsic scattering sources and the impact of finite-thickness-dependent skin effect is necessary for realistic performance analysis of MLGNR interconnects in the worst-case scenario.

2.3.3 Electromigration Effects in MLGNR Interconnects

Electromigration refers to the movement of atoms in metallic conductors, leading to the void formation (shown in Fig. 2.7) when subjected to high current densities and has been identified as a potential wear-out failure mode [130]. The resulting failure is typically in the form of an electrical open circuit caused by the apparent depletion of conductor metal. Cu exhibits deteriorating electromigration reliability due to continuous wire pitch scaling [36]. The mean time to failure due to electromigration (EM-MTF) decreases as interconnect dimensions shrink for several reasons. First, the size of the void needed to cause a failure diminishes as the wire size decreases, leading to a lesser time required to form a critical void. Additionally, grain-boundary scatterings enhance under electromigration stress [131]. EM-MTF of Cu has improved with the use of a single graphene layer as a barrier to prevent copper diffusion [36]. However, multilayer graphene exhibits better electromigration reliability compared to Cu [36].

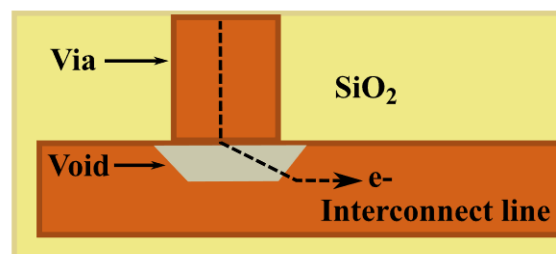

Figure 2.7 Void formation in Cu interconnects due to electromigration [131].

Murali et al. [46] studied electromigration effects in 21 device samples, each containing five to ten undoped GNRs. GNRs have width and length ranging from 16 nm to 52 nm and 0.2 µm to 1 µm, respectively. Ten-layered GNRs exhibit breakdown current density in the range of 1.2

- 2.8×10^8 A/cm^2. Moreover, the breakdown current density and resistivity of GNRs exhibit an inverse relationship.

Chen et al. [47, 59] studied EM-MTF for 4 nm thick multilayer graphene interconnects stressed under a current density of 2×10^7 A/cm^2 at 523 K. It is noted that breakdown current density degrades with an increase in interconnect resistivity and length. Moreover, EM-MTF deteriorates rapidly as resistivity increases, indicating a strong dependence on the quality of the multilayer graphene interconnects. CVD-grown multilayer graphene material with a width, thickness, and length of 3 μm, 4 nm, and 100 μm, respectively, exhibits an EM-MTF of 6 hrs without any capping. However, when a spin-on-glass capping is applied, EM-MTF is enhanced to 18 hrs, which is three-folds higher compared to Cu counterparts.

Jiang et al. [15, 20] fabricated undoped MLGNRs and $FeCl_3$-doped MLGNRs and measured EM-MTF under high-stress conditions. For worst-case EM-MTF calculations, the temperature is kept at 475 K and DC stress of 1×10^8 A/cm^2 and 2×10^8 A/cm^2 is applied. EM-MTF of 1.8 hrs and 5.2 hrs has been observed for 20.6 nm and 73.5 nm wide undoped MLGNRs, respectively, under DC stress of 1×10^8 A/cm^2. However, due to improved conductivity after intercalation doping with $FeCl_3$, no breakdown is observed for 21.6 nm and 68.6 nm wide $FeCl_3$-doped MLGNRs in the time span of 7 hrs, even under DC stress of 2×10^8A/cm^2. 50 nm wide Cu nanowires exhibit EM-MTF of 2.6 min, whereas immediate breakdown and melting of Cu is observed when self-heating is considered under DC stress of 2×10^8 A/cm^2.

Jiang et al. [57] characterized EM-MTF for a multi-tier scheme integrating CNT via and MLG interconnects. The resistance of CNT via and MLG interconnects based multi-tier scheme does not increase in the time span of 10 hrs under stress test at 673 K. Hence, the proposed scheme is resistant to electromigration due to suppressed self-heating and current crowding effects. In [132], Jiang et al. observed a resistance increase of less than 3% when 20 nm wide and 2μm long $FeCl_3$-doped MLGNR is put under DC stress of 1×10^8 A/cm^2 for 28 hrs at a temperature greater than 373 K, suggesting no impact of electromigration effects.

Kumbhare et al. [133] studied reliability concerns in MLGNR interconnects due to electromigration effects using Black's equation. In the temperature range of 500 K - 1000 K, MLGNR exhibits higher EM-MTF compared to Cu. This indicates better immunity of MLGNR to reliability issues due to electromigration effects.

Agashiwala et al. [49] investigated the electromigration reliability of multilevel (two-tier) configuration comprising Co via and $FeCl_3$-doped MLGNR interconnect. Under a constant DC stress of 2×10^8 A/cm^2 for over 40 hrs, the Co via and Co-MLGNR contact exhibits less than 2% increase in resistance, indicating negligible electromigration effects in multilevel scheme based on Co and MLGNR.

Therefore, intercalation-doped MLGNR interconnects provide significant improvements in reliability, while Cu interconnects experience immediate failure. The absence of failure under temperature and high current density stress, combined with their higher conductivity, highlights the tremendous potential of intercalation-doped MLGNRs as next-generation on-chip interconnects. However, the experimental and theoretical work in the literature on reliability concerns in MLGNR interconnects due to electromigration effects have not conducted frequency-dependent electromigration analysis in the presence of skin effect. Thus, it is essential to examine electromigration effects under the impact of performance-limiting factors like extrinsic scatterers and skin effect.

2.3.4 Impact of Process and Temperature Variations

Reddy et al. [134] analyzed variations in single-line propagation delay due to variations in process parameters of MLGNR interconnects. Variations of ±10% are taken into account for process parameters, viz., interconnect width, dielectric thickness, doping concentration, interlayer gap, and dielectric constant, while ±50% variations are considered for mean free path and contact resistance. Maximum and minimum variations in delay are compared to nominal delay varying with length and width in the range of 5 μm - 2500 μm and 5 nm - 25 nm, respectively. Maximum delay variations arise from variations in mean free path values, whereas the interlayer gap induces minimum delay variations.

Hamedani et al. [53] analyzed crosstalk-induced delay, noise area, and power dissipation for five capacitively coupled MLGNR interconnect lines with passive shielding at 7 nm and 10 nm technology nodes. The analysis is conducted by considering the impact of process and temperature variations. As the technology node shrinks from 10 nm to 7 nm, process and temperature variations exhibit a greater impact on crosstalk-induced delay and noise area. Mean free path variations cause the largest variation in crosstalk-induced delay, noise area, and power dissipation. The results indicate that for a 10 nm passively shielded MLGNR interconnect, the average maximum deviations in power consumption, crosstalk-induced delay,

and noise area due to all sources of process variations are 0.4 μW, 65 ps and 6 V.ps, respectively. In the 7 nm node, these deviations increase to 0.57 μW, 135 ps, and 12 V.ps. Moreover, with an increase in temperature from 200 K - 450 K, crosstalk-induced delay and noise area increase. A two-fold increase in crosstalk-induced delay and a 1.5 times increase in noise area is observed for 7 nm MLGNR interconnects compared to those at 10 nm.

Kolanti et al. [135] compared crosstalk-induced delay, peak noise voltage, and noise area of unshielded, passively shielded, and actively shielded MLGNR interconnects across three capacitively coupled configurations under process variations. Variations in dielectric thickness, spacing between interconnects, and width of interconnect are considered. Passively shielded MLGNR interconnects are least impacted by process parameter variations, hence, exhibit minimum variation in crosstalk-induced delay, peak noise voltage, and noise area.

Sidhu et al. [54] analyzed the impact of process and temperature variations on crosstalk-induced noise and delay in Li-D HSC-MLGNR at the subthreshold mode of operation. A transmission line analytical model for two capacitively coupled interconnect lines is employed for crosstalk analysis. Variations in interconnect length and width, fermi energy, and dielectric thickness are considered for the analysis. An increase in width, fermi energy, and dielectric thickness leads to a decrease in crosstalk-induced noise time duration and delay. However, a rise in crosstalk effects is observed when temperature and length increase.

While recent studies have examined the effects of process and temperature variations on single-line propagation delay and crosstalk-induced issues such as delay, noise, and noise area, the challenges posed by these variations in the presence of SER-limited realistic effective MFP, skin effect, crosstalk and electromigration effect at high frequencies have yet to be addressed. Thus, assessing the impact of process and temperature variations on the high-frequency performance of MLGNR interconnects is essential.

2.4 MLGNR: Prospect for Monolithic 3D ICs

The ongoing geometry and device miniaturization in conventional 2D ICs is inadequate in addressing challenges such as limited speed, bandwidth, and integration density for future systems [2, 136]. Moreover, the conventional Cu-based interconnects and vias experience substantial increase in resistivity and electromigration issues due to rigorous scaling [137]. Vias are essential components for transmitting signals between different metallization layers

[49]. To overcome these challenges, the three-dimensional (3D) IC integration based on through silicon vias (TSV) emerged as a promising solution for improved system-level performance [56, 58, 136, 138].

Liu et al. [139] modeled and characterized a system consisting of horizontal MLGNR interconnects and CNT-based TSVs for future 3D ICs in the frequency range of 1 GHz - 100 GHz. It has been indicated that the proposed graphene-based system exhibits superior performance compared to its Cu counterpart. Goswami et al. [140] developed an equivalent circuit model for MLGNR-based TSV to evaluate and compare its performance with that of the Cu counterpart. 52.1% and 56.1% average reductions in power dissipation and delay are observed for 10 μm - 30 μm long MLGNR-based TSV compared to Cu-based TSV. Hossain et al. [141] analyzed the fact that MLGNR-based TSV outperforms CNT and Cu-based TSVs in terms of power delivery consistency and transfer of heat using COMSOL Multiphysics solver. Hamedani et al. [142] employed MLGNR, and CNT-based interconnects and TSVs with micrometer-scale widths to minimize vertical crosstalk-induced noise in 3D-ICs. However, large dimensions of TSVs result in significant mechanical/thermal stress in the substrate, high parasitic capacitance and low integration density [56, 58]. A TSV has a load capacitance comparable to several thousand gates, contributing to RC delay and leading to substantial dynamic power consumption at the 7 nm technology node [56].

In its 2022 report, IRDS suggested monolithic 3D (M-3D) ICs as a promising solution to address the challenges associated with TSV-based 3D ICs [2, 56]. M-3D integration involves the sequential fabrication of vertically connected stacked tiers on the same wafer [58, 136]. Each tier is comprised of active devices, interconnects, intra-tier and inter-tier vias, and interlayer dielectric (ILD). In M-3D ICs, adjacent tiers are connected using inter-tier vias with diameters comparable to those of back-end-of-line (BEOL) intra-tier vias [58]. In comparison to TSVs, inter-tier vias provide 1000 times denser vertical connectivity, which is crucial for achieving higher energy efficiency [143, 144].

Aly et al. [143, 144] experimentally demonstrated M-3D integration by stacking CNT field-effect transistor-based logic/computing layers with resistive/spin-transfer torque magnetic random-access-memory-based memory layers, vertically connected through an ultra-dense array of nanoscale inter-tier vias. Vertical stacking of tiers enables the full utilization of M-3D integration benefits, significantly reducing both memory access latency and energy consumption. This approach significantly enhanced performance metrics such as delay and

power consumption, achieving a 1000-fold improvement in the energy-delay product compared to conventional 2D integration methods for data applications.

Experimental studies conducted by Jiang et al. [15] and Agashiwala et al. [49] demonstrated improvement in single-line delay and reliability by employing $FeCl_3$ intercalation-doped MLGNR interconnect with metal via for single-tier via-interconnect scheme (VIS). Jiang et al. [57] proposed MLGNR interconnect and CNT via based multi-tier VIS that offers improved single-line delay compared to Cu-based VIS. However, fabricating CNT via is not compatible with BEOL processes due to high growth temperature (>873 K) requirements.

Moreover, heat dissipation remains a critical concern for HTC-MLGNR as vias, owing to their limited thermal conductivities in the vertical direction [72, 74]. Nihei et al. [74] experimentally realized vertical graphene layers, resulting in a 100-fold increase in electrical conductivity and a 10-fold increase in thermal conductivity in the vertical direction. In a theoretical study, Zhao et al. [72] analyzed the potential of undoped and intercalation-doped VTC-MLGNRs as on-chip interconnects. Li-D VTC-MLGNR exhibits lower resistivity and propagation delay compared to undoped VTC-MLGNR and HTC-MLGNR, AsF_5-doped VTC-MLGNR, and Cu. FEM simulations show that the unit cell of VTC-MLGNRs exhibits the lowest temperature rise under an input power of 5 μW compared to Cu and HTC-MLGNR interconnects. This indicates improved thermal conductivity of VTC-MLGNR in the vertical direction.

Jiang et al. [58] studied the potential of a VIS that integrates $FeCl_3$-doped MLGNR-based via and interconnect to enhance signal delay and integration density of M-3D IC. A ten-fold improvement and 150% increase in integration density is observed for MLGNR-based VIS in M-3D IC compared to TSV-based 3D ICs and conventional material-based M-3D ICs, respectively.

The presented literature on the analysis of M-3D ICs reveals that intercalation-doped MLGNR-based VIS outperforms conventional VIS configurations. However, VTC-MLGNR as via material and HTC-MLGNR as interconnect material have not been analyzed for single-tier VIS as a prospect for M-3D ICs. Also, the challenges posed by extrinsic scatterers, skin effect and crosstalk effects on the performance of MLGNR-based VIS are not addressed at high frequencies. Therefore, it is imperative to analyze MLGNR-based VIS as a prospect for M-3D ICs and to evaluate the associated challenges arising from scatterers, skin effect, and crosstalk effect at high frequencies.

2.5 Chapter Summary

In this chapter, a detailed literature review has been conducted to explore the challenges encountered by conventional Cu-based on-chip interconnects as technology nodes scale down. The advantages and challenges of Cu-CNT composites, Cu-Graphene hybrids, and Cu-Carbon hybrids have been examined, emphasizing that GNR-based interconnects remain the most practical solution for future technology nodes. The potential of intercalation-doped MLGNR material for interconnect applications has also been highlighted. Additionally, it reviews the performance characteristics of MLGNR interconnects in the presence of extrinsic scattering sources, high-frequency skin effect, process and temperature variations, crosstalk and electromigration effects. The chapter also explored research on potential materials for M-3D ICs and their performance analysis.

Several theoretical and experimental studies show that the effective MFP for realistic GNRs is dependent on scattering sources like resonant scatterers, phonons, dielectric-substrate-induced defects and impurities, and edge roughness. The research also indicates that previously used edge roughness models, based on either diffusive scattering probability or perturbation theory, did not conform with experimental data for mobility and tend to overestimate the MFP values. However, no reported studies have employed a realistic effective MFP model based on experimental data, incorporating SER, to analyze the actual performance benefits of using MLGNRs as global level on-chip interconnects.

Skin depth models for conductors with semi-infinite dimensions and miniaturized conductors with finite thickness have been reported. Furthermore, prior studies have explored skin depth-based impedance modeling, and analysis of MLGNR interconnects with semi-infinite dimensions, considering edge roughness. However, there is a need for an impedance model incorporating SER-limited realistic MFP and a one-dimensional skin depth formula for miniaturized MLGNR interconnects having a finite thickness.

Numerous researchers have analyzed the performance of undoped and intercalation-doped MLGNR interconnects, focusing on metrics like crosstalk-induced delay, noise waveform, and noise area, transient response, 3-dB bandwidth gain, and relative stability in the presence of various intrinsic and extrinsic scattering sources, and crosstalk coupling effects. However, no studies have reported performance analysis of MLGNR interconnects considering the impact of SER-limited realistic MFP and finite-thickness-dependent skin effect on impedance

parameters. Additionally, a comparative performance analysis of MLGNR interconnects and MCNT bundles under these considerations remains unexplored. Therefore, it is crucial to study the performance characteristics of MLGNR interconnects under the influence of a realistic MFP model and finite-thickness-dependent skin effect and to compare the findings with those of MCNT bundle interconnects.

Experimental and theoretical work on electromigration-based reliability analysis for MLGNR interconnects has been reported. However, the impact of the high-frequency skin effect on the reliability of scattering-limited realistic MLGNR has not been analyzed and requires further investigation. Moreover, recent studies have examined the effects of process and temperature variations on performance metrics such as crosstalk-induced delay, noise, and noise area. Whereas the challenges posed by these variations in the presence of SER-limited realistic effective MFP, skin effect, crosstalk, and electromigration effect at high frequencies have yet to be addressed. Thus, it is essential to assess the impact of process and temperature variations on the high-frequency performance of MLGNR interconnects.

Numerous reports have proposed and analyzed MLGNR as a prospective material for M-3D ICs, but they have not accounted for the challenges arising from extrinsic scatterers, skin effect, and crosstalk effects at high frequencies, indicating the need for further exploration.

The next chapter presents the realistic MFP-based impedance modeling of high-frequency MLGNR interconnects with frequency-independent and frequency-dependent circuit parameters. Moreover, the impedance analysis is performed with respect to variations in temperature, corrugation amplitude, and frequency.

Chapter 3 High-Frequency Impedance Modeling and Analysis of MLGNR Interconnects

3.1 Introduction

With rapid advancements in VLSI technology, operating frequencies are now approaching the gigahertz range due to the growing demand for faster communication and computing technologies [38, 39]. At such high frequencies, circuit parasitics of MLGNR interconnects become frequency-dependent due to the skin effect, increasing resistance and further degrading signal integrity issues. While intercalation-doped MLGNRs are a potential solution for interconnect applications, their MFP is limited by various extrinsic scatterers, further degrading interconnect performance at high frequencies. To overcome these issues, developing a high-frequency impedance model that captures the effects of frequency-dependent parasitics due to skin effect and extrinsic scatterers is essential, ensuring accurate and realistic performance analysis under worst-case conditions.

Several techniques have been introduced in the literature to model the effective MFP for GNRs considering electron scatterings with intrinsic phonons, viz., acoustic and optical phonons [30, 106]. Moreover, researchers presented different formalisms to model effective MFP for realistic GNRs limited by additional scatterers such as charged impurities, surface polar phonons, resonant scatterers, atomic roughness of the corrugated dielectric surface and edge roughness alongside intrinsic phonons [10, 18, 26, 28, 34, 35, 80, 91]. However, the previous edge roughness models relied on either diffusive scattering probability [10, 18, 26, 28, 34, 35, 80, 91] or perturbation theory [92], which failed to conform with the experimental data and overestimated the values of effective MFP [27]. In contrast, the structural edge roughness (SER) model predicts the effective MFP drop in accordance with the experimental data [27]. However, prior studies have not explored the impedance modeling and analysis of MLGNR interconnects by considering an SER-limited realistic effective MFP model.

A few reports have presented skin depth and impedance models for MLGNR interconnects at high frequencies [40, 42]. However, the conventional skin depth models presented in existing literature consider MLGNR interconnects with semi-infinite dimensions and ignore the influence of the extrinsic scattering sources in MLGNR [40, 42]. The mathematical expression for one-dimensional skin depth in miniaturized conductors with finite thickness has been

formulated, but it omits the impact of momentum relaxation time [44, 45]. Moreover, existing studies do not address the impact of extrinsic scatterers and one-dimensional skin depth on the impedance parameters of practical MLGNR interconnects with finite thickness, particularly at high frequencies.

This chapter focuses on high-frequency impedance modeling and analysis of MLGNR interconnects. Section 3.2 presents a scattering-source-dependent impedance model for various MLGNR configurations, evaluating their frequency-independent circuit parameters against those of MCNT bundles and Cu interconnects across a temperature range of 300 K to 500 K. The impact of corrugation amplitude on MLGNR circuit parameters is also analyzed and compared with Cu interconnects at 300 K. Section 3.3 presents an impedance model that incorporates the scattering-limited realistic effective MFP, and a finite-thickness-dependent skin effect model to extract and study frequency-dependent circuit parameters for MLGNR interconnects. These parameters are then compared with MCNT bundles and Cu interconnects over a frequency range of 1 GHz - 10^4 GHz at 300 K.

3.2 Frequency-Independent Circuit Modeling and Analysis

This section presents circuit modeling and analysis of MLGNR interconnects with frequency-independent circuit parameters by considering the scattering-limited realistic effective MFP.

3.2.1 Circuit Modeling for MLGNR Interconnects

Figure 3.1 illustrates the 3D structure of MLGNR interconnects in various configurations, including undoped HTC-MLGNR (U-HTC-MLGNR), intercalation-doped HTC-MLGNR (*I*-D HTC-MLGNR, where *I* refer to intercalants such as AsF_5, $FeCl_3$, and Li), U-VTC-MLGNR, and U-HSC-MLGNR. In particular, these configurations of the MLGNR, viz., HTC-MLGNR, VTC-MLGNR, and HSC-MLGNR are differentiated based on the placement of each GNR layer and electrical contact pads. Here, it can be seen that in the HTC-MLGNR, only the topmost layer of GNR is coupled with the contact pads, while all the layers of GNR are physically connected with the contact pads in VTC-MLGNR and HSC-MLGNR. Here, interconnects have a width w, and thickness t, whereas interlayer dielectric (ILD) thickness is denoted as y_{ILD}. The van der Waals gap separating GNR layers is denoted by δ_s.

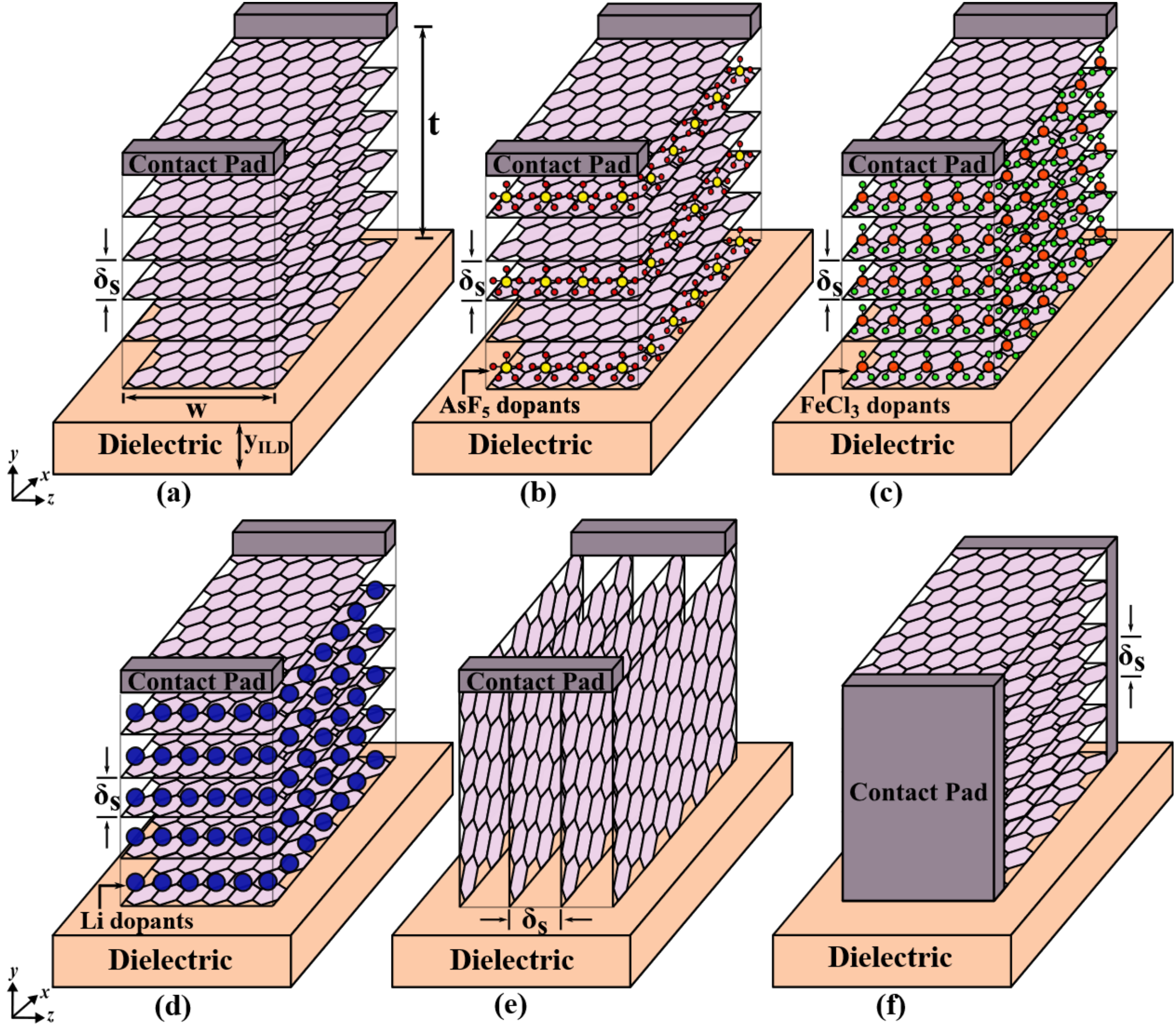

Figure 3.1 Schematics of MLGNR configurations (a) U-HTC-MLGNR, (b) stage-2 AsF_5-D HTC-MLGNR, (c) stage-1 $FeCl_3$-D HTC-MLGNR, (d) stage-1 Li-D HTC-MLGNR, (e) U-VTC-MLGNR and, (f) U-HSC-MLGNR [72, 73].

The temperature-dependent and scattering-limited equivalent circuit model of a single GNR layer is shown in Fig. 3.2. Here, R_{mc} is the resistance associated with an imperfectly coupled contact pad and GNR layer. The value of R_{mc} depends on the quality of fabricated contact pads, having a value ranging from 1 kΩ to 20 kΩ. $R_Q(T)$ is the quantum resistance that is not a function of length and arises due to the quantum confinement of electrons over the width of the GNR layer. There are various scattering sources such as acoustic and optical phonons, charged impurities, polar phonons, resonant scatterers, atomic roughness of corrugated dielectric surfaces, and SER that are responsible for the reduction of carrier mobility and MFP in GNR, and also lead to deflection of electrons from their original trajectory resulting in temperature-dependent per unit length (p.u.l.) scattering resistance $R_S(T)$. $L_k(T)$ is the temperature-dependent p.u.l. kinetic inductance resulting from the kinetic energy of electrons, and L_e is the

p.u.l. magnetic inductance arising due to the stored energy in the magnetic field. $C_q(T)$ is the p.u.l. temperature-dependent quantum capacitance arising from the small density of states, and the C_e is the p.u.l. electrostatic capacitance resulting from the energy stored in the electrostatic field. dx is the infinitesimally small element of interconnect having length l.

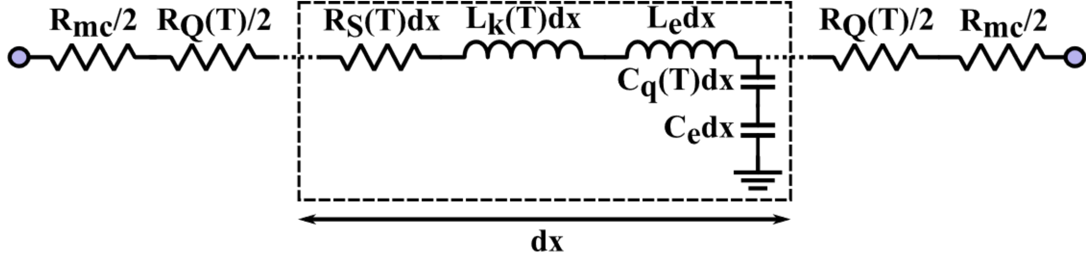

Figure 3.2 The equivalent circuit model for a single GNR layer [122].

According to the Landauer formula, the total temperature-dependent p.u.l. resistance ($R_T(T)$) of a single GNR layer is given by [145, 146]:

$$R_T(T) = \frac{h/2e^2}{N_{TM}(T)}\left(\frac{\lambda_{eff}(T)+l}{\lambda_{eff}(T)}\right) = R_Q(T) + R_S(T) \quad (3.1),$$

where, $R_Q(T) = \frac{h/2e^2}{N_{TM}(T)} \approx \frac{12.9k\Omega}{N_{TM}(T)}$ and p.u.l. $R_S(T)$ is determined by [146]:

$$R_S(T) = \frac{h/2e^2}{N_{TM}(T)\lambda_{eff}(T)} = \frac{R_Q(T)}{\lambda_{eff}(T)} \quad (3.2),$$

where, h and e are the Planck's constant and charge of the electron, respectively. $\lambda_{eff}(T)$ represents the temperature-dependent effective MFP of electrons in a single GNR layer, and l is the conductor length. $N_{TM}(T)$ is the temperature-dependent number of transverse modes in a single GNR layer, calculated by adding electron and hole populations of each sub-band and expressed as, $N_{TM}(T) = \sum_{i=0}^{n_c}\left(1 + \mathrm{e}^{\frac{E_i - E_f}{k_B T}}\right)^{-1} + \sum_{i=0}^{n_v}\left(1 + \mathrm{e}^{\frac{E_i + E_f}{k_B T}}\right)^{-1}$ [16, 97, 105]. Here, E_f depicts the fermi energy of GNR, n_c and n_v represent the number of conduction and valence sub-bands, respectively. k_B and T are the Boltzmann's constant and temperature, respectively. E_i is the lowest/highest energy of ith conduction/valence sub-band for metallic armchair GNR, given by, $E_i = \frac{hv_f}{2w}|i|$, for HTC and HSC-MLGNR, and $E_i = \frac{hv_f}{2t}|i|$, for VTC-MLGNR. Here, v_f is the fermi velocity of GNR [76].

The optimistic effective MFP ($\lambda_P(T)$) due to the electron scatterings with intrinsic phonons for perfect suspended graphene has been reported to be temperature-dependent and in the

micrometer range [16, 28]. However, the effective MFP ($\lambda_R(T)$) of a realistic graphene placed on a SiO_2 dielectric substrate is limited by additional scattering sources, including crystal defects, dielectric-substrate-induced scatterers, and edge roughness [15, 16, 26–28]. The effective MFP, $\lambda_{eff}(T)$, for intrinsic-phonon-limited perfect GNR ($\lambda_P(T)$) and scattering-limited realistic GNR ($\lambda_R(T)$) are calculated using Matthiessen's rule, given as [26]:

$$\frac{1}{\lambda_P(T)} = \frac{1}{\lambda_{ac}(T)} + \frac{1}{\lambda_{op,abs}(T)} + \frac{1}{\lambda_{op,emm}(T)} \quad (3.3),$$

$$\frac{1}{\lambda_R(T)} = \frac{1}{\lambda_{ac}(T)} + \frac{1}{\lambda_{op,abs}(T)} + \frac{1}{\lambda_{op,emm}(T)} + \frac{1}{\lambda_{RS}} + \frac{1}{\lambda_{CI}} + \frac{1}{\lambda_{SPP}(T)} + \frac{1}{\lambda_{CD}} + \frac{1}{\lambda_{SER}} \quad (3.4),$$

where, $\lambda_{ac}(T)$ is the temperature-dependent MFP associated with acoustic phonon scatterings, $\lambda_{op,abs}(T)/\lambda_{op,emm}(T)$ is the temperature-dependent MFP due to non-polar optical phonons being absorbed/emitted in graphene, λ_{RS} is the temperature-independent MFP due to scattering with atomic-scale defects in graphene called resonant scatterers, λ_{CI} is the temperature-independent MFP due to scatterings from charge impurities located at the graphene-substrate interface or adsorbed on graphene, $\lambda_{SPP}(T)$ is the temperature-dependent MFP due to scatterings in the presence of substrate surface polar phonons (SPPs), and the related mathematical formulas can be obtained from earlier research [26, 80]. λ_{CD} is the temperature-independent MFP due to (a) change in inter-carbon bond length and hopping parameter of GNR placed above the corrugated surface of the dielectric substrate and (b) the electron scatterings with atomic roughness of the corrugated dielectric surface. λ_{CD}, depending on the dielectric substrate material, can be obtained as $\lambda_{CD} = \frac{c}{\delta A^4}[nm]$, where the fitting parameter $c = 2.07\times10^9$ and δA depicts the root mean square of the fluctuations in the amplitude of corrugations present on the dielectric substrate surface [28]. λ_{SER} is the MFP depending on diffusive scattering probability as well as width variations of GNR and is described by a realistic structural edge roughness (SER) model based on experimental data, given as, $\lambda_{SER} = \frac{1}{\pi p(w+6\sigma_{SER})} \times \Big[-6p\lambda_{2D}\sigma_{SER} + 6\pi p\Lambda\sigma_{SER} + 9\sigma_{SER}^2 \ln\frac{3\sigma_{SER}}{p\lambda_{2D}+3\sigma_{SER}} + 2(w-3\sigma_{SER})^2 \tanh^{-1}\frac{p\lambda_{2D}}{2w+p\lambda_{2D}-6\sigma_{SER}} + pw\lambda_{2D} + p^2\lambda_{2D}^2 \ln\frac{p\lambda_{2D}+3\sigma_{SER}}{w+p\lambda_{2D}-3\sigma_{SER}}\Big]$, where, p is the probability of diffusively scattered electrons at the edge of GNR (p=1 for specular edges whereas $0\leq p<1$ for rough edges), σ_{SER} represents edge profile deviation from its average value, λ_{2D} (54 nm) is the MFP of two-dimensional graphene, and Λ is the auto-correlation length which represents edge roughness profile in the transport direction of the electron [27].

Next, the resistive networks shown in Fig. 3.3 are used to compute the equivalent frequency-independent p.u.l. low-bias resistance for HTC-MLGNR, HSC-MLGNR, and VTC-MLGNR. The temperature-dependent and scattering-source-dependent total p.u.l. resistance, $R(T)$, for HTC-MLGNR, VTC-MLGNR, and HSC-MLGNR can be obtained as:

$$R(T) = \begin{cases} R_{N_H} = \left(\frac{1}{R_T(T)} + \frac{1}{(R_{N_H-1}+R_Y)}\right)^{-1} + R_{mc},\ for\ HTC - MLGNR \\ \frac{R_T(T)+R_{mc}}{N_V},\ for\ VTC - MLGNR \\ \frac{R_T(T)+R_{mc}}{N_H},\ for\ HSC - MLGNR \end{cases} \quad (3.5)$$

where, $R_Y = \frac{\delta_s}{\sigma_{c-axis} w dx}$ is the c-axis resistance between GNR layers, $\sigma_{c\text{-}axis}$ depicts the conductivity in c-axis, $N_H = 1 + int.\left(\frac{t}{\delta_S}\right)$ is the number of layers in HSC-MLGNR and HTC-MLGNR, and $N_V = 1 + int.\left(\frac{w}{\delta_S}\right)$ is the number of layers in VTC-MLGNR. The temperature-dependent total p.u.l. inductance, $L(T)$, and capacitance, $C(T)$, are computed using mathematical expressions given in prior work [28, 107].

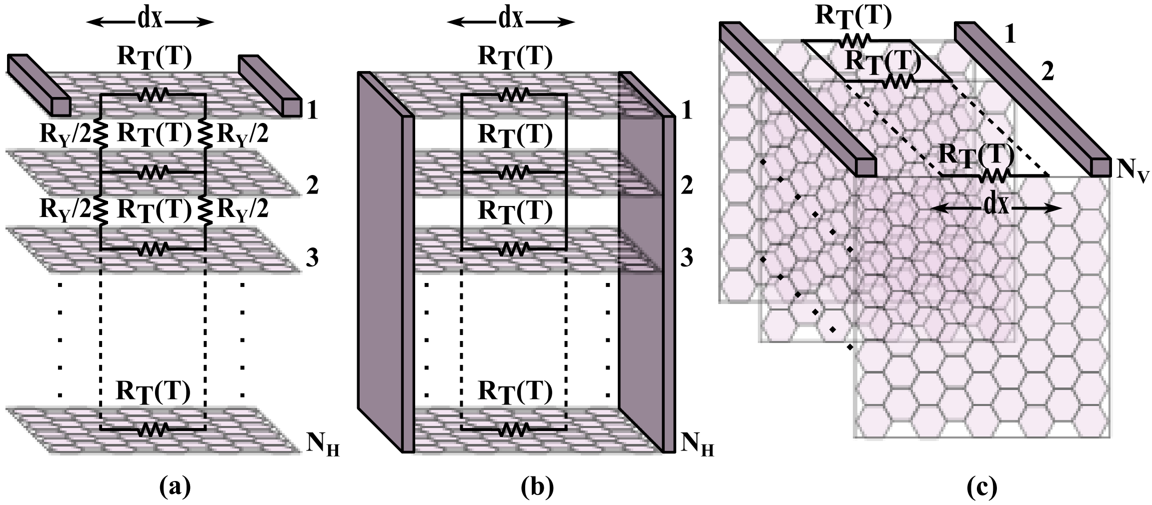

Figure 3.3 Resistive network of (a) HTC-MLGNR, (b) HSC-MLGNR, and (c) VTC-MLGNR [19, 72].

The MCNT bundle has been recognized as the most practical and effective configuration for CNT-based interconnects [68, 69, 147]. As reported in [68], MCNT bundle-VI displays superior performance in terms of single-line propagation delay and crosstalk-induced delay compared to the other five configurations of the MCNT bundle. Therefore, MCNT bundle-VI is considered for the present analysis and the circuit parameters are extracted using the

analytical expressions presented in the previous literature [68, 69]. Equation (3.3) is used to calculate $\lambda_P(T)$ for the MCNT bundle, where $\lambda_{ac}(T)$ and $\lambda_{op,abs}(T)/\lambda_{op,emm}(T)$ are obtained from [69, 148]. Also, $\lambda_R(T)$ for the MCNT bundle is obtained using a modified equation (3.4), i.e., $\frac{1}{\lambda_R(T)} = \frac{1}{\lambda_{ac}(T)} + \frac{1}{\lambda_{op,abs}(T)} + \frac{1}{\lambda_{op,emm}(T)} + \frac{1}{\lambda_{RS}} + \frac{1}{\lambda_{CI}} + \frac{1}{\lambda_{SPP}(T)} + \frac{1}{\lambda_{CD}}$ [148]. Moreover, to evaluate the performance of smooth and rough Cu interconnects accurately for temperatures ranging from 300 K - 500 K, the analytical expressions to extract circuit parasitics, viz., p.u.l resistance ($R(T)$), inductance (L), and capacitance (C) are obtained from previous work [3, 4, 60].

3.2.2 Temperature-Dependent Analysis of Circuit Parameters: MLGNR Versus MCNT Bundle, and Cu interconnects

In this subsection, the effective MFPs for intrinsic-phonon-limited perfect GNR ($\lambda_P(T)$) and scattering-limited realistic GNR ($\lambda_R(T)$) are studied. The circuit parameters of undoped MLGNR in three different configurations (i.e., VTC, HTC, and HSC), intercalation-doped HTC-MLGNR, MCNT bundle, and Cu (with smooth and rough surfaces), are analyzed at temperatures ranging from 300 K - 500 K. From intercalation-doped MLGNR point of view, prospective intercalation dopants, viz., AsF_5, $FeCl_3$, and Li are employed to improve the fermi energy and in-plane conductivity of HTC-MLGNR.

The different properties of undoped and intercalation-doped MLGNR configurations are given in Table 3.1 [18, 91]. MLGNR, placed on SiO_2 dielectric substrate with corrugation amplitude, δA=170 pm [28] and having rough edges with p=0.2 [27], is considered. To analyse the performance of global interconnects (1mm long) at 13 nm technology node, the physical parameters used in various calculations are extracted from International Technology Roadmap for Semiconductors (ITRS) 2013, given as thickness, t=46.8 nm, relative permittivity of the ILD, ε_r=2.28, spacing, s=20 nm, width, w=20 nm, and ILD thickness, y_{ILD}=30 nm [7]. The resistivity of smooth and rough Cu is obtained as 7.84 μΩ.cm and 8.55 μΩ.cm, respectively, using mathematical expressions given in previous work [3]. For the MCNT bundle, the configuration includes 38 SWCNTs with a diameter of 1 nm and 10 MWCNTs with an outer diameter of 8 nm [68, 69]. The spacing between MWCNTs and SWCNTs, as well as the inter-shell spacing for MWCNTs is set at 0.34 nm [68, 69].

Table 3.1 Different properties of undoped MLGNR (viz., HTC, VTC, and HSC) and intercalation-doped HTC-MLGNR (with AsF_5, $FeCl_3$, and Li dopants) interconnects [18, 91].

Properties	Undoped HTC, VTC, and HSC MLGNR	AsF_5-D HTC-MLGNR	$FeCl_3$-D HTC-MLGNR	Li-D HTC-MLGNR
δ_s [nm]	0.34	0.575	0.394	0.37
E_f [eV]	0.2	0.6	0.68	1.5
$\sigma_{c\text{-}axis}$ $[\Omega.\text{cm}]^{-1}$	1/30	0.24	1	1.8×10^4

Figure 3.4 illustrates the MFPs due to the deflection of electrons by various scattering sources in GNR (viz., $\lambda_{ac}(T)$, $\lambda_{op}(T)$, λ_{RS}, λ_{CI}, $\lambda_{SPP}(T)$, λ_{CD}, and λ_{SER}) and effective MFPs of GNR ($\lambda_P(T)$ and $\lambda_R(T)$), varying with temperature (300 K - 500 K). It is noted that as the temperature rises, the MFP of GNR decreases for temperature-dependent scattering sources, viz., $\lambda_{ac}(T)$, $\lambda_{op}(T)$, and $\lambda_{SPP}(T)$. Whereas, the MFP of GNR remains constant with temperature for temperature-independent scattering sources, viz., λ_{RS}, λ_{CI}, λ_{CD} and λ_{SER}. Here, intrinsic-phonon-limited MFP of perfect GNR ($\lambda_P(T)$, equation (3.3)) decreases more rapidly with temperature in comparison to scattering-limited MFP of realistic GNR ($\lambda_R(T)$, equation (3.4)) due to the presence of dominant temperature-dependent scattering sources in $\lambda_P(T)$. The SER-limited MFP, λ_{SER}, demonstrates the lowest value compared to MFPs associated with other scattering sources in GNR. Also, due to the presence of a dominant scattering source with least value i.e., λ_{SER} in $\lambda_R(T)$, there is a significant decline in $\lambda_R(T)$ compared to $\lambda_P(T)$. Hence, it is worth noting that scattering sources in realistic GNR limit the value of $\lambda_R(T)$ to the nanometer range.

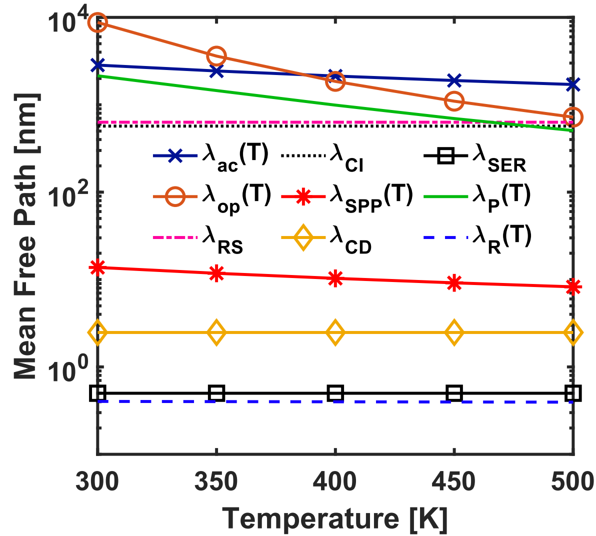

Figure 3.4 Mean free path versus temperature curves for GNR.

Table 3.2 Interconnect circuit parameters for undoped MLGNR (viz., VTC, HTC, and HSC), intercalation-doped HTC-MLGNR (with AsF_5, $FeCl_3$, and Li dopants) and MCNT bundle, considering effective MFPs $\lambda_P(T)$ and $\lambda_R(T)$ (T=300 K - 500 K).

Circuit parameters	T[K]	Undoped MLGNR			Doped HTC-MLGNR			MCNT bundle
		VTC	HTC	HSC	AsF_5	$FeCl_3$	Li	
$R(T)$ [Ω/μm] for $\lambda_P(T)$	300	20.92	15.67	15.66	9.55	6.33	2.54	30.2
	350	31.23	23.48	23.47	14.17	9.36	3.75	41.4
	400	46.41	34.95	34.94	20.9	13.77	5.5	57.8
	450	66.99	50.47	50.46	29.93	19.68	7.84	79.5
	500	93.09	70.1	70.09	41.26	27.08	10.77	106.6
$R(T)$ [kΩ/μm] for $\lambda_R(T)$	300	25.91	83.3	83	50.87	33.71	13.52	18.24
	350	26.78	85.1	84.9	51.39	33.95	13.6	18.47
	400	27.69	86.7	86.2	51.91	34.2	13.67	18.76
	450	28.64	88.3	87.5	52.42	34.47	13.75	18.99
	500	29.61	89.9	89	52.95	34.75	13.82	19.24
$L(T)$ [pH/μm]	300	30.02	23.92	22.96	15.69	11.35	6.222	81.2
	350	30.36	24.25	23.29	15.76	11.37	6.224	78.7
	400	30.72	24.56	23.60	15.83	11.39	6.225	76.3
	450	31.1	24.85	23.89	15.89	11.41	6.227	73.8
	500	31.48	25.13	24.17	15.95	11.44	6.229	71.5
$C(T)$ [aF/μm]	300	13.348	13.251	13.251	13.355	13.363	13.413	88.9203
	350	13.347	13.248	13.248	13.354	13.363	13.413	88.9204
	400	13.346	13.246	13.246	13.354	13.363	13.413	88.9205
	450	13.345	13.244	13.244	13.353	13.363	13.413	88.9206
	500	13.344	13.242	13.242	13.353	13.362	13.413	88.9207

Table 3.3 Interconnect circuit parameters for rough and smooth Cu (T=300 K - 500 K).

T(K)	Rough Copper			Smooth Copper		
	$R(T)$ [Ω/μm]	L [pH/μm]	C [aF/μm]	$R(T)$ [Ω/μm]	L [pH/μm]	C [aF/μm]
300	90.99	2.978	65.47	83.74	3.123	53.11
350	108.7	2.978	65.47	100.1	3.123	53.11
400	126.5	2.978	65.47	116.4	3.123	53.11
450	144.2	2.978	65.47	132.7	3.123	53.11
500	162	2.978	65.47	149.1	3.123	53.11

The calculated *p.u.l* values of resistance (*R(T)*), inductance (*L(T)*), and capacitance (*C(T)*) for undoped MLGNR in three different configurations (i.e., VTC, HTC, and HSC), intercalation-doped HTC-MLGNR (with AsF_5, $FeCl_3$, and Li dopants), and MCNT bundle are given in Table 3.2, for temperature varying from 300 K - 500 K, considering effective MFPs $\lambda_P(T)$ and $\lambda_R(T)$. The circuit parameters of smooth and rough Cu, varying across the temperature range of 300 K - 500 K, are given in Table 3.3. It is seen that the values of resistance for various MLGNR configurations, MCNT bundle, and Cu variants increase with a rise in the temperature for both $\lambda_P(T)$ and $\lambda_R(T)$. However, the resistance values of MLGNR variants obtained through $\lambda_R(T)$ increase slightly with the rise in temperature. This is because $\lambda_R(T)$ is a weak function of temperature (see Fig. 3.4). The resistance of rough copper is higher than that of smooth copper due to increased electron scattering at the rough surfaces. It is also noted that the resistance of U-HTC-MLGNR is slightly higher than that of U-HSC-MLGNR. Moreover, the resistance of both smooth and rough Cu is several orders larger than all the variants of MLGNR when $\lambda_P(T)$ is considered. This is due to the fact that the MFP of electrons in Cu is smaller than MLGNR. Whereas, for realistic effective MFP $\lambda_R(T)$, the resistance of all MLGNR variants becomes several orders larger than both smooth and rough Cu because of the enhanced deflection of electrons in MLGNR from all the scattering sources given in equation (3.4). Consequently, the effective MFP $\lambda_R(T)$ decreases, resulting in increased resistance values.

Table 3.2 indicates that the MCNT bundle shows higher resistance than all the MLGNR variants for $\lambda_P(T)$, whereas Li-D HTC-MLGNR has lower resistance than MCNT bundle for $\lambda_R(T)$. Also, in comparison to the resistance obtained through $\lambda_P(T)$, the resistance values of all variants of MLGNR obtained through $\lambda_R(T)$ show a significant increase for a given temperature range. It is because $\lambda_R(T) << \lambda_P(T)$. Furthermore, the Li-D HTC-MLGNR has the lowest resistance in comparison to other MLGNR variants for both cases of $\lambda_P(T)$ and $\lambda_R(T)$ because of two factors: (a) highest fermi energy (see Table 3.1) contributing to highest number of transverse modes and hence lowest scattering resistance, and (b) lowest c-axis resistivity (see Table 3.1) leading to lowest c-axis resistance.

As depicted in Table 3.2, MLGNR interconnects exhibit lower inductance and capacitance than MCNT bundle. The inductance of smooth and rough Cu is smaller than MLGNR variants, and reverse is true for capacitance, as shown in Tables 3.2 and 3.3. The inductance and capacitance of smooth and rough Cu are not dependent on the temperature; therefore, constant values are obtained. Meanwhile, the value of inductance ($L(T)$) for MLGNR variants is dominated by

$L_k(T)$, as its value is substantially larger than L_e. Also, $L_k(T)$ is inversely proportional to the number of transverse modes, which decrease slightly with a rise in temperature [109, 149]. Hence, $L_k(T)$ increases less rapidly with rise in temperature from 300 K - 500 K. On the contrary, the value of total capacitance ($C(T)$) for MLGNR variants is dominated by C_e because $C_e << C_q(T)$. This justifies two results for the MLGNR variants, i.e., (a) a minute decrease in values of the capacitance with the increase in temperature, and (b) no significant difference in the capacitance values of various MLGNR configurations.

3.2.3 Corrugation-Amplitude-Dependent Analysis of Circuit Parameters for MLGNR and Cu interconnects

In this subsection, the impact of SER (in terms of p and w) and corrugated dielectric surface (in terms of corrugation amplitude) on an effective MFP of GNR and the resistance of various MLGNR configurations is studied. Undoped MLGNR in two different configurations (i.e., HTC and VTC) and intercalation-doped HTC-MLGNR are considered for this study at room temperature, i.e., 300 K. Intercalation dopants like Li, $FeCl_3$, and AsF_5 are used, which increases fermi energy and conductivity of the undoped MLGNR. The properties of all the undoped and intercalation-doped MLGNR configurations are given in Table 3.1. For global interconnects (l=1 mm) at 13 nm technology node, the geometrical and physical parameters used for calculations and simulations are obtained from ITRS 2013 [7], as given in section 3.2.2.

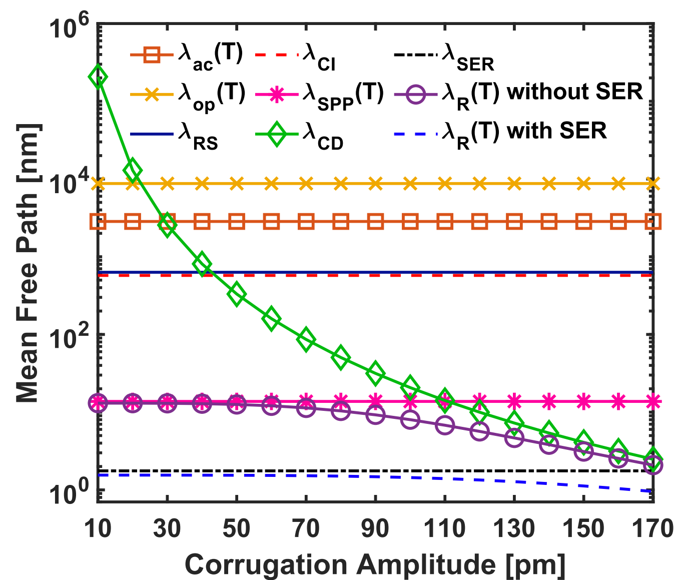

Figure 3.5 Mean free path versus corrugation amplitude for GNR.

The corrugation amplitude (δA) is considered in a range of 10 pm - 170 pm, where 10 pm, 70 pm, and 170 pm are values for SiC, BN, and SiO_2 dielectric materials, respectively [28]. The variation of MFPs associated with each scattering source and $\lambda_R(T)$ (with and without SER) with δA is shown in Fig. 3.5. $\lambda_{ac}(T)$, $\lambda_{op}(T)$, $\lambda_{RS,}$ λ_{CI}, $\lambda_{SPP}(T)$ and λ_{SER} are not dependent on δA, hence remain constant with change in δA, whereas, λ_{CD} decreases with an increase in δA. It can be observed that $\lambda_R(T)$ without SER is determined by $\lambda_{SPP}(T)$ for δA=10 pm to 110 pm, whereas λ_{CD} dominates $\lambda_R(T)$ for δA =110 pm to 170 pm. Also, λ_{SER} (p=1, w=20 nm) dominates and determines $\lambda_R(T)$ with SER for δA ranging from 10 pm to 170 pm.

Furthermore, GNRs with SER (having various widths (w) and probability of edge scattering (p)) and GNRs without SER are analyzed. Figure 3.6 compares the effective MFP of realistic GNRs ($\lambda_R(T)$) with SER as a function of δA to that of GNRs without SER. The MFP of GNRs decreases with increasing δA due to the increased electron scattering rate arising from a high degree of atomic roughness of the corrugated dielectric surface. Also, the MFP of GNRs with SER is always shorter than that of GNRs without SER, which indicates that λ_{SER} dominates the effective MFP ($\lambda_R(T)$) compared to other scattering sources. For GNRs with SER, the MFP increases with increasing width due to the receding impact of rough edges in wider GNRs. Also, the GNR with specular edges (p=1) at each specific width has the longest MFP. However, the impact of p on wider GNRs is less than narrower GNRs. Hence, the GNR without SER on SiC (δA =10 pm) has the longest MFP, whereas the one on SiO_2 (δA =170 pm) has the shortest MFP.

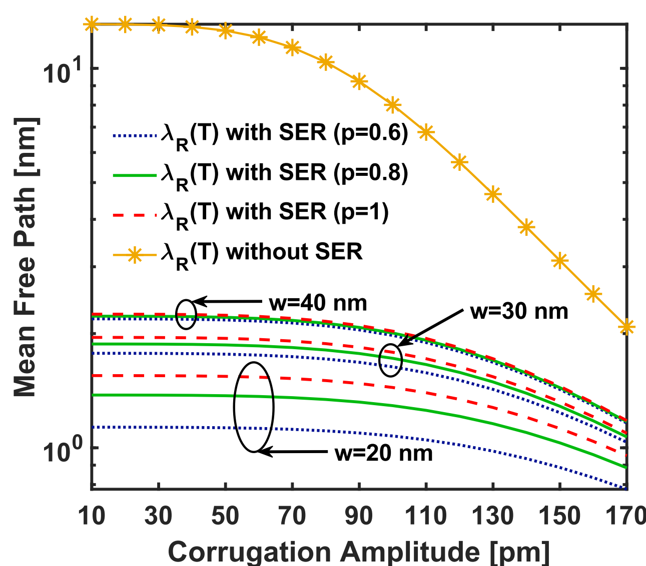

Figure 3.6 Effective mean free path versus corrugation amplitude for GNRs with (having different w and p) and without SER.

The p.u.l. resistance ($R(T)$) versus δA curves of undoped and intercalation-doped MLGNR interconnects with SER (p=1) are compared with that of Cu (with smooth and rough surfaces) in Fig. 3.7(a). As seen, the MLGNR resistance increases by increasing δA due to enhanced carrier scatterings with atomic roughness of the corrugated dielectric surface and decreasing effective MFP as shown in Figs. 3.5 and 3.6. The resistance of MLGNRs on SiC (δA=10 pm), BN (δA=70 pm), and SiO_2 (δA=170 pm) is always larger than Cu counterparts due to decreased effective MFP of realistic GNR in the presence of scattering sources given in equation (3.4). Also, Li-D HTC-MLGNR exhibits the highest fermi energy (E_f) and c-axis conductivity ($\sigma_{c\text{-}axis}$) (see Table 3.1), leading to an increase in transverse modes and a decrease in interlayer resistance, respectively. These factors result in the least resistance values for Li-D HTC-MLGNR among all MLGNR variants. In Fig. 3.7(b), Li-D HTC-MLGNR without SER as well as with SER (p=1 and p=0.6) is compared to Cu (with smooth and rough surfaces) as a function of δA. While the resistance of Li-D HTC-MLGNR interconnects without SER on SiC (δA=10 pm) and BN (δA=70 pm) is less than that of Cu variants, the MLGNR on SiO_2 (δA=170 pm) has the resistance more than Cu counterparts. However, the resistance of Li-D HTC-MLGNR interconnect, with SER (p=1 and p= 0.6) and placed on SiC, BN and SiO_2, is always larger than that of Cu variants.

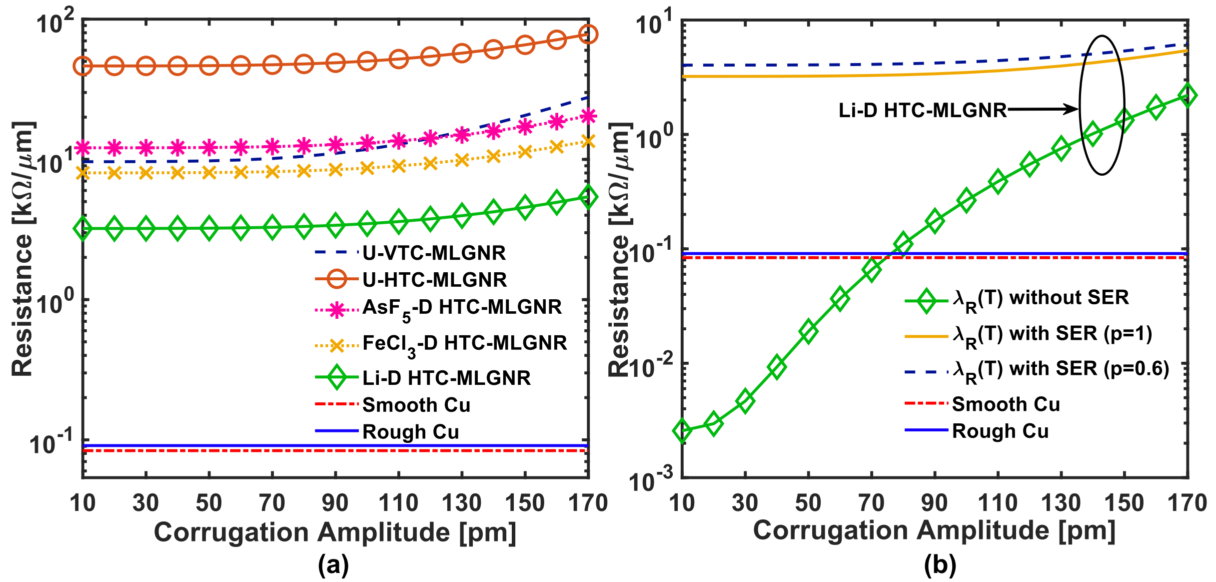

Figure 3.7 Resistance p.u.l versus corrugation amplitude for (a) undoped and intercalation-doped MLGNR (with SER, p=1) and Cu interconnects, and (b) Li-D HTC-MLGNR (without SER and with SER (p=1 and p=0.6)) and Cu interconnects.

3.3 Frequency-Dependent Circuit Modeling and Analysis

This section delves into the development and analysis of a frequency-dependent circuit model for MLGNR interconnects. The proposed model incorporates the scattering-limited realistic effective MFP to account for the impact of extrinsic scattering sources, such as SER, charged impurities, surface polar phonons, and corrugated dielectric surfaces. Additionally, a finite-thickness-dependent skin effect model is integrated to evaluate the frequency-varying behavior of impedance parameters. By combining these effects, the model captures the dynamic changes in resistance, inductance, and capacitance over a frequency range spanning 1 GHz to 10^4 GHz. The circuit parameters are analyzed for undoped and intercalation-doped MLGNR variants, and comparisons are drawn against MCNT bundles and Cu interconnects. This analysis provides insights into the frequency-dependent performance of MLGNR interconnects, highlighting their suitability for high-frequency applications and the influence of substrate properties, temperature, and material configurations on their impedance characteristics.

3.3.1 Frequency-Dependent Circuit Modeling for MLGNR Interconnects

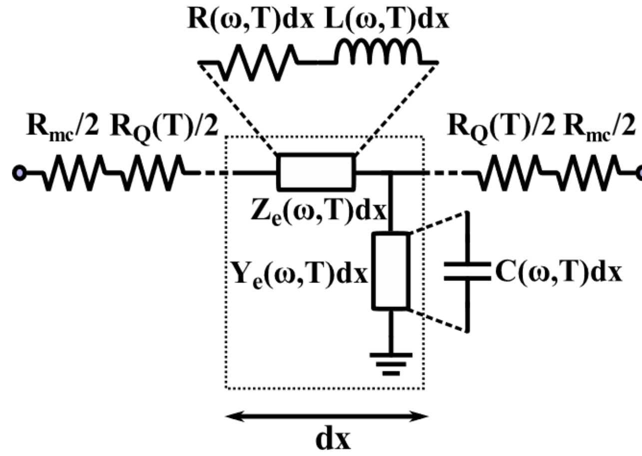

Figure 3.8 The scattering-source-dependent, temperature-dependent, and frequency-dependent equivalent transmission line model for MLGNR interconnect [150]**.**

Figure 3.8 presents the equivalent electrical transmission line model for MLGNR interconnects in which the impact of scattering sources, temperature, and skin effect are considered [41, 151]. $Z_e(\omega,T)$ and $Y_e(\omega,T)$ are the temperature-dependent, scattering-limited and frequency-varying p.u.l. series impedance and shunt admittance, respectively, of the distributed section of MLGNR interconnect having length dx at a temperature T. Here, $R(\omega,T)$, $L(\omega,T)$, and $C(\omega,T)$ are the p.u.l. effective resistance, inductance, and capacitance, respectively, of the MLGNR interconnects. $R(\omega,T)dx$, $L(\omega,T)dx$, and $C(\omega,T)dx$ are the scattering-source-dependent,

temperature-dependent, and frequency-dependent parameters. The MLGNR interconnects are modeled as uniform transmission lines with finite conductor loss and zero dielectric loss (perfect dielectric). The telegrapher's propagation equations are given as $\frac{dV(x)}{dx} = -Z_e(\omega, T)I(x)$ and $\frac{dI(x)}{dx} = -Y_e(\omega, T)V(x)$, where, $Z_e(\omega, T) = R(\omega, T) + j\omega\big(L(\omega, T)\big)$ and $Y_e(\omega, T) = j\omega(C(\omega, T))$ [150].

The skin depth is useful for estimating the penetration of electromagnetic fields in a conductor. The calculations conventionally used for skin depth are based on the assumption of a conductive material in the form of a semi-infinite slab [40–42]. However, for modern ICs, the thickness of the conductor is approximately equivalent to a skin depth [44]. Hence, a formula for the one-dimensional effective skin depth is proposed that accounts for an MLGNR interconnect with finite thickness and considers momentum relaxation time. According to the relation obtained using Maxwell's equations [41]

$$\nabla^2\vec{E} = j\omega\mu\sigma(\omega, T)\vec{E} \qquad (3.6),$$

where, $\vec{E}$, and ω is the electric field and the angular frequency, respectively. $\omega=2\pi f$, where f is the frequency. μ is the permeability of GNR. A homogeneous MLGNR characterized by longitudinal conductivity is considered. For frequencies ranging from 1 GHz - 10^4 GHz, the complex, frequency-dependent conductivity can be modeled using Drude's formula [152, 153]. $\sigma(\omega, T)$ is the scattering-source-dependent, temperature-dependent, and frequency-dependent complex conductivity given as [41]:

$$\sigma(\omega, T) = \sigma_{dc}(T)/(1 + j\omega\tau(T)) \qquad (3.7),$$

where, $\sigma_{dc}(T)$ and $\tau(T)$ are the temperature-dependent and scattering-limited effective dc conductivity [72] and the momentum relaxation time [40, 41] of GNR, respectively, given as $\sigma_{dc}(T) = 1/(R(T) \times wt)$ and $\tau(T) = \lambda_{eff}(T)/2v_f$. Here, $\lambda_{eff}(T)$ and $R(T)$ represent the effective MFP of GNR and total p.u.l. frequency-independent resistance of MLGNR interconnects, respectively, as discussed in subsection 3.2.1.

An MLGNR transmission line with finite dimensions, t, w, and l in the y, z, and x directions, respectively, is considered as shown in Fig. 3.9(a). In this configuration, the electromagnetic wave is assumed to propagate in the y direction, with the electric field oriented in the x

direction. Considering the electric field variations in the y direction only and by eliminating $\sigma(\omega,T)$ term using equations (3.6) and (3.7), one can obtain:

$$\nabla^2\vec{E} = \frac{\partial^2 E_x}{\partial y^2}\hat{x} = \frac{j\omega\mu\sigma_{dc}(T)}{1+j\omega\tau(T)}E_x\hat{x} = \Gamma^2 E_x\hat{x} \quad (3.8)$$

Γ is the complex propagation constant given from equation (3.8) as:

$$\Gamma = \sqrt{\frac{j\omega\mu\sigma_{dc}(T)}{1+j\omega\tau(T)}} = \sqrt{\frac{(\omega\tau(T)+i)\omega\mu\sigma_{dc}(T)}{1+(\omega\tau(T))^2}} = \alpha + j\beta \quad (3.9),$$

where, $\alpha = \sqrt{\pi f\mu\sigma_{dc}(T) \times \frac{\sqrt{1+(\omega\tau(T))^2}+\omega\tau(T)}{1+(\omega\tau(T))^2}}$ and $\beta = \sqrt{\pi f\mu\sigma_{dc}(T) \times \frac{\sqrt{1+(\omega\tau(T))^2}-\omega\tau(T)}{1+(\omega\tau(T))^2}}$ are the attenuation and phase constants, respectively, of MLGNR interconnects [41]. The electric field propagating in the x direction, i.e., $E_x = E_{0x}e^{-\Gamma y} = E_{0x}e^{-\alpha y-j\beta y}$, is obtained by solving equation (3.8) [41]. Due to the high-frequency skin effect, the amplitude of electric field strength (E_{0x}) decays exponentially along the direction of propagation of the electromagnetic wave (y direction) inside the MLGNR interconnects, as shown in Fig. 3.9(b) [151]. The E_{0x} attenuates in accordance with the function $e^{-\alpha y}$, where α is the attenuation constant of the MLGNR interconnects [151]. $e^{-\beta x}$ represents a change in the phase of the electromagnetic wave along MLGNR interconnects.

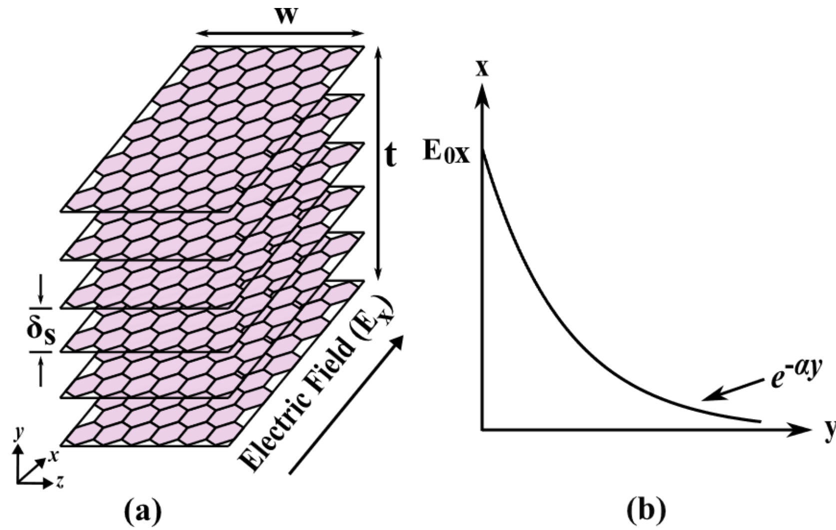

Figure 3.9 Schematic of (a) electric field (E_x) in the x-direction inside an MLGNR interconnect, and (b) exponentially decaying electric field strength inside an MLGNR interconnect along the y-direction [41, 151].

The proposed temperature-dependent and scattering-limited skin depth formula for MLGNR interconnects with finite thickness, considering $\tau(T)$, is derived using [40, 44, 45] and given as:

$$\Delta_{SD} = \int_0^t e^{-\alpha y} dy = \Delta' \times \left(1 - e^{-t/\Delta'}\right) \quad (3.10),$$

where, the conventional skin depth formula is $\Delta' = \frac{1}{\alpha} = \sqrt{1/\left(\pi f \mu \sigma_{dc}(T)\right)} \times \sqrt{\left[1 + \left(\omega\tau(T)\right)^2\right] \times \left[\sqrt{1 + \left(\omega\tau(T)\right)^2} - \omega\tau(T)\right]}$.

According to Harnwell, the instantaneous value of current density J is given by decay in its initial value at the surface (J_0) with the thickness of MLGNR interconnect, as [126]:

$$J = J_0 e^{-\Gamma y} \quad (3.11),$$

For MLGNR interconnect, the total current I_{tot} is [126]:

$$I_{tot} = \int_{y=0}^{t} \int_{z=0}^{w} J dz dy = w \int_{y=0}^{t} J dy \quad (3.12)$$

I_{tot} is obtained by solving equation (3.12) using equations (3.9) and (3.11), as:

$$I_{tot} = wJ_0 \int_{y=0}^{t} e^{-\Gamma y} dy = \frac{wJ_0}{\sqrt{j\omega\mu\sigma(\omega,T)}} \left(1 - e^{-\Gamma t}\right) \quad (3.13)$$

The value of surface electric field strength E_{0x} along the length (l) of MLGNR Tx-L is given by [126]:

$$E_{0x} = (J_0 l)/(\sigma(\omega, T)) \quad (3.14)$$

The effective impedance due to the skin effect, considering scattering sources and temperature, is [126, 151]:

$$Z_e(\omega, T) = E_{0x}/I_{tot} \quad (3.15)$$

Substituting equations (3.13) and (3.14) into equation (3.15) and using equation (3.7), $Z_e(\omega,T)$ is obtained as:

$$Z_e(\omega,T)=\frac{l}{w(1-e^{-\Gamma t})}\sqrt{\frac{\pi f\mu}{\sigma_{dc}(T)}}\times\left[\sqrt{\sqrt{1+\left(\omega\tau(T)\right)^2}-\omega\tau(T)}+i\sqrt{\sqrt{1+\left(\omega\tau(T)\right)^2}+\omega\tau(T)}\right]$$

(3.16)

The scattering-source-dependent, temperature-dependent, and frequency-dependent effective resistance, $R(\omega,T)$, and inductance, $L(\omega,T)$ in the presence of skin effect in MLGNR interconnects is given as [151]:

$$R(\omega,T)=Real\left(Z_e(\omega,T)\right), L(\omega,T)=Imag\left(Z_e(\omega,T)\right)/\omega \quad (3.17)$$

3.3.2 Frequency-Dependent Analysis of Circuit Parameters: MLGNR Versus MCNT bundle and Cu interconnects

This subsection begins by examining the effective MFP of electrons deflecting from different scatterers of GNR. The scattering-limited realistic effective MFP is evaluated for both case 1 ($\lambda_R(T)$ excluding $\lambda_{SPP}(T)$ and λ_{SER}) and case 2 ($\lambda_R(T)$, equation (3.4)) at T=300 K. In case 1, MLGNRs without substrate polar phonons and rough GNR edges are considered, whereas in case 2, a realistic MLGNR with all the scatterers of equation (3.4) (considering p=1) is taken into account. Based on the frequency-dependent impedance model considering one-dimensional skin depth and $\tau(T)$, the frequency dependence of skin depth, p.u.l. resistance $R(\omega,T)$, and p.u.l. inductance $L(\omega,T)$ is analyzed for case 1 and case 2 of $\lambda_R(T)$. MLGNR interconnect variants, namely undoped MLGNR in two configurations (viz., HTC and VTC), and intercalation-doped HTC-MLGNR (doped with AsF_5, $FeCl_3$, and Li), are analyzed and compared with the Cu variants and MCNT bundle. Copper having smooth and rough surfaces [3, 4] and MCNT bundle-VI [68] are considered for the comparison, as discussed in subsection 3.2.1. The modeling for equivalent circuits of MCNT bundle and Cu can be referred to in [3, 4, 41, 68]. For the MCNT bundle, the configuration includes 78 SWCNTs with a diameter of 1 nm and 12 MWCNTs with an outer diameter of 6.44 nm [68, 69]. The global level interconnect (l=1 mm) simulation parameters are extracted from IRDS-2022, given as w=16 nm, t=40 nm, y_{ILD}=24 nm, spacing, s=16 nm, and ILD constant, ε_r=2.95 [2].

Figure 3.10(a) represents temperature-dependent MFPs, viz., $\lambda_{ac}(T)$, $\lambda_{op}(T)$, and $\lambda_{SPP}(T)$, and temperature-independent MFPs, viz., λ_{RS}, λ_{CI}, λ_{CD}, and λ_{SER}, varying with temperature (considering p=1 and SiO_2 dielectric substrate with δA=170 pm). $\lambda_{ac}(T)$, $\lambda_{op}(T)$, and $\lambda_{SPP}(T)$ decrease with the rise in temperature, whereas, owing to temperature invariant nature, λ_{RS}, λ_{CI},

λ_{CD}, and λ_{SER} remain constant. Moreover, the effective MFP, $\lambda_R(T)$, in both case 1 and case 2, demonstrates minimal dependency on temperature as they are dominated by the temperature-independent nature of corrugations on the dielectric surface and rough GNR edges, respectively. Figure 3.10(b) illustrates the variation of different MFPs as a function of corrugation amplitude (δA) for GNR placed on various dielectric substrates, namely, SiC, SiO_2, and BN, at 300 K. As δA increases, both λ_{CD} and $\lambda_R(T)$ (in case 1 and case 2) decrease, whereas λ_{SER}, $\lambda_{SPP}(T)$, λ_{CI}, λ_{RS}, $\lambda_{op}(T)$, and $\lambda_{ac}(T)$ remain constant as they are independent of δA. The results indicate that for δA values ranging from 10 pm to 50 pm, $\lambda_{eff}(T)$ for case 1 is primarily governed by λ_{CI}, as charged impurities dominate overall scatterings. Whereas λ_{CD} determines $\lambda_{R(T)}$ case 1 for δA ranging from 50 pm to 170 pm because the maximum deflection of electrons occurs due to corrugations on the dielectric surface. Moreover, $\lambda_R(T)$ case 2 is mainly determined by λ_{SER} for δA in the range of 10 pm-170 pm because edge scatterings dominate overall scattering phenomena. A longer $\lambda_R(T)$ for case 1 is observed compared to $\lambda_R(T)$ for case 2 due to a lower scattering rate in case 1 than in case 2. Furthermore, since SiC has the lowest amplitude of dielectric corrugations, the GNR placed on SiC always exhibits the longest $\lambda_R(T)$ for both case 1 and case 2. However, GNR placed on SiO_2 has the smallest $\lambda_R(T)$ for both case 1 and case 2.

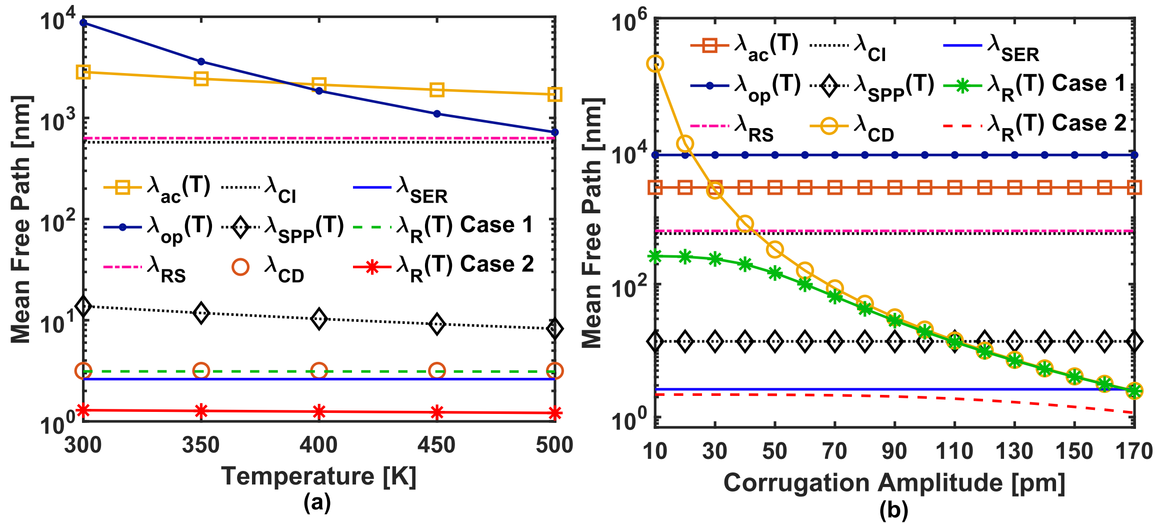

Figure 3.10 Mean free path as a function of (a) temperature (T), and (b) corrugation amplitude (δA) (T=300 K) for GNRs.

The calculated frequency-independent properties of undoped and intercalation-doped MLGNR (for case 2 considering p=1 and SiO_2 dielectric substrate with δA=170 pm), Li-D HTC-MLGNR (placed on various dielectric substrates for case 1 and case 2), Cu (with smooth and

rough surfaces), and MCNT bundle interconnects are given in Table 3.4. $R(T)$, $\sigma_{dc}(T)$, and $\tau(T)$ are calculated using equations given in subsection 3.3.1.

Table 3.4 Properties of different interconnect variants.

Interconnect variants		Properties		
		$R(T)$ [kΩ/μm]	$\sigma_{dc}(T)$ [μΩ.cm]$^{-1}$	$\tau(T)$ [s]
U-HTC-MLGNR (case 2)		39.1	0.4	7.2×10^{-16}
U-VTC-MLGNR (case 2)		34.3	0.46	7.2×10^{-16}
AsF_5-D HTC-MLGNR (case 2)		25.3	0.62	7.2×10^{-16}
$FeCl_3$-D HTC-MLGNR (case 2)		15.4	1.01	7.2×10^{-16}
Li-D HTC-MLGNR (case 2)		6.8	2.3	7.2×10^{-16}
Li-D HTC-MLGNR (case 1)	SiC	0.03	504	1.6×10^{-13}
	BN	0.12	127.7	4.0×10^{-14}
	SiO_2	3.21	4.9	1.5×10^{-15}
Li-D HTC-MLGNR (case 2)	SiC	3.61	4.3	1.3×10^{-15}
	BN	3.71	4.2	1.3×10^{-15}
	SiO_2	6.8	2.3	7.2×10^{-16}
Smooth Cu		0.146	106.4	8.9×10^{-15}
Rough Cu		0.160	97.6	7.7×10^{-15}
MCNT bundle		15.16	1.03	1.3×10^{-15}

The findings from Table 3.4 suggest that U-HTC-MLGNR placed on SiO_2 dielectric substrate has the highest $R(T)$ and lowest $\sigma_{dc}(T)$. This is because the scattering rate of electrons increases due to rough GNR edges, leading to smaller $\lambda_R(T)$ for case 2 (≈1 nm). Moreover, due to smaller $\lambda_R(T)$, a reduction in the average time between collisions of electrons with GNR scatterers, i.e., $\tau(T)$ is observed. Li-D HTC-MLGNR exhibits the lowest $R(T)$ and highest $\sigma_{dc}(T)$ compared to other MLGNR variants for case 2 and MCNT bundle because Li doping increases the number of conducting channels ($N_{TM}(T)$). However, Li-D HTC-MLGNR has inferior properties compared to Cu variants. Therefore, in order to improve $R(T)$ and $\sigma_{dc}(T)$, Li-D HTC-MLGNR placed on SiC, BN and SiO_2 is analyzed considering case 1 and case 2. When placed on SiC for case 1, Li-D HTC-MLGNR exhibits the lowest $R(T)$ and highest $\sigma_{dc}(T)$ compared to Cu variants and Li-D HTC-MLGNR placed on SiO_2 (case 1 and case 2), BN (case 1 and case 2) and SiC (case 2). This is attributed to longer $\lambda_R(T)$ (case 1) resulting from decreased scattering

rate of electrons due to several factors, including smooth GNR edges, absence of substrate SPPs and reduced corrugations on SiC dielectric surface.

The finite-thickness-dependent skin depth (Δ_{SD}) versus frequency for undoped MLGNR (viz., HTC and VTC), intercalation-doped HTC-MLGNR, Cu, and MCNT bundle interconnects is shown in Fig. 3.11. The Δ_{SD} decreases with an increase in frequency because current flow is reinforced on the surface and partially canceled at the center of the interconnect by eddy currents. In Fig. 3.11(a), a comparison between MLGNR (case 2, considering p=1 and δA=170 pm), Cu variants, and MCNT bundle indicates that U-HTC-MLGNR owing to its lowest $\sigma_{dc}(T)$ (see Table 3.4), exhibits the highest Δ_{SD}. This is attributed to the fact that Δ_{SD} is inversely proportional to $\sigma_{dc}(T)$ as per equation (3.10). However, the skin depth for Cu, MCNT bundle, and MLGNR variants (case 2) does not saturate due to the lower $\tau(T)$ (see Table 3.4), resulting in negligible $\omega\tau(T)$ values for frequencies below 10^4 GHz. The decrease in $\tau(T)$ for MLGNR variants (case 2) is attributed to an increased scattering rate, resulting in a smaller MFP ($\lambda_R(T)$, case 2). Figure 3.11(b) demonstrates that the Δ_{SD} values for Li-D HTC-MLGNR placed on SiC (case 1) saturates at 2 THz, where $\omega\tau(T)\approx 1$. Moreover, it exhibits higher saturated Δ_{SD} values, compared to Cu variants, which can be attributed to larger $\tau(T)$ values. $\tau(T)$ exhibits improved values due to enhanced $\lambda_R(T)$ of GNR in case 1 for SiC having low δA.

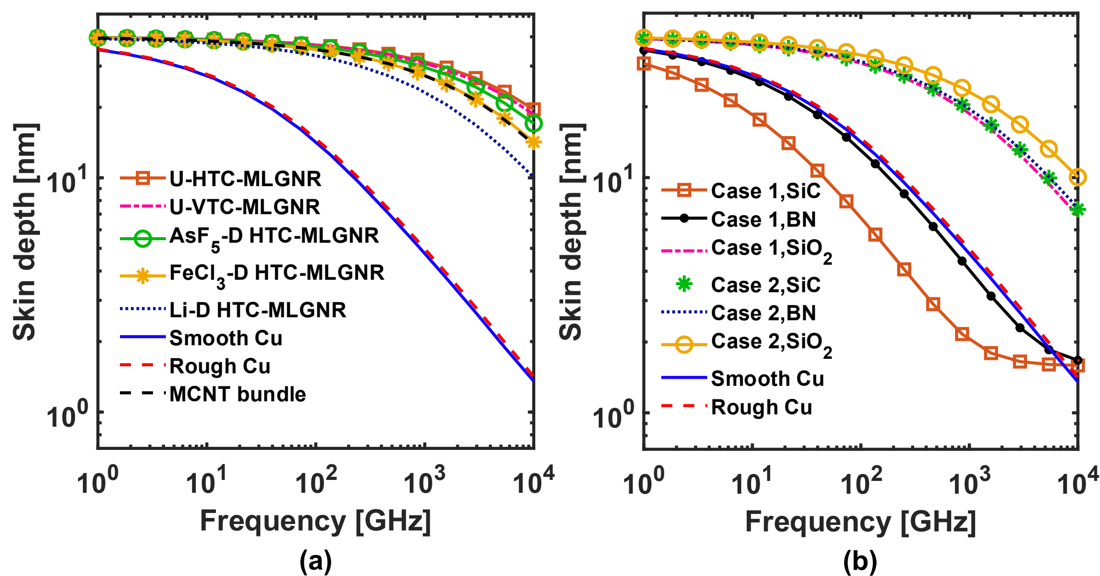

Figure 3.11 Skin depth variation with frequency for (a) MLGNR (case 2), Cu variants, and MCNT bundle, (b) Li-D HTC-MLGNR (placed on various dielectric substrates for case 1 and case 2) and Cu variants.

Figure 3.12 represents the variation of p.u.l. effective resistance ($R(\omega,T)$) with frequency for MLGNR variants and the results are compared with the Cu and MCNT bundle counterparts. $R(\omega,T)$ increases with frequency because Δ_{SD} decreases as frequency rises, leading to more confinement of the current towards the surface of the interconnect. The plot in Fig. 3.12(a) for MLGNR (case 2, considering p=1 and δA=170 pm), Cu variants, and MCNT bundle indicates that U-HTC-MLGNR has the highest $R(\omega,T)$ due to its lowest $\sigma_{dc}(T)$ value. Whereas smooth Cu owing to its highest $\sigma_{dc}(T)$, has the lowest $R(\omega,T)$. The $R(\omega,T)$ for Cu and MLGNR variants does not saturate due to a decrease in $\tau(T)$ (see Table 3.4). Li-D HTC-MLGNR exhibits the lowest $R(\omega,T)$, owing to its highest $\sigma_{dc}(T)$ values, compared to other MLGNR variants and MCNT bundle interconnects. Figure 3.12(b) compares the frequency dependence of the $R(\omega,T)$ for Li-D HTC-MLGNR placed on different dielectric substrates for case 1 and case 2 with Cu variants. It is found that the Li-D HTC-MLGNR on SiO_2 (case 1 and case 2), BN (case 2), and SiC (case 2) exhibit higher $R(\omega,T)$, owing to lower $\sigma_{dc}(T)$ values (see Table 3.4), than that of Cu variants. However, Li-D HTC-MLGNR on SiC and BN (case 1) always have lower $R(\omega,T)$ than Cu variants due to longer MFP of electrons and improved $\sigma_{dc}(T)$ values. In addition, due to larger $\tau(T)$ values, $R(\omega,T)$ for Li-D HTC-MLGNR on SiC saturates at 2 THz compared to Cu in which $R(\omega,T)$ keeps increasing. Therefore, placing Li-D HTC-MLGNR on SiC for case 1 minimizes the impact of frequency variations and skin effect.

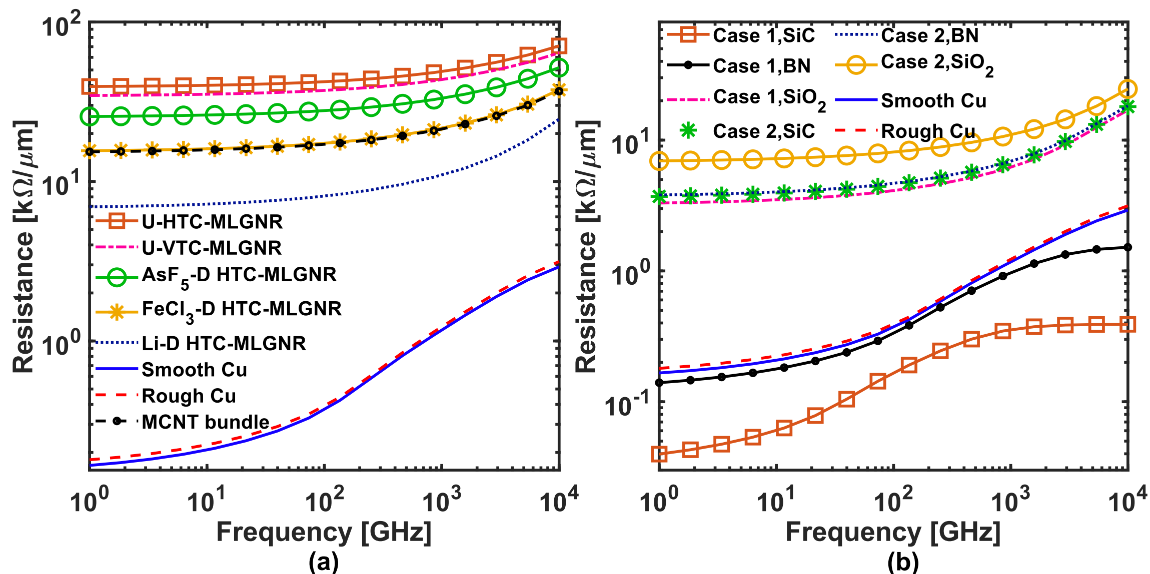

Figure 3.12 Resistance p.u.l. ($R(\omega,T)$) versus frequency for (a) MLGNR (case 2), Cu variants, and MCNT bundle, (b) Li-D HTC-MLGNR (placed on various dielectric substrates for case 1 and case 2) and Cu variants.

The high-frequency p.u.l. resistance ($R(\omega,T)$) to dc resistance ($R(T)$) ratio increases when varied with frequency, as shown in Fig. 3.13 for MLGNR, Cu variants, and MCNT bundle. Figure 3.13(a) indicates that compared to Cu variants, MLGNR variants (case 2, considering p=1and δA=170 pm) and MCNT bundle show less increase in resistance with frequency, indicating the reduced impact of skin effect. However, Cu variants show a substantial increment in frequency-dependent resistance, implying a significant impact of the skin effect. In Fig. 3.13(b), Li-D HTC-MLGNR variants (placed on various dielectric substrates for case 1 and case 2) have less resistance increase with frequency due to lower impact of skin effect, as compared to Cu variants. Also, $R(\omega,T)$ to $R(T)$ ratio saturates at 2 THz for Li-D HTC-MLGNR on SiC (case 1).

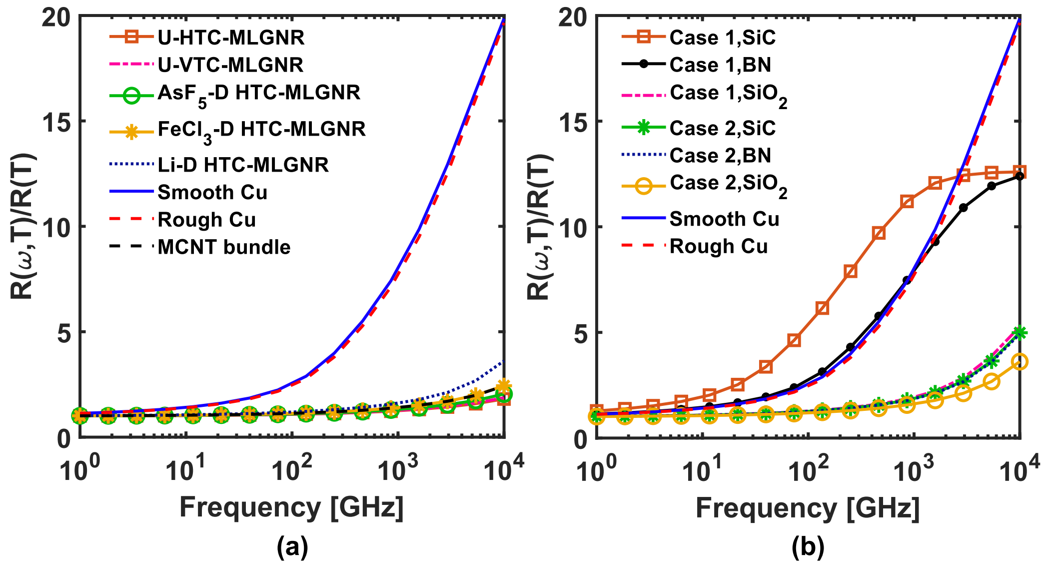

Figure 3.13 High-frequency p.u.l. resistance ($R(\omega,T)$) to dc resistance ($R(T)$) ratio for (a) MLGNR (case2), Cu variants, and MCNT bundle, (b) Li-D HTC-MLGNR (placed on various dielectric substrates for case 1 and case 2), and Cu variants, as a function of frequency.

In Fig. 3.14, p.u.l. effective inductance ($L(\omega,T)$) versus frequency for MLGNR, Cu variants, and MCNT bundle is shown. It is observed that initially, $L(\omega,T)$ decreases with an increase in frequency. This phenomenon occurs because the current tends to limit itself more toward the edges of the interconnect with an increase in frequency due to the skin effect, resulting in a reduction of the magnetic flux and a subsequent decrease in $L(\omega,T)$ [1]. However, at higher frequencies, $L(\omega,T)$ saturates as the term $\omega\tau(T)$ approaches to 1. Also, all the curves merge at higher frequencies as they have a negligible difference in current distributions. Another important point to note in Fig. 3.14(a) is that the $L(\omega,T)$ of U-HTC-MLGNR (case 2, considering p=1and δA=170 pm) is highest as it exhibits the largest Δ_{SD}, compared to other

MLGNR (case 2, considering p=1and δA=170 pm), Cu variants, and MCNT bundle interconnects. However, in Fig. 3.14(b), Li-D HTC-MLGNR placed on SiC and BN for case 1 shows lower $L(\omega,T)$ values compared to Cu variants.

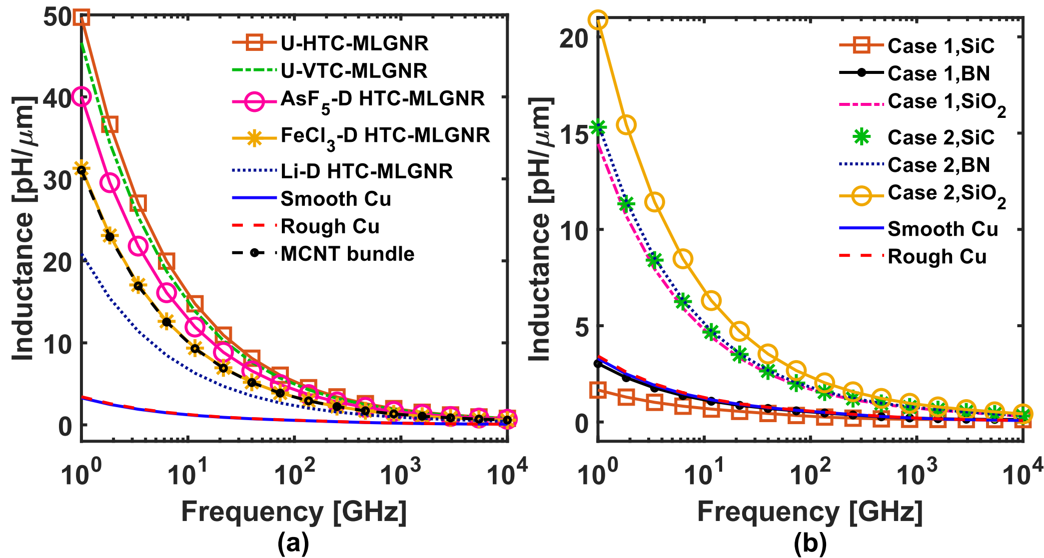

Figure 3.14 Inductance p.u.l. $L(\omega,T)$ for (a) MLGNR (case 2), Cu variants, and MCNT bundle, (b) Li-D HTC-MLGNR (placed on various dielectric substrates for case 1 and case 2), and Cu variants, as a function of frequency.

In Fig. 3.15(a), the finite-thickness-dependent skin effect model from this work is compared and validated against the existing skin effect models from [40–42], and [44, 45] for Li-D HTC-MLGNR on SiC (case 1). It is noted that the model outlined in [40–42] initially overestimates the skin depth values from 1 GHz - 30 GHz, as it does not account for the dependence of skin depth on the thickness of the conductor. However, from 30 GHz - 10^4 GHz, the model outlined in [40–42] show good agreement with the model presented in this work. Moreover, a good agreement is observed between the skin effect model presented in [44, 45] and the model from this work in the frequency range of 1 GHz - 30 GHz. However, from 30 GHz - 10^4 GHz, the skin depth values from the model outlined in [44, 45] exhibit a continuous decrease and do not saturate in the absence of the $\omega\tau(T)$ term.

Figure 3.15(b) illustrates the comparison and validation of the impedance model from this work with the model outlined in [40, 42] for Li-D HTC-MLGNR on SiC (case 1). A deviation is evident between the resistance and inductance values obtained from this work and the model in [40, 42], and the deviation decreases with the increase in frequency. The observed deviation stems from the fact that the impedance model in [40, 42] does not consider the finite-thickness-

dependent skin effect model. However, a good agreement is observed between the impedance model from this work and the model outlined in [40, 42] for frequencies beyond 30 GHz.

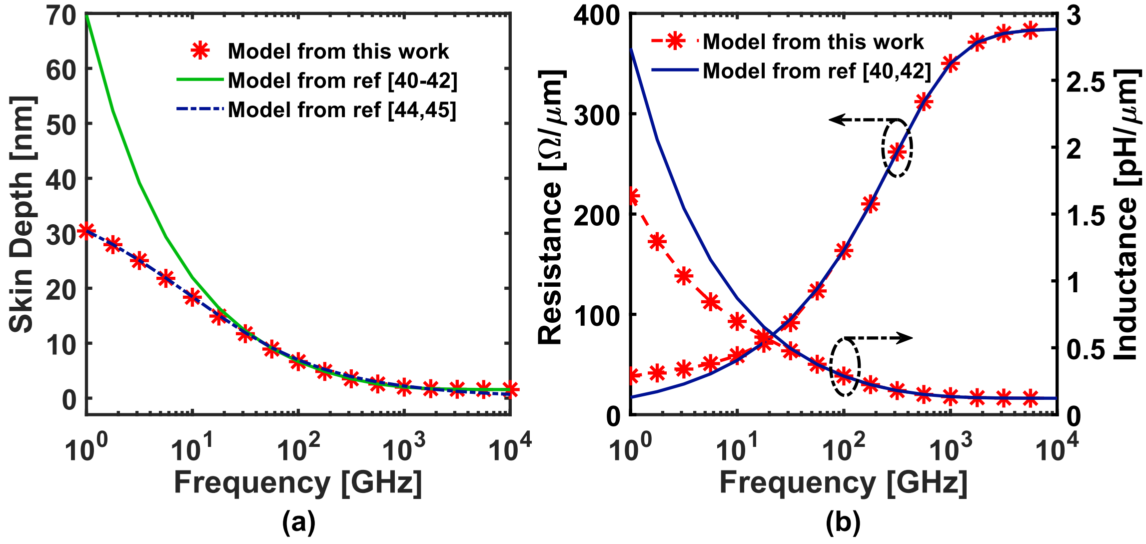

Figure 3.15 Comparison of (a) the skin depth model outlined in this work with models from [40–42], and [44, 45], and (b) the resistance and inductance model from this work with the model outlined in [40, 42], for Li-D HTC-MLGNR on SiC (case 1), as a function of frequency.

3.4 Chapter Summary

An impedance model incorporating the scattering-limited realistic effective MFP is developed for MLGNR-based interconnect variants, including undoped MLGNR in three different configurations (i.e., HTC, HSC and VTC) and intercalation-doped HTC-MLGNR (with Li, $FeCl_3$, and AsF_5 dopants) to extract frequency-independent circuit parameters. The circuit parameters for MLGNR variants, considering perfect ($\lambda_P(T)$) and realistic ($\lambda_R(T)$) effective MFP values, are extracted and compared to MCNT bundles and Cu (with both smooth and rough surfaces) across a temperature range of 300 K to 500 K. It is worth noting that $\lambda_R(T)$ decreases with rise in temperature and is limited to the nanometer range, with λ_{SER} being the dominant factor that determines $\lambda_R(T)$. The resistance and inductance values for MLGNR variants increase with increasing temperature, while a minute decrease is observed for capacitance. The results show that the MLGNR variants exhibit lower resistance compared to the MCNT bundle and Cu interconnects for $\lambda_P(T)$. Moreover, the resistance of all MLGNR variants and MCNT bundle interconnect become several orders larger than that of both smooth and rough Cu for $\lambda_R(T)$, whereas only Li-D MLGNR exhibits lower resistance than MCNT bundle for $\lambda_R(T)$.

Furthermore, the circuit parameters of MLGNR variants, considering $\lambda_R(T)$ (with and without SER), are obtained and compared to the Cu counterpart in the range of 10 pm to 170 pm. It is observed that $\lambda_R(T)$ decreases as δA increases, and $\lambda_R(T)$ with SER is always shorter than that of without SER. Also, the MLGNR interconnects without SER on SiC (δA =10 pm) exhibit the longest MFP, while the one on SiO_2 (δA =170 pm) with SER shows the shortest MFP. The results show that MLGNR variants exhibit resistance increase by increasing δA. Moreover, the resistance of MLGNRs on SiC (δA =10 pm), BN (δA =70 pm), and SiO_2 (δA =170 pm) is always larger than Cu counterparts when $\lambda_R(T)$ with SER is considered. Whereas the resistance of Li-D HTC-MLGNR without SER on SiC and BN is less than that of Cu, and the MLGNR on SiO_2 has more resistance than Cu counterparts.

An impedance model was developed for both undoped and intercalation-doped MLGNR interconnects, accounting for scattering-limited effective MFP and finite thickness skin effects. By employing the proposed impedance model, frequency-dependent circuit parameters for MLGNR interconnects are obtained and compared to MCNT bundle and Cu interconnects. The results show that the resistance increases while inductance decreases with an increase in frequency from 1 GHz to 10^4 GHz. Realistic MLGNR and MCNT bundle interconnects (considering $\lambda_R(T)$) exhibit higher resistance and inductance values compared to their Cu counterparts. However, Li-D HTC-MLGNR exhibits lower resistance and inductance than other MLGNR variants, and MCNT bundle interconnects. Furthermore, Li-D HTC-MLGNR interconnects, when optimized by placing on SiC and BN substrates and with factors like SPP and SER excluded from $\lambda_R(T)$, demonstrate lower resistance and inductance than Cu interconnects.

Based on the impedance modeling and circuit parameter analysis presented in this chapter, the next chapter explores the signal integrity analysis in three coupled MLGNR interconnects under the influence of performance limiting factors like scattering sources, dielectric losses, temperature, skin effects, and crosstalk. The developed impedance model with frequency-independent circuit parameters is utilized to analyze key signal integrity aspects like crosstalk-induced delay, transient response, 3-dB bandwidth, and relative stability of MLGNR interconnects. Additionally, the frequency-dependent impedance model is employed to assess how frequency variations influence the performance of MLGNR interconnects in terms of crosstalk-induced delay, overshoot amplitude, and overshoot width.

Chapter 4 Signal Integrity Analysis in MLGNR Interconnects

4.1 Introduction

As highlighted in Chapter 2, crosstalk—caused by electromagnetic coupling between densely packed interconnects—adversely affects signal functionality, reliability, and timing in high-frequency MLGNR interconnects [39]. Functional crosstalk-induced noise raises reliability concerns due to device stress, while dynamic crosstalk delay complicates timing estimation. Additionally, transient behavior in MLGNR interconnect models contributes to rise-time degradation, reduced 3-dB bandwidth, and compromised stability [102, 103].

Previous studies have explored the performance degradation of MLGNR interconnects under scattering effects [26, 72, 104] and improvements through intercalation doping [18, 91]. However, these studies have not accounted for the impact of crosstalk effects arising from coupling between MLGNR interconnects. Crosstalk analysis of three capacitively coupled MLGNR interconnect lines has been presented in [30, 106], but the MFP model accounted solely for scatterings from intrinsic phonons. Moreover, researchers have conducted crosstalk analysis of coupled MLGNR interconnect lines, incorporating extrinsic scattering-limited realistic effective MFP [108, 109, 111–113]. An ABCD-parameter-based analytical model that incorporates the effect of extrinsic scatterers has been utilized for performance analysis of coupled MLGNR interconnects considering crosstalk effects [80, 105, 107, 123, 125].

However, the impact of structural edge roughness (SER), one-dimensional skin depth, and their interplay with crosstalk effects remain largely unaddressed in the existing literature. This chapter aims to bridge these gaps by analyzing the high-frequency signal integrity of MLGNR interconnects under realistic conditions.

This chapter presents a frequency-independent and frequency-dependent performance analysis of MLGNR interconnects, incorporating a scattering-limited realistic effective MFP and a finite-thickness-dependent, skin-effect-based impedance model developed in Chapter 3. Section 4.2 employs a scattering-limited, realistic effective MFP-based impedance model with frequency-independent circuit parameters for crosstalk-induced delay analysis of MLGNR interconnects using SPICE simulations over a temperature range of 300 K to 500 K. The results are compared with MCNT bundle and Cu interconnects, and the MLGNR interconnect width is optimized to minimize crosstalk-induced delay. Additionally, an analytical model and

decoupling technique are utilized to analyze the transient response, 3-dB bandwidth, and relative stability of MLGNR interconnects. In Section 4.3, an impedance model incorporating realistic effective MFP and a finite-thickness-dependent skin effect model is used to evaluate frequency-dependent crosstalk-induced delay, overshoot amplitude, and overshoot width for MLGNR interconnects using SPICE simulations over a frequency range of 1 GHz to 10^4 GHz. The results are then compared with those for Cu and MCNT bundle interconnects.

4.2 Frequency-Independent Crosstalk Analysis

This section begins by analyzing the impact of scattering sources on crosstalk-induced delay for undoped and intercalation-doped MLGNR interconnects. The crosstalk-induced delay results are then compared to those of MCNT bundle and Cu (with both rough and smooth surfaces) interconnects over a temperature range of 300 K to 500 K. Additionally, width optimization is performed for undoped and intercalation-doped MLGNR, and smooth and rough Cu interconnects at 300 K, with the goal of minimizing crosstalk delay considering $\lambda_P(T)$ and $\lambda_R(T)$. Lastly, the transient step response, 3-dB bandwidth, and relative stability of undoped and intercalation-doped MLGNR interconnects are evaluated and compared to smooth and rough Cu interconnects at 300 K for global interconnect lengths (l=1 mm). The cross-sectional geometry of capacitively coupled aggressor and victim nets with spacing s, width w, and thickness t, placed at a distance y_{ILD} from both ground planes, is depicted in Fig. 4.1 [72] and its driver interconnect load (DIL) architecture is depicted in Fig. 4.2.

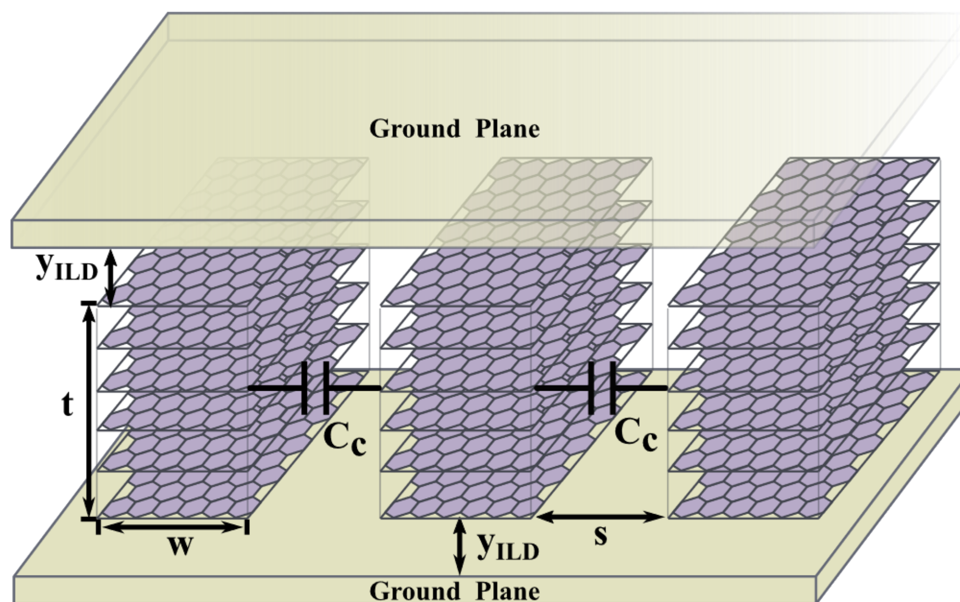

Figure 4.1 Schematic of three capacitively coupled interconnects.

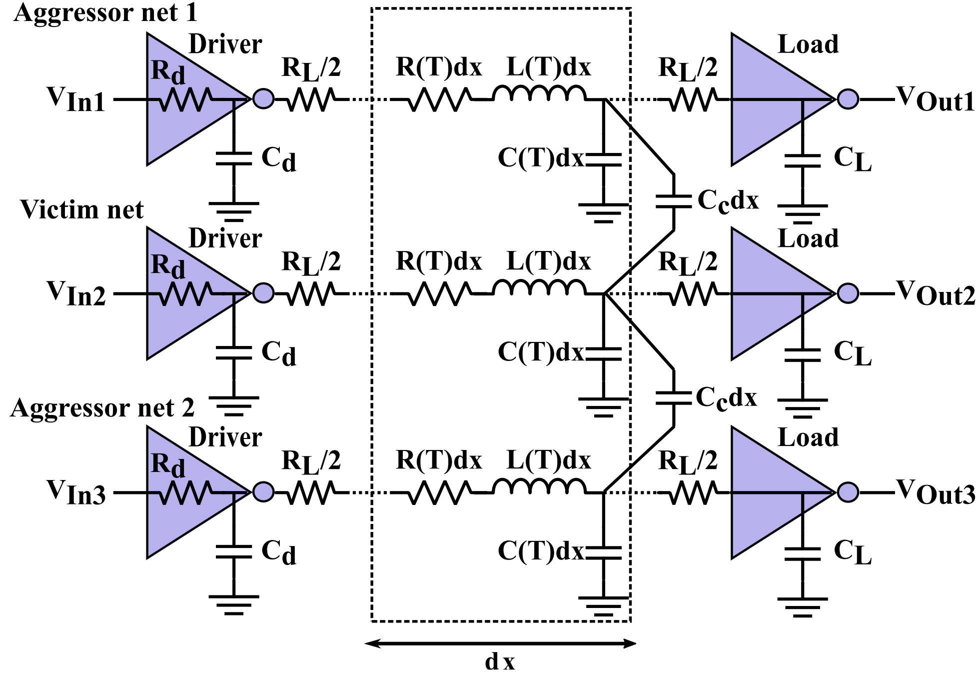

Figure 4.2 Equivalent capacitively coupled three-line DIL architecture.

To analyse the performance of global interconnects (1mm long) at 13 nm technology node, the physical parameters used in various calculations are extracted from ITRS 2013 and are summarized in section 3.2.2 [7]. Figure 4.2 demonstrates DIL architecture for three capacitively coupled interconnect lines, where R_d, C_d, and C_L are driver resistance, driver capacitance and load capacitance, respectively. C_c is the coupling capacitance p.u.l. between two adjacent interconnects, calculated by mathematical formulations given in prior work [4, 60]. However, unlike prior work, which primarily focused on conventional Cu interconnects and lacked a frequency-dependent analysis, this study extends the analysis by incorporating a frequency-dependent analysis of MLGNR-based interconnects. The lumped resistance, R_L, is given as, $R_L = R_{mc} + R_Q(T)$.

4.2.1 Temperature-Dependent Crosstalk-Induced Delay Analysis

The impact of scattering sources is presented in this subsection by considering two different models of effective MFP, i.e., $\lambda_P(T)$ and $\lambda_R(T)$, on the crosstalk-induced delay calculated for adjacent interconnects of undoped MLGNR (viz., VTC, HSC, and HTC) and intercalation-doped HTC-MLGNR. Moreover, the obtained delay results are compared with that of MCNT bundle interconnects and Cu counterparts exhibiting rough and smooth surfaces, with temperature varying in range of 300 K - 500 K. The most common and consistent intercalation dopants viz., AsF_5, Li, and $FeCl_3$ are taken into account to study the behaviour of MLGNR in

detail. The C_c for MLGNR variants, smooth Cu, and rough Cu is obtained as 57.32 aF/µm, 57.32 aF/µm and 59.56 aF/µm using formulas given in prior work [4, 60].

The dynamic crosstalk-induced delay at the far end of victim net, considering MCNT bundle and all the variants of Cu and MLGNR interconnects, are evaluated and discussed under in-phase switching conditions to observe the impact on critical timing issue of the signal propagating in VLSI interconnects. Under in-phase switching condition for coupled configuration of interconnects (Fig. 4.2), victim net and both the aggressor nets switch simultaneously in same phase. For example, when the victim net switches from logic 0 → 1, at the same time the aggressor nets are switched from logic 0 → 1 or vice-versa. Capacitively coupled three-line bus architecture, given in Fig. 4.2, is used for dynamic crosstalk-induced delay analysis. The values of $R(T)$, $L(T)$, and $C(T)$ for interconnect variants are extracted from Tables 3.2 and 3.3. TSPICE simulator is used to simulate the temperature-dependent, scattering-source-dependent, and CMOS-driven equivalent circuit operating at a power supply (V_{DD}) of 0.8 V and terminated with C_L=0.14 fF [106]. The ratio of optimal to minimum driver size is taken as 100. R_d = 18.33 KΩ and C_d = 0.03 fF are considered for the minimum sized gate[111].

Table 4.1 Optimal number of repeaters to reduce crosstalk-induced delay of intercalation-doped and undoped MLGNR, Cu, and MCNT bundle interconnects (l=1 mm).

Interconnect variants	Number of repeaters	
	$\lambda_P(T)$	$\lambda_R(T)$
Li-D HTC-MLGNR	5	91
$FeCl_3$-D HTC-MLGNR	5	151
AsF_5-D HTC-MLGNR	5	201
U-HSC-MLGNR	5	291
U-HTC-MLGNR	5	291
U-VTC-MLGNR	5	131
Smooth Cu	7	7
Rough Cu	7	7
MCNT bundle	17	291

Optimal repeater insertion mitigates the effects of extrinsic scatterers by dividing the interconnect into shorter segments, significantly minimizing the crosstalk-induced delay and ensuring reliable high-speed performance in on-chip interconnects. The optimal number of

repeaters calculated from simulations for global length interconnects (~1 mm long) are given in Table 4.1 for $\lambda_P(T)$ and $\lambda_R(T)$. It is observed that, as MLGNR variants exhibit higher resistance for $\lambda_R(T)$ than $\lambda_P(T)$ (see Table 3.2), a greater number of repeaters are employed for MLGNR variants compared to Cu in the case of $\lambda_R(T)$. However, MLGNR variants utilize a smaller number of repeaters than the MCNT bundle for both $\lambda_R(T)$ and $\lambda_P(T)$.

Crosstalk between coupled interconnects induces signal delay, and the presence of scatterers further amplifies this effect, severely degrading the performance of MLGNR interconnects. Figure 4.3 demonstrates crosstalk-induced delay at the far end of the victim net, varying as a function of temperature in the range of 300 K - 500 K for global interconnects (l=1 mm) considering $\lambda_P(T)$ and $\lambda_R(T)$. It is observed that, with the temperature increasing from 300 K - 500 K, the crosstalk-induced delay of MLGNR, Cu, and MCNT bundle interconnects increases for $\lambda_P(T)$ and $\lambda_R(T)$, because resistance also increases with a rise in temperature as shown in Tables 3.2 and 3.3. However, for $\lambda_R(T)$, the crosstalk-induced delay of MLGNR variants increases at a slower rate with rising temperature, as the resistance exhibits a weaker dependence on temperature.

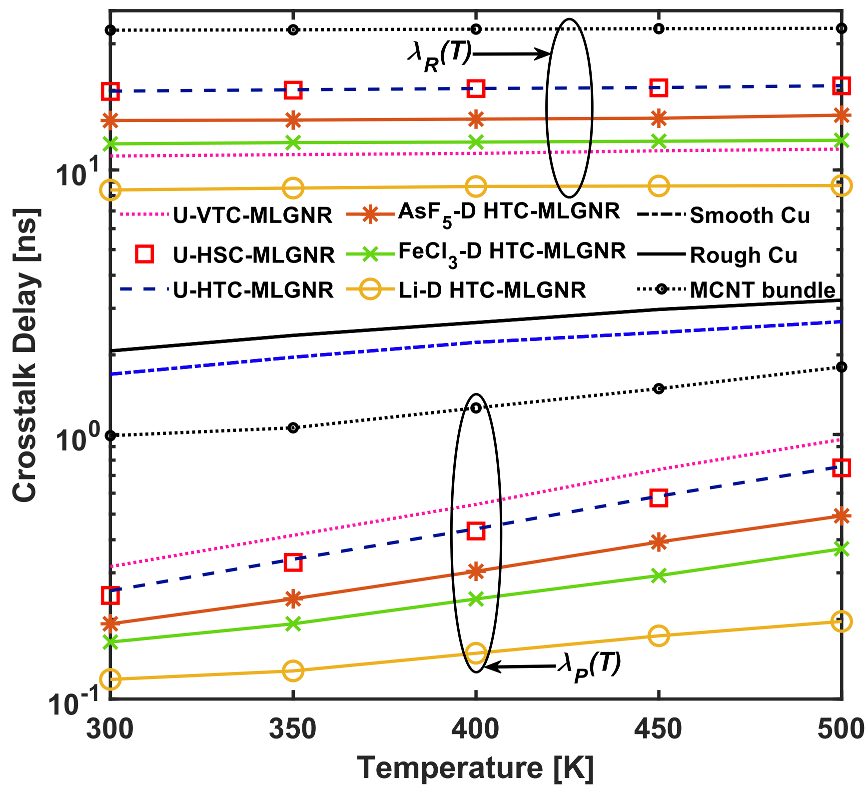

Figure 4.3 Crosstalk-induced delay vs temperature curves for undoped MLGNR (viz., VTC, HSC, and HTC), intercalation-doped HTC-MLGNR (with AsF_5, $FeCl_3$, and Li dopants), and smooth and rough Cu, and MCNT bundle interconnects.

In Fig. 4.3, the Li-D HTC-MLGNR, owing to its lowest resistance values for $\lambda_P(T)$, exhibits the smallest crosstalk-induced delay values compared to MCNT bundle and other MLGNR and Cu variants. On the contrary, smooth Cu has the lowest crosstalk-induced delay values in comparison to rough Cu, MCNT bundle, and MLGNR variants for $\lambda_R(T)$. Also, Li-D HTC-MLGNR exhibits lower crosstalk-induced delay values compared to other MLGNR variants and MCNT bundle for $\lambda_R(T)$.

Furthermore, for the MLGNR variants at the global length of l =1 mm, the average relative penalty (ARP) is calculated by averaging the relative penalty in crosstalk-induced delay (XT-D), given as ((XT-D $_{\lambda R(T)}$ - XT-D $_{\lambda P(T)}$)/XT-D $_{\lambda P(T)}$×100%), computed at equal steps of 50 K over 300-500 K temperature range when $\lambda_R(T)$ is considered w.r.t $\lambda_P(T)$. ARP in crosstalk-induced delay for MLGNR variants is obtained as 21.58×10^2 %, 48.14×10^2 %, 49.35×10^2 %, 52.68×10^2 %, 53.92×10^2 % and 57.09×10^2 % for U-VTC-MLGNR, U-HTC-MLGNR, U-HSC-MLGNR, AsF_5-D HTC-MLGNR, $FeCl_3$-D HTC-MLGNR and Li-D HTC-MLGNR, respectively. It is observed that the crosstalk-induced delay of MLGNR variants significantly increases when the scattering-limited realistic MLGNR ($\lambda_R(T)$) is considered, compared to the intrinsic-phonon-limited perfect MLGNR ($\lambda_P(T)$), due to the enhanced electron deflection caused by various scattering sources in $\lambda_R(T)$. Also, the Li-D HTC-MLGNR, with the best delay structure among MLGNR variants, has the largest ARP of 57.09×10^2 %, while U-VTC-MLGNR has least ARP of 21.58×10^2 % in terms of crosstalk-induced delay. It is because of the corresponding largest and smallest ARP in resistance values for Li-D HTC-MLGNR and U-VTC-MLGNR, respectively, when $\lambda_R(T)$ is used w.r.t $\lambda_P(T)$ (see Table 3.2). Moreover, the Li-D HTC-MLGNR exhibits a decrease of 85.48% and 74.67% in dynamic in-phase crosstalk-induced delay as compared to the MCNT bundle, for $\lambda_P(T)$ and $\lambda_R(T)$, respectively.

4.2.2 Optimizing Width for Minimum Crosstalk-Induced Delay

In this subsection, the width of the interconnect is optimized to obtain minimum crosstalk-induced delay for intercalation-doped MLGNR, undoped MLGNR, and Cu (rough and smooth surface) considering $\lambda_P(T)$ and $\lambda_R(T)$, at 300 K. The crosstalk analysis is performed using the simulation setup discussed in subsection 4.2.1. Figures 4.4(a) and (b) demonstrate the variation of the number of conducting channels ($N_{TM}(T)$) and the number of layers (N_H/N_V) with w_{Int}/w_{ITRS} ratio, respectively (calculated using expressions given in subsection 3.2.1). w_{Int} represents the variable interconnect width. The fixed interconnect width, w_{ITRS}, is set at 20 nm as per ITRS 2013 guidelines for global interconnects at 13 nm technology node to balance continued scaling

and related challenges such as signal integrity, fabrication feasibility, and high-frequency performance. The $N_{TM}(T)$ increases with an increase in w_{Int}/w_{ITRS} ratio and fermi energy (E_f) for undoped MLGNR (viz., HSC and HTC) and intercalation-doped HTC-MLGNR, whereas it remains constant for U-VTC-MLGNR as illustrated in Fig. 4.4(a). However, as seen in Fig. 4.4(b), the number of layers for U-VTC-MLGNR increases with w_{Int}/w_{ITRS} ratio, whereas it remains constant for undoped MLGNR (viz., HSC and HTC) and intercalation-doped HTC-MLGNR. Hence, with an increase in w_{Int}, $N_{TM}(T)$ and the number of layers increase, leading to a decrease in effective resistance and an increase in equivalent capacitance of MLGNR. Hence, the optimum interconnect width exists for obtaining the minimum value of crosstalk-induced delay.

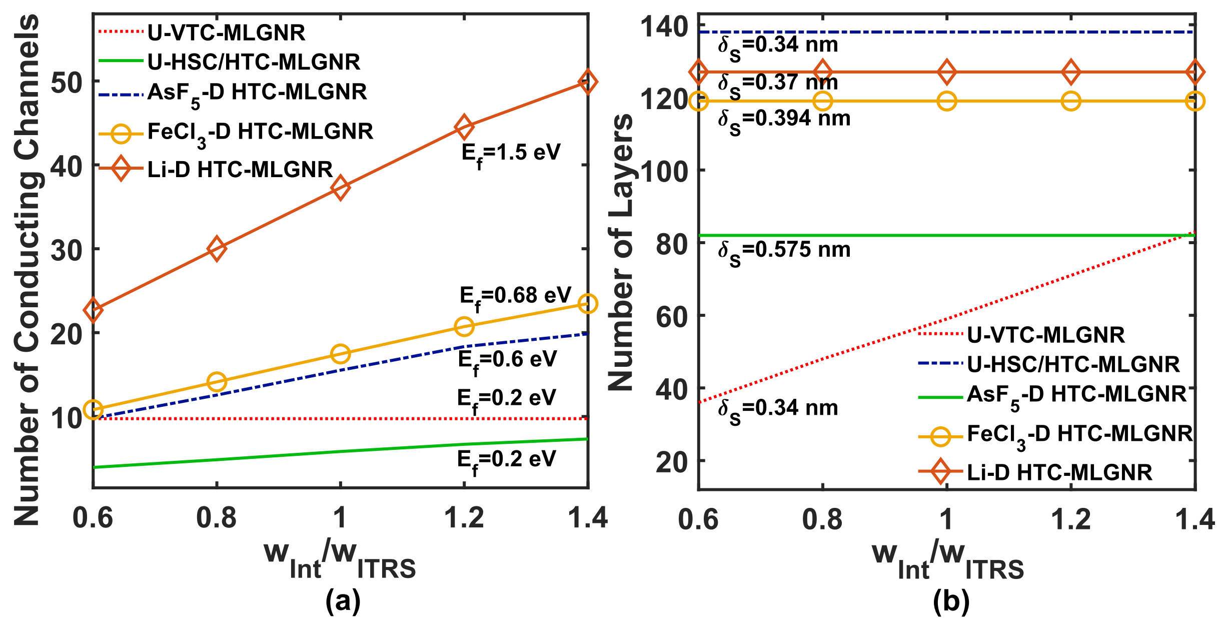

Figure 4.4 (a) Number of conducting channels ($N_{TM}(T)$), and (b) number of layers (N_H/N_V) as a function of interconnect width for undoped MLGNR (viz., VTC, HSC, and HTC), and intercalation-doped HTC-MLGNR (with AsF_5, $FeCl_3$, and Li dopants) (T=300 K).

Figures 4.5(a) and (b) exhibit the crosstalk-induced delay variations with w_{Int}/w_{ITRS} ratio for $\lambda_P(T)$ and $\lambda_R(T)$, respectively. It is observed that the optimum width values required for obtaining minimum crosstalk-induced delay in U-VTC-MLGNR, U-HSC-MLGNR, U-HTC-MLGNR, AsF_5-D HTC-MLGNR, $FeCl_3$-D HTC-MLGNR and Li-D HTC-MLGNR is 28 nm, 20 nm, 20 nm, 20 nm, 16 nm and 20 nm, respectively for $\lambda_P(T)$ while it is 16 nm, 20 nm, 20 nm, 20 nm, 20 nm, 20 nm, respectively for $\lambda_R(T)$. Minimum crosstalk-induced delay for smooth and rough Cu is obtained at an optimized width of 28 nm. However, Li-D HTC-MLGNR interconnects with optimized width exhibit minimum crosstalk-induced delay among all the MLGNR variants for $\lambda_P(T)$ and $\lambda_R(T)$. Also, Li-D HTC-MLGNR exhibits (≈89.58 ps) 10.59×

lower and (≈8.4 ns) 8.85× higher crosstalk-induced delay for $\lambda_P(T)$ and $\lambda_R(T)$, respectively, compared to smooth Cu.

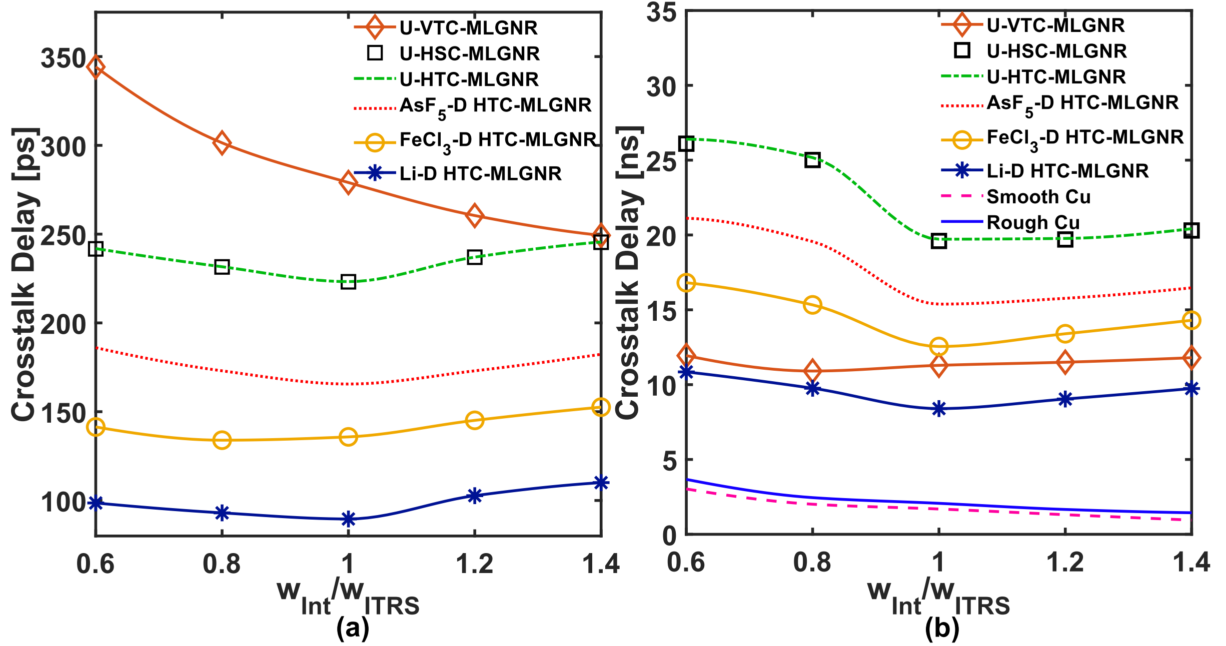

Figure 4.5 Crosstalk-induced delay variation with interconnect width for U-MLGNR (viz., VTC, HSC, and HTC), D-HTC-MLGNR (with AsF_5, $FeCl_3$, and Li dopants), and Smooth and Rough Cu for (a) $\lambda_P(T)$, and (b) $\lambda_R(T)$ (T=300 K).

From the obtained results in subsections 4.2.1 and 4.2.2, it can be deduced that the Li-D HTC-MLGNR is a promising candidate for on-chip interconnects when optimistic intrinsic-phonon-limited effective MFP model ($\lambda_P(T)$) is considered. Whereas scattering-limited realistic effective MFP model ($\lambda_R(T)$) severely degrades the performance of undoped and intercalation-doped MLGNR as compared to Cu counterparts in terms of crosstalk-induced delay. This occurs because, at smaller widths, the scatterings induced by structural edge roughness become dominant compared to intrinsic-phonon-limited scatterings, leading to an increase in MLGNR resistance [27]. Therefore, all the scattering sources present in $\lambda_R(T)$ must be incorporated in design considerations for a realistic comparison of prospective interconnect materials in the worst-case scenario.

4.2.3 Transient Response and 3-dB Bandwidth Analysis

The transient response ensures timing integrity by determining how quickly the interconnect can react to abrupt input signals, thus preventing signal delays and potential logic errors, while 3-dB bandwidth defines the frequency range within which signals are transmitted with minimal distortion, ensuring data integrity in high-speed circuits. This subsection analyzes and

compares the transient step response and 3-dB bandwidth of undoped and intercalation-doped MLGNR interconnects to Cu (exhibiting smooth and rough surfaces) interconnects at 300 K for global level (l=1 mm). HTC-MLGNR and VTC-MLGNR are considered in the case of undoped MLGNR, while intercalation-doped HTC-MLGNR is considered for the analysis. The behavior of HTC-MLGNR, doped with intercalation dopants like Li, $FeCl_3$, and AsF_5, is studied. The values of $R(T)$, $L(T)$, and $C(T)$ for interconnect variants are extracted from Fig. 3.7 and Tables 3.2 and 3.3. The impact of crosstalk due to coupling on the victim net, due to aggressor nets 1 and 2, for three interconnect line system given in Fig. 4.2 is calculated using the decoupling technique [121, 154]. In this technique, the victim net is represented as an independent decoupled interconnect as shown in Fig. 4.6, where $R_{de}(T)$, $L_{de}(T)$, and $C_{de}(T)$ are the decoupled p.u.l resistance, inductance and capacitance, respectively. Here, $R_{de}(T) = R(T)$, $L_{de}(T) = L(T)$, $C_{de}(T) = \eta C_q(T)$, $\eta = 1 - 2g - h$, $g = \frac{ab}{ab^2+b^3-2a^2b}$, $h = \frac{b^2}{ab^2+b^3-2a^2b}$, $a = \frac{C_c}{C_q(T)}$, and $b = \frac{C_e+C_q(T)+C_C}{C_q(T)}$ [121].

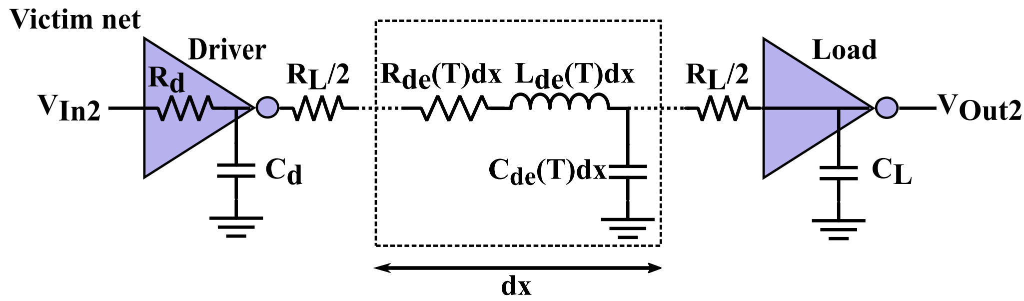

Figure 4.6 Equivalent circuit model of decoupled victim net.

The analysis of three capacitively coupled adjacent interconnect lines is done using the transfer function ($T(s)$) of equivalent decoupled victim net (see Fig. 4.6). $T(s)$ is given by ratio of output to input voltage of decoupled victim interconnect and is obtained using ABCD parameters of the two-port network, formulated as [122]:

$$T(s) = \frac{V_{Out2}(s)}{V_{In2}(s)} = \frac{1}{A+sBC_L} \tag{4.1}$$

where, $A = X(1 + sC_{de}(T)Y) + sR_dC_{de}(T)$, $B = X\big((R_L/2) + (1 + Z)Y\big) + R_d(1 + Z)$, $X = (1 + sR_dC_d)$, $Y = (sL_{de}(T) + R_{de}(T) + (R_L/2))$, and $Z = sC_{de}(T)(R_L/2)$. R_d = 18.33 KΩ, C_d = 0.03 fF and C_L = 0.065 fF are considered for the calculations [111]. The simulations are carried out in a standard desktop environment using MATLAB R2022a for 13 nm technology node.

The transient step response is the time domain response at the output of the victim net when the unit step voltage pulse is applied at the input of the decoupled victim net. Transient step response reveals the quickness of a circuit's output response to abruptly changing input signals [102]. MATLAB simulation is performed by feeding step input to transfer function block and visualizing the output response on the scope. In Figs. 4.7 and 4.8, step response and frequency response are plotted, respectively, for MLGNR variants with SER (p=1) on SiO_2 and compared to Cu variants. The values of 50% delay time (t_d), rise time (t_r) and 3-dB bandwidth extracted from Figs. 4.7 and 4.8 are presented in Table 4.2.

As can be observed from Fig. 4.7, Smooth Cu has the fastest and steepest step response and lowest t_d and t_r, as given in Table 4.2. This is due to the lowest value of $R_{de}(T)$ (see Fig. 3.7(a)), which dominates overall t_d and t_r, whereas the impact of a higher value of $C_{de}(T)$ (see Table 3.2) is negligible. In contrast, undoped HTC-MLGNR has the highest t_d and t_r (owing to the highest value of $R_{de}(T)$), hence showing the slowest and sluggish step response. Li-D HTC-MLGNR shows the steepest step response among all the MLGNR variants owing to its lowest $R_{de}(T)$ value. Li-D HTC MLGNR exhibits 1264.8% and 1250.4% increase in t_d and t_r, respectively, compared to smooth Cu.

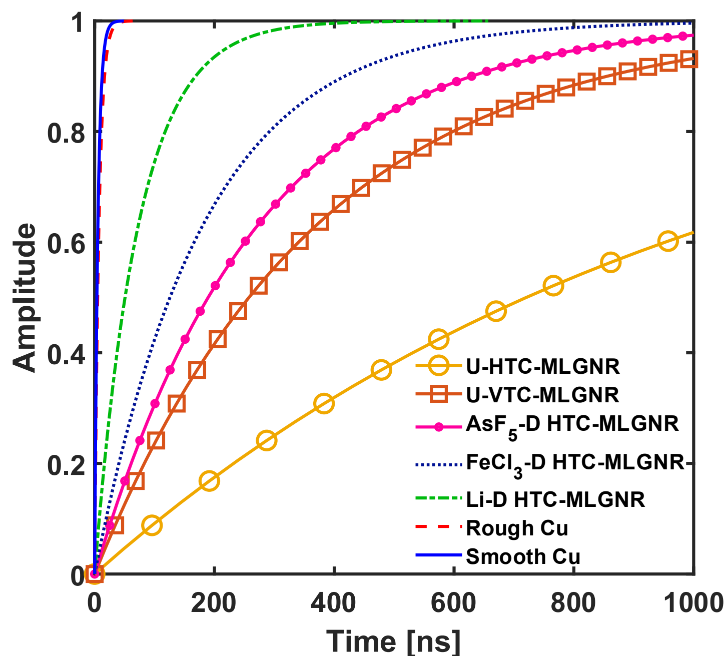

Figure 4.7 Step response of undoped and intercalation-doped MLGNR (with SER, p=1, and δA =170 pm) and Cu interconnects.

The absolute frequency response shown in Fig. 4.8 is obtained from transfer function *T(s),* which determines the frequency range over which the output signal at the victim line can be

reproduced without losing information present in the input signal. It is observed that smooth Cu outperforms all the MLGNR variants and rough Cu in terms of cut-off frequency (f_c), which further depends on dominant parasitic parameters of the interconnect, i.e., $R_{de}(T)$ and $C_{de}(T)$. The absolute frequency response is similar to that of an RC low-pass filter having a cut-off frequency $f_c = 1/2\pi R_{de}(T)C_{de}(T)$ [122]. Smooth Cu has the highest, and undoped HTC-MLGNR has the lowest 3-dB bandwidth due to their lowest and highest $R_{de}(T)$ values (dominates overall f_c), respectively.

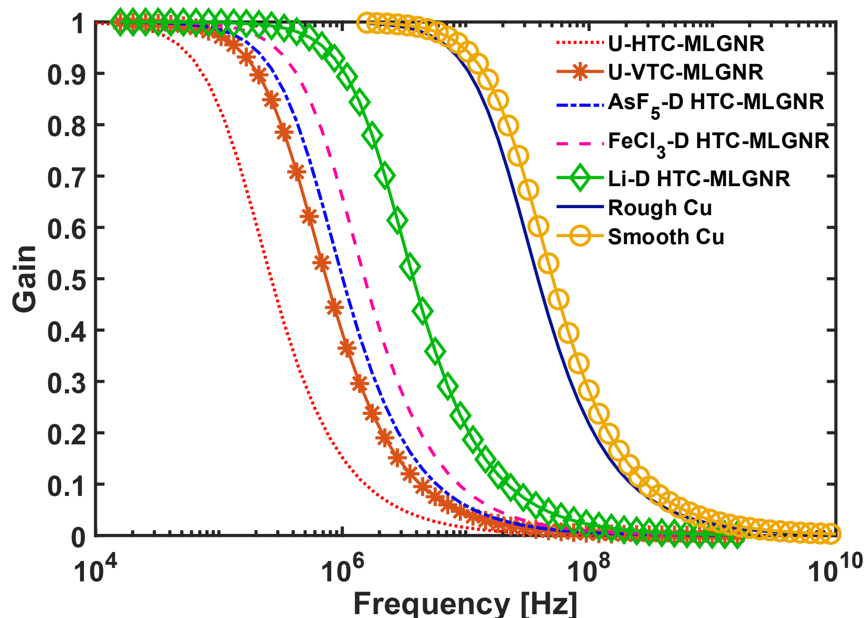

Figure 4.8 Frequency response of undoped and intercalation-doped MLGNR (with SER, p=1, and δA =170 pm) and Cu interconnects.

Table 4.2. t_d, t_r, and 3-dB bandwidth for different configurations of undoped and intercalation-doped MLGNR (with SER, p=1, and δA =170 pm) and Cu interconnects.

Interconnect variants	50% delay time, t_d [ns]	Rise time, t_r [ns]	3-dB Bandwidth [MHz]
U-HTC-MLGNR	718	2283	0.15
U-VTC-MLGNR	256	816	0.43
AsF_5-D HTC-MLGNR	188	600	0.58
$FeCl_3$-D HTC-MLGNR	125	398	0.87
Li-D HTC-MLGNR	50.5	160.7	2.17
Rough Cu	4.9	15.7	22.2
Smooth Cu	3.7	11.9	29.2

It is found from Table 4.2 that interconnects with a large 3-dB bandwidth have the smallest t_r because high-frequency signals pass easily, leading to a faster interconnect system. On the contrary, due to low 3-dB bandwidth, interconnect system response becomes slow and sluggish (having the highest t_r) as comparably low-frequency signals are passed. Li-D HTC MLGNR has a 92.56% decrease in 3-dB bandwidth compared to smooth Cu.

Figure 4.9 compares the step response of Li-D HTC-MLGNR (without SER and with SER (p=1)) on different substrates (SiC (δA = 10 pm), BN (δA =70 pm) and SiO_2 (δA =170 pm)) to that of Cu counterparts. The transient step response becomes slow with increasing δA value for Li-D HTC-MLGNRs (without and with SER) because $R_{de}(T)$ increases with an increase in δA (see Fig. 3.7(b)). Also, the SER present in Li- HTC-MLGNRs elevates $R_{de}(T)$ values substantially, leading to higher damping of transient step response than Li-D HTC-MLGNRs without SER. Although Li-D HTC-MLGNR without SER on SiC and BN shows a steeper step response than Cu variants, the Li-D HTC-MLGNR with edge roughness (p=1) on SiO_2 has a far more sluggish step response than its Cu counterparts. This is because Li-D HTC-MLGNR without SER on SiC and BN exhibits the lowest diffusive scatterings and a longer MFP, leading to a lower $R_{de}(T)$ value and t_d. Li-D HTC-MLGNR without SER shows a 94.64% and 94.7% decrease in t_d and t_r, respectively, when placed on SiC, compared to smooth Cu.

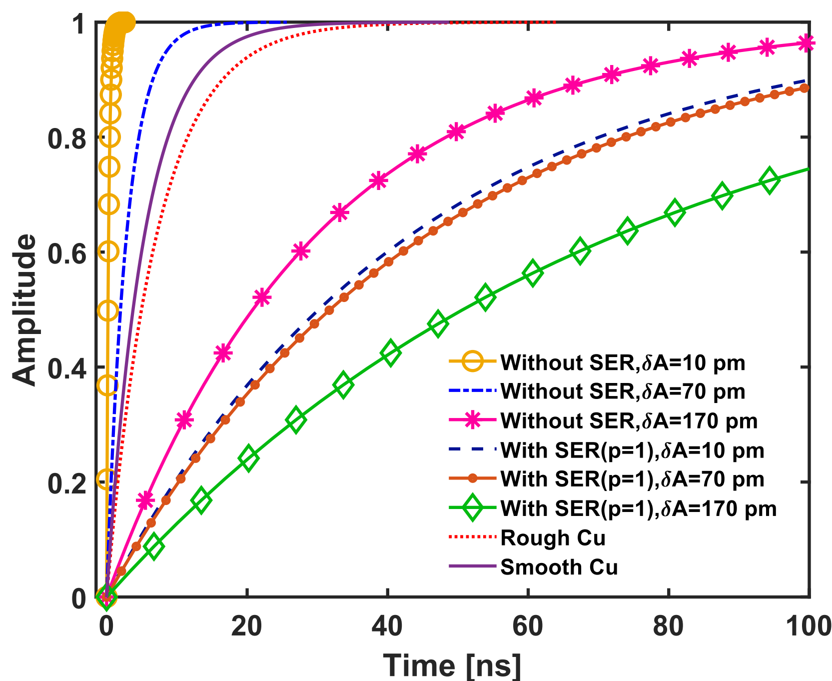

Figure 4.9 Step response of Li-D HTC-MLGNR (without SER and with SER (p=1)) and Cu interconnects.

Figure 4.10 compares the transient step response obtained using the analytical model (given in equation (4.1)) and TSPICE simulation for the equivalent circuit model of the decoupled victim interconnect given in Fig. 4.6 at 13 nm technology node for Li-D HTC-MLGNR (without SER and δA =10 pm). A deviation of 6.64% is observed between the analytical model and TSPICE simulation results for transient step response.

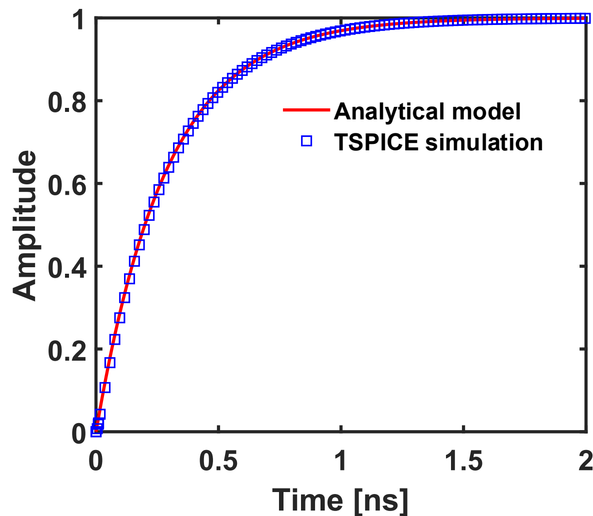

Figure 4.10 Step response of Li-D HTC-MLGNR using analytical transfer function and TSPICE simulation.

4.2.4 Relative Stability Analysis

This subsection analyzes and compares the relative stability of undoped MLGNR (viz., HTC and VTC) and intercalation-doped MLGNR (with Li, $FeCl_3$, and AsF_5 dopants) to smooth and rough Cu interconnects at 300 K for global level (l~1 mm). The relative stability of the DIL system of decoupled victim net (Fig. 4.6), in the presence of crosstalk effects, is determined using the frequency domain Nyquist plot. The transfer function $T(s)$ given in equation (4.1) and the simulation setup given in subsection 4.2.3 is used for the relative stability analysis. Relative stability analysis is required to check if the output of the DIL system is within operating limits for some finite input signal provided [102]. It is stated that a system is considered stable if the Nyquist plot does not enclose the critical point (-1,j0). Also, the system having a maximum distance between its Nyquist plot and (-1,j0) point is relatively more stable [102, 122].

It is observed from Fig. 4.11 that all the encirclements of the Nyquist plot considering MLGNR (with SER (p=1) on SiO_2) and Cu variants do not enclose the critical point (-1,j0), hence are stable. Also, undoped HTC-MLGNR has the highest system stability as its encirclement is

farthest from (-1,j0) point. It is due to more damped transient step response resulting from the highest $R_{de}(T)$ (see Fig. 3.7(a)) and rise time (t_r) values (see Fig. 4.7 and Table 4.2). In addition, smooth Cu with the fastest rise time is closest to (-1,j0) point, hence is the least stable.

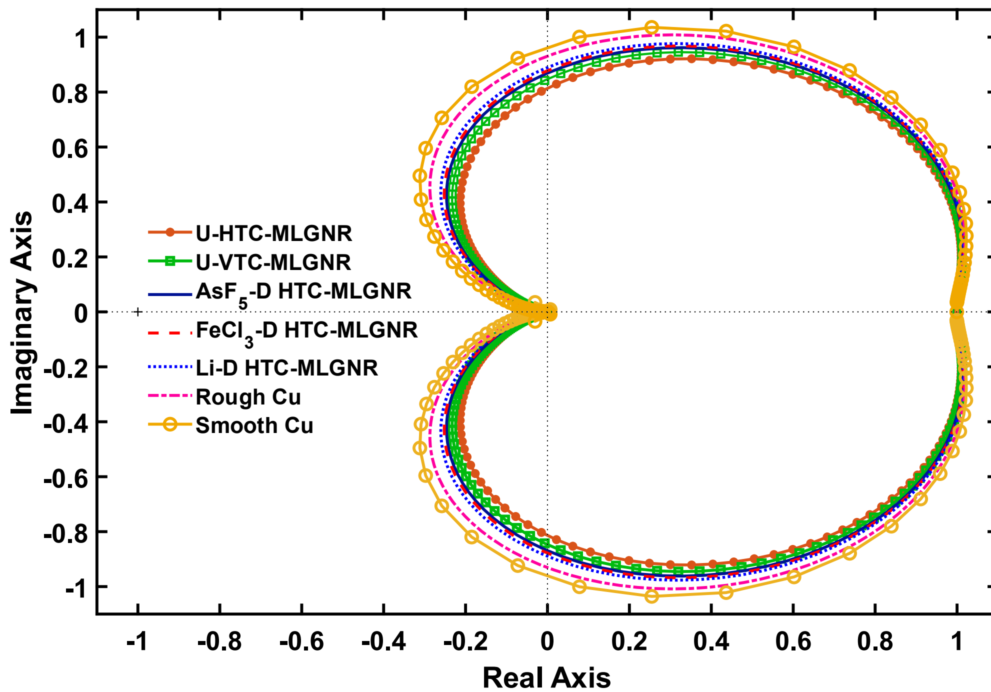

Figure 4.11 Nyquist plot of MLGNR (δA =170 pm, p=1) and Cu interconnects.

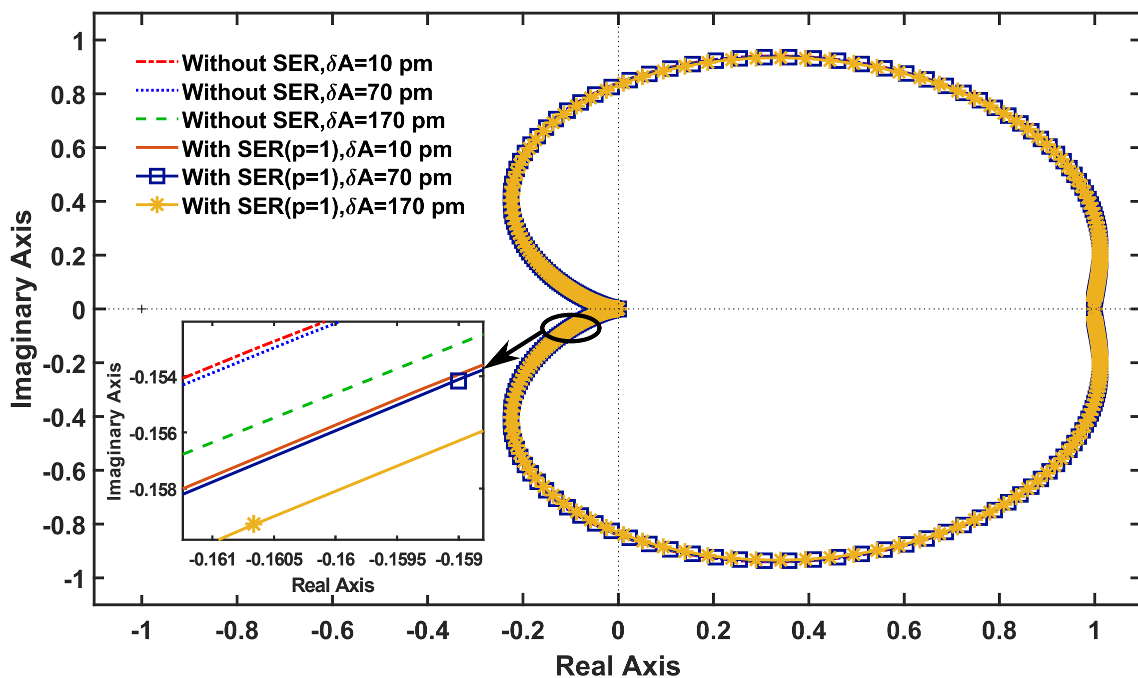

Figure 4.12 Nyquist plot of Li-D HTC-MLGNR interconnect with (having different δA and p=1), and without edge roughness (for various δA).

The Nyquist plot of Li-D HTC-MLGNR interconnect (with SER (p=1) and without SER) on different substrates (SiC (δA =10 pm), BN (δA =70 pm) and SiO_2 (δA =170 pm)) is shown in Fig. 4.12. It is observed from the inset image that the encirclements start moving away from (-1,j0) point with a rise in corrugation amplitude (δA) (for both cases of with and without SER), leading to improvement in system stability. This is because rise time (t_r) increases with an increase in δA (see Fig. 4.9). The SER improves the stability of Li-D HTC-MLGNR when compared to the ones without SER. In addition, Li-D HTC-MLGNR with edge roughness (p=1) on SiO_2 is relatively more stable due to the higher value of the $R_{de}(T)$ (see Fig. 3.7(b)) and t_r (see Fig. 4.9). However, Li-D HTC-MLGNR without edge roughness on SiC, is the least stable.

Therefore, from the results presented in subsections 4.2.3 and 4.2.4, it is inferred that all the variants of MLGNR interconnects with rough edges on SiO_2 have inferior performance in terms of transient step response and 3-dB bandwidth while improved relative stability in comparison to conventional Cu (smooth and rough surface) counterparts. However, Li-D HTC-MLGNR without edge roughness exhibits the fastest transient step response and lowest stability when placed on SiC dielectric. SiC owing to its large dielectric constant value, i.e., 9.7, is not suitable for interconnect applications, as it will increase the value of capacitance and hence overall delay [26]. On this basis, we conclude that SER and corrugated dielectric surface, if not evaluated accordingly, can critically degrade the performance of MLGNR against Cu interconnects. Therefore, for practical implementation of MLGNR as on-chip interconnects, scattering sources like SER and roughness of dielectric surface need to be eradicated.

4.3 Frequency-Dependent Crosstalk Analysis

This section examines the impact of skin effect and crosstalk effects on the performance of temperature-dependent and scattering-limited realistic MLGNR interconnects for both case 1 ($\lambda_R(T)$ excluding $\lambda_{SPP}(T)$ and λ_{SER}) and case 2 ($\lambda_R(T)$, equation (3.4)) for frequencies ranging from 1 GHz - 10^4 GHz and compares the results with MCNT bundle and Cu counterparts at T=300 K. To analyse the performance of global interconnects, the physical parameters are extracted from IRDS-2022, and are summarized in subsection 3.3.2 [2]. As illustrated in Fig. 4.13, three capacitively coupled MLGNR interconnects are considered for crosstalk analysis consisting of victim net and aggressor nets 1 and 2. The interference induced by the signals switching in aggressor nets 1 and 2 impacts the signal on the victim net. The peak amplitude and width of the overshoot noise pulse impacting the overall reliability of the circuit are examined in this section for far-end functional crosstalk noise analysis where both aggressor

nets (e.g., 1 and 2) switch from 0→1 and victim net is constant at logic 1. However, for far-end dynamic crosstalk-induced delay analysis, the worst-case scenario impacting the timing of signal in terms of out-phase delay is considered, in which both aggressor net 1 and 2 switch from 1→0 and victim net switches from 0→1. The circuit given in Fig. 4.13 is simulated in the TSPICE simulator considering CMOS as a driver, a capacitive load of 0.14 fF, a power supply of 0.7 V [2], the length of global level interconnect, l =1 mm, and circuit parameters are extracted from subsection 3.3.2. The p.u.l. coupling capacitance (C_c) for smooth Cu, rough Cu, MLGNR variants, and MCNT bundle is 78.49 aF/µm, 102.181 aF/µm, 78.49 aF/µm and 78.49 aF/µm, respectively.

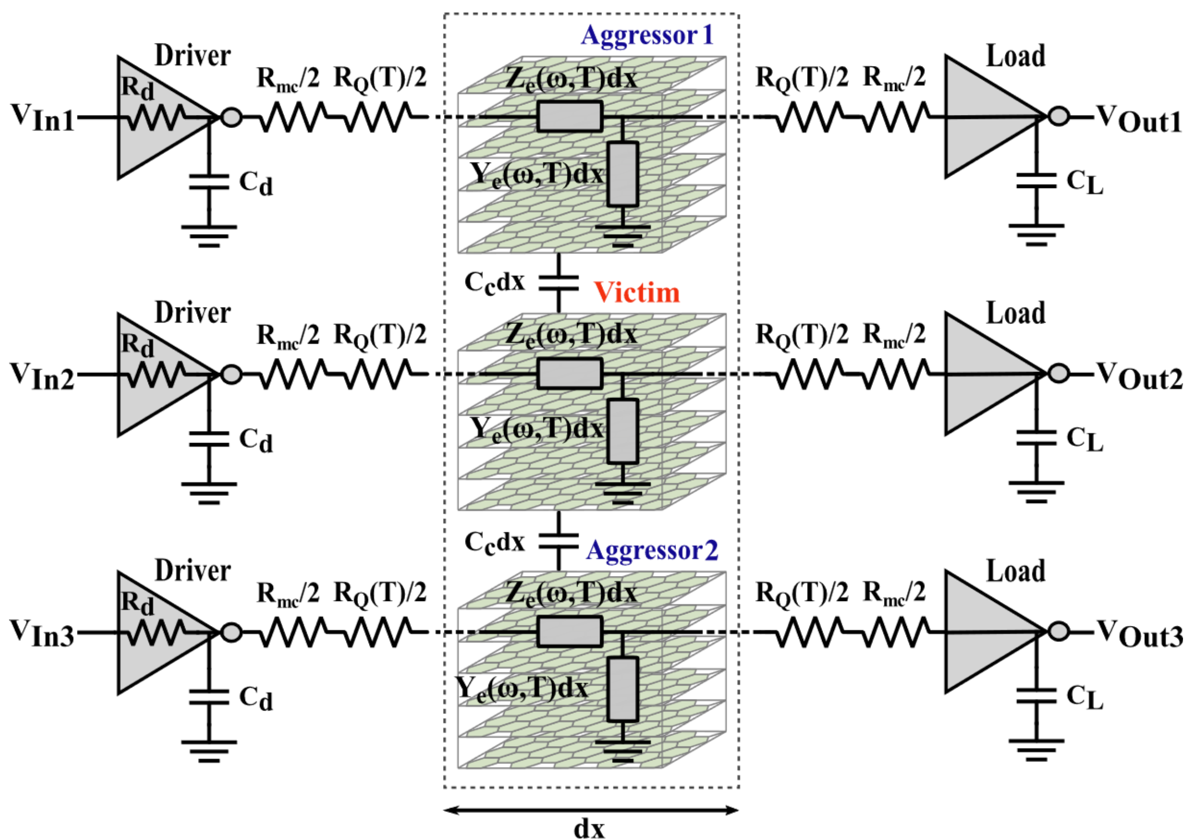

Figure 4.13 Aggressor-victim configuration for capacitively coupled MLGNR interconnects with CMOS as the driver.

The overshoot peak amplitude and width at the victim net of MLGNR (undoped and intercalation-doped), Cu (smooth and rough), and MCNT bundle interconnects, as a function of frequency, are shown in Figs. 4.14 and 4.15, respectively. It is noted that the overshoot peak amplitude and width increase as the frequency rises. This effect is attributed to the rise in resistance ($R(\omega,T)$, see Fig. 3.12) with the frequency that dominates over the impact of inductance ($L(\omega,T)$, see Fig. 3.14). According to the reported findings, overshoot peak

amplitude decreases with an increase in resistance when a low-loss approximation model for transmission lines is assumed [96]. However, the present study deals with quasi-lossy transmission lines that exhibit high resistance, and thus cannot be accurately modeled as low-loss transmission lines. Hence, it can be inferred from the reported studies on quasi-lossy transmission lines that an increase in resistance leads to an increase in overshoot peak amplitude at the victim net far-end [21, 101]. Additionally, reported studies suggest that the width of the overshoot increases with a rise in resistance [96]. In Figs. 4.14(a) and 4.15(a), smooth Cu has the lowest overshoot peak amplitude and width, respectively, for the entire frequency range due to its least $R(\omega,T)$ values, compared to MLGNR variants (case 2), rough Cu, and MCNT bundle interconnects. In comparison to other MLGNR variants (case 2) and MCNT bundle interconnects, Li-D HTC-MLGNR, owing to its least $R(\omega,T)$ for entire frequency spectra, exhibits the smallest overshoot amplitude and width. Figures 4.14(b) and 4.15(b) compare the overshoot amplitude and width, respectively, of Li-D HTC-MLGNR placed on various dielectric substrates considering case 1 and case 2, with Cu variants. It is noted that Li-D HTC-MLGNR placed on SiC and BN for case 1 have lower overshoot amplitude and width compared to Cu variants. This is attributed to their lower $R(\omega,T)$ values relative to Cu variants, resulting from longer MFP of electrons and improved $\sigma_{dc}(T)$.

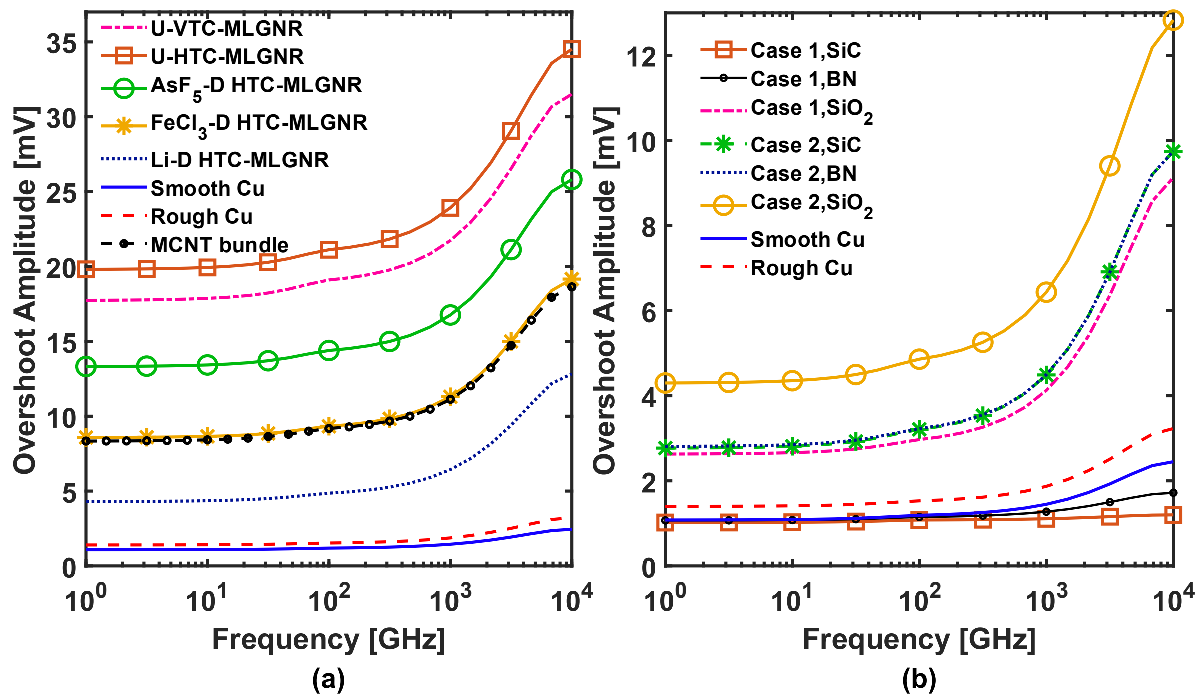

Figure 4.14 Overshoot amplitude variation with frequency for (a) MLGNR (case 2), Cu, and MCNT bundle interconnects, (b) Li-D HTC-MLGNR (placed on various dielectric substrates for case 1 and case 2), and Cu variants.

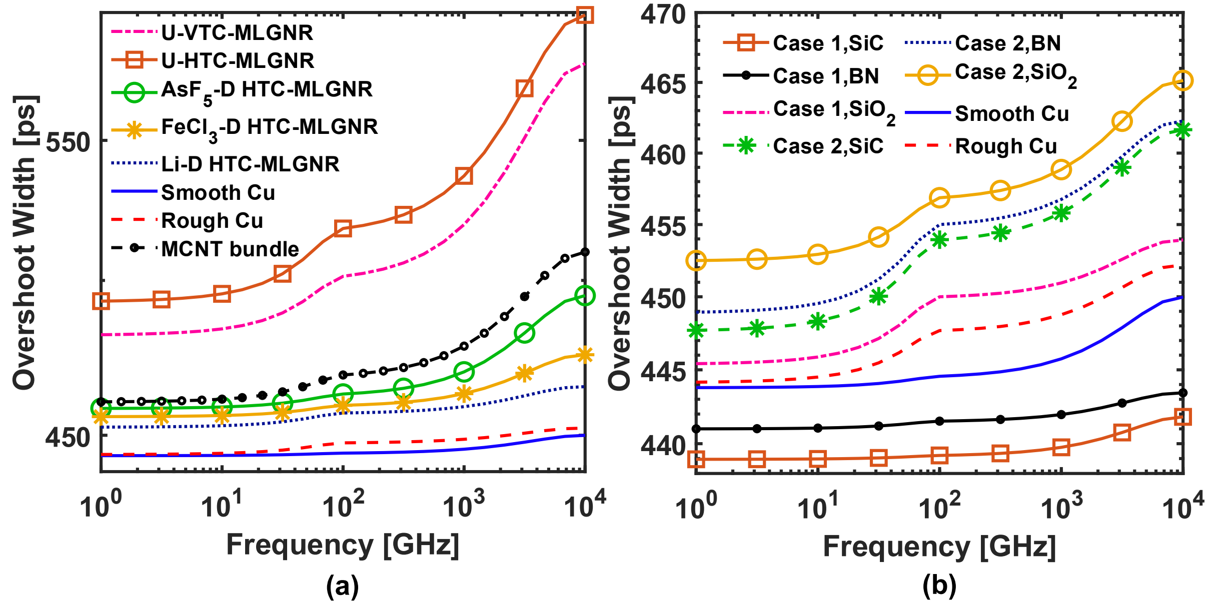

Figure 4.15 Overshoot width versus frequency for (a) MLGNR (case 2), Cu, and MCNT bundle interconnects, (b) Li-D HTC-MLGNR (placed on various dielectric substrates for case 1 and case 2), and Cu variants.

Furthermore, from Figs. 4.14 and 4.15, the average percentage increase (API) of overshoot peak amplitude or width from 1 GHz to 10^4 GHz is obtained by averaging the relative percentage increase in overshoot amplitude or width (OA/W) at frequencies f=1 GHz, 10 GHz, 10^2 GHz, 10^3 GHz and 10^4 GHz, with respect to f=1 GHz. The relative percentage increase is computed as $((OA/W_f - OA/W_{f=1\ \mathrm{GHz}})/OA/W_{f=1\ \mathrm{GHz}} \times 100\%)$ at each frequency point. In the case of the overshoot peak amplitude (width), the Li-D HTC-MLGNR (case 1), when placed on SiC and BN, displays API values of 6.6% (0.18%) and 17.6% (0.19%), respectively. Meanwhile, smooth Cu has an API of 34.4% (0.41%). It is interesting to observe that Li-D HTC-MLGNR placed on SiC (case 1) has minimum API, implying minimum impact of frequency variations and skin effect on overshoot peak amplitude and width. Consequently, Li-D HTC-MLGNR placed on SiC (case 1) is least prone to overshoot-induced MOS gate oxide breakdown and reliability issues in ICs at high frequencies.

Out-phase dynamic crosstalk-induced delay is depicted in Fig. 4.16, varying with frequency for MLGNR, Cu, and MCNT bundle interconnects. An increase in out-phase crosstalk-induced delay is observed as the frequency increases. This is attributed to the frequency-dependent increase in $R(\omega,T)$ [111]. In Fig. 4.16(a), crosstalk-induced delay for smooth Cu is found to have minimum values compared to MLGNR variants (case 2) and MCNT bundle interconnects, owing to its lowest $R(\omega,T)$. However, in case 2, Li-D HTC-MLGNR exhibits superior performance, attributed to its lower $R(\omega,T)$ values, compared to other MLGNR variants and

MCNT bundle interconnects in terms of crosstalk-induced delay. Figure 4.16(b) compares the crosstalk-induced delay of Li-D HTC-MLGNR placed on various substrates for case 1 and case 2 with Cu interconnects. Li-D HTC-MLGNR exhibits the least values of crosstalk-induced delay when placed on SiC and BN for case 1 attributed to their lowest $R(\omega, T)$ values. The API in dynamic crosstalk-induced delay is observed as 66.6%nd 15.6% (22.4%) for smooth Cu and Li-D HTC-MLGNR placed on SiC (BN) for case 1, respectively. Accordingly, a minimum effect of frequency and skin effect is observed for Li-D HTC-MLGNR placed on SiC (case 1), which leads to less susceptibility towards crosstalk-delay-induced timing errors at high frequencies.

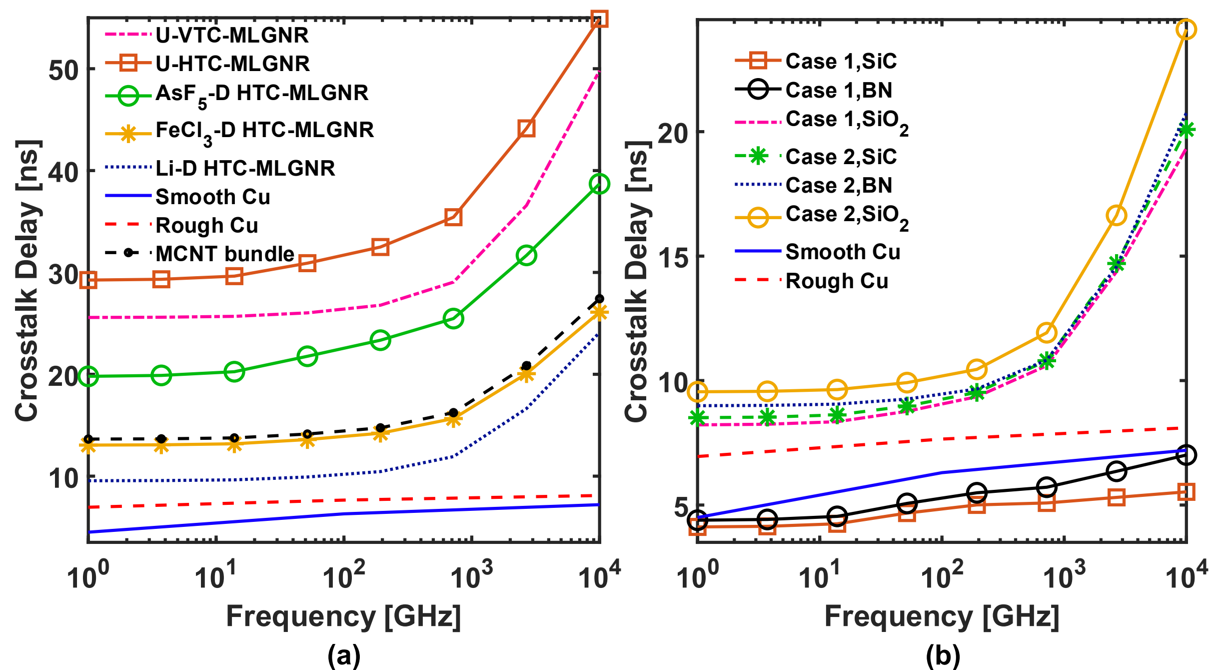

Figure 4.16 Crosstalk-induced delay for (a) MLGNR (case 2), Cu, and MCNT bundle interconnects, (b) Li-D HTC-MLGNR (placed on various dielectric substrates for case 1 and case 2), and Cu variants, as a function of frequency.

From the results presented, it can be inferred that the presence of scatterers and skin effect, exacerbates resistance of MLGNR variants (case 2), leading to their inferior performance compared to conventional Cu counterparts, for a frequency range of 1 GHz - 10^4 GHz. However, Li-D HTC-MLGNR (case 1), in the absence of substrate polar phonons and rough GNR edges, exhibits lower crosstalk-induced delay and noise compared to Cu variants only when placed on SiC and BN dielectric substrate. Furthermore, at high frequencies, nano on-chip interconnect systems are highly prone to failure due to gate-oxide breakdown and timing issues. These challenges can be resolved by utilizing optimized Li-D HTC-MLGNR (O-Li-D

HTc-MLGNR), i.e., Li-D HTC-MLGNR placed on SiC (case 1) as on-chip interconnect for practical applications, as they are least prone to frequency variations and skin effect. Therefore, to benefit from the advantages of MLGNR-based interconnects at high frequencies, intercalation doping with Li, utilizing dielectric SiC as substrate, and eliminating scatterings with rough edges and substrate SPPs are desired.

This study assumes a perfect dielectric, neglecting frequency-dependent dielectric losses modeled as shunt conductance in high-speed circuits, leading to signal attenuation and potential false switching. Moreover, the signal integrity analysis in this work is limited to symmetric interconnects. Future work could explore the impact of both shunt conductance and asymmetric interconnect lines to gain an understanding of realistic crosstalk behavior.

4.4 Chapter Summary

This chapter presents a comprehensive, temperature-dependent performance analysis of various interconnect materials, including smooth and rough Cu, undoped MLGNRs (VTC, HSC, and HTC), intercalation-doped HTC-MLGNRs (doped with AsF_5, $FeCl_3$, and Li), and MCNT bundles, focusing on crosstalk-induced delay in capacitively coupled configurations under a low-bias regime. The inclusion of scattering effects ($\lambda_R(T)$)) ensures a realistic evaluation of interconnect performance.

Notably, intrinsic-phonon-limited Li-D HTC-MLGNR interconnects outperform MCNT bundles, other MLGNR variants, and Cu interconnects in terms of crosstalk-induced delay. However, when scatterers are present, realistic MLGNRs demonstrate inferior performance compared to Cu.

Among all the variants of scattering-limited realistic MLGNR, Li-D HTC-MLGNR has shown superior performance as a nanoscale interconnect. When compared to MCNT bundle interconnects, the Li-D HTC-MLGNR shows a decrease of 85.48% and 74.67% in crosstalk-induced delay values for $\lambda_P(T)$ and $\lambda_R(T)$, respectively. Moreover, the interconnect width of MLGNR and Cu interconnects has been optimized to obtain improved performance in the presence of crosstalk effects. Li-D HTC-MLGNR interconnects with optimized width exhibits 10.59× lower (≈89.58 ps) and 8.85× higher crosstalk-induced delay (≈8.4 ns) for $\lambda_P(T)$ and $\lambda_R(T)$, respectively, compared to smooth Cu interconnects.

Afterwards, the transient response, 3-dB bandwidth and Nyquist stability of MLGNR interconnects (with and without structural edge roughness (SER)) on the corrugated dielectric surface are investigated and compared with Cu interconnects. It is shown that while the SER and higher corrugation amplitude of dielectric improve the stability of the MLGNR DIL system, it also leads to a slow and sluggish step response and a decrease in 3-dB bandwidth. Moreover, it is observed that while all the MLGNR variants with SER on SiO_2 have higher rise time and small 3-dB bandwidth than Cu variants, Li-D HTC-MLGNR interconnects without edge roughness on SiC and BN have faster rise time than Cu counterparts. In particular, Li-D HTC MLGNR with SER on SiO_2 exhibits a 1264.8% and 1250.4% increase in t_d and t_r, respectively, and a 92.56% decrease in 3-dB bandwidth, compared to smooth Cu. However, Li-D HTC MLGNR without SER on SiC shows a 94.64% and 94.7% decrease in t_d and t_r, respectively, compared to smooth Cu. In addition, U-HTC-MLGNR with SER on SiO_2 has the highest system stability, whereas smooth Cu is the least stable.

Moreover, the frequency-dependent crosstalk analysis of intercalation-doped HTC-MLGNR interconnects is conducted by considering the impact of scatterers and skin effect, and compared with U-VTC-MLGNR, U-HTC-MLGNR, Cu, and MCNT bundle counterparts. It is noted that realistic MLGNR variants with all scatterers present in $\lambda_R(T)$ and placed on SiO_2, in the presence of significant skin effect and scatterers, exhibit inferior performance compared to conventional Cu variants. However, the minimum impact of frequency variations and skin effect is observed for optimized Li-D HTC-MLGNR (O-Li-D HTC-MLGNR), obtained by placing on SiC and in the absence of surface polar phonons and SER, which exhibits the lowest average percentage increase in overshoot peak amplitude, overshoot width, and delay of 6.6%, 0.18%, and 15.6%, respectively, for the entire frequency range.

Finally, this chapter identifies O-Li-D HTC-MLGNR as the optimal structure, exhibiting minimal sensitivity to frequency variations and skin effect. The next chapter will address the challenges posed by process and temperature variations, focusing on the circuit parameters and performance of O-Li-D HTC-MLGNR as a practical on-chip interconnect.

Chapter 5 High-Frequency Challenges under Process and Temperature Variations

5.1 Introduction

The complex nature of manufacturing processes introduces variations and uncertainties in the physical and geometric parameters of interconnects [50–54]. These process-related variations, combined with temperature fluctuations dependent on operational conditions, result in uncertainties and deviations in interconnect performance metrics [50, 52, 53].

Understanding the high-frequency performance of interconnects is critical for modern VLSI circuits, where process-induced variations and temperature-dependent changes significantly affect reliability and functionality. These variations, combined with high-frequency phenomena such as skin effect and scattering-limited MFP, introduce complexities in predicting circuit behavior. Moreover, challenges such as crosstalk and electromigration become more pronounced at higher frequencies, necessitating a detailed investigation of their impact.

Electromigration poses a limitation on the reliability of MLGNR interconnects by reducing their lifetime and mean time to failure [15, 36, 46–49]. While recent studies have examined the effects of process and temperature variations on single-line propagation delay and crosstalk-induced issues such as delay, noise, and noise area [50–55], the challenges posed by these variations in the presence of scattering-limited realistic effective MFP, skin effect, crosstalk, and electromigration effects at high frequencies remains unexplored. Thus, it is essential to assess the impact of process and temperature variations on the high-frequency performance of MLGNR interconnects.

This chapter analyzes the impact of process and temperature variations on circuit parameters of optimized Li-D HTC-MLGNR (O-Li-D HTC-MLGNR) interconnects under the influence of SER-limited realistic effective MFP and skin effect. Moreover, the frequency-dependence of maximum variations introduced in performance metrics, including crosstalk-induced delay and noise area and mean time to failure due to electromigration (EM-MTF), is analyzed considering process and temperature variations at high frequencies. The frequency-dependent circuit model developed in subsection 3.3.1 is employed for the analysis. Subsequently, the

variations introduced in performance metrics due to process and temperature variations are analyzed at a fixed frequency of 10^4 GHz.

5.2 Impact of Process and Temperature Variations on Circuit Parameters

In this section, variations in resistance p.u.l and inductance p.u.l. are analyzed and discussed as a function of frequency for O-Li-D HTC-MLGNR by considering process and temperature variations. The O-Li-D HTC-MLGNR, specifically Li-D HTC-MLGNR on SiC (case 1), is obtained from subsection 3.3.2. In O-Li-D HTC-MLGNR, factors such as temperature-dependent polar phonons in the substrate and scattering of the electrons with rough edges of GNR are not considered in $\lambda_R(T)$, and a δA value of 10 pm for SiC substrate [26] is adopted. The process parameters incorporated for the analysis include corrugation amplitude (δA), width (w), fermi energy (E_f), and van der Waals gap (δ_s). The variable parameters of the O-Li-D HTC-MLGNR interconnect, along with their nominal value, variation range, and source, are given in Table 5.1.

Table 5.1 Interconnect parameters (viz., process and temperature) with their nominal values and variation range.

Parameters	Nominal value	Variations	Source of variations
δA [pm]	60	± 50 pm	Depends on the structure of the dielectric material and the related manufacturing and surface polishing methods used [26, 155].
T [K]	400	± 25%	Increasing current density, resistivity, thermal coupling, Joule heating, and use of low-k dielectrics [52, 53, 156].
w [nm]	16	± 10%	Error in photolithography and etching process [51–53].
E_f [eV]	1.5	± 10%	Change in the charge density due to variation in dopant concentration [18, 53].
δ_s [nm]	0.37	± 10%	Change in inter-carbon atomic forces between MLGNR layers due to variation in aspect ratio [50, 52].

Figures 5.1(a-e) exhibit the variations in resistance p.u.l. ($R(\omega,T)$) and inductance p.u.l. ($L(\omega,T)$) as a function of frequency for O-Li-D HTC-MLGNR, considering the deviations of process parameters and temperature from their nominal values.

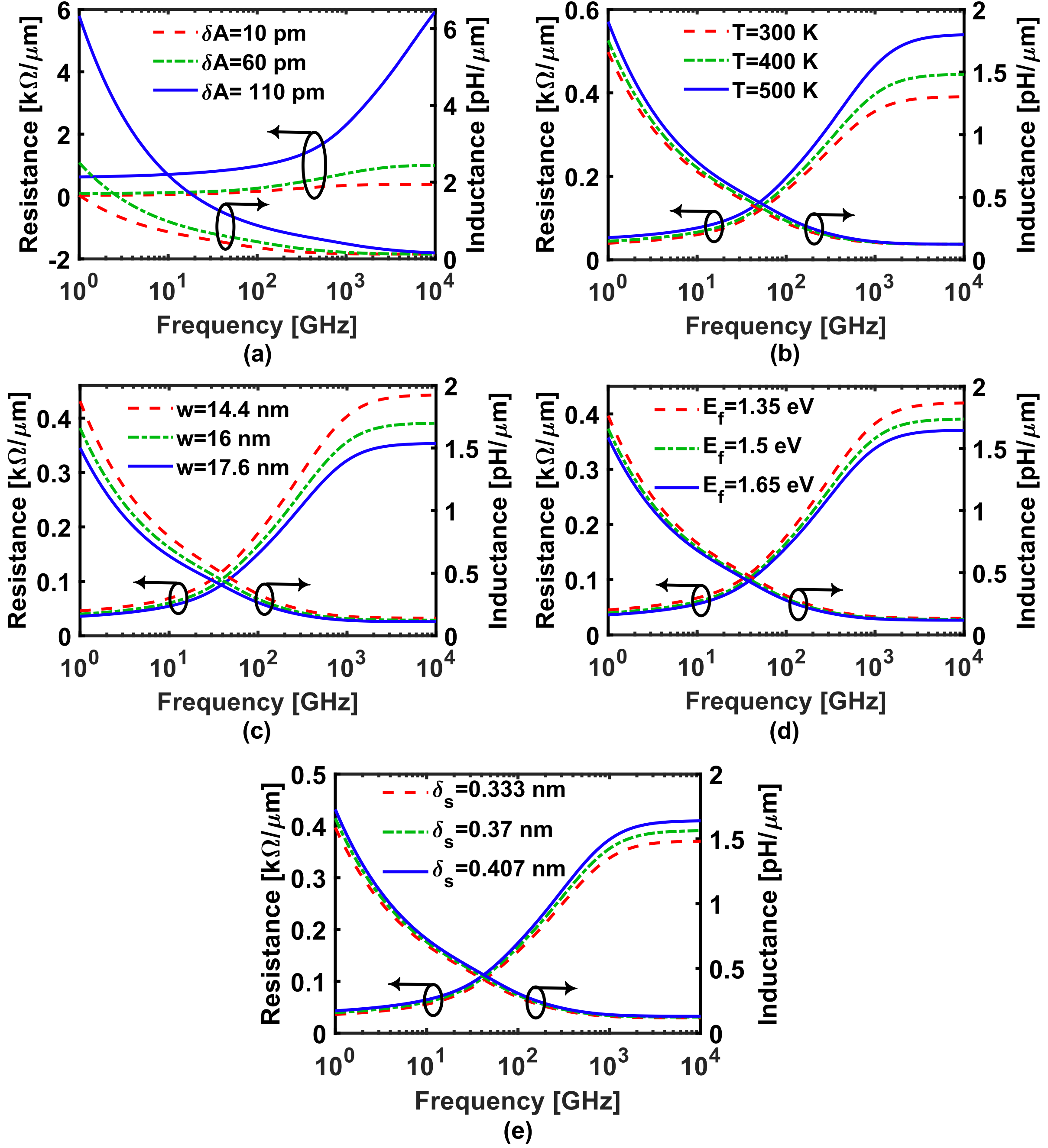

Figure 5.1 Resistance and inductance as a function of frequency, considering variations in (a) δA, (b) T, (c) w, (d) E_f, and (e) δ_s for O-Li-D HTC-MLGNR.

In Fig. 5.1(a) (for δA=10 pm and 60 pm) and Figs. 5.1(b-e), $R(\omega,T)$ increases with frequency because Δ_{SD} decreases as frequency rises, leading to more confinement of the current towards the surface of the interconnect. Additionally, due to larger $\tau(T)$ values (see table 3.4), $R(\omega,T)$

saturates at 2 THz. Moreover, it is observed that $L(\omega,T)$ decreases with an increase in frequency, whereas, at higher frequencies, $L(\omega,T)$ saturates as the term $\omega\tau(T)$ approaches to 1. However, in Fig. 5.1(a) (for δA=110 pm), $R(\omega,T)$ keeps increasing while $L(\omega,T)$ keeps decreasing with frequency.

The average variations in $R(\omega,T)$ due to deviations in nominal values of δA, T, w, E_f, and δ_s relative to their lower bound values are 0.25 MΩ, 0.02 MΩ, 0.026 MΩ, 0.016 MΩ, and 0.011 MΩ, respectively, as calculated from Fig. 5.1. In contrast, the average variations of 2.05 MΩ, 0.04 MΩ, 0.02 MΩ, 0.011 MΩ, and 0.01 MΩ are observed in $R(\omega,T)$ due to deviations in nominal values of δA, T, w, E_f, and δ_s with respect to their upper bound values, respectively. As per the findings, the highest average deviation in $R(\omega,T)$ is observed for δA compared T, w, E_f, and δ_s. This is because variations in δA lead to the highest conductivity ($\sigma_{dc}(T)$) variations of 300.9 $[\mu\Omega.cm]^{-1}$ and 169 $[\mu\Omega.cm]^{-1}$ for the lower and upper bound, respectively, compared to T, w, E_f, and δ_s.

The average variations in $L(\omega,T)$ due to deviations in nominal values of δA, T, w, E_f, and δ_s relative to their lower bound values are 0.33 pH, 0.036 pH, 0.092 pH, 0.048 pH, and 0.033 pH, respectively, as calculated from Fig. 5.1. In contrast, the average variations of 1.44 pH, 0.06 pH, 0.064 pH, 0.03 pH, and 0.027 pH are observed in $L(\omega,T)$ due to deviations in nominal values of δA, T, w, E_f, and δ_s with respect to their upper bound values, respectively. As per the findings, the highest average deviation in $L(\omega,T)$ is observed for δA compared T, w, E_f, and δ_s. This is because variations in δA lead to the highest conductivity ($\sigma_{dc}(T)$) variations of 300.9 $[\mu\Omega.cm]^{-1}$ and 169 $[\mu\Omega.cm]^{-1}$ for the lower and upper bound, respectively, compared to T, w, E_f, and δ_s.

5.3 Impact of Process and Temperature Variations on Frequency-Dependent MLGNR Performance

In this subsection, variations in performance parameters of O-Li-D HTC-MLGNR, including crosstalk-induced delay, and noise area, and EM-MTF, are evaluated corresponding to variations in process parameters and temperature (T) at high frequencies. The simulation setup given in section 4.3 is used for the crosstalk analysis. The crosstalk-induced noise area is computed by approximating the overshoot (OS) at v_{Out2} as a triangular shape and applying the formula: (0.5 × OS peak × OS width) [99].

The EM-MTF is calculated using [47, 130]:

$$EM - MTF = c_A J_D^{-n} e^{\left(E_a/_{Tk_b}\right)} \tag{5.1}$$

where, $c_A = wt\sigma(\omega, T)^x$ [47, 130], $J_D = a\sigma(\omega, T)^m$ is the scattering-source, temperature, and frequency-dependent breakdown current density [46], exponent n ranges from $1 \leq n \leq 2$, x, a, and m are the constant fitting parameters, activation energy E_a=1.97 eV for MLGNR/MCNT bundle, and E_a=1.2 eV for rough Cu [36], k_b= 8.617.*(10^-5) eV/K is the Boltzmann's constant. The analysis and simulations for EM-MTF are performed using MATLAB R2022a.

The maximum variation (Δ_{max}) in crosstalk-induced delay and noise area of O-Li-D HTC-MLGNR is plotted as a function of frequency for various interconnect parameters in Figs. 5.2(a) and (b), respectively. Δ_{max}= max$|X_{\pm} - X_{Nominal}|$, where X_+, X_-, and $X_{Nominal}$ represent the value of performance parameters corresponding to the upper bound, lower bound, and nominal value of interconnect parameters given in Table 5.1. Δ_{max} uses the max function to return the greater value between $|X_+ - X_{Nominal}|$ and $|X_- - X_{Nominal}|$.

It is noted that the maximum variations (Δ_{max}) in crosstalk-induced delay and noise area increase with the escalation of frequency for all interconnect parameters, as illustrated in Figs. 5.2(a) and (b), respectively. This is because of the corresponding increase in $R(\omega,T)$ variations with frequency for each parameter, viz., δA, w, E_f, δ_s and T. As per the findings, δA variations have a more pronounced impact on variations in crosstalk-induced delay and noise area compared to w, E_f, δ_s, and T at each given frequency. This is because variations in δA lead to the highest average $R(\omega,T)$ variations of 2.05 MΩ for the entire frequency range. However, variations in w, E_f, δ_s, and T exhibit comparatively lower increase in $R(\omega,T)$ variations of 0.026 MΩ, 0.016 MΩ, 0.011 MΩ, and 0.04 MΩ, respectively. The average maximum variations in crosstalk-induced delay and noise area due to δA variations is 0.78 ns and 166.42 mV.ps, respectively.

The maximum variations (Δ_{max}) in EM-MTF at each given frequency is given in Table 5.2 for O-Li-D HTC-MLGNR considering all interconnect parameters, viz., δA, w, E_f, δ_s, and T. It is noted that the maximum variations in EM-MTF decrease with the rise in frequency for all interconnect parameters. This is because EM-MTF exhibits a direct correlation with $\sigma(\omega,T)$ (see equation 5.1), and maximum variations in $\sigma(\omega,T)$ decrease with frequency for each

parameter, viz., δA, w, E_f, δ_s, and T (see Table 5.2). Moreover, variations in T have a more pronounced impact on variations in EM-MTF compared to δA, w, E_f, and δ_s at each given frequency. This is because of the combined effect of $\sigma(\omega,T)$ and T on EM-MTF (see equation (5.1)). Here, the variations in T have a lower impact on average variations of $\sigma(\omega,T)$ compared to δA, w, and E_f (see Table 5.2). However, owing to the dominant inverse dependence of EM-MTF on T [47, 130], the highest overall variations in EM-MTF are observed due to variations in T. The average maximum variation in EM-MTF due to T variations is 9.96×10^{12} hours.

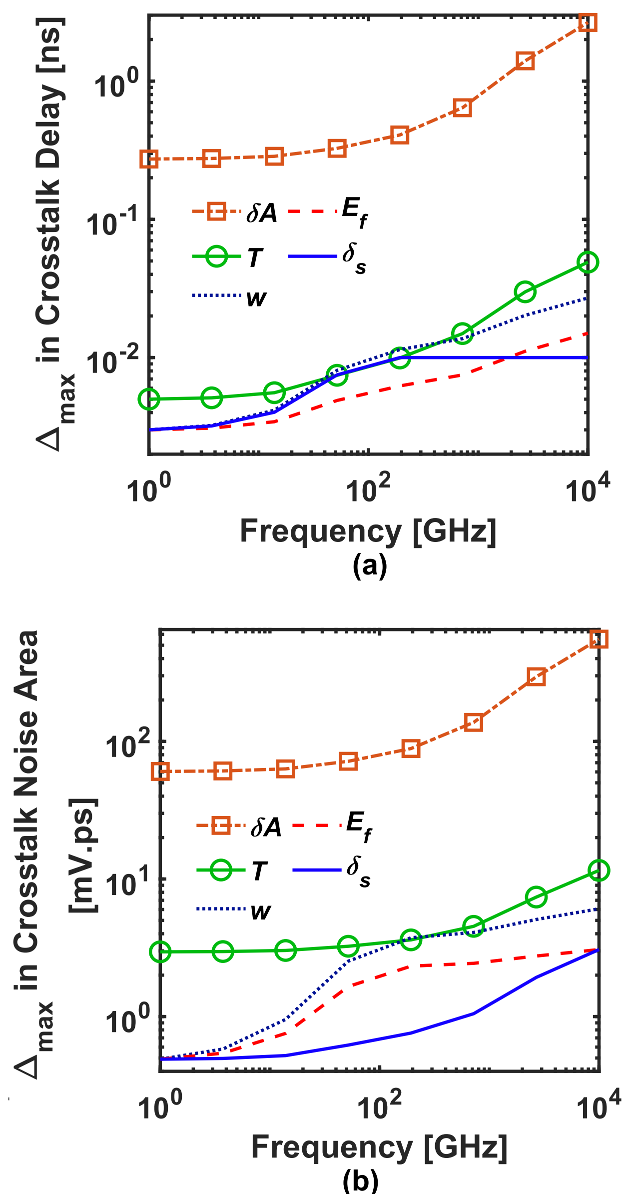

Figure 5.2 Maximum variations (Δ_{max}) in (a) crosstalk-induced delay and (b) crosstalk-induced noise area with frequency for O-Li-D HTC-MLGNR, considering process and temperature variations.

Table 5.2 Maximum variations (Δ_{max}) in EM-MTF with frequency for O-Li-D HTC-MLGNR considering process and temperature variations.

Frequency [GHz]	Δ_{max} ([μΩ.cm]$^{-1}$) in $\sigma(\omega,T)$					Δ_{max} ($\times10^{12}$ hours) in EM-MTF				
	δA	T	w	E_f	δ_s	δA	T	w	E_f	δ_s
1	233.9	45.4	46.4	52.8	34.7	18.04	25.5	3.94	4.5	3.19
10^2	35.4	6.31	10	6.31	5.4	1.63	3.37	0.45	0.31	0.27
10^4	24.52	4.88	4.54	2.78	2.16	0.75	1.02	0.14	0.1	0.08
Average Δ_{max}	97.94	18.86	20.31	20.63	14.09	6.81	9.96	1.51	1.65	1.18

5.4 Impact of Process and Temperature Variations on MLGNR Performance at Fixed Frequency

Figure 5.3 illustrates the variations in crosstalk-induced delay and noise area for O-Li-D HTC-MLGNR, considering the deviations of δA and T from their nominal values at f=10^4 GHz. Both crosstalk-induced delay and noise area increase with an increase in δA and T. Increasing the δA reduces $\lambda_R(T)$ (see Fig. 3.10(b)) [26] and $\sigma_{dc}(T)$ and consequently increases the $R(\omega,T)$. Furthermore, a rise in T leads to a decrease in $N_{TM}(T)$ [109, 149] and $\lambda_R(T)$ (see Fig. 3.10(a)), thereby reducing $\sigma_{dc}(T)$ and subsequently contributing to an increase in $R(\omega,T)$. Therefore, an increase in $R(\omega,T)$ with δA and T results in a subsequent increase in crosstalk-induced delay and noise area.

The variations in EM-MTF at f=10^4 GHz, taking into account the deviations of δA and T from their nominal values, is given in Table 5.3. As mentioned earlier, $R(\omega,T)$ increases with δA because increasing the δA reduces $\lambda_R(T)$ and $\sigma_{dc}(T)$. Moreover, a rise in T leads to a decrease in $N_{TM}(T)$ and $\lambda_R(T)$, thereby increasing $R(\omega,T)$ values. This increase in $R(\omega,T)$ leads to a reduction in values of $\sigma(\omega,T)$, consequently leading to a reduction in EM-MTF with an increase in δA and T. This is because EM-MTF exhibits a direct correlation with $\sigma(\omega,T)$ (see equation 5.1).

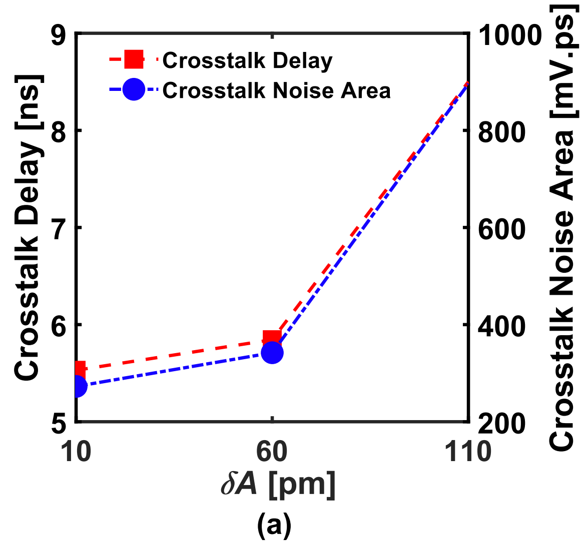

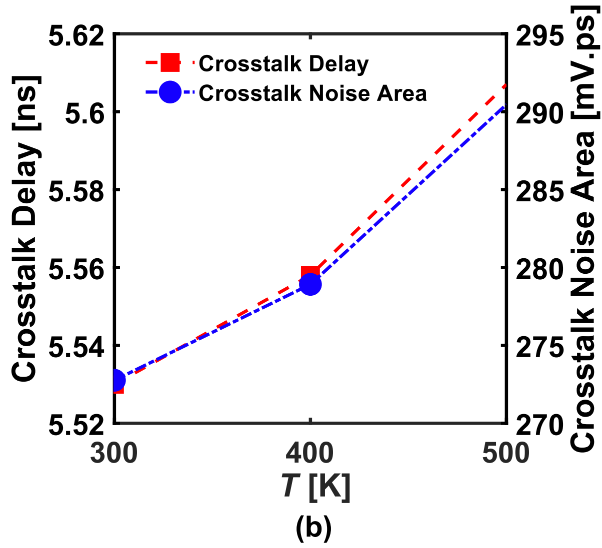

Figure 5.3 Variations in crosstalk delay and crosstalk noise area with (a) corrugation amplitude (δA) and (b) temperature (T) for O-Li-D HTC-MLGNR at f=10^4 GHz.

Table 5.3 Variations in EM-MTF with corrugation amplitude (δA) and temperature (T) for O-Li-D HTC-MLGNR at f=10^4 GHz.

Parameter	Value	EM-MTF [hours]
	10	10.18×10^{11}
δA [pm]	60	2.7×10^{11}
	110	0.22×10^{11}
	300	10.18×10^{11}
T [K]	400	4.52×10^{3}
	500	0.0374

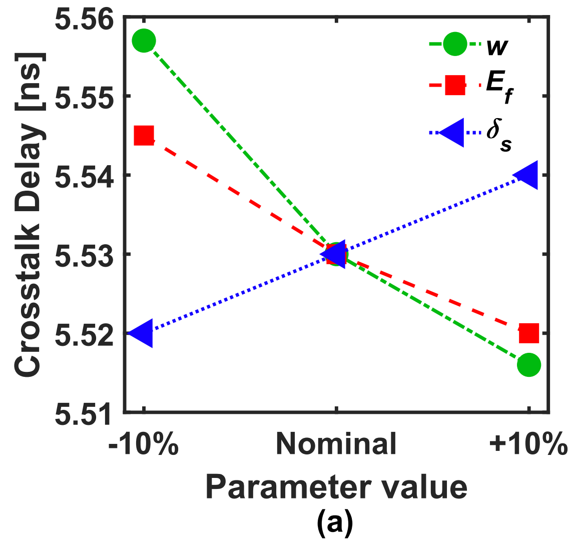

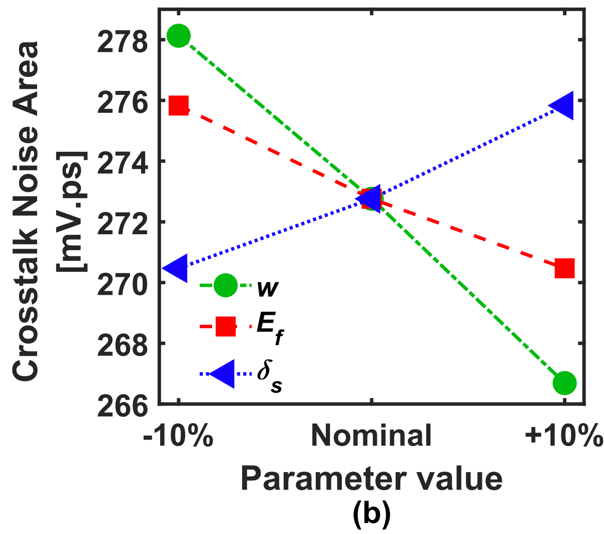

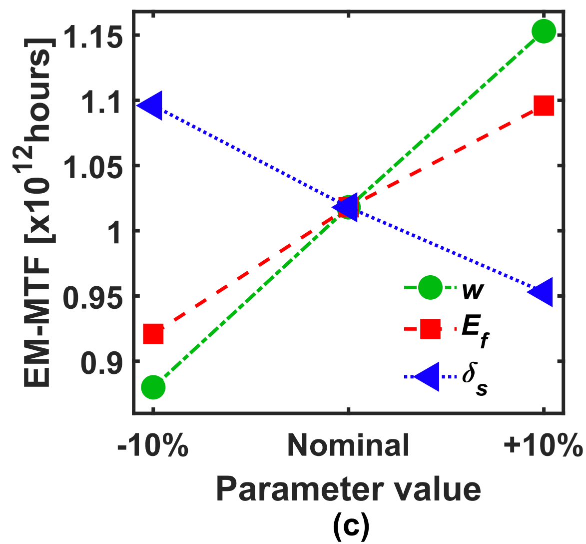

Figure 5.4 Variations in (a) crosstalk-induced delay, (b) crosstalk-induced noise area, and (c) EM-MTF with width (w), fermi energy (E_f), and van der Waals gap (δ_s) for O-Li-D HTC-MLGNR at f=10^4 GHz.

Figure 5.4 depicts the variation in crosstalk-induced delay and noise area, and EM-MTF, taking into account the deviations of w, E_f, and δ_s from their nominal values for O-Li-D HTC-MLGNR at f=10^4 GHz. In Figs. 5.4(a) and (b), the crosstalk-induced delay and noise area, respectively, decrease with an increase in w and E_f, whereas they demonstrate an increase with an increase in δ_s. Increasing the δ_s reduces the number of layers in O-Li-D HTC-MLGNR, which decreases $\sigma_{dc}(T)$ and consequently increases the $R(\omega,T)$. Furthermore, a rise in w and E_f leads to an increase in $N_{TM}(T)$, thereby increasing $\sigma_{dc}(T)$ and subsequently contributing to a decrease in $R(\omega,T)$. Therefore, a decrease in $R(\omega,T)$ with w and E_f results in a subsequent decrease in crosstalk-induced delay and noise area. Conversely, due to an increase in $R(\omega,T)$ with δ_s, crosstalk-induced delay and noise area increases. In Fig. 5.4(c), the EM-MTF increases with an increase in w and E_f, attributed to the corresponding increase in $\sigma(\omega,T)$ induced by the decrease in $R(\omega,T)$. Also, the EM-MTF reduces with an increase in δ_s, owing to the corresponding reduction in $\sigma(\omega,T)$ induced by the increase in $R(\omega,T)$. Furthermore, from Figs. 5.3 and 5.4 and Table 5.3, it can be deduced that the variation in δA results in the highest average variations of 6.62 ns and 503.58 mV.ps in crosstalk-induced delay and noise area, respectively. However, the largest average variation of 1.02×10^{12} hours in EM-MTF is caused by variations in T.

5.5 Chapter Summary

The frequency-dependent performance characterization of O-Li-D HTC-MLGNR is done in the presence of scatterers, skin effect, and process and temperature variations. The analysis highlights the critical role of these variations in shaping the high-frequency behavior of interconnects, particularly their influence on reliability and signal integrity. The findings indicate that the maximum variations in crosstalk effects (viz., delay and noise area) and EM-MTF show an increase and decrease, respectively, with frequency, attributed to fluctuations in process parameters and temperature. The variations in δA and T result in the highest average maximum variations of 0.78 ns (166.42 mV.ps) and 9.96×10^{12} hours in crosstalk-induced delay (noise area) and EM-MTF, respectively, for the entire frequency range. Furthermore, at a fixed f=10^4 GHz, crosstalk and EM-MTF effects increase and decrease, respectively, with an increase in δA, T, and δ_s. However, with an increase in w and E_f, crosstalk and EM-MTF effects decrease and increase, respectively. This study underscores the frequency-dependent interplay between physical design parameters and thermal/process variations, emphasizing their significance in optimizing performance and extending interconnect lifespan. Also, the variations in δA and T

result in the highest average variations of 6.62 ns (503.58 mV.ps) and 1.02×10^{12} hours in crosstalk-induced delay (noise area) and EM-MTF, respectively. The impact of process and temperature variations gets enhanced at higher frequencies for O-Li-D HTC-MLGNR and, hence, must be eradicated for reliable interconnect design and operation. These findings offer crucial insights into the optimization of interconnects for advanced VLSI circuits, highlighting the need for robust design strategies to mitigate adverse effects under high-frequency conditions.

The next chapter presents the circuit modeling and performance analysis of MLGNR-based via-interconnect scheme (VIS) as a prospect for M-3D ICs by incorporating the impact of extrinsic scatterers, skin effect, and crosstalk effect.

Chapter 6 MLGNR-Based Via-Interconnect Scheme (VIS) for Monolithic 3D ICs

6.1 Introduction

The ongoing geometry and device miniaturization in conventional two-dimensional (2D) ICs is inadequate in addressing challenges such as limited speed, bandwidth, and integration density for future systems [2, 136]. To overcome these challenges, the three-dimensional (3D) IC integration based on through silicon vias (TSV) emerged as a promising solution for improved system-level performance [56, 58, 136, 138]. However, large dimensions of TSVs result in significant mechanical/thermal stress in the substrate, high parasitic capacitance, and low integration density [56, 58]. In its 2022 report, IRDS suggested monolithic 3D (M-3D) ICs as a promising solution to address the challenges associated with conventional 2D ICs and TSV-based 3D ICs [2, 56].

Numerous research works suggested M-3D ICs as a promising solution to address the challenges associated with conventional 2D ICs and TSV-based 3D ICs. Experimental studies conducted by Jiang et al. [15] and Agashiwala et al. [49] demonstrated improvement in single-line delay and reliability by employing doped MLGNR interconnect with metal via for single-tier via-interconnect scheme (VIS). Jiang et al. [57] proposed MLGNR interconnect and CNT via based multi-tier VIS that offers improved single-line delay compared to Cu-based VIS. However, fabricating CNT via is not compatible with back end of line processes, due to high growth temperature (>600°C) requirements. Moreover, heat dissipation remains a critical concern for HTC-MLGNR as vias, owing to their limited thermal conductivities in the vertical direction [72, 74]. Nihei et al. [74] experimentally realized vertical graphene layers to enhance electrical and thermal conductivity in the vertical direction. In a theoretical study, Zhao et al. [72] analyzed the potential of VTC-MLGNRs as on-chip interconnect. Jiang et al. [58] studied the potential of a VIS that integrates doped MLGNR-based via and interconnect to improve signal delay and integration density of M-3D IC. However, VTC-MLGNR as via material and HTC-MLGNR as interconnect material have not been analyzed for single-tier VIS as a prospect for M-3D ICs. Moreover, the challenges posed by scatterers, skin effect, and crosstalk effect on the performance of MLGNR-based VIS remains unexplored at high frequencies. Therefore, it is imperative to analyze MLGNR-based VIS as a prospect for M-3D ICs and to evaluate the

associated challenges arising from scatterers, skin effect, and crosstalk effects at high frequencies.

This chapter presents a combined equivalent circuit model for MLGNR-based VIS and analyzes challenges induced by scatterers, skin effect, and crosstalk effect. In section 6.2, a frequency-independent and frequency-dependent combined equivalent circuit model for single-tier VIS, considering VTC-MLGNR-based via and HTC-MLGNR-based interconnect, is developed. The equivalent circuit of MLGNR VIS is obtained by combining individual equivalent circuits of HTC-MLGNR interconnect and VTC-MLGNR via. In section 6.3, width-dependent and frequency-dependent analysis of circuit parameters is performed for realistic MLGNR VIS ($\lambda_R(T)$) constrained by scatterers and compared to perfect MLGNR VIS ($\lambda_P(T)$). In section 6.4, the performance of realistic and perfect MLGNR-based VIS is analyzed in terms of crosstalk-induced delay for width ranging from 5 nm - 30 nm. Moreover, at a width of 16 nm, the crosstalk-induced delay of realistic and perfect configurations of VIS is analyzed in the frequency range of 1 GHz - 10^4 GHz.

6.2 Equivalent Circuit Modeling of MLGNR-Based VIS

The cross-sectional view of Li-D HTC-MLGNR interconnect, and VTC-MLGNR via in two configurations, i.e., undoped (U-VTC-MLGNR via) and intercalation-doped (Li-D VTC-MLGNR via) is shown in Figs. 6.1(a-c) [72]. In this setup, the intercalation dopant utilized is Li, while carbon-doped oxide (SiCOH) is the interlayer dielectric (ILD) [2, 18, 23]. HTC-MLGNR interconnect (VTC-MLGNR via) is described by width, w_{int} (w_{via}) and thickness, t_{int} (t_{via}). y_{ILD} is the ILD thickness. δ_s is the Van der Waals spacing between two neighboring GNR layers. Figure 6.1(d) shows the schematic of a single-tier driver-via-interconnect-load (DVIL) structure embedded into SiCOH ILD for a M-3D IC [15, 49, 58]. The equivalent circuit of MLGNR VIS is obtained by combining individual equivalent circuits of HTC-MLGNR interconnect and VTC-MLGNR via [15, 49, 58]. R_{int}, L_{int}, and C_{int} are the per unit length (p.u.l.) resistance, inductance, and capacitance, respectively, of HTC-MLGNR interconnect. dy is the infinitesimal section along the HTC-MLGNR interconnect length, l. VTC-MLGNR via is characterized by resistance, R_{via}, inductance, L_{via}, and capacitance, C_{via}. R_L is the lumped resistance given as $R_L = R_{mc} + R_Q(T)$, where R_{mc} and $R_Q(T)$ are obtained from subsection 3.2.1. R_d and C_d are the CMOS driver resistance and capacitance, respectively, and C_L represents the load capacitance.

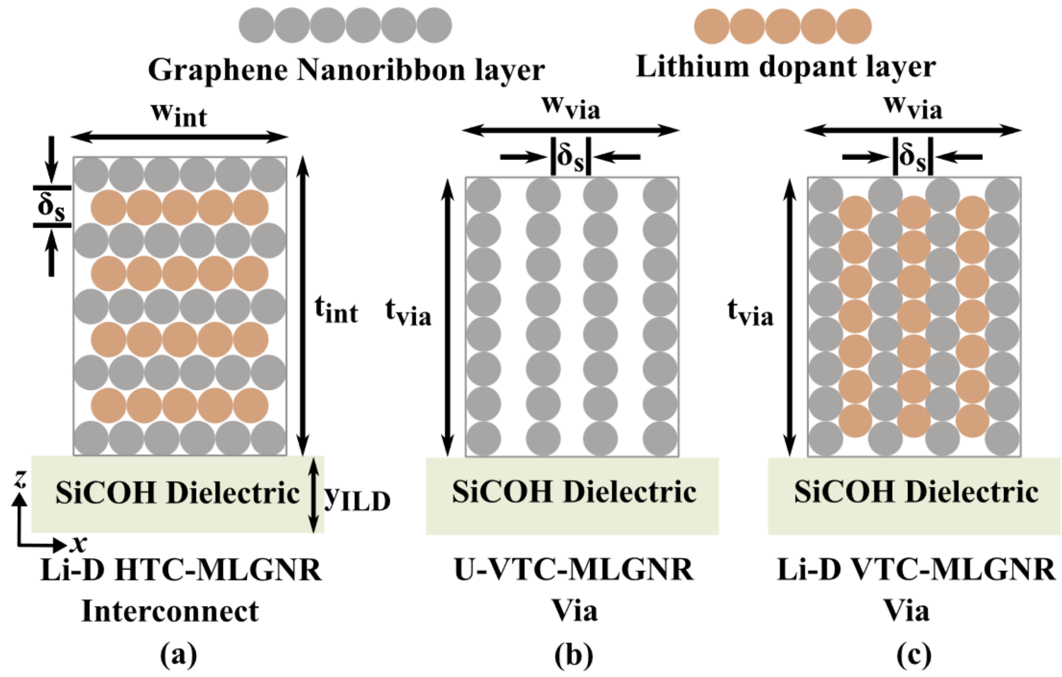

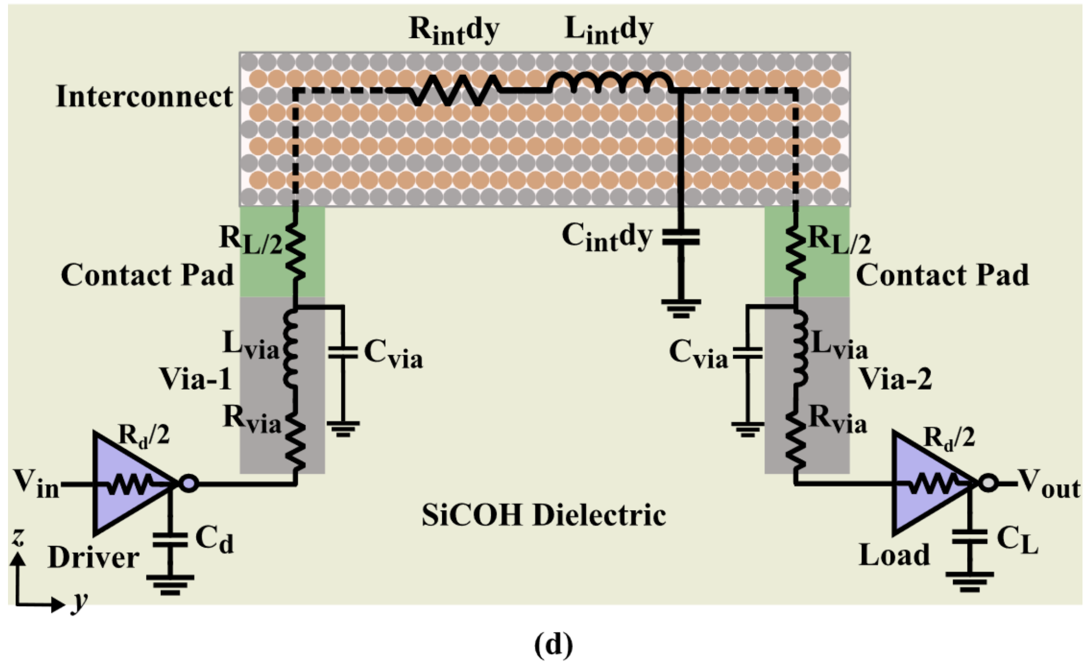

Figure 6.1 Schematic showing (a) Li intercalation-doped HTC-MLGNR (Li-D HTC-MLGNR) interconnect, (b) undoped VTC-MLGNR via (U-VTC-MLGNR via), (c) Li-D VTC-MLGNR via, and (d) equivalent single-tier driver-via-interconnect-load (DVIL) circuit for a M-3D IC [15, 49, 58].

6.2.1 *Frequency-Independent Circuit Model*

The p.u.l. resistance for HTC-MLGNR interconnect (R_{int}), and resistance of VTC-MLGNR via (R_{via}) can be evaluated using formulations given in subsection 3.2.1 (equation (3.5)) and is expressed as:

$$R_{int} = R_{N_{L,int}} = \left(\frac{1}{R_S(T)} + \frac{1}{\left(R_{N_{L,int}-1} + R_z\right)}\right)^{-1}, R_{via} = \frac{R_S(T)t_{via}}{N_{L,via}} \quad (6.1),$$

where, $R_S(T) = \frac{12.9k\Omega}{N_{TM}(T)\lambda_{eff}(T)}$ is the p.u.l. scattering resistance of GNR, $R_Z = \frac{\delta_s}{\sigma_{c-axis}wdy}$ is the c-axis interlayer resistance, $N_{TM}(T)$ are the number of transverse modes in GNR, and $\lambda_{eff}(T)$ is the temperature-aware effective MFP for GNR. $\lambda_{eff}(T)$ for realistic GNR ($\lambda_R(T)$) and perfect GNR ($\lambda_P(T)$) are obtained from subsection 3.2.1, equations (3.4) and (3.3), respectively. The number of layers in HTC-MLGNR interconnect and VTC-MLGNR via is given as $N_{L,int} = 1 + int.\left(\frac{t_{int}}{\delta_s}\right)$ and $N_{L,via} = 1 + int.\left(\frac{w_{via}}{\delta_s}\right)$, respectively. The mathematical formulations for computing L_{int} (L_{via}) and C_{int} (C_{via}) are acquired from prior work [28, 107] and given as:

$$L_{int} = L_e + L_k(T), L_{via} = t_{via}(L_e + L_k(T)) \quad (6.2),$$

$$C_{int} = \left(\frac{1}{C_e} + \frac{1}{C_q(T)}\right)^{-1}, C_{via} = t_{via}\left(\frac{1}{C_e} + \frac{1}{C_q(T)}\right)^{-1} \quad (6.3),$$

where, L_e, $L_k(T)$, C_e, and $C_q(T)$ are acquired from prior work [28, 107].

6.2.2 Frequency-Dependent Circuit Model

At high frequencies, owing to the skin effect phenomena, the amplitude of electric field strength undergoes exponential attenuation along the direction of electromagnetic wave propagation (i.e. along z and y direction for HTC-MLGNR interconnect and VTC-MLGNR via, respectively) as discussed in subsection 3.3.1 [41, 44, 45, 126]. The electric field strength E_{0y}, attenuates according to the function $e^{-\alpha_{int}z}$, for HTC-MLGNR interconnect [41]. Whereas, for VTC-MLGNR via, the electric field strength E_{0z} undergoes an attenuation as per the function $e^{-\alpha_{via}y}$. The attenuation constant is $\alpha_{int} = \sqrt{\eta\pi f \mu\sigma_{int}}$ for HTC-MLGNR interconnect and $\alpha_{via} = \sqrt{\eta\pi f \mu\sigma_{via}}$ for VTC-MLGNR via [41]. Here, $\eta = \left(\sqrt{1 + \varphi_{int/via}^2} + \varphi_{int/via}\right)/\left(1 + \varphi_{int/via}^2\right)$, $\varphi_{int} = \omega\tau_{int}$, $\varphi_{via} = \omega\tau_{via}$, and μ is the permeability of GNR. The dc conductivity for HTC-MLGNR interconnect and VTC-MLGNR via is given as $\sigma_{int} = (R_{int} \times w_{int}t_{int})^{-1}$ and $\sigma_{via} = (R_{via} \times w_{via}^2)^{-1}$, respectively [72]. $\tau_{int/via} = \lambda_{eff}(T)/2v_f$ is the momentum relaxation time for HTC-MLGNR interconnect/VTC-MLGNR via, and v_f is the fermi velocity [40]. The one-dimensional skin depth Δ_{SD} for HTC-MLGNR interconnect (Δ_{int}) and VTC-MLGNR via (Δ_{via}) is obtained from subsection 3.3.1, equation (3.10), and expressed as:

$$\Delta_{int} = \int_0^{t_{int}} e^{-\alpha_{int}z}dz = \Delta'_{int} \times \left(1 - e^{-t_{int}/\Delta'_{int}}\right) \quad (6.4),$$

$$\Delta_{via} = \int_0^{w_{via}} e^{-\alpha_{via} y} dy = \Delta'_{via} \times \left(1 - e^{-w_{via}/\Delta'_{via}}\right) \quad (6.5),$$

where, conventional skin depth for MLGNR-based interconnect and via is $\Delta'_{int} = 1/\alpha_{int} = \sqrt{\xi/(\pi f \mu \sigma_{int})}$, and $\Delta'_{via} = 1/\alpha_{via} = \sqrt{\xi/(\pi f \mu \sigma_{via})}$, respectively, and $\xi = \left(1 + \varphi^2_{int/via}\right) \times \left(\sqrt{1 + \varphi^2_{int/via}} - \varphi_{int/via}\right)$.

HTC-MLGNR interconnect and VTC-MLGNR via are characterized by the effective impedance $Z_{int}(\omega,T)$ and $Z_{via}(\omega,T)$, respectively, determined as follows:

$$Z_{int}(\omega, T) = \frac{l}{w_{int}(1-e^{-\Gamma t_{int}})} \sqrt{\frac{\pi f \mu}{\sigma_{int}}} \times \left[\sqrt{\sqrt{1 + \varphi_{int}{}^2} - \varphi_{int}} + i\sqrt{\sqrt{1 + \varphi_{int}{}^2} + \varphi_{int}}\right] \quad (6.5),$$

$$Z_{via}(\omega, T) = \frac{t_{via}}{w_{via}(1-e^{-\Gamma w_{via}})} \sqrt{\frac{\pi f \mu}{\sigma_{via}}} \times \left[\sqrt{\sqrt{1 + \varphi_{via}{}^2} - \varphi_{via}} + i\sqrt{\sqrt{1 + \varphi_{via}{}^2} + \varphi_{via}}\right] \quad (6.6),$$

where, Γ, f, and ω ($2\pi f$) are the propagation constant of electromagnetic wave, frequency, and angular frequency, respectively. The analytical expression for Γ can be obtained from equation (3.9) [41].

The effective frequency-dependent resistance and inductance for HTC-MLGNR interconnect (VTC-MLGNR via) are denoted as $R_{int}(\omega,T)$ ($R_{via}(\omega,T)$) and $L_{int}(\omega,T)$ ($L_{via}(\omega,T)$), respectively, and given as:

$$R_{int}(\omega, T) = Real\left(Z_{int}(\omega, T)\right), L_{int}(\omega, T) = Imag\left(Z_{int}(\omega, T)\right)/\omega \quad (6.7),$$

$$R_{via}(\omega, T) = Real\left(Z_{via}(\omega, T)\right), L_{via}(\omega, T) = Imag\left(Z_{via}(\omega, T)\right)/\omega \quad (6.8)$$

6.3 Analysis of Circuit Parameters for MLGNR-Based VIS

This section investigates the impact of width variations on effective MFP, $N_{TM}(T)$, and N_L, and consequently on the resistance, inductance, and capacitance of Li-D HTC-MLGNR interconnect, U-VTC-MLGNR via and Li-D VTC-MLGNR via. The technology parameters for interconnect and via are obtained from IRDS-2022 and defined as y_{ILD} = 24 nm, $w_{int/via}$ = 16 nm, AR_{int}=2.5, AR_{via}=1.5, t_{int} = 40 nm, t_{via} =24 nm, dielectric constant ε_r = 2.95, and spacing between two parallel interconnects s = 16 nm [2]. The width of interconnect and via is varied within the range of 5 nm to 30 nm while maintaining a constant aspect ratio (AR). A fermi energy (van der Waals spacing) of E_f =0.2 eV (δ_s=0.34 nm) for undoped GNR and E_f =1.5 eV (δ_s=0.37 nm) for Li intercalation-doped GNR has been reported [18, 23]. The amplitude of corrugations on the SiCOH dielectric surface is δA=340 pm [157]. Furthermore, an analysis is

conducted to explore the impact of frequency variations on skin depth, and effective impedance of Li-D HTC-MLGNR interconnect and Li-D VTC-MLGNR via, at 16 nm width.

6.3.1 Width-Dependent Analysis

Figures 6.2(a-c) illustrate the effective MFP of realistic GNR ($\lambda_R(T)$) and perfect GNR ($\lambda_P(T)$), number of transverse modes ($N_{TM}(T)$), and number of layers (N_L) varying with width for corresponding GNR-based interconnect and via materials, respectively.

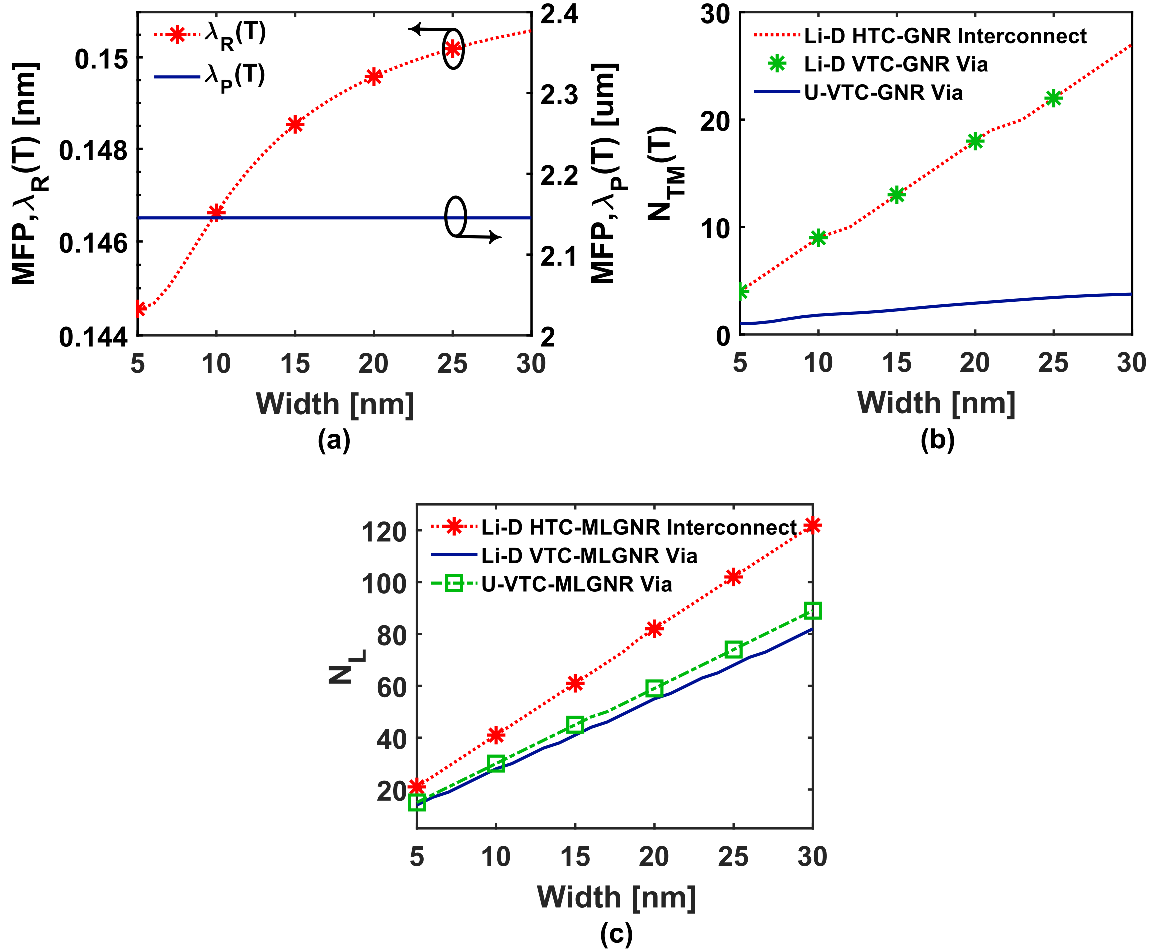

Figure 6.2 (a) Effective mean free path (MFP) of realistic GNR ($\lambda_R(T)$) and perfect GNR ($\lambda_P(T)$) varying with width. (b) Number of transverse modes ($N_{TM}(T)$), and (c) Number of layers (N_L) varying with width for corresponding GNR-based interconnect and via materials.

Figure 6.2(a) depicts the effective MFP of realistic GNR ($\lambda_R(T)$) and perfect GNR ($\lambda_P(T)$) varying with width. $\lambda_R(T)$ exhibits significantly lower values compared to $\lambda_P(T)$ due to enhanced electron scatterings in realistic GNR. $\lambda_R(T)$ increases with width due to the direct proportionality of λ_{SER} to width as observed from subsection 3.2.3, Fig. 3.6. Moreover, the rise in $\lambda_R(T)$ is relatively small because corrugated-dielectric-surface-dependent λ_{CD}, which

dominates the overall $\lambda_R(T)$, is independent of width. A constant value of $\lambda_P(T)$ is observed as $\lambda_{ac}(T)$ and $\lambda_{op}(T)$ are not dependent on width [26]. Figure 6.2(b) illustrates that $N_{TM}(T)$ for interconnect and vias rise with width as the number of populated sub-bands increase with width [16, 76]. Li-D HTC-GNR interconnect and Li-D VTC-GNR via exhibit similar $N_{TM}(T)$ values, which are higher compared to U-VTC-GNR via. Li-D GNR exhibits higher $N_{TM}(T)$ compared to its undoped counterpart due to the effect of intercalation-doping, which increases the E_f, resulting in an increased number of populated sub-bands. Figure 6.2(c) demonstrates an increase in N_L values with width for both interconnect and vias. Li-D HTC-MLGNR interconnect exhibits the highest N_L values compared to Li-D VTC-MLGNR via and U-VTC-MLGNR via.

Table 6.1 Comparison of MFP ($\lambda_R(T)$) values from present work with reported data.

Ref.	Interconnect Material	$\lambda_R(T)$	Dielectric	σ [μΩ.cm]$^{-1}$
[23, 113]	Li-D GNR	1.76 μm	Smooth Glass	0.3036
[10, 24]	AsF_5-D GNR	1.03 μm	Suspended	0.63
[15]	U-GNR	100 nm	SiO_2, δA =320 pm	0.00125
[15]	$FeCl_3$-D GNR	44.13 nm	SiO_2, δA =730 pm	0.2
[3]	Cu	10 nm	SiO_2, δA =7 nm and 2.5 nm	0.0434
Present work	Li-D GNR	0.149 nm	SiCOH, δA =340 pm	0.275

Table 6.1 compares the effective MFP, $\lambda_R(T)$, for realistic Li-D GNR with MFP data from the literature for Cu, undoped GNR (U-GNR), AsF_5-D GNR, $FeCl_3$-D GNR, and Li-D GNR. Suspended AsF_5-D GNR [10, 24] and Li-D GNR placed on a smooth glass substrate [23, 113] exhibit MFPs in micrometer range in the absence of edge and substrate-induced scatterers. At a width of 20 nm, $FeCl_3$-D GNR exhibits a lower MFP (44.13 nm) compared to U-GNR (100 nm) due to the significantly rough surface of the ILD and pronounced edge scatterings [15]. This is caused by the increased ILD and edge roughness resulting from $FeCl_3$ condensation on the ILD and GNR surfaces during the intercalation doping process. However, $FeCl_3$-D GNR demonstrates higher electrical conductivity than U-GNR, as intercalation doping enhances carrier mobility and carrier concentration ($\approx 1.75\times10^{14}$ cm^{-2}), compensating for the reduced MFP [15]. In the presence of significant surface roughness in global level Cu interconnects an MFP value of 10 nm is observed for a width of 15 nm [3]. The realistic Li-D GNR in the present work exhibits the lowest MFP (0.149 nm) at 16 nm width, primarily due to enhanced scatterings

from rough edges and corrugated surface of ILD. However, Li-D GNR in the present work shows higher conductivity compared to U-GNR [15], $FeCl_3$-D GNR [15], and Cu [3], owing to its higher doping concentration (≈6×10^{14} cm^{-2}) and elevated carrier density.

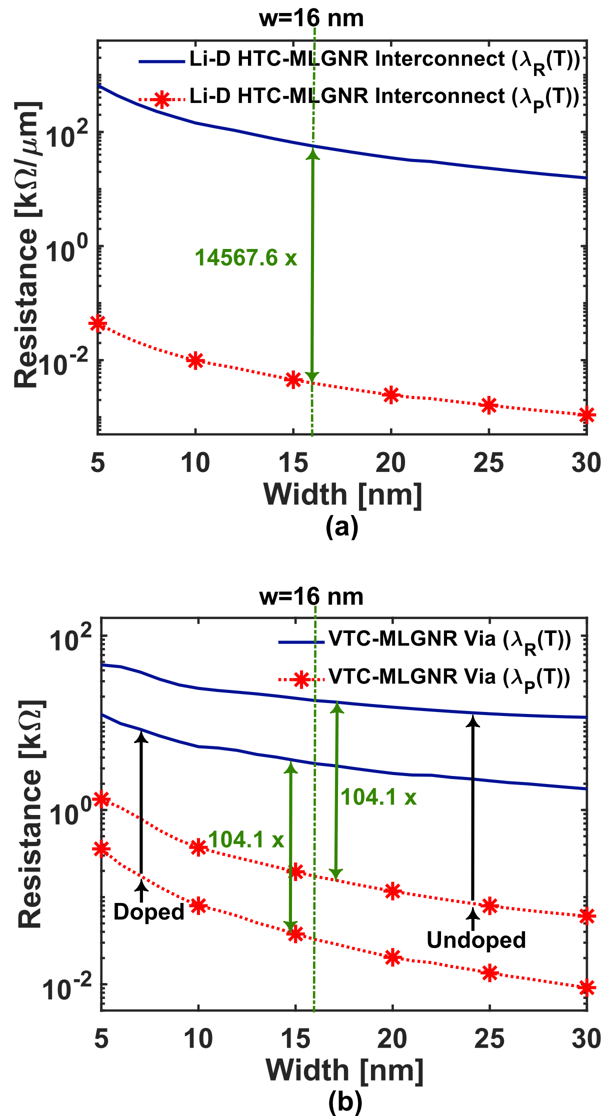

Figure 6.3 Resistance versus width for realistic ($\lambda_R(T)$) and perfect ($\lambda_P(T)$) configurations of (a) Li-D HTC-MLGNR interconnect, and (b) undoped and Li-D VTC-MLGNR via.

Figure 6.3 compares the width dependence of resistance ($R_{int/via}$) for realistic and perfect cases of both Li-D HTC-MLGNR interconnect and VTC-MLGNR vias. A decrease in the resistance is observed as the width increases. This is attributed to the inverse relationship between resistance and factors such as MFP, $N_{TM}(T)$, and N_L, all of which increase with width, as illustrated in Fig. 6.2. In Fig. 6.3(a), realistic Li-D HTC-MLGNR interconnect ($\lambda_R(T)$) demonstrates significantly higher resistance compared to perfect Li-D HTC-MLGNR interconnect ($\lambda_P(T)$). This increase in resistance can be attributed to a reduction in $\lambda_R(T)$ in the

presence of scatterers, compared to $\lambda_P(T)$. At a width of 16 nm, a realistic Li-D HTC-MLGNR interconnect ($\lambda_R(T)$) exhibits 14567.6 times higher resistance compared to the perfect Li-D HTC-MLGNR counterpart ($\lambda_P(T)$). Observations from Fig. 6.3(b) reveal that realistic VTC-MLGNR via ($\lambda_R(T)$) exhibits higher resistance than perfect VTC-MLGNR via ($\lambda_P(T)$) in both undoped and Li intercalation-doped configurations. This is due to the enhanced scatterings resulting in lower values of $\lambda_R(T)$ for realistic VTC-MLGNR via compared to the higher value of $\lambda_P(T)$ for perfect VTC-MLGNR via. Moreover, the intercalation-doped configurations of both realistic and perfect VTC-MLGNR vias demonstrate lower resistance owing to their larger $N_{TM}(T)$ values compared to the undoped counterparts. The realistic VTC-MLGNR via ($\lambda_R(T)$) exhibits 104.1 times higher resistance than perfect VTC-MLGNR via $\lambda_P(T)$ in both undoped and Li intercalation-doped configurations, at a width of 16 nm.

Figure 6.4 represents the trend followed by inductance ($L_{int/via}$) and capacitance ($C_{int/via}$) of both HTC-MLGNR interconnects and VTC-MLGNR via. Figures 6.4(a) and (b) illustrate that there is a decrease in inductance with width for Li-D HTC-MLGNR interconnects and VTC-MLGNR via (undoped and Li intercalation-doped), respectively. This is attributed to kinetic inductance ($L_k(T)$) dominating the overall inductance due to its higher value compared to magnetic inductance (L_e). Moreover, $L_k(T)$ exhibits an inverse relation with $N_{TM}(T)$, which increases with width. Consequently, the inductance of Li-D HTC-MLGNR interconnects, U-VTC-MLGNR via, and Li-D VTC-MLGNR via decreases with width. Furthermore, a minute increase in capacitance with width is observed for Li-D HTC-MLGNR interconnects in Fig. 6.4(a), as well as for U-VTC-MLGNR via, and Li-D VTC-MLGNR via in Fig. 6.4 (b). This is because electrostatic capacitance (C_e) dominates overall capacitance due to its substantially lower value than quantum capacitance ($C_q(T)$). Additionally, C_e remains constant with width due to a constant aspect ratio, while $C_q(T)$ is directly proportional to $N_{TM}(T)$, which increase with width. Therefore, a minute increase in capacitance is observed as the width increases. Figure 6.4 (b) shows that Li-D VTC-MLGNR via has lower inductance and slightly higher capacitance owing to higher $N_{TM}(T)$ values in comparison to U-VTC-MLGNR via. The capacitance values of U-VTC-MLGNR via and Li-D VTC-MLGNR via do not differ significantly, as C_e dominates overall capacitance.

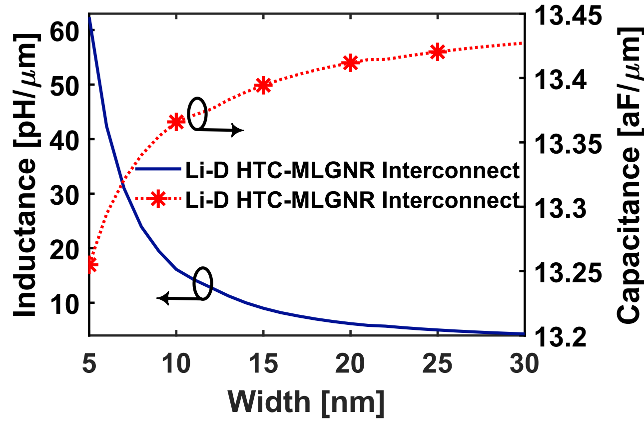

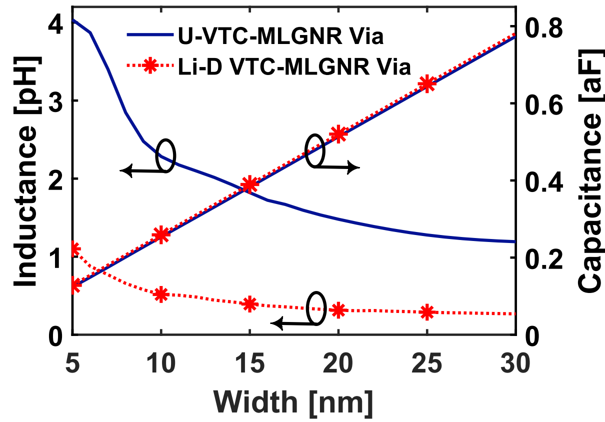

Figure 6.4 Inductance and Capacitance versus width for (a) Li-D HTC-MLGNR interconnects, and (b) undoped and Li-D VTC-MLGNR via.

Table 6.2 Properties of Li-D HTC-MLGNR interconnect and Li-D VTC-MLGNR via.

Properties	Li-D HTC-MLGNR interconnect		Li-D VTC-MLGNR via	
	$\lambda_R(T)$	$\lambda_P(T)$	$\lambda_R(T)$	$\lambda_P(T)$
$R_{int/via}$	56.81 kΩ/μm	3.94 Ω/μm	3.4 kΩ	32.7 Ω
$\sigma_{int/via}$ [μΩ.cm]$^{-1}$	0.275	3965.7	4.8×10^{-4}	6.97
$\tau_{int/via}$ [s]	9.3×10^{-17}	1.34×10^{-12}	9.3×10^{-17}	1.34×10^{-12}

At a width of 16 nm, the properties for realistic ($\lambda_R(T)$) and perfect ($\lambda_P(T)$) cases of both Li-D HTC-MLGNR interconnect and Li-D VTC-MLGNR via are listed in Table 6.2. In the realistic case, Li-D HTC-MLGNR interconnect ($\lambda_R(T)$) and Li-D VTC-MLGNR via ($\lambda_R(T)$) exhibits higher resistance ($R_{int/via}$), lower dc conductivity ($\sigma_{int/via}$), and shorter momentum relaxation time ($\tau_{int/via}$) compared to their perfect ($\lambda_P(T)$) counterparts.

6.3.2 Frequency-Dependent Analysis

Figures 6.5(a) and (b) illustrate the skin depth of Li-D HTC-MLGNR interconnect (Δ_{int}) and Li-D VTC-MLGNR via (Δ_{via}) as a function of frequency, respectively. As the frequency increases, both Δ_{int} and Δ_{via} decrease due to the skin effect, which results in partial elimination of current at the center due to eddy currents and predominant flow of current along the surface of the interconnect/via. Realistic ($\lambda_R(T)$) configuration of both Li-D HTC-MLGNR interconnect and Li-D VTC-MLGNR via, characterized by lower $\sigma_{int/via}$ values, exhibits higher skin depth compared to their perfect ($\lambda_P(T)$) counterparts. Moreover, the skin depth for perfect ($\lambda_P(T)$) configuration of Li-D HTC-MLGNR interconnect and Li-D VTC-MLGNR via saturates at 400 GHz, where $\omega\tau_{int/via}$ approaches 1.

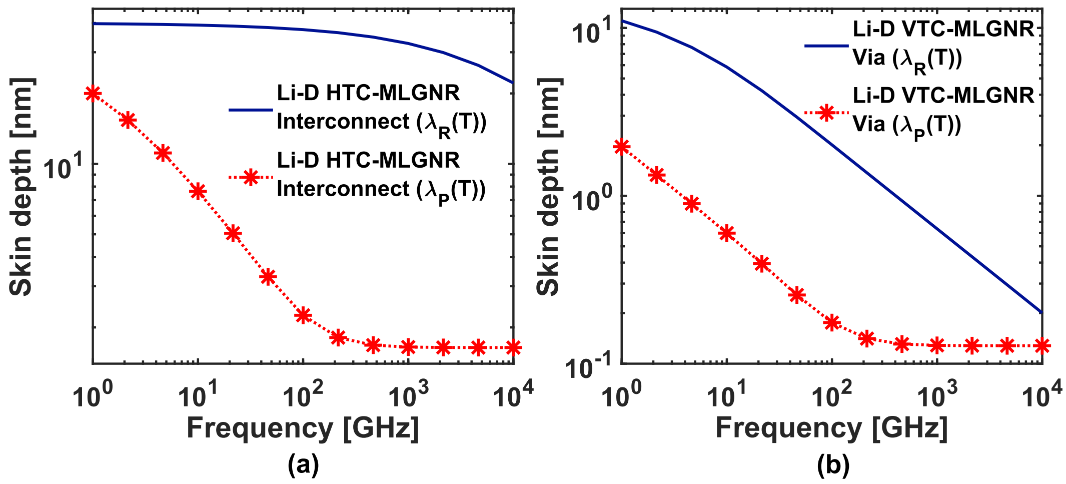

Figure 6.5 Skin depth varying with frequency for realistic ($\lambda_R(T)$) and perfect ($\lambda_P(T)$) configurations of (a) Li-D HTC-MLGNR interconnects and (b) Li-D VTC-MLGNR via.

Table 6.3 Comparison of skin depth (Δ_{SD}) model from present work with existing models.

Frequency [GHz]	Δ_{SD} [nm] [40, 42]	Δ_{SD} [nm] [44, 45]	Δ_{SD} [nm] [Present work]
1	3034.8	39.7	39.7
10^2	303.4	37.5	37.5
10^4	30.26	22.1	22.1

A comparison of the one-dimensional skin depth model from the present work with the existing skin depth models is illustrated in Table 6.3 for realistic Li-D HTC-MLGNR interconnects at 1 GHz, 10^2 GHz, and 10^4 GHz. The model in ref. [40, 42] tends to overestimate the skin depth (Δ_{SD}) at 1 GHz and 10^2 GHz, as it does not account for the finite thickness of miniaturized conductors. However, at 10^4 GHz, comparable values of skin depth are observed for the present

work and ref. [40, 42]. Moreover, similar skin depth values are observed for the model presented in ref. [44, 45] and the present work.

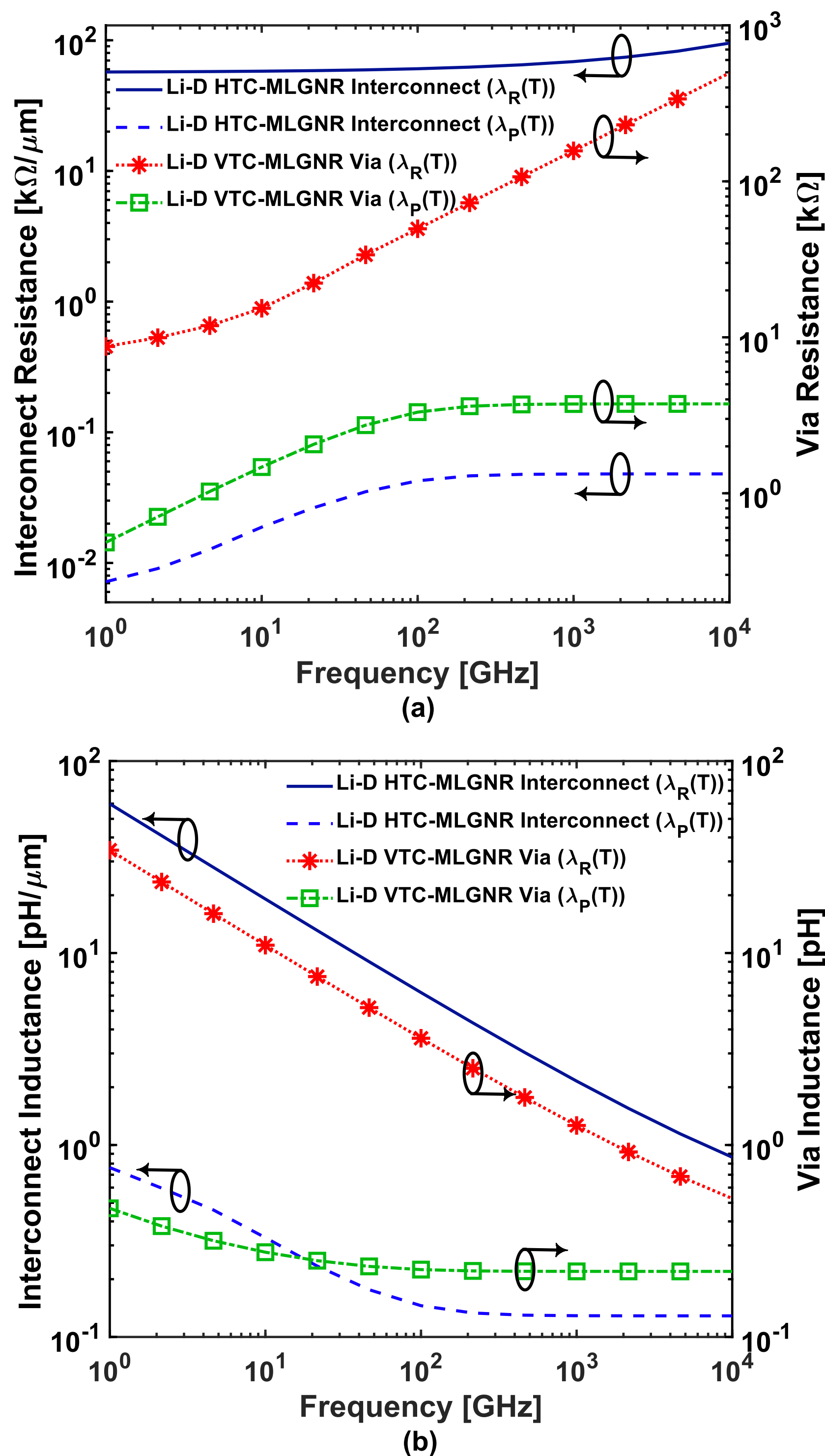

Figure 6.6 (a) Resistance, and (b) inductance versus frequency for realistic ($\lambda_R(T)$) and perfect ($\lambda_P(T)$) configurations of Li-D HTC-MLGNR interconnects, and Li-D VTC-MLGNR via.

Figure 6.6(a) depicts that the resistance ($R_{int/via}(\omega,T)$) for realistic and perfect cases of both Li-D HTC-MLGNR interconnects and Li-D VTC-MLGNR via increases with the rise in frequency. This is attributed to the decrease in skin depth of interconnect/via with frequency. However, the resistance for perfect case ($\lambda_P(T)$) of both Li-D HTC-MLGNR interconnects and Li-D VTC-MLGNR via saturates at 400 GHz owing to their longer momentum relaxation time compared to realistic case ($\lambda_R(T)$) of both Li-D HTC-MLGNR interconnects and Li-D VTC-MLGNR via, respectively. Additionally, perfect case ($\lambda_P(T)$) of both Li-D HTC-MLGNR interconnects and Li-D VTC-MLGNR via exhibit lower resistance attributed to their large $\lambda_P(T)$ and higher $\sigma_{int/via}$ values compared to their realistic ($\lambda_R(T)$) counterparts. Observations from Fig. 6.6(b) reveal that the inductance for Li-D HTC-MLGNR interconnects and Li-D VTC-MLGNR via decreases with a rise in frequency due to a decrease in magnetic flux caused by current flowing predominantly at the edges of the interconnect/via. However, saturation in inductance values of the perfect case ($\lambda_P(T)$) of both Li-D HTC-MLGNR interconnects and Li-D VTC-MLGNR via is observed at 400 GHZ, where $\omega\tau_{int/via}$ approaches 1. Also, perfect case ($\lambda_P(T)$) of both Li-D HTC-MLGNR interconnects and Li-D VTC-MLGNR via exhibit lower inductance attributed to their lower skin depth values compared to their realistic ($\lambda_R(T)$) counterparts.

6.4 Crosstalk Analysis in MLGNR-Based VIS

In this section, dynamic crosstalk-induced delay of Li-D HTC-MLGNR interconnects and VTC-MLGNR via (viz., undoped and Li intercalation-doped) based via-interconnect scheme (VIS) is examined, considering perfect ($\lambda_P(T)$) and realistic ($\lambda_R(T)$) scenarios at l=4.8 µm and 1 mm. The crosstalk delay analysis on TSPICE simulator employs mutually-coupled three-line single-tier driver-via-interconnect-load (DVIL) architecture depicted in Fig. 6.7. C_L=0.14 fF and 0.7 V power supply is employed for worst-case crosstalk delay analysis where V_{in2} switches from 1→0 while V_{in1} and V_{in3} transition from 0→1 under dynamic signal switching conditions. M and C_c represent inductive and capacitive coupling between mutually-coupled aggressor and victim lines, respectively. The p.u.l. M and C_c for both realistic VIS ($\lambda_R(T)$) and perfect VIS ($\lambda_P(T)$) are computed using the mathematical formulations given in the prior work [105] and [4, 60], respectively. The obtained value of M=3.31 pH/µm, whereas C_c for VIS ($\lambda_P(T)$) and VIS ($\lambda_R(T)$) is 78.49 aF/µm and 102.181 aF/µm, respectively.

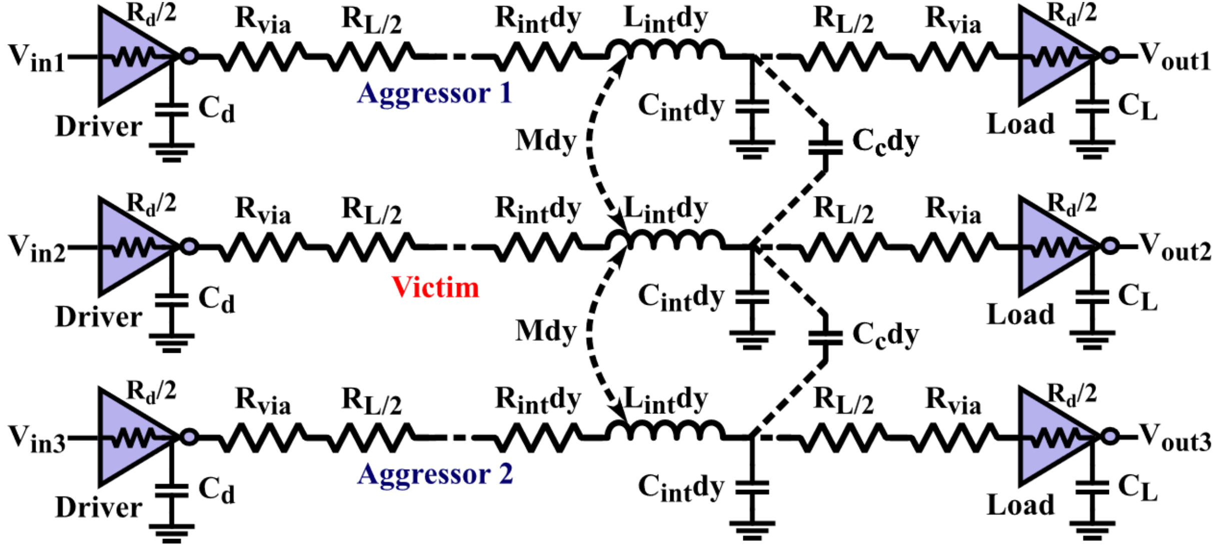

Figure 6.7 Mutually-coupled three-line single-tier DVIL architecture.

6.4.1 Width-Dependent Analysis

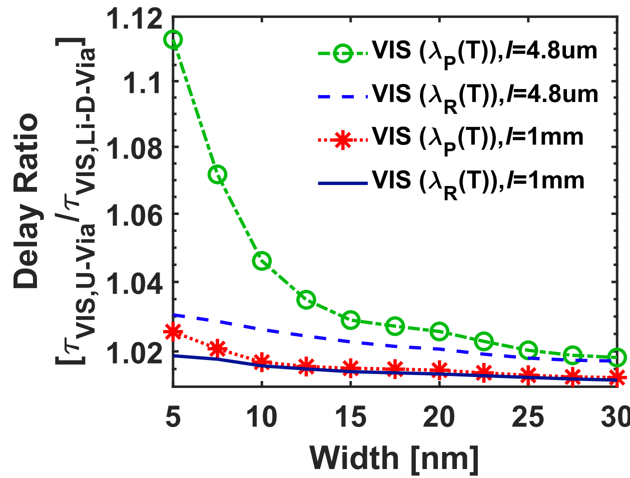

Figure 6.8 Normalized crosstalk-induced delay versus width for MLGNR-based VIS with undoped via and Li-D VTC-MLGNR via.

The crosstalk-induced delay of VIS with undoped VTC-MLGNR via ($\tau_{VIS,U\text{-}Via}$) normalized by delay values of VIS with Li-D VTC-MLGNR via ($\tau_{VIS,Li\text{-}D\text{-}Via}$) is plotted against width in Fig. 6.8, for both cases of perfect ($\lambda_P(T)$) VIS and realistic ($\lambda_R(T)$) VIS at l=4.8 µm and 1 mm. It is observed that $\tau_{VIS,U\text{-}Via}$ is always higher than $\tau_{VIS,Li\text{-}D\text{-}Via}$, and their delay ratio follows a decreasing trend with width for both cases of realistic VIS ($\lambda_R(T)$) and perfect VIS ($\lambda_P(T)$) at l=4.8 µm and 1 mm. This can be explained by the fact that U-VTC-MLGNR via exhibits higher resistance compared to Li-D VTC-MLGNR via, along with resistance being the dominant parasitic, which decreases with increasing width (see Fig. 6.3(b)). Moreover, the sharp decrease in delay ratio of perfect VIS ($\lambda_P(T)$) at l=4.8 µm with width indicates a significant impact of via on overall

VIS performance, particularly when the perfect case of VIS at smaller lengths, i.e., l=4.8 μm is considered.

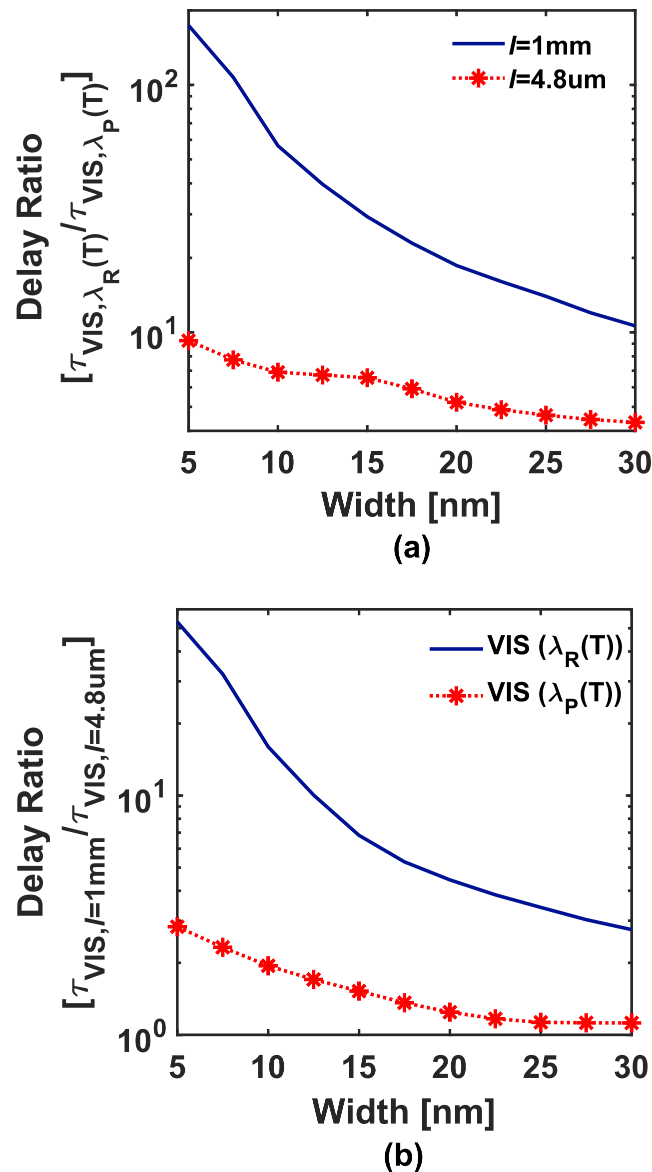

Figure 6.9 Normalized crosstalk-induced delay of MLGNR-based VIS with Li-D VTC-MLGNR via for (a) l=4.8 μm and 1 mm, and (b) realistic ($\lambda_R(T)$) VIS and perfect ($\lambda_P(T)$) VIS, at varying widths.

Figure 6.9(a) illustrates crosstalk-induced delay of realistic ($\lambda_R(T)$) VIS ($\tau_{VIS,\lambda R(T)}$) normalized by delay values of perfect ($\lambda_P(T)$) VIS ($\tau_{VIS,\lambda P(T)}$) considering Li-D VTC-MLGNR via at l=4.8 μm and 1 mm. There is a significant increase in $\tau_{VIS,\lambda R(T)}$ compared to $\tau_{VIS,\lambda P(T)}$, and their ratio decreases with an increase in width for l=4.8 μm and 1 mm. This is due to the fact that resistance of realistic ($\lambda_R(T)$) VIS is significantly higher compared to perfect ($\lambda_P(T)$) VIS, and it decreases with increase in width (see Fig. 6.3). The average increase in delay of realistic

($\lambda_R(T)$) VIS is 6.05 times (45.58 times) for l=4.8 µm (l=1 mm) compared to perfect ($\lambda_P(T)$) VIS. Figure 6.9 (b) shows the delay of VIS at l=1 mm ($\tau_{VIS,l=1mm}$) normalized to the delay of VIS at l=4.8 µm ($\tau_{VIS,l=4.8\mu m}$) for realistic ($\lambda_R(T)$) VIS and perfect ($\lambda_P(T)$) VIS considering Li-D VTC-MLGNR via. It is noted that $\tau_{VIS,l=1mm}$ is significantly higher than $\tau_{VIS,l=4.8\mu m}$, and their delay ratio follows a decreasing trend with increasing width for both realistic ($\lambda_R(T)$) VIS and perfect ($\lambda_P(T)$) VIS. This is because resistance increases with length and decreases with width. The average delay increases for VIS at l=1 mm is 12.82 times (1.59 times) for realistic ($\lambda_R(T)$) VIS (perfect ($\lambda_P(T)$) VIS) compared to VIS at l=4.8 µm.

Table 6.4 presents the relative percentage increase in crosstalk delay, calculated as τ (%) =100 × (($\tau_{VIS,\lambda R(T)}$ - $\tau_{VIS,\lambda P(T)}$)/$\tau_{VIS,\lambda P(T)}$)), for MLGNR-based VIS with Li-D VTC-MLGNR via, when realistic VIS is considered with respect to perfect VIS at l=4.8 µm and 1 mm. The average τ (%) for widths ranging from 5 nm - 30 nm is 617.76% for l=4.8 µm and 59.46×10^2% for l=1 mm. The data shows a significant rise in crosstalk delay for realistic VIS relative to perfect VIS, primarily due to enhanced scatterings from rough edges and corrugated surface of ILD.

Table 6.4 Relative percentage increase in crosstalk delay τ (%) of MLGNR-based VIS with Li-D VTC-MLGNR via for realistic VIS ($\lambda_R(T)$) with respect to perfect VIS ($\lambda_P(T)$) at l=4.8 µm and 1 mm.

Width [nm]	l=4.8 µm			l=1 mm		
	$\tau_{VIS,\lambda P(T)}$ [ns]	$\tau_{VIS,\lambda R(T)}$ [ns]	τ (%)	$\tau_{VIS,\lambda P(T)}$ [ns]	$\tau_{VIS,\lambda R(T)}$ [ns]	τ (×10^2%)
5	1.24	11.48	825.8	3.51	610.54	172.94
10	1.214	8.38	590.3	2.36	134.02	55.79
15	1.208	7.92	555.6	1.84	54	28.35
20	1.206	6.29	421.5	1.5	27.94	17.63
25	1.205	5.58	362.8	1.36	19.02	12.99
30	1.204	5.21	332.7	1.35	14.34	9.62
Average			617.76			59.46

Kumari et al. [113] conducted a simulation-based crosstalk delay analysis for three-line capacitively-coupled DVIL architecture at l=1 mm. The VIS used in the study incorporates Li-D HSC-MLGNR interconnect and Cu via. The optimistic effective MFP is considered for the analysis, excluding the impact of substrate-induced scatterers and incorporating a diffusive

edge scattering model for MFP. A comparison of crosstalk delay between the reported data [113], and the present work is given in Table 6.5. It is observed that, due to the larger width and thickness and the absence of substrate-induced scatterers, the study in ref. [113] reports lower resistance values and, consequently, reduced crosstalk delay compared to the findings of this work.

Table 6.5 Comparison of crosstalk delay for coupled single-tier VIS from present work with reported data [113].

Ref.	Length [mm]	Width [nm]	Thickness [nm]	Corrugation amplitude, δA [pm]	Crosstalk Delay [ns]
[113]	1	90	225	NA	0.5
Present work	1	16	40	340	1.76 (VIS, $\lambda_P(T)$), 47.1 (VIS, $\lambda_R(T)$)

6.4.2 Frequency-Dependent Analysis

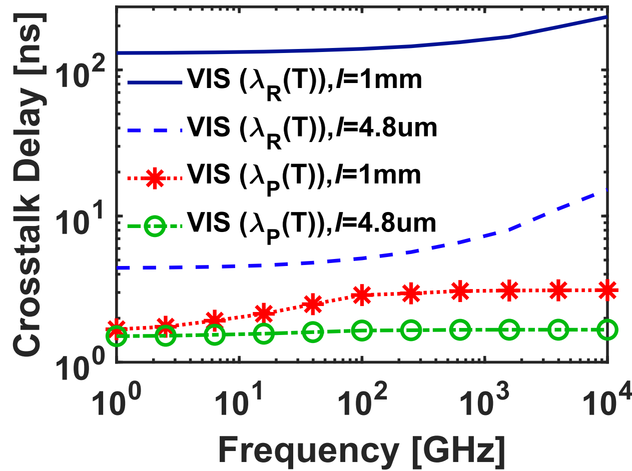

Figure 6.10 Crosstalk-induced delay versus frequency for MLGNR-based VIS with Li-D VTC-MLGNR via.

In Figure 6.10, the crosstalk-induced delay of realistic ($\lambda_R(T)$) VIS and perfect ($\lambda_P(T)$) VIS with Li-D VTC-MLGNR via is plotted as a function of frequency for l=4.8 μm and 1 mm at a width of 16 nm. As the frequency rises, crosstalk-induced delay for realistic ($\lambda_R(T)$) VIS (at l=4.8 μm and 1 mm) and perfect ($\lambda_P(T)$) VIS (at l=1 mm) increases owing to the corresponding rise in resistance. However, crosstalk-induced delay for perfect ($\lambda_P(T)$) VIS at l=1 mm saturates at 400 GHz, attributed to the corresponding saturation of resistance (see Fig. 6.6(a)). Moreover, the

delay for perfect ($\lambda_P(T)$) VIS at l=4.8 μm remains constant with the rise in frequency. It is observed that due to the enhanced resistance in the presence of scatterers, realistic ($\lambda_R(T)$) VIS exhibits higher delay than perfect ($\lambda_P(T)$) VIS at l=4.8 μm and 1 mm for the entire frequency range. The delay-based performance degradation observed in realistic ($\lambda_R(T)$) VIS compared to perfect ($\lambda_P(T)$) VIS is 243.18% and 5.3934×10^3% for l=4.8 μm and 1 mm, respectively.

At f=10^4 GHz, the impact of via resistance (R_{via}) on crosstalk-induced delay of realistic ($\lambda_R(T)$) VIS and perfect ($\lambda_P(T)$) VIS considering Li-D VTC-MLGNR via is illustrated in Fig. 6.11, for l=4.8 μm and 1 mm. For realistic ($\lambda_R(T)$) VIS, the R_{via} ranges from 100 kΩ - 1000 kΩ, while R_{via} in range of 1 kΩ - 10 kΩ is employed for perfect ($\lambda_P(T)$) VIS. It is observed that the crosstalk-induced delay for realistic ($\lambda_R(T)$) VIS at l=1 mm remains constant with an increase in R_{via}. This indicates the negligible impact of via on overall VIS performance when the realistic case of VIS at longer lengths of 1 mm is considered. However, the delay for realistic ($\lambda_R(T)$) VIS (at l=4.8 μm) and perfect ($\lambda_P(T)$) VIS (at l=4.8 μm and 1 mm) increases as the R_{via} increases, highlighting the significant impact of R_{via} on the respective VIS configurations.

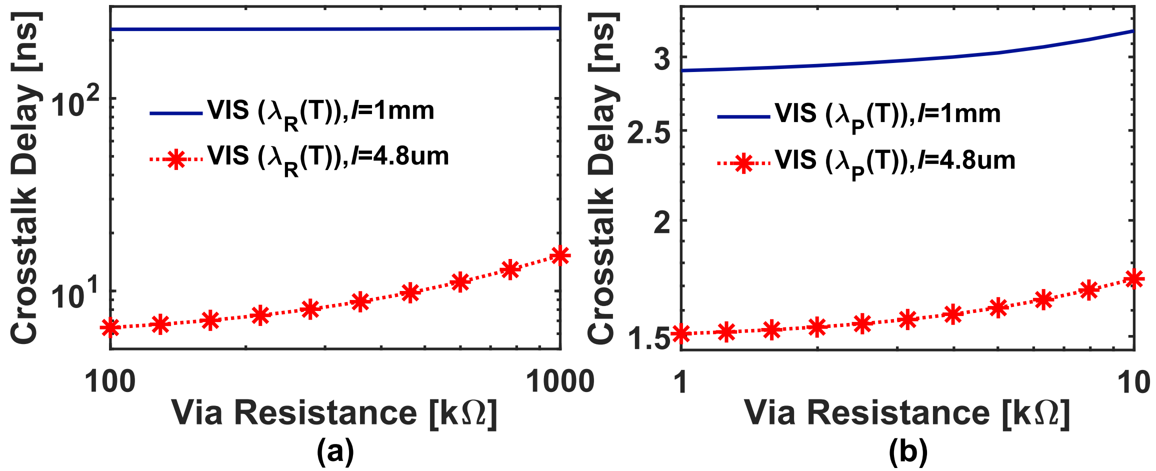

Figure 6.11 Crosstalk-induced delay versus via resistance (R_{via}) for (a) MLGNR-based realistic ($\lambda_R(T)$) VIS, and (b) MLGNR-based perfect ($\lambda_P(T)$) VIS, with Li-D VTC-MLGNR via at f=10^4 GHz.

6.5 Chapter Summary

A single-tier via-interconnect scheme (VIS) as a prospect for M-3D ICs has been proposed utilizing Li-D VTC-MLGNR via and Li-D HTC-MLGNR interconnect. The combined equivalent circuit model for MLGNR-based VIS is introduced that incorporates challenges posed by various scattering sources, high-frequency skin effect, and crosstalk effects. The

performance of MLGNR-based realistic ($\lambda_R(T)$) VIS and perfect ($\lambda_P(T)$) VIS is analyzed in terms of crosstalk-induced delay by considering capacitive and inductive coupling between adjacent MLGNR-based VIS. The findings indicate that perfect ($\lambda_P(T)$) VIS shows superior performance compared to realistic ($\lambda_R(T)$) VIS, for width ranging from 5 nm to 30 nm. This is because the absence of edge and substrate-induced scatterers results in significantly lower resistance for perfect ($\lambda_P(T)$) VIS compared to realistic ($\lambda_R(T)$) VIS. At a width of 16 nm, due to the enhanced resistance in the presence of scatterers, realistic ($\lambda_R(T)$) VIS exhibits higher delay and performance degradation of 243.18% (5.3934×10^3%) for l=4.8 µm (1 mm), respectively, than perfect ($\lambda_P(T)$) VIS for the frequency range of 1 GHz-10^4 GHz. Moreover, it is shown that while the via has negligible impact on the overall performance of realistic VIS at longer lengths of 1 mm, via significantly affects the performance of realistic ($\lambda_R(T)$) VIS (at l=4.8 µm) and perfect ($\lambda_P(T)$) VIS (at both l=4.8 µm and 1 mm). Hence, this work highlights the potential of perfect ($\lambda_P(T)$) VIS, with Li-D HTC-MLGNR interconnect and Li-D VTC-MLGNR via, as a promising solution for M-3D ICs at high frequencies.

Chapter 7 Conclusions and Future Scope

7.1 Introduction

This chapter summarizes the research work presented throughout the thesis and highlights key conclusions. Additionally, potential areas for future research are discussed. Section 7.2 provides a summary of the major findings, Section 7.3 outlines the significant contributions made, and Section 7.4 offers recommendations and explores opportunities for future work related to this topic.

7.2 Summary of Key Findings

The ongoing advancements and rapid miniaturization of device integration technology, guided by Moore's roadmap, have introduced substantial performance limitations for conventional Cu-based interconnects [2, 15, 49]. Cu interconnects have become a major bottleneck in IC performance due to challenges like surface and grain boundary scatterings, surface roughness, electromigration, high resistivity, heat dissipation and receding current density [15, 49, 134]. According to the previous studies, intercalation-doped MLGNRs, characterized by their exceptional current carrying capacity and mobility as well as higher thermal and electrical conductivity, have emerged as a promising alternative to replace Cu interconnects in future ICs [18, 23]. While intercalation doping offers significant benefits, the practical use of MLGNRs is limited by extrinsic scatterers, along with the pronounced skin effect at high frequencies, which exacerbates signal integrity issues. Signal integrity challenges like crosstalk, signal delay, dielectric losses, process variations, and high-frequency losses, intensified by technology scaling and higher interconnect densities, severely limit the performance, reliability, and functionality of high-speed ICs, especially at GHz frequencies and beyond.

This thesis presented the equivalent impedance models with frequency-independent and frequency-dependent circuit parameters for MLGNR interconnects. These models incorporate the impact of extrinsic scattering sources, temperature, skin effect, and crosstalk effects. A comprehensive signal integrity analysis is performed for MLGNR interconnects, evaluating aspects such as transient response, 3-dB bandwidth, relative stability, crosstalk-induced delay, noise pulse, and noise area. The results are then compared with those of Cu and MCNT bundle interconnects. Furthermore, the impact of process and temperature variations on the performance of MLGNR interconnects has been analyzed in the presence of SER-limited

realistic effective MFP and skin effect at high frequencies. Finally, the frequency-independent and frequency-dependent equivalent circuit model for MLGNR-based VIS, as a prospect for M-3D ICs, have been presented. The impact of scatterers and the skin effect are incorporated into the equivalent circuit model. Afterwards, the performance of MLGNR-based VIS has been analyzed in terms of crosstalk-induced delay varying with width and frequency.

7.2.1 High-Frequency Impedance Modeling and Analysis of MLGNR Interconnects

As VLSI technology advances, operating frequencies are approaching the gigahertz range. At such high frequencies, circuit parasitics become frequency-dependent due to the skin effect, which increases effective resistance and further degrades signal integrity. While intercalation-doped MLGNRs offer potential as on-chip interconnects, their MFP is limited by extrinsic scatterers, further hindering performance. Several techniques have been introduced in the literature to model the effective MFP for realistic GNRs by incorporating various extrinsic scatterers [10, 18, 26, 28, 34, 35, 65, 88], which failed to conform with the experimental data and overestimated the values of effective MFP [27]. A few reports have presented skin depth and impedance models for MLGNR interconnects at high frequencies [40, 42], which consider MLGNR interconnects with semi-infinite dimensions and exempted influence of the extrinsic scattering sources in MLGNR [40, 42]. Therefore, it is crucial to develop a realistic MFP model plagued by extrinsic scatterers and finite-thickness-dependent skin effect model for evaluating the performance of MLGNR interconnects in a practical scenario.

The initial work in this thesis focused on developing an impedance model incorporating the extrinsic scattering-limited realistic MFP for MLGNR-based interconnects (viz., undoped and intercalation-doped) to extract frequency-independent circuit parameters. The circuit parameters for MLGNR variants are extracted and compared to MCNT bundles and Cu variants across a temperature range of 300 K to 500 K. The results show that the perfect MLGNR variants exhibit lower resistance compared to the MCNT bundle and Cu interconnects for intrinsic-phonon-limited effective MFP ($\lambda_P(T)$). However, it is worth noting that the resistance of all realistic MLGNR variants becomes several orders larger than that of both smooth and rough Cu interconnects for scattering-limited realistic effective MFP ($\lambda_R(T)$), whereas only Li-D MLGNR exhibits lower resistance than MCNT bundle for $\lambda_R(T)$. Furthermore, the results show that MLGNR variants exhibit resistance increase by increasing δA. Moreover, the resistance of MLGNRs on SiC (δA =10 pm), BN (δA =70 pm), and SiO_2 (δA=170 pm) is always

larger than Cu counterparts when $\lambda_R(T)$ with SER is considered. Whereas the resistance of Li-D HTC-MLGNR without SER on SiC and BN is less than that of Cu, whereas the MLGNR on SiO_2 has the resistance more than Cu counterparts.

Moreover, an impedance model is developed for MLGNR interconnects incorporating the impact of both scattering-limited realistic effective MFP and a finite-thickness-dependent skin effect. By employing the proposed impedance model, frequency-dependent circuit parameters for MLGNR interconnects are obtained and compared to MCNT bundle and Cu interconnects. The results show that the realistic MLGNR variants and MCNT bundle interconnects (considering $\lambda_R(T)$) exhibit higher resistance and inductance values compared to Cu variants. However, Li-D HTC-MLGNR exhibits lower resistance and inductance than other MLGNR variants, and MCNT bundle interconnects. Furthermore, Li-D HTC-MLGNR interconnects, when optimized by placing on SiC and BN substrates and with factors like SPP and SER excluded from $\lambda_R(T)$, demonstrate lower resistance and inductance than Cu interconnects.

7.2.2 Signal Integrity Analysis in MLGNR Interconnects

Crosstalk between closely placed high-density interconnects affects the transient behavior, functionality, reliability, and timing of the signal propagating through interconnects at high frequencies [39]. Researchers have conducted crosstalk analysis of coupled MLGNR interconnect lines, incorporating extrinsic-scatterers-limited realistic MLGNR [108, 109, 111–113]. However, the impact of a SER-limited realistic effective MFP and one-dimensional skin depth in the presence of crosstalk effects remains unaddressed on the performance characteristics of MLGNR interconnects. Hence, it is essential to examine the impact of performance-limiting factors like SER-limited realistic MFP and skin effects on the performance of MLGNR interconnects.

After developing a scattering-limited realistic impedance model, further research work focused on temperature-dependent comparative performance analysis of MLGNR, MCNT bundle, and Cu considering the adjacent capacitively coupled configuration of interconnects under low-bias regime. By employing the developed realistic impedance model for interconnects, the crosstalk-induced delay is calculated using SPICE simulations. The results indicate that Li-D HTC-MLGNR interconnects outperform the MCNT bundle and other variants of MLGNR and Cu interconnects in terms of crosstalk-induced delay for $\lambda_P(T)$. However, for $\lambda_R(T)$, both realistic scattering-limited MLGNR and MCNT bundle interconnects have inferior

performance in comparison to Cu variants. Moreover, among the scattering-limited MLGNR variants and MCNT bundle interconnects, Li-D HTC-MLGNR has shown superior performance as a nanoscale interconnect for $\lambda_R(T)$. When compared to MCNT bundle interconnects, the Li-D HTC-MLGNR shows a decrease of 85.48% and 74.67% in crosstalk-induced delay values for $\lambda_P(T)$ and $\lambda_R(T)$, respectively. The average relative penalty (ARP) in crosstalk-induced delay for MLGNR variants, when $\lambda_R(T)$ is considered w.r.t $\lambda_P(T)$, is obtained as 21.58×10^2 %, 48.14×10^2 %, 49.35×10^2 %, 52.68×10^2 %, 53.92×10^2 % and 57.09×10^2 % for U-VTC-MLGNR, U-HTC-MLGNR, U-HSC-MLGNR, AsF_5-D HTC-MLGNR, $FeCl_3$-D HTC-MLGNR and Li-D HTC-MLGNR, respectively. The findings reveal that the scattering sources degrade the crosstalk-induced delay performance of MLGNR interconnects; therefore, these must be incorporated in design considerations for a realistic comparison of prospective interconnect materials in the worst-case scenario.

Furthermore, the transient response, 3-dB bandwidth and Nyquist stability of MLGNR interconnects (with and without SER) placed on the corrugated dielectric surface are investigated and compared with that of Cu interconnects. It is observed that all the MLGNR variants with SER, placed on SiO_2, have higher rise time and small 3-dB bandwidth than Cu variants. Among all the MLGNR variants, Li-D HTC-MLGNR exhibits the lowest increase in t_d and t_r of 1264.8% and 1250.4%, respectively, and the lowest decrease in 3-dB bandwidth of 92.56%, compared to smooth Cu. Moreover, Li-D HTC-MLGNR interconnects without SER on SiC and BN have faster rise time than Cu counterparts, demonstrating a 94.64% and 94.7% decrease in t_d and t_r, respectively. In addition, U-HTC-MLGNR with SER on SiO_2 has the highest system stability, whereas smooth Cu is the least stable. The findings demonstrate that while the SER and higher corrugation amplitude of dielectric improve the stability of the MLGNR DIL system, it also leads to a slow and sluggish step response and a decrease in 3-dB bandwidth. Therefore, for practical implementation of MLGNR as on-chip interconnects, scattering sources like SER and roughness of dielectric surface need to be eradicated.

Moreover, the frequency-dependent crosstalk analysis of MLGNR interconnects is conducted in terms of crosstalk-induced delay, overshoot amplitude, and overshoot width by considering the impact of scatterers and skin effect and compared with Cu and MCNT bundle counterparts. It is noted that MLGNR variants (for $\lambda_R(T)$) and MCNT bundle interconnects (for $\lambda_R(T)$) placed on SiO_2, in the presence of significant skin effect and scatterers, exhibit inferior performance compared to conventional Cu variants. However, in comparison to other MLGNR variants

(case 2) and MCNT bundle interconnects, Li-D HTC-MLGNR exhibits superior performance. Moreover, Li-D HTC-MLGNR, when optimized by placing on SiC in the absence of SPPs and SER, demonstrates the minimum impact of frequency variations and skin effect and superior performance compared to Cu variants. Optimized Li-D HTC-MLGNR (case 1) (O-Li-D HTC-MLGNR), when placed on SiC, displays the lowest average percentage increase (API) in crosstalk-induced overshoot peak amplitude, overshoot width, and delay of 6.6%, 0.18%, and 15.6%, respectively, for the frequency range of 1 GHz to 10^4 GHz. Consequently, O-Li-D HTC-MLGNR is least prone to overshoot induced MOS gate oxide breakdown and reliability issues along with less susceptibility towards crosstalk delay induced timing errors in ICs at high frequencies.

Therefore, to benefit from the advantages of MLGNR-based interconnects at high frequencies, intercalation doping with Li, utilizing dielectric SiC as substrate, and eliminating scatterings with rough edges and substrate SPPs are desired.

7.2.3 High-Frequency Challenges under Process and Temperature Variations

The variations and uncertainties in the physical and geometric parameters of interconnects combined with temperature fluctuations, result in uncertainties and deviations in interconnect performance metrics [50–54]. High-frequency performance analysis of interconnects under these variations become crucial for modern VLSI circuits, as factors such as scattering-limited MFP, skin effect, crosstalk, and electromigration further complicate circuit reliability and functionality. Electromigration poses a limitation on the reliability of MLGNR interconnects by reducing their lifetime and mean time to failure [7-10]. Several experimental and theoretical work in the literature studied reliability concerns in MLGNR interconnects due to electromigration effects [15, 20, 46, 47, 49, 57, 61, 128, 129]. While recent studies have examined the effects of process and temperature variations on crosstalk-induced delay, noise, and noise area [50–55], the challenges posed by these variations at high frequencies due to SER limited realistic effective MFP, skin effect, crosstalk, and electromigration effects remains remain underexplored. Thus, it is imperative to comprehensively assess the impact of process and temperature variations on the high-frequency performance of MLGNR interconnects.

The frequency-dependent performance characterization of O-Li-D HTC-MLGNR is done in the presence of scatterers, skin effect, and process and temperature variations. The findings indicate that the maximum variations in crosstalk effects and EM-MTF show an increase and

decrease, respectively, with frequency, attributed to fluctuations in process parameters and temperature. The variations in δA and T result in the highest average maximum variations of 0.78 ns (166.42 mV.ps) and 9.96×10^{12} hours in crosstalk-induced delay (noise area) and EM-MTF, respectively, for the entire frequency range.

Furthermore, at a fixed f=10^4 GHz, crosstalk and EM-MTF effects exhibit opposing trends with increasing δA, T, and δ_s, while variations in w and E_f demonstrate a reverse relationship. Notably, the variation in δA leads to the highest average variations of 6.62 ns and 503.58 mV.ps in crosstalk-induced delay and noise area, respectively. In contrast, temperature variations contribute to the largest average variation of 1.02×10^{12} hours in EM-MTF.

These findings underscore that the impact of process and temperature variations intensifies at higher frequencies for O-Li-D HTC-MLGNR, emphasizing the necessity of precise modeling and compensation strategies to mitigate their adverse effects. Future research should focus on developing robust design methodologies and material engineering techniques that can counteract these variations, ensuring the reliability and efficiency of next-generation interconnect systems.

7.2.4 MLGNR-Based Via-Interconnect Scheme (VIS) for Monolithic 3D ICs

Numerous research works suggested M-3D ICs as a promising solution to address the challenges associated with conventional 2D ICs and TSV-based 3D ICs. However, VTC-MLGNR as via material and HTC-MLGNR as interconnect material have not been analyzed for single-tier VIS as a prospect for M-3D ICs. Also, the challenges posed by scatterers, skin effect and crosstalk effect on the performance of MLGNR-based VIS remain unexplored at high frequencies. Therefore, it is imperative to analyze MLGNR-based VIS as a prospect for M-3D ICs and to evaluate the associated challenges arising from scatterers, skin effect and crosstalk effects at high frequencies.

This section of the research proposed the use of Li-D VTC-MLGNR via and Li-D HTC-MLGNR interconnect within a single-tier VIS as a prospect for M-3D ICs. The combined equivalent circuit model for MLGNR-based VIS is introduced that incorporates challenges posed by extrinsic scatterers and high-frequency skin effect. The performance of MLGNR-based realistic VIS and perfect VIS is analyzed in terms of crosstalk-induced delay by considering capacitive and inductive coupling between adjacent MLGNR VIS.

The findings indicate that perfect VIS shows superior performance compared to realistic VIS, for width ranging from 5 nm - 30 nm. The relative percentage increase in crosstalk delay, when realictic ($\lambda_R(T)$) VIS is considered with respect to perfect ($\lambda_P(T)$) VIS, is 617.76% for l=4.8 μm and 59.46×10^2% for l=1 mm. Moreover, at a width of 16 nm, realistic VIS exhibits higher delay than perfect VIS at l=4.8 μm and 1 mm for the frequency range of 1 GHz-10^4 GHz. The delay-based performance degradation observed in realistic VIS compared to perfect VIS is 243.18% and 5.3934×10^3% for l=4.8 μm and 1 mm, respectively, for the entire frequency range. Moreover, it is shown that while the via has negligible impact on the overall performance of realistic VIS at longer lengths of 1 mm, via has a significant impact on the performance of realistic VIS (at l=4.8 μm) and perfect VIS (at l=4.8 μm and 1 mm). Hence, this work highlights the potential of perfect VIS, with Li-D HTC-MLGNR interconnect and Li-D VTC-MLGNR via, as a promising solution for M-3D ICs at high frequencies.

7.3 Main Research Contributions

The contributions of the research work presented in this dissertation can be summarized as follows:

- Development of an impedance model incorporating the impact of temperature and extrinsic scattering-limited MFP for realistic MLGNR-based interconnects to extract frequency-independent circuit parameters.
- By employing this impedance model, temperature-dependent crosstalk-induced delay analysis of MLGNR interconnects is performed and compared to MCNT bundle and Cu counterparts, considering the three adjacent capacitively-coupled configuration of interconnects.
- Additionally, the transient response high-frequency signal integrity, 3-dB bandwidth, and Nyquist stability of MLGNR interconnects are investigated under varying corrugation amplitudes and edge roughness and are compared to Cu interconnects while accounting for crosstalk effects.
- To go beyond the simplifying assumptions of perfect MLGNR and conventional skin effect, an impedance model considering the impact of extrinsic scatterers and one-dimensional skin depth is proposed for extracting the frequency-dependent impedance of realistic MLGNR interconnects.

- Utilizing this impedance model, a frequency-dependent analysis of crosstalk effects is performed for MLGNR interconnects and compared to the MCNT bundle and Cu counterparts.
- The performance of O-Li-D HTC-MLGNR, limited by process and temperature variations, is analyzed in terms of crosstalk and electromigration effects at high frequencies under the influence of extrinsic scatterers and skin effect. The findings indicate a substantial increase in crosstalk noise and signal distortion at higher frequencies, reinforcing the need for precise impedance modeling and mitigation techniques.
- An MLGNR-based single-tier VIS is proposed as a prospect for M-3D ICs. The combined equivalent circuit models are developed for MLGNR-based VIS to extract frequency-independent and frequency-dependent impedance parameters. This study establishes the feasibility of MLGNR VIS as a high-speed alternative for next-generation interconnect architectures.
- The challenges induced by scatterers, skin effect and crosstalk effect in perfect MLGNR VIS and realistic MLGNR VIS are analyzed. Additionally, a design methodology is proposed to optimize interconnect geometries and reduce the impact of process variations, thereby enhancing circuit performance and reliability.

7.4 Future Scope of the Work

Despite extensive research in the field of MLGNR-based interconnects over the past few decades, several challenges remain unresolved. The following are some potential avenues for future research based on the findings of this work:

- The performance analysis of realistic MLGNR degrades in the presence of challenges posed by extrinsic scatterers, skin effect and crosstalk effect. However, exploring the impact of these challenges on realistic MLGNR interconnects working in sub-threshold regime for ultra-low power systems remains a subject for future research. In addition, the performance of realistic MLGNR interconnects has been analyzed at the global level and can be further extended to local and intermediate interconnect levels.
- Theoretical studies suggest that the equivalent resistance of intercalation-doped VTC-MLGNR is substantially lower and may become a suitable candidate for MLGNR-based on-chip interconnects. However, fabricated VTC-MLGNRs are not yet available

and its related fabrication process is challenging. Therefore, this challenge can be addressed as a potential area for future research.

- An all-graphene-based driver interconnect load scheme can be an interesting problem to explore considering extrinsic scatterers, skin effect and crosstalk effect.
- The impact of extrinsic scatterers, skin effect and crosstalk effect on the performance of Cu-carbon nanotube composites, Cu-Graphene hybrids, and Cu-Carbon hybrids need to be analyzed.
- Edge passivation with fluorine and boron atoms can be explored to enhance the electronic and transport properties of armchair GNRs for interconnect applications.

References

[1] V. R. Kumbhare *et al.*, "High-Speed Interconnects: History, Evolution, and the Road Ahead," *IEEE Microw Mag*, vol. 23, no. 8, pp. 66-82, Aug. 2022, doi: 10.1109/MMM.2021.3136268.

[2] IRDS, "The International Roadmap for Devices and Systems 2022," Accessed: Mar. 30, 2023. [Online]. Available: https://irds.ieee.org/editions/2022

[3] S. Kumar and R. Sharma, "Analytical model for resistivity and mean free path in on-chip interconnects with rough surfaces," *IEEE Trans Emerg Top Comput*, vol. 6, no. 2, pp. 233-243, Apr. 2018, doi: 10.1109/TETC.2016.2597542.

[4] S. Kumar and R. Sharma, "Analytical modeling and performance benchmarking of on-chip interconnects with rough surfaces," *IEEE Transactions on Multi-Scale Computing Systems*, vol. 4, no. 3, pp. 272-284, Jul. 2018, doi: 10.1109/TMSCS.2017.2696941.

[5] J. S. Chawla, F. Gstrein, K. P. O'Brien, J. S. Clarke, and D. Gall, "Electron scattering at surfaces and grain boundaries in Cu thin films and wires," *Phys Rev B Condens Matter Mater Phys*, vol. 84, no. 23, Dec. 2011, doi: 10.1103/PhysRevB.84.235423.

[6] W. Steinhögl, G. Schindler, G. Steinlesberger, and M. Engelhardt, "Size-dependent resistivity of metallic wires in the mesoscopic range," *Phys Rev B Condens Matter Mater Phys*, vol. 66, no. 7, pp. 1-4, Aug. 2002, doi: 10.1103/PhysRevB.66.075414.

[7] ITRS, "The International Technology Roadmap 2013," Accessed: Oct. 30, 2019. [Online]. Available: https://www.semiconductors.org/resources/2013-international-technology-roadmap-for-semiconductors-itrs/

[8] J. D. Meindl, "Beyond Moore's Law: the interconnect era," *Comput Sci Eng*, vol. 5, no. 1, pp. 20-24, Jan. 2003, doi: 10.1109/MCISE.2003.1166548.

[9] H. Li, C. Xu and K. Banerjee, "Carbon Nanomaterials: The Ideal Interconnect Technology for Next-Generation ICs," *IEEE Des Test Comput*, vol. 27, no. 4, pp. 20-31, Mar. 2010, doi: 10.1109/MDT.2010.55.

[10] C. Xu, H. Li, and K. Banerjee, "Modeling, analysis, and design of graphene nano-ribbon interconnects," *IEEE Trans Electron Devices*, vol. 56, no. 8, pp. 1567-1578, Jul. 2009, doi: 10.1109/TED.2009.2024254.

[11] B. K. Kaushik, M. K. Majumder and V. R. Kumar, "Carbon Nanotube Based 3-D Interconnects - A Reality or a Distant Dream," *IEEE Circuits Syst Mag*, vol. 14, no. 4, pp. 16-35, Nov. 2014, doi: 10.1109/MCAS.2014.2360787.

[12] A. K. Geim and K. S. Novoselov, "The rise of graphene," *Nature Mater*, vol. 6, pp. 183-191, Mar. 2007, doi: 10.1038/nmat1849.

[13] S. S. Datta, D. R. Strachan, S. M. Khamis, and A. T. C. Johnson, "Crystallographic etching of few-layer graphene," *Nano Lett*, vol. 8, no. 7, pp. 1912-1915, Jul. 2008, doi: 10.1021/nl080583r.

[14] C. Berger, Z. Song, X. Li, X. Wu, N. Brown, C. Naud, D. Mayou, T. Li, J. Hass, A. N. Marchenkov, E. H. Conrad, P. N. First, and W. A. D. Heer, "Electronic Confinement and Coherence in Patterned Epitaxial Graphene." *Sci*, vol. 312, no. 5777, pp. 1191-1196, May 2006. doi: 10.1126/science.1125925.

[15] J. Jiang, J. Kang, W. Cao, X. Xie, H. Zhang, J. H. Chu, W. Liu, and K. Banerjee, "Intercalation Doped Multilayer-Graphene-Nanoribbons for Next-Generation Interconnects," *Nano Lett*, vol. 17, no. 3, pp. 1482-1488, Mar. 2017, doi: 10.1021/acs.nanolett.6b04516.

[16] A. Naeemi and J. D. Meindl, "Compact physics-based circuit models for graphene nanoribbon interconnects," *IEEE Trans Electron Devices*, vol. 56, no. 9, pp. 1822-1833, Sept. 2009, doi: 10.1109/TED.2009.2026122.

[17] T. Kaur, M. K. Rai, and R. Khanna, "Analysis of Temperature-Dependent Functional and Dynamic Crosstalk Noise in Adjacent Interconnects of Doped Multilayer Graphene Nanoribbon with Armchair and Zigzag Edges," *physica status solidi (a)*, vol. 216, no. 22, pp. 1900591(1-8), Nov. 2019, doi: 10.1002/pssa.201900591.

[18] A. K. Nishad and R. Sharma, "Lithium-Intercalated Graphene Interconnects: Prospects for On-Chip Applications," *IEEE J Electron Devices Soc*, vol. 4, no. 6, pp. 485-489, Nov. 2016, doi: 10.1109/JEDS.2016.2614813.

[19] A. K. Nishad and R. Sharma, "Analytical time-domain models for performance optimization of multilayer GNR interconnects," *IEEE J Sel Top Quantum Electron*, vol. 20, no. 1, Jan. 2014, doi: 10.1109/JSTQE.2013.2272458.

[20] J. Jiang, J. Kang, and K. Banerjee, "Characterization of self-heating and current-carrying capacity of intercalation doped graphene-nanoribbon interconnects," in *IEEE Int Reliab Phys Symp Proc*, Monterey, CA, USA, May 2017, pp. 6B-1.1-6B-1.6, doi: 10.1109/IRPS.2017.7936339.

[21] S. Das, S. Bhattacharya, D. Das, and H. Rahaman, "Modeling and Analysis of Electro-Thermal Impact of Crosstalk Induced Gate Oxide Reliability in Pristine and Intercalation Doped MLGNR Interconnects," *IEEE Trans. Device Mater Reliab*, vol. 19, no. 3, pp. 543-550, Sep. 2019, doi: 10.1109/TDMR.2019.2933035.

[22] T. Kaur, M. K. Rai, and R. Khanna, "Effect of temperature on the performance analysis of MLGNR interconnects," *J Comput Electron*, vol. 18, no. 2, pp. 722-736, Jun. 2019, doi: 10.1007/s10825-018-01297-w.

[23] W. Bao, J. Wan, X. Han, X. Cai, H. Zhu, D. Kim, D. Ma, Y. Xu, J. N. Munday, H. D. Drew, M. S. Fuhrer, and L. Hu, "Approaching the limits of transparency and conductivity in graphitic materials through lithium intercalation," *Nat Commun*, vol. 5, no. 4224, Jul. 2014, doi: 10.1038/ncomms5224.

[24] L.R. Hanlon, E.R. Falardeau, and J.E. Fischer, "Metallic reflectance of AsF_5 graphite intercalation compounds," *Solid State Commun*, vol. 24, no. 5, no. 377-381, Nov. 1977, doi: 10.1016/0038-1098(77)90986-3.

[25] B. K. Kaushik, V. R. Kumar, and A. Patnaik, *Crosstalk in Modern On-Chip Interconnects: A FDTD Approach*. Singapore: Springer, 2016.

[26] S. Rakheja, V. Kumar, and A. Naeemi, "Evaluation of the potential performance of graphene nanoribbons as on-chip interconnects," *Proc IEEE*, vol. 101, no. 7, pp. 1740-1765, Jul. 2013, doi: 10.1109/JPROC.2013.2260235.

[27] A. Contino, I. Ciofi, X. Wu, I. Asselberghs, U. Celano, C. J. Wilson, Z. Tökei, G. Groeseneken, B. Sorée, "Modeling of edge scattering in graphene interconnects," *IEEE Electron Device Lett*, vol. 39, no. 7, pp. 1085-1088, Jul. 2018, doi: 10.1109/LED.2018.2833633.

[28] M. Sanaeepur, "Dielectric surface roughness scattering limited performance of MLGNR interconnects," *IEEE Trans Electromagn Compat*, vol. 61, no. 2, pp. 532-537, Apr. 2019, doi: 10.1109/TEMC.2018.2830182.

[29] S. B. Touski and M. Pourfath, "Substrate surface corrugation effects on the electronic transport in graphene nanoribbons," *Appl Phys Lett*, vol. 103, no. 14, pp. 143506(1-3), Sep. 2013, doi: 10.1063/1.4824362.

[30] R. Sidhu, M. K. Rai, and B. K. Kaushik, "Temperature-dependent crosstalk between adjacent MLGNR interconnects of different dimensions and its impact on gate oxide reliability," *J Comput Electron*, vol. 19, no. 1, pp. 191-205, Mar. 2020, doi: 10.1007/s10825-020-01444-2.

[31] E. Pop, D. A. Mann, K. E. Goodson, and H. Dai, "Electrical and thermal transport in metallic single-wall carbon nanotubes on insulating substrates," *J Appl Phys*, vol. 101, no. 9, pp. 093710(1-10), May 2007. doi: 10.1063/1.2717855.

[32] R. Sidhu and M. K. Rai, "Electronic transport in doped and dielectric inserted MLGNR interconnects: Crosstalk induced delay and stability analyses at sub-threshold regime," *Microelectron J*, vol. 128, no. 105524, pp. 1-12, Oct. 2022, doi: 10.1016/j.mejo.2022.105524.

[33] G. Deepthi and M. Tatineni, "Crosstalk analysis of dielectric inserted side contact multilayer graphene nanoribbon interconnects for ternary logic system using unconditionally stable FDTD model," *Microelectron J*, vol. 133, no. 105698, pp. 1-10, Mar. 2023, doi: 10.1016/j.mejo.2023.105698.

[34] Q. Wu and Z. Pan, "Crosstalk optimization and gate oxide reliability analysis in intercalation doped MLGNR with reduced vertical thickness," *Microelectron Reliab*, vol. 155, no. 115363, pp. 1-10, Apr. 2024, doi: 10.1016/j.microrel.2024.115363.

[35] F. Zou, Z. Pan, and P. Xu, "Modeling and performance analysis of coupled multilayer graphene nanoribbon (MLGNR) interconnects with intercalation doping," *Microelectron J*, vol. 141, no. 105971, pp. 1-16, Nov. 2023, doi: 10.1016/j.mejo.2023.105971.

[36] L. Li and H.-S. P. Wong, “Integrating Graphene into Future Generations of Interconnect Wires,” in *IEEE Int Electron Devices Meeting (IEDM)*, San Francisco, CA, USA, Jan. 2019, pp. 5.5.1-5.5.4, doi: 10.1109/IEDM.2018.8614651.

[37] K. Banerjee, S. Im, and N. Srivastava, “Interconnect Modeling and Analysis in the Nanometer Era: Cu and Beyond,” in *Proc Adv Metallization Conf*, Colorado Springs, CO, Sep. 2005. [Online]. Available: https://www.researchgate.net/publication/268256873_Interconnect_Modeling_and_Analysis_in_the_Nanometer_Era_Cu_and_Beyond

[38] R. Achar and M. S. Nakhla, “Simulation of high-speed interconnects,” in *Proc IEEE*, vol. 89, no. 5, pp. 693-728, May 2001, doi: 10.1109/5.929650.

[39] R. Achar, “Modeling of high-speed interconnects,” *IEEE Microw Mag*, vol. 12, no. 5, pp. 61-74, Aug. 2011, doi: 10.1109/MMM.2011.941414.

[40] D. Sarkar, C. Xu, H. Li, and K. Banerjee, “High-frequency behavior of graphene-based interconnects-Part I: Impedance modeling,” *IEEE Trans Electron Devices*, vol. 58, no. 3, pp. 843-852, Mar. 2011, doi: 10.1109/TED.2010.2102031.

[41] H. Li and K. Banerjee, “High-frequency analysis of Carbon Nanotube interconnects and implications for on-chip inductor design,” *IEEE Trans Electron Devices*, vol. 56, no. 10, pp. 2202-2214, Oct. 2009, doi: 10.1109/TED.2009.2028395.

[42] D. Sarkar, C. Xu, H. Li, and K. Banerjee, “High-frequency behavior of graphene-based interconnects-Part II: Impedance analysis and implications for inductor design,” *IEEE Trans Electron Devices*, vol. 58, no. 3, pp. 853-859, Mar. 2011, doi: 10.1109/TED.2010.2102035.

[43] M. D'Amore, M. S. Sarto and A. G. D'Aloia, “Skin-effect modeling of carbon nanotube bundles: The high-frequency effective impedance,” *IEEE Int Symp Electromagn Compat*, Fort Lauderdale, FL, USA, Jul. 2010, pp. 847-852, doi: 10.1109/ISEMC.2010.5711390.

[44] Y. Eo and W. R. Eisenstadt, “High-speed VLSI interconnect modeling based on S-parameter measurements,” *IEEE Trans Comp Hybrids Manuf Technol*, vol. 16, no. 5, pp. 555-562, Aug. 1993, doi: 10.1109/33.239889.

[45] S. M. Wentworth, M. E. Baginski, D. L. Faircloth, S. M. Rao and L. S. Riggs, "Calculating Effective Skin Depth for Thin Conductive Sheets," IEEE Antennas and Propagation Society International Symposium, Albuquerque, NM, USA, Jul. 2006, pp. 4845-4848, doi: 10.1109/APS.2006.1711728.

[46] R. Murali, Y. Yang, K. Brenner, T. Beck, and J. D. Meindl, "Breakdown current density of graphene nanoribbons," *Appl Phys Lett*, vol. 94, no. 24, pp. 243114(1-4), Jun. 2009, doi: 10.1063/1.3147183.

[47] X. Chen, D. H. Seo, S. Seo, H. Chung and H.-S. P. Wong, "Graphene interconnect lifetime under high current stress," *Symp VLSI Technol*, Honolulu, HI, USA, Jul. 2012, pp. 121-122, doi: 10.1109/VLSIT.2012.6242491.

[48] K. J. Lee, A. P. Chandrakasan, and J. Kong, "Breakdown current density of CVD-grown multilayer graphene interconnects," *IEEE Electron Device Lett*, vol. 32, no. 4, pp. 557-559, Apr. 2011, doi: 10.1109/LED.2011.2108259.

[49] K. Agashiwala, J. Jiang, K. Parto, D. Zhang, C. H. Yeh, and K. Banerjee, "Demonstration of CMOS-Compatible Multi-Level Graphene Interconnects with Metal Vias," *IEEE Trans Electron Devices*, vol. 68, no. 4, pp. 2083-2091, Apr. 2021, doi: 10.1109/TED.2021.3061637.

[50] M. H. Moaiyeri, Z. M. Taheri, M. R. Khezeli, and A. Jalali, "Efficient passive shielding of MWCNT interconnects to reduce crosstalk effects in multiple-valued logic circuits," *IEEE Trans Electromagn Compat*, vol. 61, no. 5, pp. 1593-1601, Oct. 2019, doi: 10.1109/TEMC.2018.2863378.

[51] A. Nieuwoudt and Y. Massoud, "On the impact of process variations for carbon nanotube bundles for VLSI interconnect," *IEEE Trans Electron Devices*, vol. 54, no. 3, pp. 446-455, Mar. 2007, doi: 10.1109/TED.2006.890364.

[52] P. Lamberti and V. Tucci, "Impact of the variability of the process parameters on CNT-based nanointerconnects performances: A comparison between SWCNTs bundles and MWCNT," *IEEE Trans Nanotechnol*, vol. 11, no. 5, pp. 924-933, Jul. 2012, doi: 10.1109/TNANO.2012.2207124.

[53] S. Gharavi Hamedani and M. H. Moaiyeri, "Impacts of Process and Temperature Variations on the Crosstalk Effects in Sub-10 nm Multilayer Graphene Nanoribbon

Interconnects," *IEEE Trans Device Mater Reliab*, vol. 19, no. 4, pp. 630-641, Dec. 2019, doi: 10.1109/TDMR.2019.2937789.

[54] R. Sidhu and M. K. Rai, "Transient analysis in doped MLGNR for subthreshold interconnects under process-induced physical and geometrical parameters," *J Comput Electron*, vol. 22, no. 1, pp. 581-595, Feb. 2023, doi: 10.1007/s10825-022-01967-w.

[55] M. R. Khezeli, A. Jalali, and M. H. Moaiyeri, "On the impacts of process and temperature variations on the crosstalk effects in MWCNT bundle nanointerconnects in ternary logic," *IEEE Trans Nanotechnol*, vol. 17, no. 2, pp. 238-249, Mar. 2018, doi: 10.1109/TNANO.2018.2789999.

[56] K. Dhananjay, P. Shukla, V. F. Pavlidis, A. Coskun, and E. Salman, "Monolithic 3D Integrated Circuits: Recent Trends and Future Prospects," *IEEE Trans Circuits Syst II: Express Briefs*, vol. 68, no. 3, pp. 837-843, Mar. 2021, doi: 10.1109/TCSII.2021.3051250.

[57] J. Jiang, J. Kang, J. H. Chu, and K. Banerjee, "All-carbon interconnect scheme integrating graphene-wires and carbon-nanotube-vias," in *IEEE Int Electron Devices Meeting*, San Francisco, CA, USA, Dec. 2017, pp. 14.3.1-14.3.4, doi: 10.1109/IEDM.2017.8268389.

[58] J. Jiang, K. Parto, W. Cao, and K. Banerjee, "Ultimate Monolithic-3D Integration With 2D Materials: Rationale, Prospects, and Challenges," *IEEE J Electron Devices Soc*, vol. 7, pp. 878-887, Jun. 2019, doi: 10.1109/jeds.2019.2925150.

[59] X. Chen, D. H. Seo, S. Seo, H. Chung, and H. S. P. Wong, "Graphene interconnect lifetime: A reliability analysis," *IEEE Electron Device Lett*, vol. 33, no. 11, pp. 1604-1606, Sep. 2012, doi: 10.1109/LED.2012.2211564.

[60] S. Pathania, S. Kumar, and R. Sharma, "Analyzing Crosstalk-Induced Effects in Rough On-Chip Copper Interconnects," *IEEE Trans Compon Packaging Manuf Technol*, vol. 9, no. 10, pp. 1984-1992, Oct. 2019, doi: 10.1109/TCPMT.2019.2941871.

[61] K. Zhou, *Carbon Nanomaterials: Modeling, Design, and Applications*. Boca Raton: CRC Press, 2019.

[62] B. K. Kaushik, V. R. Kumar, M. K. Majumder, and A. Alam, *Through silicon vias materials, models, design, and performance.* Boca Raton: CRC Press, 2016.

[63] J. K. Thind, M. Kumar and B. K. Kaushik, "Electrical Tuning of Optical Delay in Graphene-Based Photonic Crystal Waveguide," *IEEE J Quantum Electron*, vol. 51, no. 10, pp. 1-5, Oct. 2015, doi: 10.1109/JQE.2015.2476353.

[64] A. K. Upadhyay, A. K. Kushwaha, P. Rastogi, Y. S. Chauhan and S. K. Vishvakarma, "Explicit Model of Channel Charge, Backscattering, and Mobility for Graphene FET in Quasi-Ballistic Regime," *IEEE Trans Electron Devices*, vol. 65, no. 12, pp. 5468-5474, Dec. 2018, doi: 10.1109/TED.2018.2877631.

[65] D. Warepam, K. J. Singh, R. S. Dhar, "CNT-based enhanced GaAs/InAs multiple quantum well solar cell," *J Comput Electron*, vol. 23, pp. 382-395, Apr. 2024, doi.org/10.1007/s10825-024-02138-9

[66] W.-Y. Yin and W.-S. Zhao, "Modeling of carbon nanotube (CNT) interconnects," in *IEEE Workshop Signal Propag Inter*, Naples, Italy, May 2011, pp. 79-82, doi: 10.1109/SPI.2011.5898845.

[67] J. Kumar, M. K. Majumder, B. K. Kaushik, S. Dasgupta and S. K. Manhas, "Novel modeling approach for multi-walled CNT bundle in global VLSI interconnects," in *IEEE International Conference on Communications, Devices and Intelligent Systems*, Kolkata, India, Jan. 2013, pp. 476-479, doi: 10.1109/CODIS.2012.6422242.

[68] M. K. Majumder, B. K. Kaushik, and S. K. Manhas, "Analysis of delay and dynamic crosstalk in bundled carbon nanotube interconnects," *IEEE Trans Electromagn Compat*, vol. 56, no. 6, pp. 1666-1673, Dec. 2014, doi: 10.1109/TEMC.2014.2318017.

[69] M. K. Rai, H. Garg, and B. K. Kaushik, "Temperature-Dependent Modeling and Crosstalk Analysis in Mixed Carbon Nanotube Bundle Interconnects," *J Electron Mater*, vol. 46, no. 8, pp. 5324-5337, Aug. 2017, doi: 10.1007/s11664-017-5538-1.

[70] D. Das and H. Rahaman, *Carbon Nanotube and Graphene Nanoribbon Interconnects.* Boca Raton: CRC Press, 2017.

[71] T. Yu, C. W. Liang, C. Kim, E. S. Song, and B. Yu, "Three-dimensional stacked multilayer graphene interconnects," *IEEE Electron Device Lett*, vol. 32, no. 8, pp. 1110-1112, Aug. 2011, doi: 10.1109/LED.2011.2158385.

[72] W. S. Zhao *et al.*, "Vertical Graphene Nanoribbon Interconnects at the End of the Roadmap," *IEEE Trans Electron Devices*, vol. 65, no. 6, pp. 2632-2637, Jun. 2018, doi: 10.1109/TED.2018.2822664.

[73] W. Li, W. S. Zhao, P. W. Liu, J. Wang, and G. Wang, "Optimal repeater insertion for horizontal and vertical graphene nanoribbon interconnects," *Int J Numer Model: Electron Netw Devices Fields*, vol. 33, no. 2, pp. 1-14, Mar. 2020, doi: 10.1002/jnm.2696.

[74] M. Nihei, A. Kawabata, T. Murakami, M. Sato and N. Yokoyama, "Improved thermal conductivity by vertical graphene contact formation for thermal TSV," in *IEEE Int Electron Devices Meet*, San Francisco, CA, USA, Dec. 2012, pp. 33.5.1-33.5.4, doi: 10.1109/IEDM.2012.6479159.

[75] M. S. Dresselhaus and G. Dresselhaus, "Intercalation compounds of graphite," *Adv Phys*, vol. 30, no. 2, pp. 139-326, Jan. 1981, doi: 10.1080/00018738100101367.

[76] A. Naeemi and J. D. Meindl, "Conductance modeling for graphene nanoribbon (GNR) interconnects," *IEEE Electron Device Lett*, vol. 28, no. 5, pp. 428-431, May 2007, doi: 10.1109/LED.2007.895452.

[77] J. Lee *et al.*, "Understanding Electromigration in Cu-CNT Composite Interconnects: A Multiscale Electrothermal Simulation Study," *IEEE Trans Electron Devices*, vol. 65, no. 9, pp. 3884-3892, Sep. 2018, doi: 10.1109/TED.2018.2853550.

[78] A. Singh, B. Kumar Kaushik, and R. Dhiman, "Modeling and Analysis of Cu-Carbon Nanotube Composites for Sub-Threshold Interconnects," *IEEE Open J Nanotechnol*, vol. 3, pp. 236-243, Nov. 2022, doi: 10.1109/OJNANO.2022.3221141.

[79] A. Kumar and B. Kaushik, "Transient Analysis of Hybrid Cu-CNT On-Chip Interconnects Using MRA Technique," *IEEE Open J Nanotechnol*, vol. 3, pp. 24-35, 2022, doi: 10.1109/OJNANO.2021.3138344.

[80] Z. H. Cheng *et al.*, "Analysis of Cu-Graphene Interconnects," *IEEE Access*, vol. 6, pp. 53499-53508, Sep. 2018, doi: 10.1109/ACCESS.2018.2869468.

[81] B. Kumari, R. Kumar, R. Sharma, and M. Sahoo, "Design, Modeling and Analysis of Cu-Carbon Hybrid Interconnects," *IEEE Access*, vol. 9, pp. 113577-113584, Aug. 2021, doi: 10.1109/ACCESS.2021.3104299.

[82] B. Kumari, R. Sharma, and M. Sahoo, "Electro-thermal modeling and reliability analysis of Cu-carbon hybrid interconnects for beyond-CMOS computing," *Appl Phys Lett*, vol. 121, no. 10, pp. 101901(1-6), Sep. 2022, doi: 10.1063/5.0101329.

[83] R. M. Sundaram, A. Sekiguchi, M. Sekiya, T. Yamada, and K. Hata, "Copper/carbon nanotube composites: Research trends and outlook," *R Soc Open Sci*, vol. 5, no. 11, pp. 180814(1-21), Nov. 2018. doi: 10.1098/rsos.180814.

[84] X. Chen, D. Akinwande, K.-J. Lee, G. Close, S. Yasuda, B. C. Paul, S. Fujita, J. Kong and H.-S. P. Wong., "Fully integrated graphene and carbon nanotube interconnects for gigahertz high-speed CMOS electronics," *IEEE Trans Electron Devices*, vol. 57, no. 11, pp. 3137-3143, Nov. 2010, doi: 10.1109/TED.2010.2069562.

[85] S. J. Han, A. V. Garcia, S. Oida, K. A. Jenkins, and W. Haensch, "Graphene radio frequency receiver integrated circuit," *Nat Commun*, vol. 5, no. 3086, pp. 1-6, Jan. 2014, doi: 10.1038/ncomms4086.

[86] R. Murali, K. Brenner, Y. Yang, T. Beck, and J. D. Meindl, "Resistivity of graphene nanoribbon interconnects," *IEEE Electron Device Lett*, vol. 30, no. 6, pp. 611-613, Jun. 2009, doi: 10.1109/LED.2009.2020182.

[87] X. Du, I. Skachko, A. Barker, and E. Y. Andrei, "Approaching ballistic transport in suspended graphene," *Nat Nanotechnol*, vol. 3, no. 8, pp. 491-495, Jul. 2008, doi: 10.1038/nnano.2008.199.

[88] K. I. Bolotin *et al.*, "Ultrahigh electron mobility in suspended graphene," *Solid State Commun*, vol. 146, no. 9-10, pp. 351-355, Jun. 2008, doi: 10.1016/j.ssc.2008.02.024.

[89] W. Bao *et al.*, "Stacking-dependent band gap and quantum transport in trilayer graphene," *Nat Phys*, vol. 7, no. 12, pp. 948-952, Sep. 2011, doi: 10.1038/NPHYS2103.

[90] X. Wang, Y. Ouyang, X. Li, H. Wang, J. Guo, and H. Dai, "Room-temperature all-semiconducting sub-10-nm graphene nanoribbon field-effect transistors," *Phys Rev Lett*, vol. 100, no. 20, pp. 206803(1-4), May 2008, doi: 10.1103/PhysRevLett.100.206803.

[91] S. Das, D. Das, and H. Rahaman, "Electro-thermal RF modeling and performance analysis of graphene nanoribbon interconnects," *J Comput Electron*, vol. 17, no. 4, pp. 1695-1708, Dec. 2018, doi: 10.1007/s10825-018-1245-2.

[92] A. Y. Goharrizi, M. Pourfath, M. Fathipour, H. Kosina, and S. Selberherr, “An analytical model for line-edge roughness limited mobility of graphene nanoribbons,” *IEEE Trans Electron Devices*, vol. 58, no. 11, pp. 3725-3735, Nov. 2011, doi: 10.1109/TED.2011.2163719.

[93] G. Antonini, A. Orlandi and M. D'Amore, “Skin and proximity effects modeling in micro-wires based on carbon nanotube bundles,” in *IEEE Inter Symp Electromagn Compat*, York, UK, Sep. 2011, pp. 345-350.

[94] S. X. D. Tan, H. Amrouch, T. Kim, Z. Sun, C. Cook, and J. Henkel, “Recent advances in EM and BTI induced reliability modeling, analysis and optimization (invited),” *Integr*, vol. 60, pp. 132-152, Jan. 2018, doi: 10.1016/j.vlsi.2017.08.009.

[95] M. N. O. Sadiku, E. M. Issa, J. O. Attia and O. D. Momoh, “Substrate coupling in mixed signal integrated circuits,” in *Proceedings of IEEE Southeastcon*, Nashville, TN, USA, Apr. 2011, pp. 401-404, doi: 10.1109/SECON.2011.5752974.

[96] K. Agarwal, D. Sylvester, and D. Blaauw, “Modeling and analysis of crosstalk noise in coupled RLC interconnects,” *IEEE Trans Computer-Aided Des Integr Circuits Syst*, May 2006, pp. 892-901. doi: 10.1109/TCAD.2005.855961.

[97] W.-S. Zhao and W.-Y. Yin, “Comparative Study on Multilayer Graphene Nanoribbon (MLGNR) Interconnects,” *IEEE Trans Electromagn Compat*, vol. 56, no. 3, pp. 638-645, June 2014, doi: 10.1109/TEMC.2014.2301196.

[98] D. Sylvester and C. Wu, “Analytical modeling and characterization of deep-submicrometer interconnect,” *Proc IEEE*, vol. 89, no. 5, pp. 634-664, 2001, doi: 10.1109/5.929648.

[99] D. Das and H. Rahaman, “Analysis of Crosstalk in Single- and Multiwall Carbon Nanotube Interconnects and Its Impact on Gate Oxide Reliability,” *IEEE Trans Nanotechnol*, vol. 10, no. 6, pp. 1362-1370, 2011, doi: 10.1109/TNANO.2011.2146271.

[100] M. Sahoo and H. Rahaman, “Modeling and analysis of crosstalk induced overshoot/undershoot effects in multilayer graphene nanoribbon interconnects and its impact on gate oxide reliability,” *Microelectron Reliab*, vol. 63, pp. 231-238, Aug. 2016, doi: 10.1016/j.microrel.2016.06.017.

[101] D. Das and H. Rahaman, “Crosstalk and Gate Oxide Reliability Analysis in Graphene Nanoribbon Interconnects,” in *IEEE Int Symp Electron Syst Des*, Kochi, India, Dec. 2011, pp. 182-187, doi: 10.1109/ISED.2011.54.

[102] F. Golnaraghi and B.C. Kuo, *Automatic control systems*. New York: McGraw-Hill Education, 2017.

[103] H. Aghababa and N. Masoumi, “Time-Domain Analysis of Carbon Nanotubes,” in *IEEE Workshop Signal Propag Inter*, Avignon, France, May 2008, pp. 1-4, doi: 10.1109/SPI.2008.4558405.

[104] V. Kumar, S. Rakheja, and A. Naeemi, “Performance and energy-per-bit modeling of multilayer graphene nanoribbon conductors,” *IEEE Trans Electron Devices*, vol. 59, no. 10, pp. 2753-2761, 2012, doi: 10.1109/TED.2012.2208753.

[105] J. P. Cui, W. S. Zhao, W. Y. Yin, and J. Hu, “Signal transmission analysis of multilayer graphene nano-ribbon (MLGNR) interconnects,” *IEEE Trans Electromagn Compat*, vol. 54, no. 1, pp. 126-132, Feb. 2012, doi: 10.1109/TEMC.2011.2172947.

[106] M. K. Rai, S. Arora, and B. K. Kaushik, “Temperature-dependent modeling and performance analysis of coupled MLGNR interconnects,” *Int J Circuit Theory Appl*, vol. 46, no. 2, pp. 299-312, Feb. 2018, doi: 10.1002/cta.2384.

[107] M. Sanaeepur, “Crosstalk Delay and Stability Analysis of MLGNR Interconnects on Rough Surface Dielectrics,” *IEEE Trans Nanotechnol*, vol. 18, pp. 1181-1187, Oct. 2019, doi: 10.1109/TNANO.2019.2945354.

[108] S. G. Hamedani and M. H. Moaiyeri, “Comparative Analysis of the Crosstalk Effects in Multilayer Graphene Nanoribbon and MWCNT Interconnects in Sub-10 nm Technologies,” *IEEE Trans Electromagn Compat*, vol. 62, no. 2, pp. 561-570, Apr. 2020, doi: 10.1109/TEMC.2019.2903567.

[109] T. Kaur, M. K. Rai, and R. Khanna, “Temperature-Dependent Circuit Modeling and Performance Evaluation Due to Crosstalk in Capacitively Coupled Interconnects of Intercalation-Doped Multilayer Graphene Nanoribbon,” *Arab J Sci Eng*, vol. 46, no. 2, pp. 1079-1093, Feb. 2021, doi: 10.1007/s13369-020-04892-x.

[110] V. K. Nishad, A. K. Nishad, B. K. Kaushik, and R. Sharma, “First-Principle Analysis of Transition Metal Edge-Passivated Armchair Graphene Nanoribbons for Nanoscale

Interconnects," *IEEE Trans Nanotechnol*, vol. 20, pp. 92-98, Jan. 2021, doi: 10.1109/TNANO.2020.3048734.

[111] A. Kumar and B. K. Kaushik, "Edge-Roughness Aware EM-RA Model for Signal Integrity Analysis in MLGNR Interconnects," *IEEE Trans Compon Packaging Manuf Technol*, vol. 11, no. 2, pp. 273-283, Feb. 2021, doi: 10.1109/TCPMT.2020.3043198.

[112] A. Kumar and B. Kaushik, "Edge and Dielectric Surface Roughness-Aware EM-RA Model for MLGNR Interconnects," *IEEE Trans Nanotechnol*, vol. 20, pp. 567-575, Jun. 2021, doi: 10.1109/TNANO.2021.3093174.

[113] B. Kumari, R. Sharma, and M. Sahoo, "Performance and reliability improvement in intercalated MLGNR interconnects using optimized aspect ratio," *Sci Rep*, vol. 12, no. 1, pp. 1475(1-14), Dec. 2022, doi: 10.1038/s41598-022-05222-x.

[114] R. Sidhu and M. K. Rai, "Scattering-induced circuit modelling and performance analysis of coupled hybrid Interconnections: Sub-threshold performance evaluation," *Micro Nanostructures*, vol. 185, pp. 207707(1-15), Jan. 2024, doi: 10.1016/j.micrna.2023.207707.

[115] V. Ramesh Kumar, B. K. Kaushik, and A. Patnaik, "Crosstalk noise modeling of multiwall carbon nanotube (MWCNT) interconnects using finite-difference time-domain (FDTD) technique," *Microelectron Reliab*, vol. 55, no. 1, pp. 155-163, Jan. 2015, doi: 10.1016/j.microrel.2014.09.001.

[116] B. K. Kaushik, S. Sarkar, R. P. Agarwal, and R. C. Joshi, "Crosstalk analysis of simultaneously switching interconnects," *Int J Electron*, vol. 96, no. 10, pp. 1095-1114, Oct. 2009, doi: 10.1080/00207210902977806.

[117] B. K. Kaushik, S. Sarkar, and R. P. Agarwal, "Waveform analysis and delay prediction for a CMOS gate driving RLC interconnect load," *Integr*, vol. 40, no. 4, pp. 394-405, Jul. 2007, doi: 10.1016/j.vlsi.2006.06.001.

[118] B. K. Kaushik and S. Sarkar, "Crosstalk analysis for a CMOS gate driven inductively and capacitively coupled interconnects," *Microelectron J*, vol. 39, no. 12, pp. 1834-1842, Dec. 2008, doi: 10.1016/j.mejo.2008.03.015.

[119] X. C. Li, J. F. Mao, and M. Swaminathan, "Transient analysis of CMOS-gate-driven RLGC interconnects based on FDTD," *IEEE Trans Comput-Aided Des Integr Circuits Syst*, vol. 30, no. 4, pp. 574-583, Apr. 2011. doi: 10.1109/TCAD.2010.2095650.

[120] V. Ramesh Kumar, A. Alam, B. K. Kaushik, and A. Patnaik, "An unconditionally stable FDTD model for crosstalk analysis of VLSI interconnects," *IEEE Trans Compon Packaging Manuf Technol*, vol. 5, no. 12, pp. 1810-1817, Dec. 2015, doi: 10.1109/TCPMT.2015.2494519.

[121] M. Sahoo, P. Ghosal, and H. Rahaman, "Modeling and Analysis of Crosstalk Induced Effects in Multiwalled Carbon Nanotube Bundle Interconnects: An ABCD Parameter-Based Approach," *IEEE Trans Nanotechnol*, vol. 14, no. 2, pp. 259-274, Mar. 2015, doi: 10.1109/TNANO.2014.2388252.

[122] V. R. Kumar, M. K. Majumder, N. R. Kukkam, and B. K. Kaushik, "Time and Frequency Domain Analysis of MLGNR Interconnects," *IEEE Trans Nanotechnol*, vol. 14, no. 3, pp. 484-492, May 2015, doi: 10.1109/TNANO.2015.2408353.

[123] L. Akbari and R. Faez, "Crosstalk stability analysis in multilayer graphene nanoribbon interconnects," *Circuits Syst Signal Process*, vol. 32, no. 6, pp. 2653-2666, Dec. 2013, doi: 10.1007/s00034-013-9606-3.

[124] L. Qian, Y. Xia, S. Ge, Y. Ye, and J. Wang, "Stability analysis for coupled multilayer graphene nanoribbon interconnects," *Microelectron J*, vol. 58, pp. 32-38, Dec. 2016, doi: 10.1016/j.mejo.2016.10.007.

[125] T. Kaur, M. K. Rai, and R. Khanna, "Analytical Frequency-Domain Model for Coupled Interconnects of Doped Multilayer Graphene Nanoribbons and Mixed Carbon Nanotube Bundles," *physica status solidi (a)*, vol. 218, no. 4, pp. 2000588(1-15), Feb. 2021, doi: 10.1002/pssa.202000588.

[126] H. A. Wheeler, "Formulas for the Skin Effect," *IEEE Proc IRE*, vol. 30, no. 9, pp. 412-424, Sept. 1942, doi: 10.1109/JRPROC.1942.232015.

[127] X. Li, L. S. Wu, and J. F. Mao, "High-Frequency Analysis of Intercalated Multilayer Graphene (IMLG) and Implication for Tunable Terahertz Resonator Design," *IEEE Access*, vol. 5, pp. 7532-7541, May 2017, doi: 10.1109/ACCESS.2017.2701506.

[128] M. Kaur, N. Gupta, S. Kumar, B. Raj, and A. K. Singh, "Comparative radio-frequency and crosstalk analysis of carbon-based nano-interconnects," *IET Circuits Devices Syst*, vol. 15, no. 6, pp. 493-503, Sep. 2021, doi: 10.1049/cds2.12044.

[129] M. Kaur, N. Gupta, S. Kumar, B. Raj, and A. K. Singh, "RF analysis of intercalated graphene nanoribbon-based global-level interconnects," *J Comput Electron*, vol. 19, no. 3, pp. 1002-1013, Sep. 2020, doi: 10.1007/s10825-020-01530-5.

[130] J. R. Black, "Electromigration—A brief survey and some recent results," *IEEE Trans Electron Devices*, vol. 16, no. 4, pp. 338-347, Apr. 1969, doi: 10.1109/T-ED.1969.16754.

[131] J. P. Gambino, T. C. Lee, F. Chen and T. D. Sullivan, "Reliability challenges for advanced copper interconnects: Electromigration and time-dependent dielectric breakdown (TDDB)," in *IEEE Int Symp Phys Failure Analysis Integr Circuits*, Suzhou, China, Jul. 2009, pp. 677-684, doi: 10.1109/IPFA.2009.5232553.

[132] J. Jiang, J. H. Chu and K. Banerjee, "CMOS-Compatible Doped-Multilayer-Graphene Interconnects for Next-Generation VLSI," in *IEEE Int Electron Devices Meet (IEDM)*, San Francisco, CA, USA, Dec. 2018, pp. 34.5.1-34.5.4, doi: 10.1109/IEDM.2018.8614535.

[133] V. R. Kumbhare, P. P. Paltani, and M. K. Majumder, "Analysis of top- and side-contact MLGNR interconnects: impact on crosstalk, stability, and electromigration," *J Comput Electron*, vol. 19, no. 4, pp. 1588-1596, Dec. 2020, doi: 10.1007/s10825-020-01558-7.

[134] K. N. Reddy, M. K. Majumder, and B. K. Kaushik, "Delay uncertainty in MLGNR interconnects under process induced variations of width, doping, dielectric thickness and mean free path," *J Comput Electron*, vol. 13, no. 3, pp. 639-646, 2014, doi: 10.1007/s10825-014-0582-z.

[135] T. N. J. Kolanti and V. P. Kerehalli Shankar Rao, "Crosstalk noise analysis in ternary logic multilayer graphene nanoribbon interconnects using shielding techniques," *Int J Circuit Theory Appl*, vol. 48, no. 12, pp. 2041-2055, Dec. 2020, doi: 10.1002/cta.2889.

[136] M. D. Bishop, H. S. P. Wong, S. Mitra, and M. M. Shulaker, "Monolithic 3-D Integration," *IEEE Micro*, vol. 39, no. 6, pp. 16-27, Nov. 2019, doi: 10.1109/MM.2019.2942982.

[137] I. Ciofi *et al.*, “RC Benefits of Advanced Metallization Options,” *IEEE Trans Electron Devices*, vol. 66, no. 5, pp. 2339-2345, May 2019, doi: 10.1109/TED.2019.2902031.

[138] V. R. Kumar, M. K. Majumder, and B. K. Kaushik, “Graphene-based on-chip interconnects and TSVs: Prospects and challenges,” *IEEE Nanotechnol Mag*, vol. 8, no. 4, pp. 14-20, Dec. 2014, doi: 10.1109/MNANO.2014.2355275.

[139] Y. F. Liu, W. S. Zhao, Z. Yong, Y. Fang, and W. Y. Yin, “Electrical modeling of three-dimensional carbon-based heterogeneous interconnects,” *IEEE Trans Nanotechnol*, vol. 13, no. 3, pp. 488-495, Feb. 2014, doi: 10.1109/TNANO.2014.2307344.

[140] D. Goswami and M. K. Majumder, “Performance analysis of graphene nanoribbon based vertical interconnects — Through silicon vias,” in *IEEE Int Conf Comput Electr Commu Eng(ICCECE)*, Kolkata, India, 2016, pp. 1-4, doi: 10.1109/ICCECE.2016.8009559.

[141] N. M. Hossain, M. Hossain, A. H. B. Yousuf and M. H. Chowdhury, “Thermal aware Graphene based Through Silicon Via design for 3D IC,” in *IEEE Int 3D Syst Integr Conf* (3DIC), San Francisco, CA, USA, Oct. 2013, pp. 1-4, doi: 10.1109/3DIC.2013.6702385.

[142] S. G. Hamedani, M. H. Moaiyeri, M. Meghdadi, and M. R. Khezeli, “Vertical Noise Reduction in 3-D Mixed-Signal Integrated Circuits with Graphene Nanoribbon and Carbon Nanotube Interconnects,” *IEEE Trans Compon Packaging Manuf Technol*, vol. 11, no. 2, pp. 302-311, Feb. 2021, doi: 10.1109/TCPMT.2020.3045877.

[143] M. M. Sabry Aly *et al.*, “The N3XT Approach to Energy-Efficient Abundant-Data Computing,” *Proc IEEE*, vol. 107, no. 1, pp. 19-48, Jan. 2019, doi: 10.1109/JPROC.2018.2882603.

[144] M. M. Sabry Aly *et al.*, “Energy-Efficient Abundant-Data Computing: The N3XT 1,000x,” *Comput*, vol. 48, no. 12, pp. 24-33, Dec. 2015, doi: 10.1109/MC.2015.376.

[145] S. Datta, *Quantum Transport: Atom to Transistor*. Cambridge: Cambridge University Press, 2005.

[146] S. Datta, *Electronic Transport in Mesoscopic Systems*. Cambridge: Cambridge University Press, 1995.

[147] M. G. Kumar, Y. Agrawal, V. R. Kumar, R. Chandel, “A prominent unified crosstalk model for linear and sub-threshold regions in mixed CNT bundle interconnects,” *Microelectron J.*, vol. 118, no. 105294, pp. 1-11, Dec. 2021, doi.org/10.1016/j.mejo.2021.105294.

[148] R. Sharma, M. K. Rai, and R. Khanna, “Structure optimization: Configuring optimum performance of randomly distributed mixed carbon nanotube bundle interconnects,” *Int J Circuit Theory Appl*, vol. 51, no. 8, pp. 3949-3967, Mar. 2023, doi: 10.1002/cta.3605.

[149] S. H. Nasiri, R. Faez, and M. K. Moravvej-Farshi, “Compact formulae for number of conduction channels in various types of graphene nanoribbons at various temperatures,” *Modern Phys Lett B*, vol. 26, no. 1, pp. 1150004(1-5), Jan. 2012, doi: 10.1142/S0217984911500047.

[150] M. S. Sarto and A. Tamburrano, “Electromagnetic analysis of radio-frequency signal propagation along SWCN bundles,” in *IEEE Conf Nanotechnol*, Cincinnati, OH, USA, Jul. 2006, pp. 201-204, doi: 10.1109/NANO.2006.247607.

[151] M. N. O. Sadiku, *Elements of Electromagnetics*. Oxford University Press, 2010.

[152] L. Calderín, V. V. Karasiev, and S. B. Trickey, “Kubo–Greenwood electrical conductivity formulation and implementation for projector augmented wave datasets,” *Comput Phys Commun*, vol. 221, pp. 118-142, Dec. 2017, doi: 10.1016/j.cpc.2017.08.008.

[153] S. Dash and A. Patnaik, “Performance of Graphene Plasmonic Antenna in Comparison with Their Counterparts for Low-Terahertz Applications,” *Plasmonics*, vol. 13, no. 6, pp. 2353-2360, Dec. 2018, doi: 10.1007/s11468-018-0761-z.

[154] J. Zhang and E. G. Friedman, “Decoupling technique and crosstalk analysis for coupled RLC interconnects,” in *Proc IEEE Int Symp Circuits Syst*, Vancouver, BC, Canada, May 2004, pp. II-521, doi: 10.1109/ISCAS.2004.1329323.

[155] ITRS, “International Technology Roadmap for Semiconductors 2007.” Accessed: Oct. 30, 2019. [Online]. Available: https://www.semiconductors.org/resources/2007-international-technology-roadmap-for-semiconductors-itrs/

[156] K. Banerjee and A. Mehrotra, “Global (interconnect) warming,” *IEEE Circuits and Devices Magazine*, vol. 17, no. 5, pp. 16-32, Sep. 2001, doi: 10.1109/101.960685.

[157] W. Wirth, J. Comeaux, and S. Jang, "Characterization of flexible low-dielectric constant carbon-doped oxide (SiCOH) thin films under repeated mechanical bending stress," *J Mater Sci*, vol. 57, no. 46, pp. 21411-21431, Dec. 2022, doi: 10.1007/s10853-022-07987-y.

List of Publications

1. Akanksha Upadhyay, Mayank Kumar Rai and Rajesh Khanna, “Crosstalk Analysis of Multilayer Graphene Nanoribbon Interconnects in GHz Regime: Unraveling Scattering Induced Effects,” *Nano Communication Networks,* vol. 42, pp. 100552(1-11), Dec. 2024, doi: 10.1016/j.nancom.2024.100552.
2. Akanksha Upadhyay, Mayank Kumar Rai and Rajesh Khanna, “Analyzing Multilayer Graphene Nanoribbon Based Via-Interconnect Scheme: Prospects and Challenges for Monolithic 3D ICs,” *Physica status solidi (a)*, Nov. 2024, doi: 10.1002/pssa.202400469.
3. Akanksha Upadhyay, Mayank Kumar Rai and Rajesh Khanna, “High-frequency characteristics of multilayer graphene nanoribbon interconnects: Exploring the implications of skin-effect,” *Micro and Nanostructures*, vol. 189, pp. 207822(1-10), May 2024, doi: 10.1016/j.micrna.2024.207822.
4. Akanksha Upadhyay, Mayank Kumar Rai and Rajesh Khanna, “Delay Characterization of Multilayer Graphene Nanoribbon Interconnects in Presence of Scattering and Thermal Effects,” *International Journal of Numerical Modelling: Electronic Networks, Devices and Fields*, vol. 37, no. 1, pp. e3148(1-16), Jan. 2024, doi:10.1002/jnm.3148.
5. Akanksha Upadhyay, Mayank Kumar Rai and Rajesh Khanna, “Analysis of Multilayer Graphene Nanoribbon Interconnects constrained by Structural Edge Roughness and Corrugated Surface Dielectric,” *physica status solidi (a)*, vol. 219, no. 22, pp. 2200431(1-11), Nov. 2022, doi:10.1002/pssa.202200431.